MATERIAL CONSIDERATIONS FOR THE DEVELOPMENT OF SUPERCONDUCTING BORON DOPED NANOCRYSTALLINE DIAMOND DEVICES

DISSERTATION
submitted in partial fulfilment
of the requirements for the degree of
Doctor of Philosophy
in Physics

by

SCOTT MANIFOLD

Department of Physics and Astronomy
Cardiff University

October, 2022

For my mother, the best person I know.

And my father, I think you would have been proud…

"Ludwig Boltzman, who spent much of his life studying statistical mechanics, died in 1906, by his own hand. Paul Ehrenfest, carrying on the work, died similarly in 1933. Now it is our turn to study statistical mechanics. Perhaps it will be wise to approach the subject cautiously" - Opening lines of "States of Matter", by D.L. Goodstein

ABSTRACT

The work in this thesis is part of an ongoing project concerned with the development of superconducting devices using boron doped nanocrystalline diamond (B-NCD). Two aspects of device development were the focus of this work: the fabrication of low resistance ohmic metal electrical contacts and the investigation of the physics B-NCD Josephson junctions.

The contact resistance of titanium, chromium, molybdenum, tantalum and palladium contacts was investigated between 1.9 and 300 K. All contacts showed mechanical stability, robust to several temperature sweeps. All contact schemes remained ohmic throughout and showed low resistances ranging from Ti/Pt/Au with (8.83±0.10) × 10^{-4} Ω.cm to Ta/Pt/Au with (8.07±0.62) × 10^{-6} Ω.cm.

The candidate Josephson junction devices were investigated both in varying temperature and field. The temperature dependence of the superconducting gap Δ and critical currents I_c showed strong agreement across all device types and geometries, with all being well described by standard BCS theory and the model proposed by *Ambegaokar and Baratoff*. Fluctuation spectroscopy analysis was performed on temperature dependent conductance data from three structures, confirming that the effects of the material's granularity on the superconductivity still dominate in the smaller geometries of the devices. The field dependence of the critical currents for all devices was again insensitive to device type or geometry and does not conform to the expected Fraunhofer diffraction pattern. Instead, using the grain size distribution to provide the magnetically transparent dimensions of the junctions, a model was developed that accounts for the power law type drop off in $I_c(B)$. Given the results above, it is impossible for the geometry of the devices to be determining their behaviour. Instead, the distribution of grain sizes in the devices is what governs the physics of the Josephson junctions.

ACKNOWLEDGEMENTS

I am grateful to many people for their help, guidance and support throughout my PhD. Firstly, I must acknowledge my supervisors Prof. Oliver Williams and Prof. Sean Giblin. Not only did Prof. Williams provide the initial framework this project, both directly and indirectly through the running of the Cardiff Diamond Foundry, but I always enjoyed our discussions (scientific and otherwise) and appreciated the academic and personal support he provided me throughout my time in the research group. Prof. Giblin's contributions cannot be understated. Without his hands-on assistance with experimental issues, appreciation of the importance of teamwork and vociferously unsubtle personal style I'm confident that completing this work would have been impossible. I must also acknowledge Dr Georgina Klemencic for the vast amount of time she invested into training me in many aspects of experiment procedure. George's wise words from the first couple of months of my PhD, passed down from her PhD supervisor, of "it takes a long time to learn how to be careful enough to conduct this type of science" stuck with me and helped form the basis of my approach. The other excellent researchers from the group also made invaluable contributions. Often, I was reminded of Dr Soumen Mandal's wealth of experience, and he must be recognised for growing the films and conducting the bulk of the process flow for the junction devices. On top of this, Soumen provided critical training on various complex pieces of equipment and we enjoyed many excursions to the Swansea clean room (and one heist at Warwick) where we always agreed on the choice of restaurant. Dr Evan Thomas was also present on these field trips and contributed to my training, and I will forever appreciate the opportunity to learn from someone with an unsurpassed consideration of detail. Last, and certainly not least of the group, it was always a joy to work with Dr Jerome Cuenca. I could always rely on Jerome for assistance and was inspired by his excitement for the scientific process. I will never forget the speed and dexterity of his Labview coding when appropriately fuelled. Other PhD students also contributed

significantly to the junction experiments. I joined Dr Majdi Salman in wrestling with the procedure and the various successes and failures were a bonding experience. I will remember those times fondly. More recently, it was Yehya Megmmi's turn to join me in the lab, and I hope I was able to provide useful training and guidance. Many other people provided scientific assistance to me. I must acknowledge Dr Angela Sobiesierski and the rest of the team past and present from the Cardiff ICS cleanroom, including Tyrone Jones, Saleem Shabbir, Tom Peach and Samuel Everest. Another significant contribution came from Christopher Dunscombe, who patiently taught me the mystical arts of wire bonding.

I also would have struggled significantly more to complete me PhD without the support of existing and new friendships. If it were not for the humour and support of Henry Bland, with whom I shared many laughs and stories of the common frustrations of PhD life, I would have surely gone mad. Similarly, the support and friendship of William Pickering and James Hetherington was critical to navigating the isolation of pandemic lockdowns. Max Williams was always a kind and generous presence throughout my Masters studies at Warwick, and with Henry we enjoyed various conference adventures. There are countless others I am grateful for, particularly as bearers of baked goods and snacks. Chief amongst these is my partner Amelia, who has offered tireless and generous support during my writing period. I would also like to heartily thank Bob Health for his countless supportive conversations and guidance, and for helping me grow flowers around the lake.

Finally, I am forever grateful for having such a loving and supportive family. My nieces, Rosa and Emmeline, receive my gratitude for always being ridiculous, curious and kind. My sister and brother-in-law, Laura and Tom, for always listening and caring. My brother, Dominic, for reminding me who I am. My mother, Lindsay, who has an apparently limitless capacity for support, inspires me to be better and encouraged me to never to give up. And my father, Barry, who once said, "I think you should be an engineer, you'd be good at it." Close enough, I guess?

PUBLICATIONS

1. Salman, M., Klemencic, G. M., Mandal, S., Manifold, S., Mustafa, L., Williams, O. A., & Giblin, S. R. (2019). Quantitative analysis of the interaction between a dc SQUID and an integrated micromechanical doubly clamped cantilever. *Journal of Applied Physics*, *125*(22), 224503.

2. Manifold, S. A., Klemencic, G., Thomas, E. L. H., Mandal, S., Bland, H., Giblin, S. R., & Williams, O. A. (2021). Contact resistance of various metallisation schemes to superconducting boron doped diamond between 1.9 and 300 K. *Carbon*, *179*, 13–19.

3. Klemencic, G. M., Perkins, D. T. S., Fellows, J. M., Muirhead, C. M., Smith, R. A., Mandal, S., Manifold, S., Salman, M., Giblin, S. R., & Williams, O. A. (2021). Phase slips and metastability in granular boron-doped nanocrystalline diamond microbridges. *Carbon*, *175*, 43–49.

4. Cuenca, J. A., Brien, T., Mandal, S., Manifold, S., Doyle, S., Porch, A., Klemencic, G. M., & Williams, O. A. (2023). Superconducting boron doped nanocrystalline diamond microwave coplanar resonator. *Carbon*, *201*, 251–259.

CONTENTS

LIST OF FIGURES

LIST OF TABLES

1 INTRODUCTION

1.1 THE MATERIAL APPEAL OF DIAMOND

Diamond is a unique material that combines many extreme properties and, in many cases, far exceeds the performance of similar substances, offering distinctive opportunity for the development of devices that require a combination of these superlative properties. Of interest to the work related to this thesis is the high Young's Modulus (1200 GPa), thermal conductivity and the fact that sufficient boron doping can induce a metal-insulator transition and allow a superconducting state at approximately 4 K [1,2]. In this superconducting state, diamond shows high upper critical field values of up to 7 T [3,4]. Diamond also offers the opportunity for tuneable growth which can drastically alter its properties [5,6]. However, as will be discussed later there are several fabrication challenges when working with diamond, and the study of its superconducting properties is relatively incomplete in some key areas.

1.2 ONGOING PROJECT

The work contained in this thesis is part of an ongoing project within the Cardiff Diamond Foundry which aims to study the superconducting properties of boron

doped nanocrystalline diamond (B-NCD) and to use its remarkable properties to realise the design goals of micro and nano-electromechanical systems (MEMS and NEMS). These systems have received increasing attention for many technological applications and in the study of physical phenomena [7,8].

A key component of the MEMS or NEMS devices of interest is the mechanical resonator, which allows for the development of various types of highly sensitive detectors including those for the measurement of mass, acceleration, force, charge and displacement [7,9–11]. For example, it has been shown that a suspended nanowire can act as a mass sensor with a sensitivity of 10^{-24} kg [11]. Quality factor (Q-factor) represents the energy loss of a resonator over time, quantifying the ratio of energy stored in the resonator to the energy dissipated per cycle of vibration. High-quality factors are desirable for applications such as sensing, where the resonator's sensitivity is proportional to its Q-factor. Recent research has produced nanomechanical resonators with exceptional Q-factors, including values greater than 10^8 [12]. These high-Q resonators can be made from a variety of materials such as silicon, silicon nitride, and diamond. The Q-factor of a resonator is strongly influenced by the material and fabrication process. For example, the use of diamond can result in a Q-factor greater than 10^6 [13]. The frequency of a resonator is given by:

$$f_n = \eta_n \sqrt{\frac{E}{\rho}\frac{d}{\ell^2}} \tag{1.1}$$

where η_n is the mode number (equal to 1.028 for a doubly clamped resonator), E is the Young's Modulus, ρ is the density, d is the thickness and ℓ is the length [8]. Because the material's acoustic velocity $\sqrt{E/\rho}$ is proportional to the devices resonant frequency for a given mode number and geometry, it is a useful metric

for comparing potential device materials. Common material choices for MEMS and NEMS are silicon, silicon nitride and silicon carbide which have acoustic velocities of 8500 m/s, 10850 m/s and 13200 m/s respectively [14–16]. Diamond has a clear advantage here with an acoustic velocity of approximately 18000 m/s [17].

Cooling nanomechanical resonators to the vibrational ground state, where they have zero-point motion and minimal thermal noise, is essential for achieving the highest possible sensitivity and coherence in quantum information processing.

$$\bar{n} = \left(\frac{k_B T_R}{h f_R}\right) - \frac{1}{2}. \tag{1.2}$$

Equation (1.2) describes the thermal occupation of the resonator, where f_R is the resonant frequency, T_R is the temperature of the resonator, k_B is the Boltzman constant and h is the Plank constant [18]. The resonator is in the ground state with $\bar{n} \lesssim 1$, which indicates that a higher frequency allows ground state operation at higher temperatures. For example, a 1 GHz resonator would need to be cooled to approximately 50 mK, which is possible with the dilution refrigeration techniques discussed later. Zero-point motion refers to motion in the ground state due to the Heisenberg uncertainty principle. For an undriven beam, the amplitude of the zero-point motion has an amplitude $u_0 = \sqrt{h/4\pi m f_R}$ with m the resonator mass. A detector that can reach this level of precision is said to be at the quantum limit.

Nanoscale mechanical resonators have been produced with resonant frequencies in the MHz to GHz range. Examples of these devices include a silicon resonator with $f_R = 18$ MHz and SiC devices with $f_R = 134$ MHz or even as high as 1.029 GHz [19–22]. However, silicon has only exhibited superconductivity when doped

with boron and has a low superconducting transition temperature of $T_c = 0.15$ K, while doped SiC provides only a slightly higher value of $T_c = 1.5$ K [23,24]. Coupling a resonator to a superconducting circuit or qubit allows for quantum-coherent measurements which preserve the quantum states in the system that would experience rapid decoherence if coupled to a classical measurement system [25,26]. This was first achieved by *Etaki et al.* who showed that it was possible to achieve high precision motion detection with a resonator of length $\ell = 50\,\mu$m embedded in a superconducting quantum interference device (SQUID) fabricated from Niobium, shown in Figure 1.1. Niobium has an acoustic velocity of ~5000 m/s [27]. The resonator operated at a frequency of 2 MHz and achieved a precision of 133 fm, which is 36 times the quantum limit. In order to improve upon this sensitivity, and for the development in other applications, frequencies approaching 1 GHz must be achieved [8].

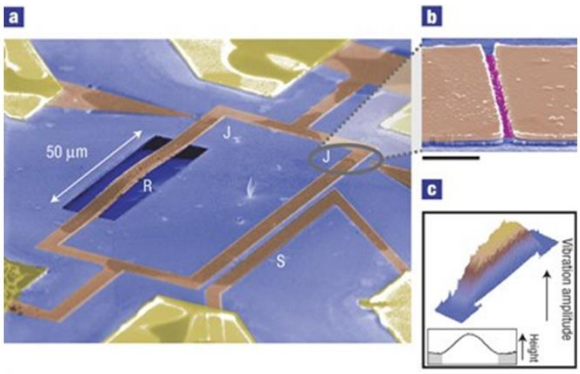

Figure 1.1: Micromechanical resonator embedded in a SQUID. a) Scanning electron micrograph of the device. b) One of the 200 nm long Josephson junctions. c) Three-dimensional image of the vibrational amplitude of the resonator, with the inset showing the static buckling profile. From *Etaki et al.* [26].

Diamond exhibits the highest known acoustic velocity of ~18000 m/s, so it is an obvious choice for device development [28]. NCD has been shown to maintain

similar properties to its single crystal variety and allows the 1 GHz limit to be pushed with device dimensions and temperatures within reach of fabrication techniques and cooling methods [29,30].

Bautze et al. have produced a resonator from superconducting B-NCD, as shown in Figure 1.1 [31]. This device operates at a resonant frequency of 10 MHz and was shown to remain in a superconducting state in fields of at least 3 T, paving the way for further integration into superconducting circuits. More recently, *Mandal et al.* fabricated a SQUID from B-NCD that demonstrated operation up to 4 T [3]. Despite this success, the disparity between the apparent Ginzburg-Landau coherence length of the material and the geometry of the Josephson in the SQUID raised questions about the physics underpinning the system. The details and consequences of this disparity will be discussed later.

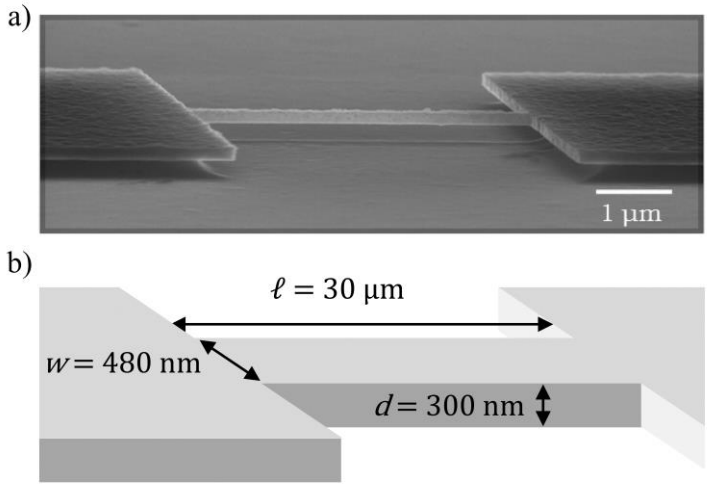

Figure 1.2: A superconducting B-NCD resonator. a) Scanning electron micrograph of the resonator, from *Bautze et al.* [31]. b) Diagram illustrating the dimensions of the device, with width w = 480 nm, length ℓ = 30 μm and thickness d = 300 nm.

1.3 THESIS MOTIVATION

The goal of the work contained within this thesis is to add further understanding to the specific fabrication and material considerations related to the design and implementation of B-NCD superconducting devices. Specifically, the physics governing the behaviour of the Josephson junctions that form a B-NCD SQUID device are not sufficiently well understood, and questions remain about the optimisation of electrical contacts to sensitive low temperature devices.

Chapter 2 introduces the theoretical background necessary for comprehension of the various principles investigated in this thesis. First, the concepts underpinning carrier transport in semiconductors are introduced. Included next is a discussion of the theories established by *Bardeen*, *Cooper* and *Schrieffer* (BCS), *Ginzburg* and *Landau* and also the London equations. Following on from this, superconducting interfaces are explained, providing context for a description of the Josephson effect and equations describing the temperature and field dependence of Josephson junctions are provided. Finally, this chapter provides a brief review of the latest understanding of the physics of superconductivity in B-NCD.

The experimental methods used throughout the work of this thesis are detailed in Chapter 3, including an explanation of various aspects of the process flow of device fabrication and how certain well-established techniques that need to be modified for B-NCD. Specifically, the growth methods used for the B-NCD films, photolithography and electron beam lithography, the etching method used for the films and wire bonding. Also discussed are the principles of Raman spectroscopy and dilution refrigeration.

Anecdotally, direct wire bonding to NCD films presents various challenges. Bond adhesion can be unreliable, particularly in the case of polished films, with

connections failing due to heat cycling induced stress. For this reason, a critical aspect of robust device realisation must be the development of reliable, ohmic and low contact resistance metal contacts. As is discussed at length in Section 4.1, the majority of the literature in this area is focussed on higher temperatures with the assumption that best practices established here apply to low temperature device operation. Due to the sensitive nature of nanoscale superconducting devices, these assumptions were investigated in Chapter 4.

Chapters 5-7 detail the experimental procedure and analysis performed on candidate Josephson junction devices. Chapter 5 introduces the discussion with reference to prior work and preliminary observations at low temperature and zero field, including an explanation of some of the analytical techniques used. Chapter 6 presents the analysis and discussion of the temperature dependence results from the devices, and Chapter 7 reports on their magnetic field dependence. The analysis in Chapter 7 required the development of a fitting algorithm that draws random samples from the grain size distribution established for the B-NCD film, the process of which is also explained here.

2 CARRIER TRANSPORT AND SUPERCONDUCTIVITY IN B-NCD

This chapter will first introduce the concepts central to understanding charge carrier transport in semiconductors and build on some of these topics to cover the background theory for metal-semiconductor electrical contacts superconductivity and Josephson junctions. Occasionally, these topics will be built upon later in this work during relevant pieces of analysis. Also contained in this section is an overview of the superconducting properties of B-NCD.

2.1 CARRIER TRANSPORT IN SEMICONDUCTORS

The study of different forms of matter is the focus of various specialities within physics. To understand the states known as insulators, semiconductors and metals we must look to the field of condensed matter physics. What follows is a discussion of some of the fundamental concepts and quantities relevant to the work presented in this thesis. Much of the more basic content of this subsection references the textbooks "Solid state electronic devices" by *Streetman & Banerjee*

[32], "Introduction to solid state physics" by *Kittel* [33] and "Physics of Semiconductor Devices" by *Sze* [34], which provide excellent reference for further detail. To comprehend charge transport in a material we consider the factors that dictate the position and movement of electrons and electron holes, which are quasiparticles denoting an empty electron state. While the electrons of single atoms occupy discrete energy levels with electron orbitals, when considered as an ensemble in a crystalline lattice these energy levels overlap and become highly hybridised forming what are effectively continuous bands.

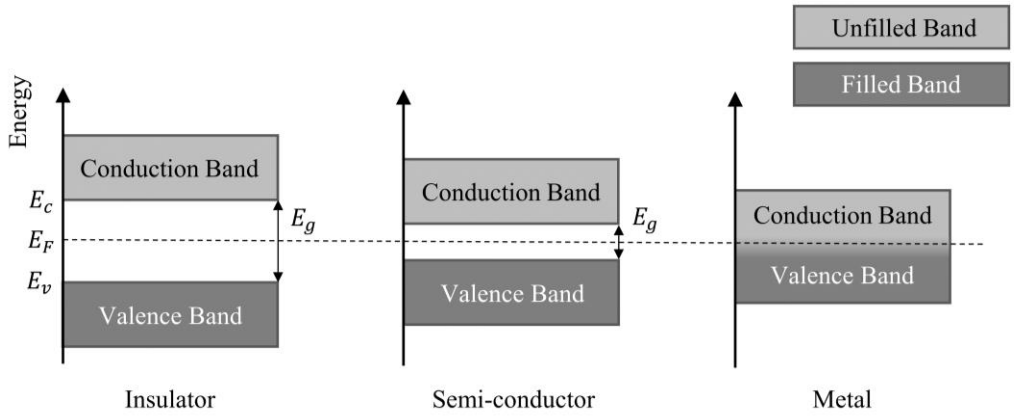

Figure 2.1: Simplified band structure for insulators, semi-conductors and metals at zero temperature. Insulators have a large separation between the conduction and valance bands, with the Fermi level E_F lying between them. The forbidden energy gap, E_g, is significantly smaller for semiconductors. In metals, the bands overlap with the Fermi surface describing the highest occupied state at zero temperature.

In non-metals at $T = 0$, the valance band contains the highest energy occupied states, and the conduction band contains the lowest unoccupied states. When electrons in the valance band are provided with sufficient energy, they can be excited into the conduction band leaving behind a hole. Both charge carriers can

contribute to current flow. The highest energy states of the valance band E_v and lowest energy states of the conduction band E_c are of particular interest as they are separated by a gap E_g where electron occupation is forbidden. These levels are indicated in Figure 2.1. At thermodynamic equilibrium, the probability distribution of state occupancy described by Fermi-Dirac statistics as follows:

$$f(E) = \frac{1}{e^{(E-E_F)/k_BT} + 1}. \tag{2.1}$$

Here, E is the energy, T is the temperature and k_B is the Boltzmann constant. At $T = 0$ K, all states below the Fermi level E_F must be filled and all those above it must be empty. For $T \neq 0$ K, Equation (2.1) evaluated at $E = E_F$ is ½, implying that if there are electronic states at the Fermi level half of them will be filled. The material types mentioned above can be defined based on the size of E_g and the proximity of the valance and conduction bands with the Fermi level, as shown in a simplified diagram in Figure 2.1. The larger energy gap of an insulator compared to a semiconductor corresponds to the additional energy required for electrons to be excited into the conduction band, with E_F lying in the gap with no allowed states. The situation is different for metals, with the valance and conduction bands at least partially overlapping and E_F positioned within the overlapping region. In the ground state at $T = 0$ electron occupation occurs from the bottom up in the valance band with the highest possible occupancy at E_v for insulators and semiconductors. However, in metals because the Fermi level intersects the overlapped band, electrons occupy states up to E_F. These concepts are central to band theory, which is used to explain the range of allowed energy levels for electrons in a system and accounts for broad range of electrical properties observed in these materials. Band theory assumes an ordered stationary periodic potential as in Bloch's theorem and does not consider strong

electron-electron interactions, causing it to break down in situations where these factors are significant.

Band theory is also a useful lens through which to view doping in semiconductors. As shown in Figure 2.1, semiconductors have a moderate forbidden energy gap that can be overcome by thermal excitations. In the case of *p-type* doping, acceptor atoms with unfilled orbitals are injected into the lattice forming acceptor sites with concentration N_A and a dopant band close to but above the valance band maximum. *N-type* doping involves donor atoms and associated acceptor sites with concentration N_D close to but below the conduction band minimum. These sites influence the density of states as illustrated in Figure 2.2 and discussed later. The presence of unoccupied sites lowers the Fermi level, so E_F now also depends on N_A [35]. The addition of boron to diamond is an example of *p-type* doping, with a shallow acceptor level at E_A = 0.36 eV above the valance band [36,37]. At sufficiently high doping levels the dopant band broadens due to interactions and coupling between the boron atoms and the surrounding lattice and carriers, causing it to overlap with the valance band. In the case of *p-type* semiconductor doping, sufficiently high doping concentrations for this overlap causes the material to undergo a metal-insulator-transition (MIT) where the semiconductor becomes degenerate with its Fermi level entering the hybridised valence band [38]. Diamond has been found to undergo an MIT resulting in a significant increase in electrical conductivity [105], which occurs at boron doping concentrations of ~4.5×10^{20} cm^{-3} [39].

A semiconductor is said to be degenerate if the Fermi level lies within the conduction or valance band and the energy states within that band are fully or nearly fully occupied (i.e., state occupancy is degenerate at the Fermi level with $T \rightarrow 0$). Degeneracy can be achieved with sufficient doping, causing the material to behave more like a metal. It should be noted that while true Fermi level

degeneracy is only possible in the limit of low temperatures, degenerate semiconductors retain this classification as it marks a useful delineation of electronic properties.

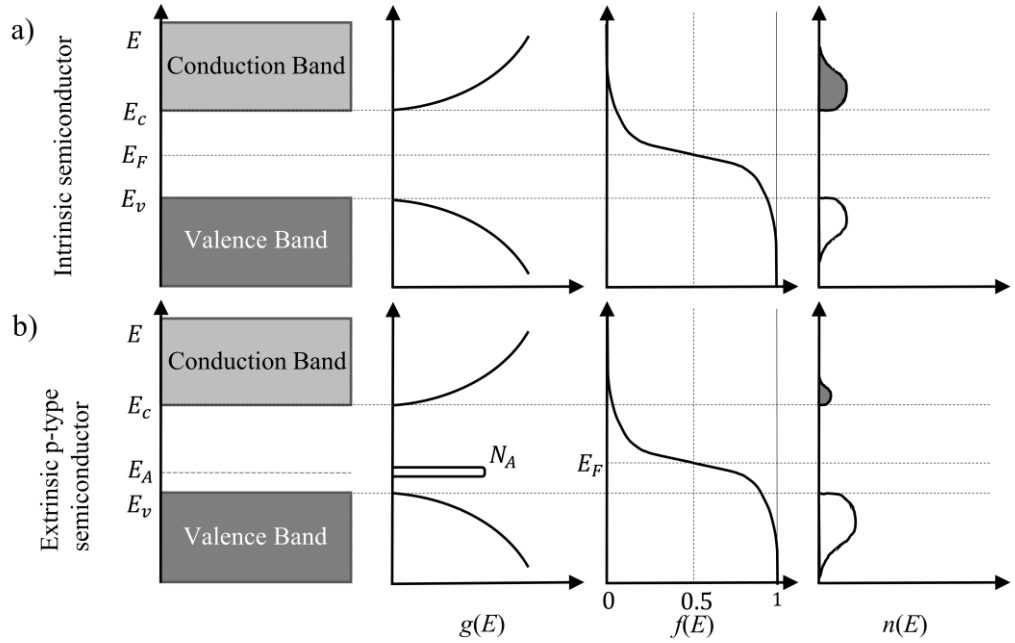

Figure 2.2: The density of states $g(E)$, Fermi distribution $f(E)$ and carrier concentration $n(E)$ for: a) An intrinsic semiconductor and b) an extrinsic *p-type* semiconductor.

For metallic materials the electrons in the valance band are in close proximity with unoccupied states which allows for conduction even at low temperatures. The Fermi surface is a term used to describe the separation in reciprocal space of occupied and unoccupied electron states at zero temperature.

The conductivity of a semiconductor is determined by two factors: the concentration and mobility of free carriers available to conduct current. For an ideal intrinsic semiconductor, these carriers take the form of either electrons in the conduction band or holes in the valance band. To understand the

concentration of these carriers we first look to the density of states $g(E)$ available for occupancy:

$$g(E) = \frac{(2m_e^*)^{3/2}}{2\pi^2 h^3}(E - E_c)^{1/2}\,. \tag{2.2}$$

Equation (2.2) provides the density of electron states in the conduction band where m_e^* is the effective mass of an electron and h is Plank's constant. For the states in the valance band we can substitute for the effective mass of a hole m_h^* and calculate the energy relative to E_v. A visualisation can of the form of the density of states $g(E)$ can be found in Figure 2.2.

For an intrinsic semiconductor, number density of electrons in the conduction band (n_0) is given by:

$$n_0 = N_c exp\left(\frac{E_F - E_c}{k_B T}\right). \tag{2.3}$$

Here $N_c = 2[2\pi m_e^* k_B T/h^2]$ is the effective density of states, which is the number of states per unit volume with all states concentrated at E_c. Similarly for holes in the valance band (p_0) we find:

$$p_0 = N_v exp\left(\frac{E_v - E_F}{k_B T}\right). \tag{2.4}$$

Where $N_v = 2[2\pi m_h^* k_B T/h^2]$ is the effective density of states in the valance band. The resulting intrinsic carrier concentration $n(E)$ is depicted in Figure 2.2a.

For an intrinsic semiconductor all carriers (electrons n_i and holes p_i) are intrinsic and their concentrations only depend on E_g and temperature. Due to charge neutrality ($n_i = p_i$), we find that

$$n_0 p_0 = n_i p_i = n_i^2, \tag{2.5}$$

due to thermal excitations creating electron-hole pairs in the conduction and valance band. When introducing dopants into the semiconductor both electron acceptor and donor atoms are usually present. Letting N_A be the number density of acceptor atoms and N_D be the number density of donor atoms, for a *p-type* semiconductor $N_A > N_D$. Assuming thermal energy sufficient for the majority of the impurity atoms to be ionised, charge neutrality dictates that $n_0 + N_A = p_0 + N_D$. Substituting Equation (2.5) and solving, for a *p-type* semiconductor we find that $N_A - N_D \gg n_i$ and $p_o \approx N_A - N_D$ ($n_o \approx N_D - N_A$ for an *n-type* semiconductor). The Fermi level becomes dependent on the dopant concentration, and for a *p-type* semiconductor $E_F = E_i - k_B T \ln\left(\frac{p_o}{n_i}\right)$ where E_i is the intrinsic Fermi level. As shown in Figure 2.2b, the introduction of acceptor impurities can create a band at E_A with additional states and a larger proportion of holes in the valance band compared to the intrinsic case.

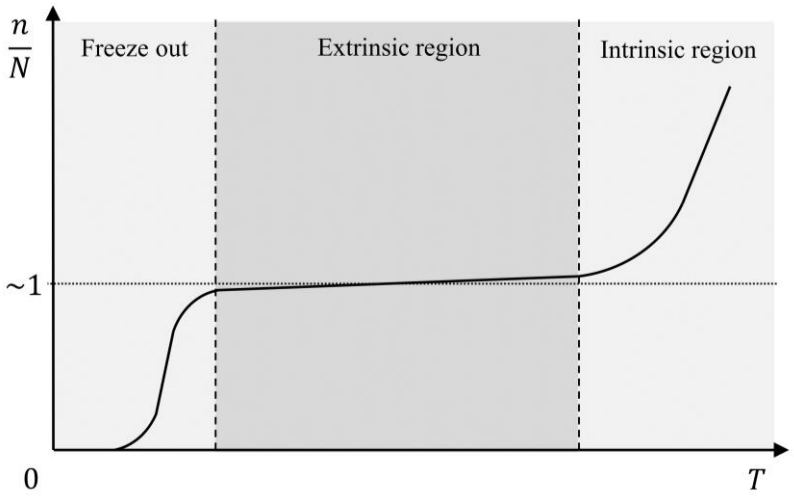

Figure 2.3: Temperature dependence of the carrier concentration in a doped semiconductor where n is the carrier concentration and N is the dopant concentration, showing the three characteristic regions.

The availability of carriers in semiconductor is influenced by several factors, including the energy level and concentration of dopants and the intrinsic properties of the material. Generally, the carrier concentration n in a semiconductor exhibits a temperature dependence typified by three characteristic effects which are depicted in Figure 2.3. In each zone, we can consider the dependence to be dominated by one of three factors. Carriers originate from either intrinsic excitations to the conduction band, excitations from the dopant band to the conduction band (*n-type*) or from the valance band to the dopant band (*p-type*). At the highest temperatures there is sufficient energy for electrons in the valance band to be readily excited into the conduction band creating electron-hole intrinsic carrier pairs through thermal excitation. Below a certain temperature the carrier concentration is dominated by excitations to or from the donor band. Ionisation of donor atoms can also liberate additional carriers, depending on the energy scale of the gaps involved. This region has a weaker temperature dependence due to the lower number of total donors. At even lower temperatures thermal energy becomes sufficiently low causing both the

reduction of thermal excitation of carrier pairs and the ionisation of impurity atoms. In this zone the carrier concentration is said to "freeze out" with $n \to 0$ as $T \to 0$.

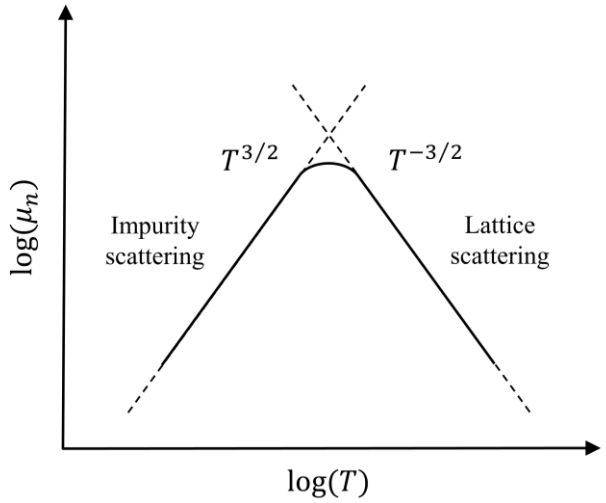

Figure 2.4: Temperature dependence of the carrier mobility in a semiconductor with respect to scattering effects, showing the two typical exponential dependencies present.

The ability of carriers to move through a material in response to an electric field is referred to as the carrier mobility, which has a temperature dependence shown approximately in Figure 2.4. Lower temperatures reduce the energy of lattice vibrations (phonons), which causes the reduction of carrier scattering by the lattice and results in a higher carrier mobility. Lattice scattering typically has a temperature dependence of $T^{-3/2}$. Carriers can also scatter from impurities in the lattice such as donor atoms or crystal defects. At lowers temperatures the slower motion of carriers gives them more time to interact with these impurities which results in lower scattering rates and a smaller reduction of mobility. At higher temperatures, impurity scattering increases and therefore the mobility decreases following a dependency of approximately $T^{3/2}$.

Upon cooling a metallic material one can observe a decrease in resistivity $\rho \propto T^n$ below the Debye temperature, where $n = 2$ in heavier metals due to electron-electron scattering, $n = 3$ for transition metals where *s-d* electron orbital scattering dominates and $n = 5$ for electron-phonon scattering [40,41].

The temperature dependence of resistivity in a semiconductor is less general but has been noted to follow $\rho \propto T^{1/2}$ relationship in disordered systems with significant electron-electron scattering [42].

2.1.1 Metal-semiconductor interfaces

Interfaces consisting of a metal brought into contact with a semiconductor (MSm) have uses including electrical contacts to devices or as devices themselves, i.e., diodes. As shown in Figure 2.5 parts a) and d) the key energy scales in each of the materials in separation can be described by some quantities that will allow for performance quantification and classification of the resulting contact. Accounting for the electron charge e, the work function $e\phi = (E_0 - E_F)$ is the energy required to bring an electron from the Fermi level of each material to the vacuum level E_0. The electron affinity $e\chi = (E_0 - E_c)$ is independent of any effects of the contacted electronic system, corresponding to the original position of the conduction band. The electron affinity is the energy required to bring an electron from the conduction band to the vacuum level which is equivalent to ϕ_m for the metal. In a *p-type* semiconductor we must regard the holes in the valance band as principal charge carriers, so the Schottky barrier height ϕ_b is given by:

$$e\phi_b = (E_c - E_v) + e\chi_s - e\phi_m = E_F - E_{v\,int}, \tag{2.6}$$

where $E_{v\,int}$ is the initial pre-contact valance band edge. The Schottky barrier height describes the potential barrier for carrier flow from metal to semiconductor, while the barrier for carriers moving in the opposite direction is known as the built in potential $eV_i = e(\phi_m - \phi_m)$. For an *n-type* semiconductor these quantities are evaluated relative to the conduction band.

Bringing the two materials into contact, the electronic systems interact and must find equilibrium. In an ideal MSm junction, the density of electronic states is typically much higher in the metal which causes the Fermi level in the semiconductor (E_{Fs}) to shift to match that of the metal (E_{Fm}). In general, we find that $\phi_m \neq \phi_s$ because the average energy of an electron added to the metal is not the same as one added to the semiconductor. Therefore, charge carriers flow across the interface until the Fermi levels are in equilibrium with $E_{Fm} = E_{Fs}$. For an *n-type* semiconductor with $\phi_m > \phi_s$ the total energy of the MSm system could be reduced by moving electrons from the semiconductor to the metal. For a *p-type* semiconductor with $\phi_m > \phi_s$ holes move from valance band to the metal (i.e., electrons flow into the valance band from metal). Charge transfer occurs until the Fermi levels are in alignment and the lowest energy configuration is reached. This one-directional charge transfer across the interface results in a volume of semiconductor with reduced carriers known as the depletion region. These factors result in band bending as shown in Figure 2.5 parts b) and e).

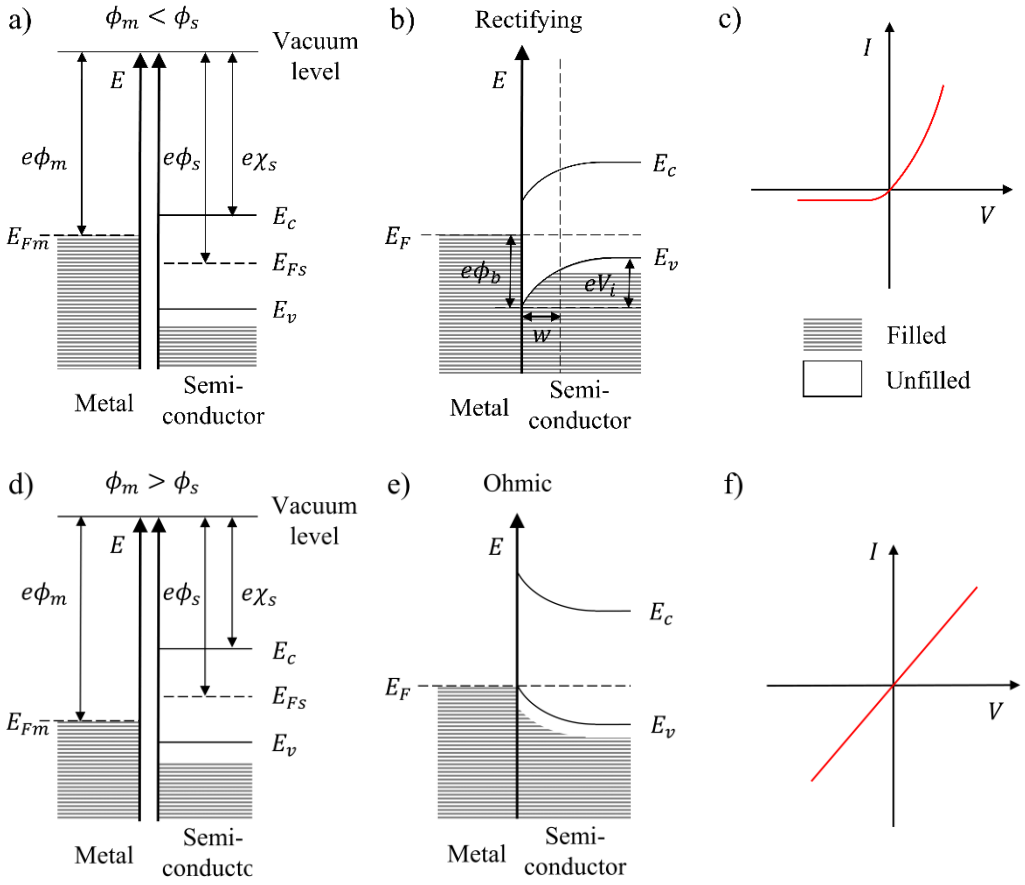

Figure 2.5: Schematic diagrams for rectifying (a-c) and ohmic (d-f) metal contacts to a p-type semiconductor. Separated band diagrams are shown in a) and d), where the work functions $\phi_{m,s}$, electron affinity χ and Fermi levels $E_{Fm,Fs}$, conduction and valance band edges E_c and E_v are indicated. Parts b) and e) show the equilibrium state of the contacted junctions with associated band bending and Schottky barrier height ϕ_b and depletion region w in the rectifying contact. Parts c) and f) show expected *I-V* characteristics for each case. It should be noted that the x-axis for the band diagrams represents an approximation of real space and distance to the interface.

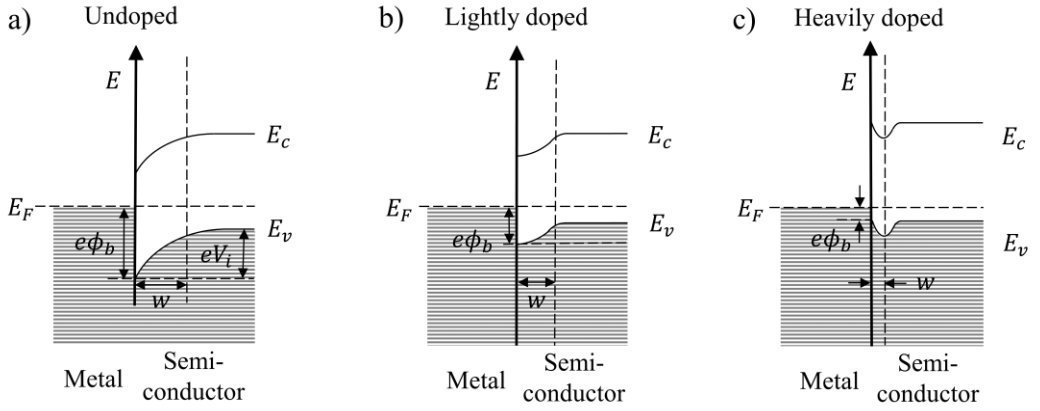

Figure 2.6: The impact of doping on the metal-semiconductor interface with a) an intrinsic or very low doping scenario, b) moderate doping showing additional band bending and a reduction of the barrier height ϕ_b and c) with a heavily doped semiconductor the depletion width and barrier width w are reduced sufficiently to allow for carrier tunnelling.

Due to the initial malalignment of the bands and subsequent band bending at contact equilibrium two types of junction emerge at MSm interfaces. For a *p-type* semiconductor with $\phi_m < \phi_s$ the junction is said to be rectifying due to current only being able to flow in one direction without additional bias as shown in Figure 2.5 parts a) to c). Rectifying contacts, also known as Schottky contacts, tend to occur in lower doping or intrinsic scenarios. Additional doping can create further band bending which reduces the barrier height as displayed in Figure 2.6b). As shown in Figure 2.6c, with higher doping concentrations the width of the depletion region can be reduced which allows carriers to tunnel through the barrier. Both effects can contribute to a junction exhibiting a linear *I-V* response and therefore fall into the category of ohmic junctions as shown in Figure 2.5 parts d) to f). Ohmic electrical contacts typically have lower resistance where transport is dominated by tunnelling.

In practice, a deviation away from the ideal MSm junction case is observed due to surface states caused by dangling bonds at the semiconductor surface. These states, which can either be donors or acceptors, lie within the band gap of the semiconductor centred around the neutral level. This neutral level tends to pin the Fermi level in the semiconductor and makes the Schottky barrier height weakly dependent on the metal work function [34].

Current transport through the junction is comprised of various contributions, of which thermionic emission and tunnelling are the most significant with one or the other dominating depending on the conditions at the interface. Thermionic emission occurs with a wide depletion region and refers to electron transport across the boundary via thermal excitation over the barrier and tends to dominate at lower doping concentrations and higher temperatures where the energy $k_B T$ is sufficient to overcome the barrier. The barrier height can be reduced by electronically active defects at the interface and doping. Field emission describes the case of carrier tunnelling through the potential barrier. This is possible with a sufficiently narrow depletion layer in the case of high doping of the semiconductor and therefore dominates in such situations and at lower temperatures.

2.2 THEORY OF SUPERCONDUCTIVITY

In the case of a superconducting material, there is a sharp reduction in the resistivity at the onset of the superconducting state, with negligible measured resistance at temperatures below this point. For a superconducting transition of finite width, i.e. some ΔT between the onset point and the point at which the resistivity is negligible, there can be some ambiguity in the definition of the critical temperature T_c. For the sake of clarity, throughout this work T_c is defined

as the temperature where the conductance significantly diverges from this regime where the resistivity is at its lowest. A schematic depicting these quantities is presented in Figure 2.7.

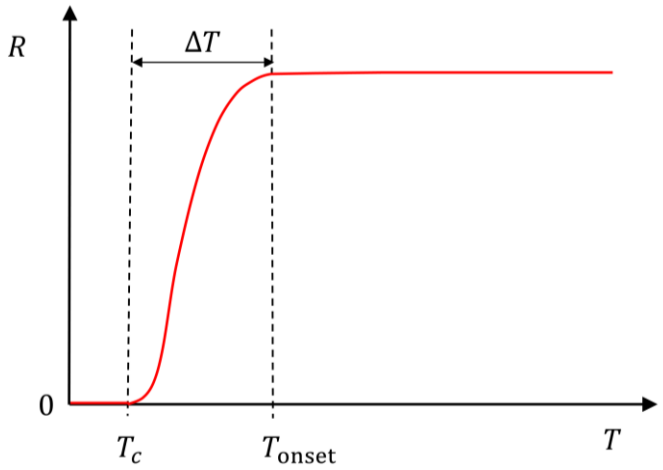

Figure 2.7: Example of a resistance vs temperature plot for a superconductor with a transition of finite width ΔT starting at T_{onset}. and achieving the lowest resistance at T_c.

2.2.1 The London Equations

Superconductivity was first discovered by Dutch physicist *Heike Kamerlingh Onnes* as a *DC* zero-resistance state [43]. It was later more completely described by the cofactor of the expulsion of magnetic flux by *W. Meissner* and *R. Ochsenfeld*, which is now dubbed the Meisner effect [44]. This quantum mechanical description classifies two types of superconductors based on their response to a magnetic field, where it was principally noted that with the onset of superconductivity comes the expulsion of magnetic fields as is the case in perfect diamagnetism. Further, when type I superconductors are exposed to critical field strength all superconductivity is destroyed in the material. Type II

superconductors are characterised by a lower (H_{c1}) and upper (H_{c2}) critical field. H_{c1} is the threshold at which some magnetic flux can penetrate through the material by forming vortices, which will be discussed in more detail shortly. H_{c2} is then the point at which the flux completely interrupts coherent superconductivity. This is shown schematically in Figure **2.8**.

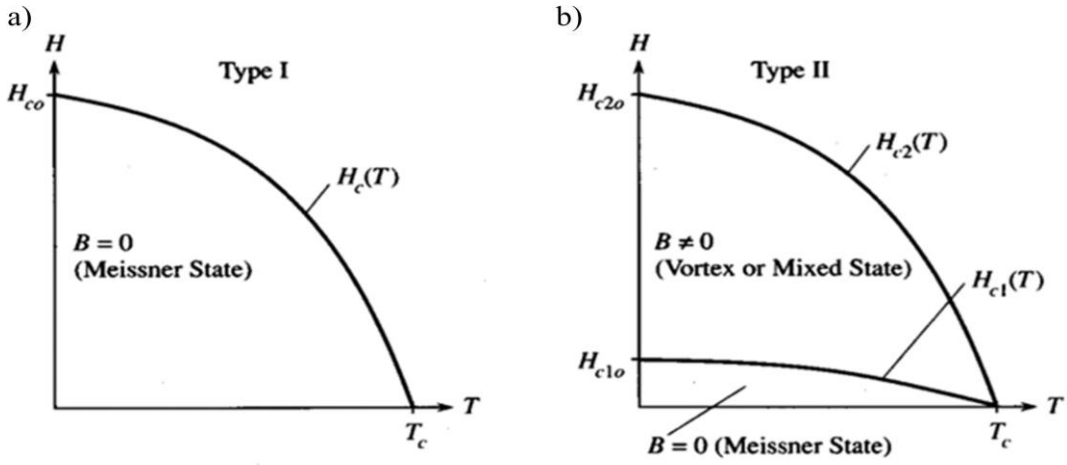

Figure 2.8: Field response in type I&II superconductors. a) Type I express a total Meissner state below the critical field H_c, b) the Meissner state in type II superconductors occurs below the first critical field H_{c1}, above which the mixed state is present until the upper critical field H_{c2} [45].

A description of the electrodynamics of superconductivity was developed by Fritz and Heinz London in 1935 that was able to properly describe the Meissner effect [46]. Starting from the two-fluid electron model, where it is assumed that the mobile electrons in a superconductor consist of fluids of normal and superconducting electrons with number densities n_n and n_s respectively. The normal electrons are subject to the classical conditions established by the Drude model where they are accelerated by an electric field $\boldsymbol{E}$ and scattered by impurities and thermal effects in the lattice. A mean drift velocity $\langle \boldsymbol{v}_n \rangle = -e\tau \boldsymbol{E}/m$

is achieved, where e and m are the electron charge and mass and τ is the average time between scattering events. These electrons flow causing a current density:

$$j_n = -n_n e\langle \boldsymbol{v}_n \rangle = \frac{n_n e^2 \tau}{m} \boldsymbol{E} \,. \tag{2.7}$$

The next step in deriving the London equations is to note that in this model the superconducting electrons are not scattered by impurities, defects or thermal effects in the lattice, so they are accelerated freely by $\boldsymbol{E}$. The equation of motion of a superconducting electron is therefore $m\frac{d\boldsymbol{v}_s}{dt} = -e\boldsymbol{E}$, where v_s is the velocity. From this, combined with the current density for the superconducting electron $j_s = -n_s e\boldsymbol{v}_s$, we find

$$\frac{dj_s}{dt} = n_s e\frac{d\boldsymbol{v}_s}{dt} = \frac{n_s e^2}{m}\boldsymbol{E} \,, \tag{2.8}$$

which is the first of the London equations. Comparing Equations (2.7) and (2.8) we can note that the lack of scattering in the superconducting electrons causes the current density to increase in a constant electric field. Considering a constant current through the material, $\frac{dj_s}{dt} = 0$ and so $\boldsymbol{E} = 0$, which means that the normal current density is zero and all the current is carried by the superconducting electrons. With no electric field, there is no voltage across the material and therefore no resistance. To account for the magnetic field in a superconductor, we first start with the example of a perfect conductor. From Maxwell's equation $\nabla \times \boldsymbol{E} = -\frac{\delta \boldsymbol{B}}{\delta t}$ and substituting $\boldsymbol{E}$ from Equation (2.8) we can obtain

$$\nabla \times \frac{\delta j_{pc}}{\delta t} = -\frac{n_{pc} e^2}{m} \frac{\delta \boldsymbol{B}}{\delta t}. \tag{2.9}$$

The London brothers stated that this equation should be replaced by the following:

$$\nabla \times j_s = -\frac{n_s e^2}{m} \boldsymbol{B}\,, \tag{2.10}$$

which is the second London equation. Although these equations do not provide a description of the microscopic system, they allow an explanation of the Meissner effect as follows. Starting from Ampère's law $\nabla \times \boldsymbol{B} = \mu_0 j_s$ (where μ_0 is the vacuum magnetic permeability) and Equation (2.10) we find $\nabla \times (\nabla \times \boldsymbol{B}) = -\frac{\mu_0 n_s e^2}{m} \boldsymbol{B} = -\frac{1}{\lambda_L^2} \boldsymbol{B}$, where

$$\lambda_L = \sqrt{\frac{m}{\mu_0 n_s e^2}}\,, \tag{2.11}$$

which is the London penetration depth of a magnetic field into a material. Considering a field $B = B_0 \hat{z}$ parallel to the boundary of a superconductor, the strength of the field will decay exponentially as per the following equation:

$$B_z(x) = B_0 e^{-x/\lambda_L}\,. \tag{2.12}$$

Referring back to the two-fluid model, the temperature dependence of the number density of the superconducting electrons [47] allows the derivation of the temperature dependence of the London penetration depth

$$\lambda_L(T) = \frac{\lambda_L(0)}{\sqrt{1-(T/T_c)^4}}. \tag{2.13}$$

2.2.2 BCS theory

The theory proposed by Bardeen, Cooper and Schrieffer (BCS) in 1957 provides a microscopic description of the macroscopic superconducting state [48]. Building on an earlier postulation of the existence of an energy gap between the ground state and quasi-particle excitations, BCS theory states that at sufficiently low temperatures below T_c, charge carriers in the system close to the Fermi level are bound into Cooper pairs via a process of phonon mediated attractive interaction.

A simple phenomenological explanation for the system that has been derived from BCS theory describes the motion of electrons through the crystal lattice, and is depicted in Figure 2.9. As a single electron passes through the lattice its charge causes a slight disturbance to the position of the ions. This shape change of the lattice creates a slight local increase in positive charge, which can interact with a second electron a distance ξ_0 away. This length is known as the BCS coherence length which is often thought of as the physical size of the Cooper pair, although this concept breaks down outside of s-wave superconductors and in high temperature superconductors [49].

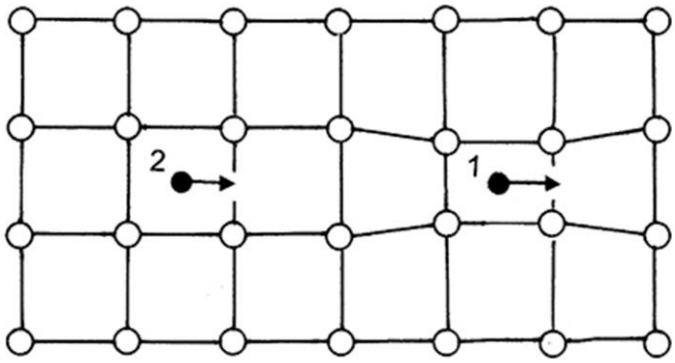

Figure 2.9: Cooper pairs in a lattice. Schematic of the lattice disruption caused by a transiting election resulting in a greater positive charge in front of a second electron, causing coherence in their movement [50].

Unbound electrons have shifted from having half integer spin and behaving as fermions to having zero spin and becoming bosonic as Cooper pairs. This allows condensation of all particles into the quantum state described by the wavefunction shown later by Equation (2.29). The lattice interactions result in the formation of Cooper pairs in the ground state and require an energy 2Δ to break apart into single electron-like quasiparticles, which causes the formation of the energy gap of the same magnitude in the energy band at E_F. The energetically forbidden gap results in the redistribution of the available occupied and unoccupied states at E_F causing the Fermi surface below T_c to become reconstructed at lower energies, as shown in Figure 2.10, which is a direct result of the phonon-mediated electron attraction causing perturbations on the Fermi sea. Contrasting this situation with metals, we can understand the emergence of zero resistance. In normal metals the presence of empty states at or near the Fermi surface means that electrons can be easily excited into them via scattering off impurities, imperfections or phonons. This inelastic scattering is dissipative, resulting in electrical resistance. In the presence of the gap, scattering can only occur in the excited states above the gap at non-zero temperatures.

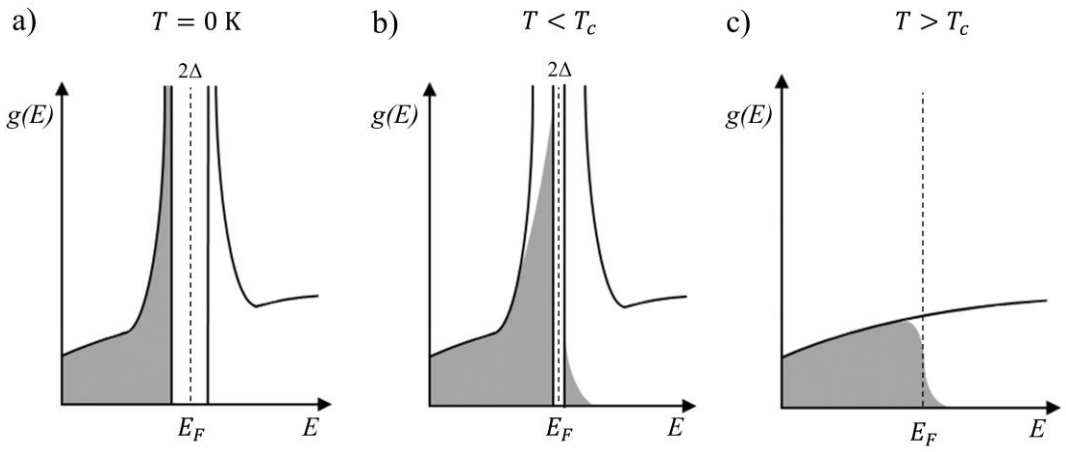

Figure 2.10: Sketch of the density of states $g(E)$ of a superconductor at a) zero temperature, where the formation of the 2Δ gap has caused the destruction of the Fermi surface, b) as the temperature approaches T_c, the gap shrinks and some states above it are occupied, c) above T_c, the energy gap breaks down and the Fermi surface is re-established. Quantities are not to scale, in reality $\boldsymbol{\Delta} \ll E_F$.

Figure 2.10 also shows schematically the relationship between the scale of the gap and density of states with temperatures relative to T_c. At the lowest temperatures the attractive interaction between the electrons causes Cooper pairing, the formation of the energy gap and destruction of the Fermi surface. At some finite temperature below T_c, the forbidden energy gap is reduced and some quasi-particle excitations are noted above the gap.

Considering the BCS pairing Hamiltonian:

$$H = \sum_{\boldsymbol{k},\sigma} (\epsilon_{\boldsymbol{k}} - \mu) c^{\dagger}_{\boldsymbol{k}\sigma}\, c_{\boldsymbol{k}\sigma} - V_0 \sum_{\boldsymbol{k},\boldsymbol{k}'} c^{\dagger}_{\boldsymbol{k}\uparrow}\, c^{\dagger}_{-\boldsymbol{k}\downarrow} c_{-\boldsymbol{k}'\downarrow} c_{\boldsymbol{k}'\uparrow} \tag{2.14}$$

where $c_{k\sigma}^{\dagger}$ creates an electron with momentum $\boldsymbol{k}$ and spin σ, $(\epsilon_{\boldsymbol{k}} - \mu) = \xi_{\boldsymbol{k}}$ is the kinetic energy of an electron with band dispersion $\epsilon_{\boldsymbol{k}}$ and chemical potential μ and V_0 is the magnitude of the pairing potential. Because of the large number of particles involved, we can apply the "mean field" approximation to reduce it to quadratic form, which is an approach used by Bogolyubov, and allows a simplified derivation summarised as follows [51]. Noting that the terms $\sum_{\boldsymbol{k}} c_{k\uparrow}^{\dagger} c_{-k\downarrow}^{\dagger}$ and $\sum_{\boldsymbol{k}'} c_{-k'\downarrow} c_{k'\uparrow}$ can be replaced by their expectation values in the ground state:

$$\langle \sum_{\boldsymbol{k}} c_{k\uparrow}^{\dagger} c_{-k\downarrow}^{\dagger} \rangle = \sum_{\boldsymbol{k}} v_{k\uparrow}^{*} u_{\boldsymbol{k}} = \frac{\Delta^{*}}{V_0} , \langle \sum_{\boldsymbol{k}} c_{-k\downarrow} c_{k\uparrow} \rangle = \sum_{\boldsymbol{k}} u_{k\uparrow}^{*} v_{\boldsymbol{k}} = \frac{\Delta}{V_0}, \tag{2.15}$$

where $u_{\boldsymbol{k}}$ and $v_{\boldsymbol{k}}$ are variational parameters, whose value can be determined by minimising the energy of the Hamiltonian. Using the expectation values in Equation (2.15) we can write

$$\begin{aligned} \sum_{\boldsymbol{k}} c_{k\uparrow}^{\dagger} c_{-k\downarrow}^{\dagger} &= \frac{\Delta^{*}}{V_0} + \left(\sum_{\boldsymbol{k}} c_{k\uparrow}^{\dagger} c_{-k\downarrow}^{\dagger} - \frac{\Delta^{*}}{V_0} \right), \\ \sum_{\boldsymbol{k}} c_{-k\downarrow} c_{k\uparrow} &= \frac{\Delta}{V_0} + \left(\sum_{\boldsymbol{k}} c_{-k\downarrow} c_{k\uparrow} - \frac{\Delta}{V_0} \right), \end{aligned} \tag{2.16}$$

and assume the second term, the fluctuation term, is small and keep only the terms which are linear in small fluctuations we can re-write the Hamiltonian as:

$$H = \sum_{\boldsymbol{k},\sigma} (\epsilon_{\boldsymbol{k}} - \mu) c_{k\sigma}^{\dagger} c_{k\sigma} - \sum_{\boldsymbol{k},\boldsymbol{k}'} \Delta c_{k\uparrow}^{\dagger} c_{-k\downarrow}^{\dagger} - \Delta^{*} c_{-k'\downarrow} c_{k'\uparrow} + \text{const.}, \tag{2.17}$$

which is the mean field approximation or BCS form and is notable for only containing quadratic terms for fermion creation and annihilation operators. Noticing that $c_{\boldsymbol{k}\uparrow}^{\dagger}$ and $c_{-\boldsymbol{k}\downarrow}$ are coupled to $c_{\boldsymbol{k}\uparrow}$ and $c_{-\boldsymbol{k}\downarrow}^{\dagger}$, and using the Nambu spinor $\begin{pmatrix} c_{\boldsymbol{k}\uparrow} & c_{-\boldsymbol{k}\downarrow}^{\dagger} \end{pmatrix}$ we obtain:

$$H = \sum_{\boldsymbol{k}} \begin{pmatrix} c_{\boldsymbol{k}\uparrow} & c_{-\boldsymbol{k}\downarrow}^{\dagger} \end{pmatrix} \begin{pmatrix} \epsilon_{\boldsymbol{k}} - \mu & -\Delta \\ -\Delta^{*} & -(\epsilon_{\boldsymbol{k}} - \mu) \end{pmatrix} \begin{pmatrix} c_{\boldsymbol{k}\uparrow} \\ c_{-\boldsymbol{k}\downarrow}^{\dagger} \end{pmatrix}. \tag{2.18}$$

From here, we can diagonalise for $\boldsymbol{k}$ and with each value of $\boldsymbol{k}$ the eigenvalues for the central part are:

$$E_k = \pm\sqrt{(\epsilon_{\boldsymbol{k}} - \mu)^2 + |\Delta|^2}\,, \tag{2.19}$$

with eigenvectors:

$$\begin{pmatrix} u_{\boldsymbol{k}} \\ v_{\boldsymbol{k}} \end{pmatrix}, \qquad \begin{pmatrix} v_{\boldsymbol{k}}^{*} \\ u_{\boldsymbol{k}}^{*} \end{pmatrix}. \tag{2.20}$$

The eigenmodes of the mean field Hamiltonian can be written as

$$b_{\boldsymbol{k}\uparrow} = u_{\boldsymbol{k}} c_{\boldsymbol{k}\uparrow} - v_{\boldsymbol{k}} c_{-\boldsymbol{k}\downarrow}^{\dagger}\,, \qquad b_{-\boldsymbol{k}\downarrow}^{\dagger} = v_{\boldsymbol{k}}^{*} c_{\boldsymbol{k}\uparrow} + u_{\boldsymbol{k}}^{*} c_{-\boldsymbol{k}\downarrow}^{\dagger}\,, \tag{2.21}$$

which are well defined fermion modes satisfying the commutation relation:

$$\{b_{\boldsymbol{k}\sigma}, b^{\dagger}_{\boldsymbol{k}'\sigma'}\} = \delta_{\boldsymbol{k}\boldsymbol{k}'}\delta_{\sigma\sigma'}\,, \qquad \{b_{\boldsymbol{k}\sigma}, b_{\boldsymbol{k}'\sigma'}\} = 0, \qquad \{b^{\dagger}_{\boldsymbol{k}\sigma}, b^{\dagger}_{\boldsymbol{k}'\sigma'}\} = 0. \tag{2.22}$$

These eigenmodes allow the Hamiltonian to be rewritten as

$$H = \sum_{\boldsymbol{k}} E_k\left(b^{\dagger}_{\boldsymbol{k}\downarrow} b_{\boldsymbol{k}\uparrow} + b^{\dagger}_{-\boldsymbol{k}\downarrow} b_{-\boldsymbol{k}\downarrow}\right). \tag{2.23}$$

The BCS wave function is defined by

$$|\Psi_{BCS}\rangle = \prod_{\boldsymbol{k}}\left(u_{\boldsymbol{k}} + v_{\boldsymbol{k}} c^{\dagger}_{\boldsymbol{k}\uparrow} c^{\dagger}_{\boldsymbol{k}\downarrow}\right)|0\rangle\,, \tag{2.24}$$

and now the ground state satisfies the condition

$$b_{\boldsymbol{k}\uparrow}|\Psi_{BCS}\rangle = 0\,, \qquad b_{-\boldsymbol{k}\downarrow}|\Psi_{BCS}\rangle = 0\,. \tag{2.25}$$

Modelling excitation, we apply $b^{\dagger}_{\boldsymbol{k}\downarrow}$ and $b^{\dagger}_{-\boldsymbol{k}\downarrow}$ to the ground state, with each costing energy

$$E_k = \sqrt{(\epsilon_{\boldsymbol{k}} - \mu)^2 + |\Delta|^2}\,. \tag{2.26}$$

A critical observation from this formula is that the energy cost has a lower bound at $|\Delta|$ irrespective of the value of $\boldsymbol{k}$. This means that all excitations above the ground state have a forbidden energy for any non-zero Δ, hence the denotation of Δ as the superconducting gap.

Further evidence of the phonon mediated electron-electron interaction was the observation of the isotope effect. The mass of the of the nuclei directly affect the dynamic response of the lattice, and testing the critical temperature of superconducting mercury yielded results that showed a scaling of T_c with the root of the atomic mass $M^{1/2}$ of the isotope [52].

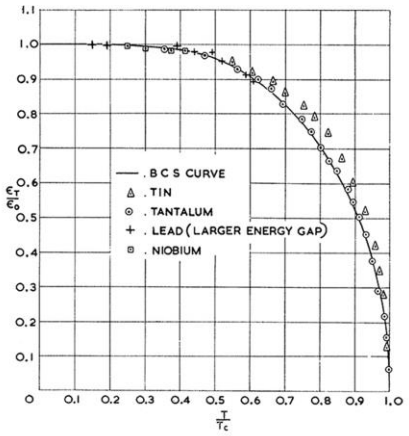

Figure 2.11: The temperature dependence of the BCS energy gap plotted with various superconductors. [53]

One of the key predictions of BCS theory is the scale of the gap 2Δ associated with breaking a Cooper pair into two quasiparticle excitations. For temperatures significantly less than the critical temperature ($T \to 0$), this scale is defined as

$$2\Delta(0) = 3.52 k_B T_c. \tag{2.27}$$

The factor 3.52 arises from solving the BCS gap equation self-consistently, and it is a numerical factor that depends on the nature of the electron-phonon interaction and the specific details of the material. At the time of the derivation of BCS theory this value was in agreement with previous theoretical estimates and measurements approximating the gap [54–56], but experimentally the ratio $\frac{2\Delta}{k_B T_c}$

in conventional superconductors varies between 3.2 and 4.2 [57]. Close to T_c the temperature dependence follows a parabolic function:

$$\frac{\Delta(T)}{\Delta(0)} \approx 1.74\left(1-\frac{T}{T_c}\right)^{1/2} \tag{2.28}$$

which is also shown in Figure **2.11**.

2.2.3 Ginzburg-Landau theory

The *Ginzburg-Landau* (GL) theory focuses directly on superconducting electrons and was originally proposed in 1950 [58]. The theory describes the superconducting condensate with density $n_s = |\Psi|^2$ in terms of a complex wave function:

$$\Psi(r) = |\Psi(r)|e^{i\phi(r)}, \tag{2.29}$$

which is also known as the order parameter [58]. Here the magnitude of the order parameter corresponds to the amplitude of the superconducting gap, $|\Psi(r)| \propto \Delta(r)$, and $\phi(r)$ is the phase. Typically, in the normal state $\Psi(r) = 0$ and with $T < T_c$ the order parameter becomes non-zero. As such, the GL theory describes the relationship between the macroscopic order parameter and the microscopic behaviour of the superconducting electrons, directly relating the condensation of Cooper pairs via Ψ and the number density of the condensate. Close to T_c, second order phase transitions can be quantified from a Taylor series expansion for the order parameter and the Gibbs free energy function as follows [59]:

$$F_s = F_n + \alpha|\Psi|^2 + \beta|\Psi|^4 + \frac{1}{2m^*}|(-i\hbar\nabla - 2eA)\Psi|^2 + \frac{|\boldsymbol{B}|^2}{2\mu_0}. \quad (2.30)$$

Here, F_n is the free energy of the normal state, α and β are treated as phenomenological parameters, m^* is the effective mass of the superconducting electrons, $\hbar$ is the reduced Planck constant, A is the magnetic vector potential and $\boldsymbol{B} = \nabla \times A$. From here, one can obtain the *Ginzburg-Landau* equations:

$$\alpha|\Psi| + \beta|\Psi|^2\Psi + \frac{1}{2m^*}(-i\hbar\nabla - 2eA)^2\Psi = 0 \quad (2.31)$$

and

$$J = \frac{2e}{m^*}|\Psi|^2(\hbar\nabla\phi - 2eA)\,. \quad (2.32)$$

Here, J denotes the dissipationless electrical current. GL theory also introduces an important length scale, now commonly known as the coherence length,

$$\xi_{GL} = \sqrt{\frac{\hbar^2}{2m|\alpha(T)|}}, \quad (2.33)$$

which is the characteristic length over which the superconducting wavefunction can vary with an increase in energy. It should be noted that while ξ_{GL} has a temperature dependence, with $\alpha(T) \to 0$ at T_c, the BCS coherence length ξ_0 associated with the size of the Cooper pair does not.

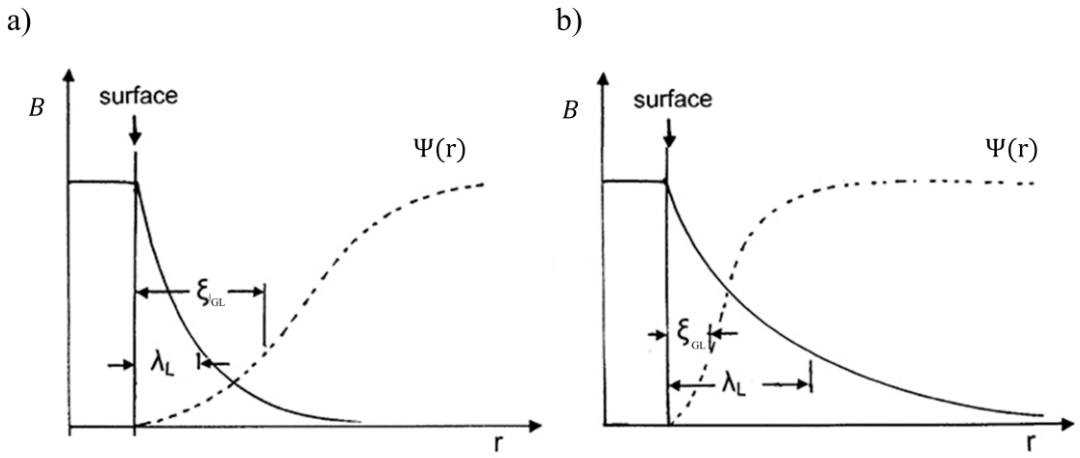

Figure 2.12: The ratio of ξ_{GL} and λ_L determines the behaviour of the superconductor in the presence of a magnetic field. In the two cases a) in a type I superconductor where $\xi_{GL} > \lambda_L$ and b) a type II superconductor where $\xi_{GL} < \lambda_L$ and it becomes energetically favourable for the field to penetrate the material. Adapted from [50].

The combination of the GL coherence length and the other characteristic length λ_L provides another quantity that allows delineation between type I and type II superconductors. This quantity, the GL parameter $\kappa = \lambda_L/\xi_{GL}$ takes value $\kappa < 1/\sqrt{2}$ for type I superconductors where all flux is expelled up to H_c (Meissner effect), and for $\kappa < 1/\sqrt{2}$ the characteristics of type II superconductivity are observed with flux penetrating between $H_{c1} < H < H_{c2}$. A sketch of this relationship is shown in Figure 2.12.

This treatment with the GL parameter was published by *Abrikosov* in work where he also described the formation of the mixed state between $H_{c1} < H < H_{c2}$ where flux penetrates the superconducting material in arrays of "flux tubes", or vortices [60]. Each vortex consists of a circulating supercurrent that causes a concentration of flux towards the vortex core, where the superconducting wavefunction goes to

zero. These Abrikosov vortices form triangular arrays, with each carrying a quantum of flux:

$$\Phi_0 = \frac{hc}{2e} = 2.07 \times 10^{-15} \text{ Wb.} \tag{2.34}$$

Modern techniques have allowed the imaging of these cores, as shown in Figure 2.13b.

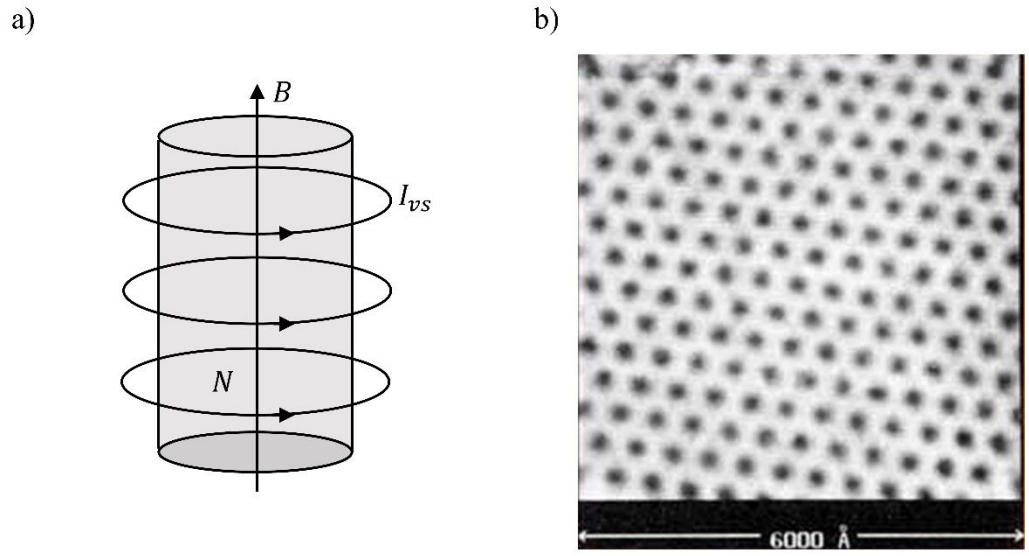

Figure 2.13: Abrikosov vortices a) Schematic of Abrikosov vortices in a superconducting material, with circulating supercurrent I_{vs} and flux lines from field B penetrating through their normal core N. b) Scanning tunnelling microscopy image of vortex cores in a superconductor [61].

2.2.4 The Clean and dirty limits for a superconductor

As discussed in the sections above, there are various length scales associated with a superconductor and the delineation between a type I and type II has been made. Another superconducting classification is whether the material is in the clean or dirty limit. In the clean limit, a superconductor is characterized by a low density of impurities and defects that can scatter electrons resulting in an electron mean free path that is significantly longer than the coherence length $l/\xi_0 \gg 1$ [62], typically associated with more pure materials. In the dirty limit, a superconductor contains higher densities of impurities, defects or other scattering centres that reduce the electron mean free path leading to $l/\xi_0 \ll 1$. Granular superconductors can exhibit characteristics of either limit depending on the disorder and degree of granularity. For example, materials with larger grains with strong intra-grain coupling might be in the clean limit, whereas those with smaller grains or more substantial grain boundaries could be subject to sufficient scattering to place them within the dirt limit.

2.3 SUPERCONDUCTING INTERFACES

2.3.1 Andreev reflection

The transfer of charge across an interface between a normal metal and a superconductor (NS interface) is possible within some constraints, converting the dissipative electrical current in the normal metal into a dissipationless supercurrent. As has been discussed above, the available energy levels in the superconductor are gapped around the Fermi energy which prevents single electrons from entering across the interface. With an electron energy greater than

the top boundary of the gap, electrons can directly enter the superconductor into the available states there. However, assuming the Fermi surface in the normal metal is in or near the energy gap of the superconductor, for electrons with energies $E < E_{Gap\ top}$ charge transfer occurs via a mechanism known as Andreev reflection [59,63]. This two-electron process describes a normal electron impinging on the NS interface being retroreflected as a hole while a Cooper pair is created across the interface in the superconductor. In terms of single excitations, this process is equivalent to two electrons entering the superconductor. Another key aspect of Andreev reflection is the phase coherence of the carriers [64]. The reflected hole carries information both about the phase of the electron state and on the macroscopic phase of the superconductor. This process is illustrated in Figure 2.14, and assumes a relatively transparent interface with minimal interaction with an insulating layer.

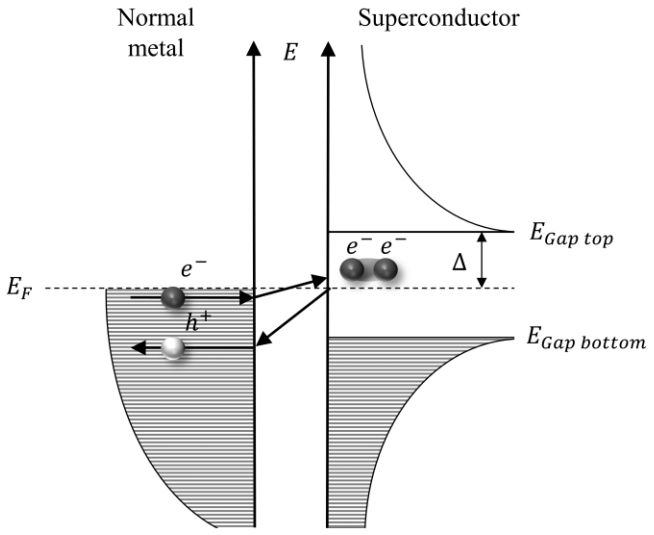

Figure 2.14: Diagram of Andreev reflection at an NS interface, with an incident electron and retroreflected hole resulting in a Cooper pair in the superconductor (not to scale and carrier paths indicated generally).

The reflected hole carries the opposite charge and momentum of the incident electron, and the Cooper pair consists of electrons with opposite momenta and spin. This means that Andreev reflection allows the conservation of both momentum and energy across the interface. In the opposite situation where an incoming hole is Andreev reflected into an electron, a Cooper pair is "pulled" from the superconductor into the normal metal. The describes how Andreev reflection is the mechanism responsible for the proximity effect, discussed later. The NS interface barrier strength and its impact on current voltage characteristics were studied in detail by *Blonder*, *Tinkham* and *Klapwijk* in the so-called BTK theory [65]. With a high barrier transparency sub-gap conductance was found to be twice the normal state conductance, indicative of the double charge transfer.

The formation of Andreev bound states is a consequence of this conversion process. Within the energy gap of the superconductor, a series of localized electronic states emerges. Below the superconducting energy gap, there exists an electron-like excitation trapped near the interface, while above the gap, there is a hole-like excitation. These states are bound to the interface and exhibit discrete energy levels within the superconducting energy gap. The wave functions of Andreev bound states are evanescent in the normal region, meaning they exponentially decay away from the interface. The energies of these states are determined by the specific geometry and material properties of the junction. The number and energy distribution of Andreev bound states depend on factors such as the interface transparency, the strength of the electron-phonon coupling, and the degree of mismatch between the Fermi surfaces of the superconductor and the normal region.

Recalling the earlier discussion of *p-type* MSm junctions and considering the case of a reducing temperature through T_c, it would be expected that transport would be dominated by MSm effects until the onset of superconductivity where the gap

forms at the Fermi level. Once T_c has been reached, transport will be dominated by Andreev reflection and quasiparticle tunnelling with a significant reduction in measured resistance.

2.3.2 Proximity effect

Another phenomenon noted at NS interfaces is a suppression of superconducting properties in the superconductor and signs of weak superconductivity in the normal material a short distance either side of the interface. These observations are explained by the proximity effect, which is illustrated in Figure 2.15.

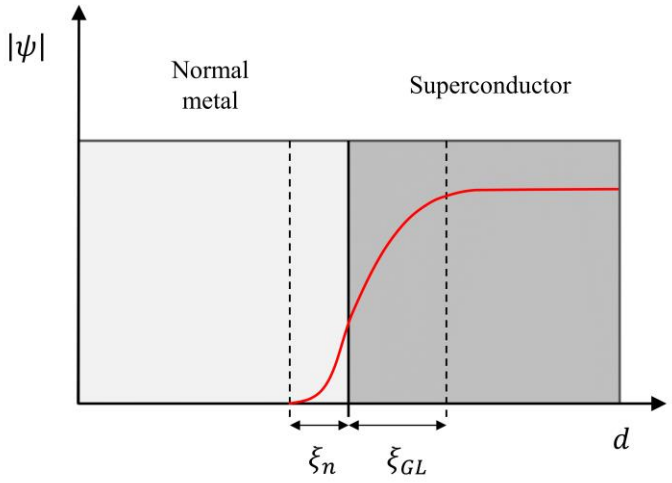

Figure 2.15: Schematic representation of the proximity effect where some degradation of the superconducting properties in the superconductor and signs of weak superconductivity in the normal material are observed at a normal-superconductor interface.

As mentioned previously, Andreev reflection provides phase coherence across the MS interface and an elementary mechanism for converting single electron states in the normal metal into Cooper pairs in the superconducting

condensate [64,66,67]. The penetration of Cooper pairs results in the modification of electronic properties in the normal material near the interface. The induced superconducting-like behaviour, changes in the local density of states, and other proximity-induced effects arise due to the presence and penetration of the Cooper pairs over a length ξ_n into the normal material where phase coherence of the Cooper wavefunction persists. In the superconductor an effect sometimes referred to as the inverse proximity effect occurs, where unpaired electrons can penetrate over a length ξ_{GL} within which the superconducting gap is reduced, and the superconducting properties suppressed. The mechanisms described above form the basis of the behaviour of SNS Josephson junctions, as discussed later. In the SNS junction, coherent superpositions of electron and hole-like quasiparticles form in the normal metal, shuttling these pairs from one superconductor to the other through the normal region. These superpositions are known as Andreev bound states. This process leads to a dissipationless supercurrent through the junction, whose maximum value is the critical current I_c.

2.3.3 Josephson junctions

One of the most widely studied components of a superconducting circuit is the Josephson junction. The general configuration of a Josephson junction is a weak link between two superconducting electrodes, as shown in Figure 2.16 where the deterioration and overlap of the superconducting wavefunctions $\Psi_{1,2}$ across the weak link is depicted. A weak link is exemplified by a local reduction in the critical current in a region that is short enough to allow for phase coherent Cooper pair transport across it. This is distinct from a strong link or a standard length of the superconducting circuit which, despite being able to experience a

suppression of superconductivity and be driven into a normally conducting state, does not allow for coherent Cooper pair transport.

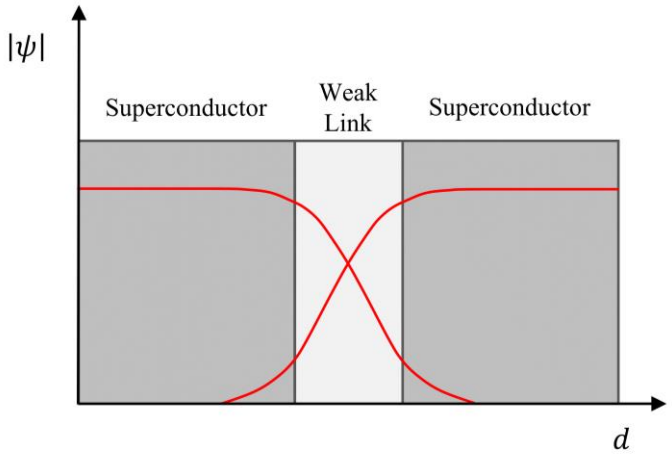

Figure 2.16: Schematic representation of superconducting wavefunction decay along the spatial dimension *d* across the weak link of a Josephson junction.

The weak link is generically a region of supressed superconductivity where supercurrents are bottlenecked, or the flow Cooper pairs disrupted. This suppression of superconductivity can be accomplished via various material or geometric approaches. When two superconducting electrodes are separated by an insulating barrier the Cooper pair tunnelling probability is determined by the thickness of the barrier. Sufficient thickness causes a significant reduction in critical current and the formation of a superconductor-insulator-superconductor (SIS) tunnel junction, as shown in in Figure 2.17a. Zero voltage current transport through SIS heterostructures was first predicted by Josephson in 1992 [68].

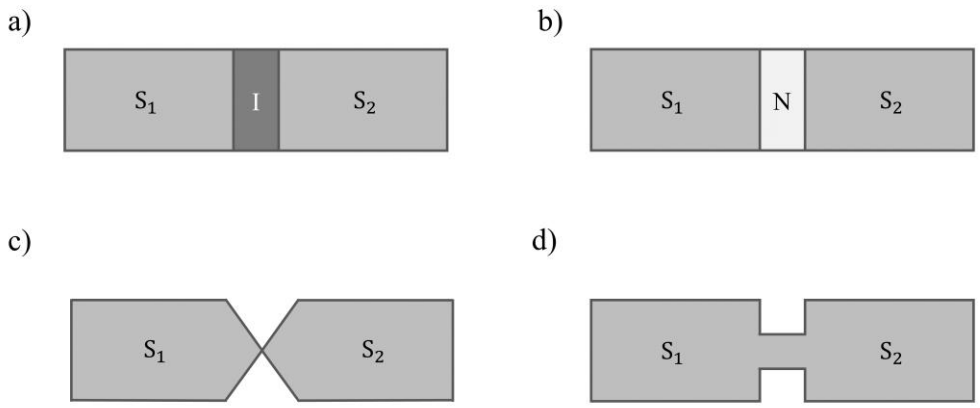

Figure 2.17: Examples of Josephson junction types. a) a superconductor-insulator-superconductor tunnel junction, b) a superconductor-normal metal-superconductor junction, c) a point contact and d) a Dayem bridge junction consisting of a constriction between two superconductors.

If two superconducting electrodes are separated by a normally conducting region, a superconductor-normal metal-superconductor (SNS) junction is formed, as illustrated in Figure 2.17b. The key characteristic of an SNS junction is the facilitation of Andreev bound state transport and the presence of the signature of the proximity effect.

As depicted in Figure 2.17c, an extreme constriction of the superconducting material can create a point contact junction, which is another structure subject to the proximity effect. As indicated in Figure 2.17d, a less severe constriction forms a structure known as a Dayem bridge. In both of these constriction-type junctions, supercurrent suppression is related to the local critical current density. In polycrystalline materials grain boundary junctions have also been extensively reported [69–72].

2.3.3.1 The Josephson effect

The Josephson effect, formalised by Josephson in 1962 [68], describes the transport properties of the superconducting electrons across the weak link. In the most standard case, the superconducting electrodes are separated by a thin insulating strip and form an SIS junction as depicted in Figure 2.17b. However, the Josephson effect is also present in other junction types such as those where the superconducting electrodes are separated by a normally conducting layer (Figure 2.17c shows an SNS junction). Various geometries have been employed to achieve practical junctions with insulating layers or weak links including vertical stacks of different layers, superconducting material grown over a step-edge feature, tunnel junctions with a vacuum gap and the Dayem bridge shown in Figure 2.17d.

The order parameter of a superconductor can be expressed as $\Psi_j(r) = (n_s/2)^{1/2} e^{i\phi_j(r)}$ $(j = 1,\ 2...)$ where n_s is again the number density of the superconducting electrons and ϕ_j is the phase. As shown schematically in Figure 2.17a, for two superconducting electrodes separated by a weak link the order parameter of each superconductor will decay across the gap. Assuming identical superconductors and a short enough weak link, the wavefunctions will overlap with matching Fermi levels resulting in the onset of phase coherence across the junction. Establishing the potential difference across the junction with fields E, $V = (E_1 - E_2)/2e$. The wavefunctions for each superconducting electrode will behave in accordance with the following equations:

$$i\hbar \frac{\delta \Psi_1}{\delta t} = E_1 \Psi_1 + C\Psi_2 \tag{2.35}$$

and

$$i\hbar \frac{\delta \Psi_2}{\delta t} = E_2 \Psi_2 + C\Psi_1, \tag{2.36}$$

where the coupling constant C dictates the interaction between the two wavefunctions. Substituting the wavefunctions into Equations (2.35) and (2.36), and separating the real and imaginary parts and with $\phi = \phi_1 - \phi_2$, yields

$$\frac{\delta n_s}{\delta t} = \frac{2}{\hbar} n_s C \sin \phi \tag{2.37}$$

and

$$\frac{\delta \phi_1}{\delta t} = \frac{C}{\hbar} \cos \phi - \frac{eV}{\hbar}. \tag{2.38}$$

From Equation (2.37) we can see that a current circulates between the two superconductors as $I = \frac{4eC}{\hbar} n_s \sin \phi$ with $V = 0$. Although the coupling constant is unknown and therefore I_c cannot be directly obtained, we can state that the magnitude of the dissipationless current though the junction is determined by the phase difference ϕ via:

$$I = I_c \sin \phi \tag{2.39}$$

which represents the *DC* Josephson effect, where it is implied that a current can flow between the two superconducting electrodes of a junction with no applied voltage. The equation describing the *AC* Josephson effect is found by subtracting Equation (2.37) from Equation (2.38), which gives

$$\frac{\delta\phi}{\delta t} = \frac{2eV}{\hbar}. \tag{2.40}$$

The *AC* Josephson effect describes the alternating supercurrent that flows through the weak link with a constant and non-zero voltage.

2.3.3.2 The RCSJ model and washboard potential

To properly quantify the conditions of the finite voltage regime, junctions are often considered in terms of the resistively and capacitively shunted junction (RCSJ) model first proposed by *Stewart* [73] and *McCumber* [74]. Here, C represents the capacitance between the electrodes and the resistance R is the dissipative response to the non-zero voltage. A sketch of an equivalent circuit is provided in Figure 2.18.

With a bias current I_b, the components of the RCSJ model are described by the following equation:

$$I_b = I_c \sin\phi + \frac{V}{R} + C\frac{dV}{dt}. \tag{2.41}$$

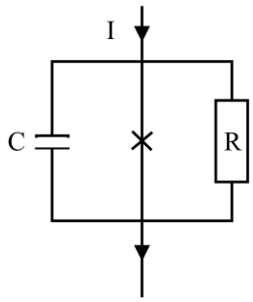

Figure 2.18: A schematic of the RCSJ circuit with bias current *I*, shunted capacitively by *C* and resistively by *R*.

Here, the second term refers to quasiparticle currents where the resistance will be of the order of the normal state R_n for most junction types near the critical temperature T_c. Assuming that $V_b = I_b R$, we also find:

$$V_b = RI_c \sin\phi + V + RC\frac{dV}{dt}. \tag{2.42}$$

By substituting with Equation (2.40) and with the introduction of dimensionless time variable $\tau = 2\pi I_c R_n t/\Phi_0$:

$$\frac{I_b}{I_c} = \frac{V_b}{I_c R} = \sin\phi + \frac{d\phi(t)}{d\tau} + Q\frac{d^2\phi(t)}{d\tau^2} \tag{2.43}$$

where Q is the damping factor and $Q^2 = \beta_c$ is the Stewart-McCumber parameter given by:

$$\beta_c = I_c C R^2 \frac{2\pi}{\Phi_0}. \tag{2.44}$$

It is useful to consider the behaviour of the junction in terms of different values of Q in conjunction with the bias current. For $I_b \ll I_c$ has static solutions for all values of Q where the phase $\phi = sin^{-1}(I_b/I_c)$. If $I_b > I_c$ the junction enters the finite voltage regime where the response of the $I_b - V$ characteristic is highly dependent on the damping parameter.

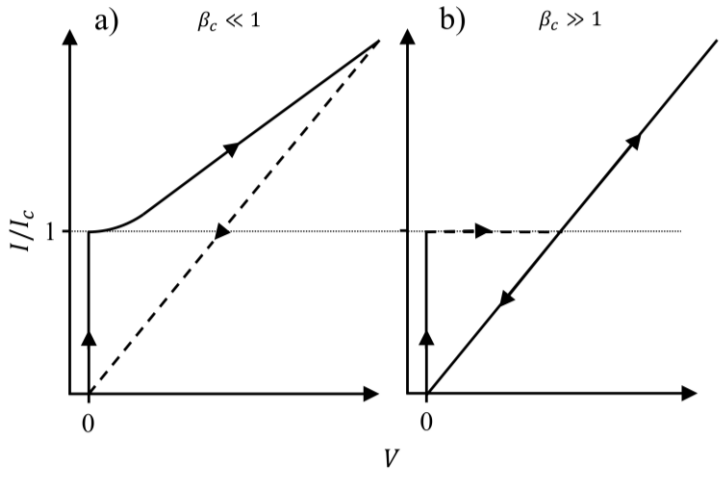

Figure 2.19: I-V characteristics for a) an overdamped and b) an underdamped junction.

The Stewart-McCumber parameter can also be thought of as the ratio between the characteristic time for the charge on the capacitor to relax (τ_{RC}) and the time for the phase to evolve (τ_J), giving $Q^2 = \frac{\tau_{RC}}{\tau_J}$. For situations where $\tau_{RC} \ll \tau_J$, when the junction enters the finite voltage regime most of the current will pass through the resistor. Next, the phase evolves causing the current and *dc* voltage to oscillate with respect to time according to the Josephson frequency $f_J = 2eV_{dc}/h$. In this situation the junction is said to be overdamped with $Q \ll 1$. Conversely, where τ_{RC} dominates we find that $Q \gg 1$ and the junction is underdamped. When the bias current is reduced from the finite voltage regime, the $I_b - V$ characteristic stays in the voltage state because the behaviour of the junction is dictated by the

RC-time constant of the circuit. This condition creates the hysteretic response seen in Figure 2.19b.

A common method for visualising these junction dynamics is in comparison to the motion of a particle moving on a tilted washboard. The equation of motion for this particle is given by Equation (2.43), where the particle has a "mass" proportional to C, a position on the washboard analogous to ϕ and experiences a viscous drag proportional to R^{-1}. In this example, depicted in Figure 2.20, the tilt of the washboard is dictated by the bias current. With $I_b < I_c$ the particle is able to sit in a local minimum of the washboard, corresponding to the zero-voltage regime.

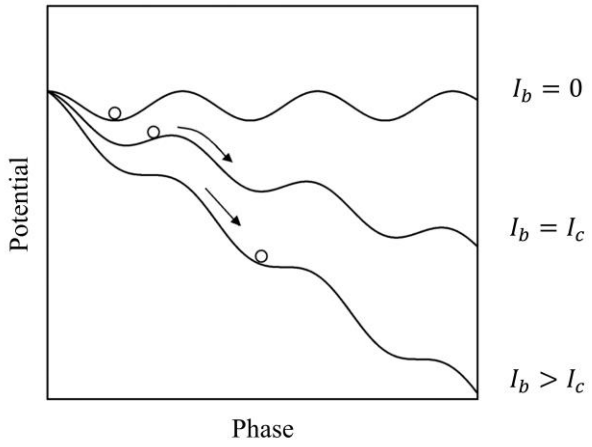

Figure 2.20: The washboard potential with different bias currents I_b.

With $I_b > I_c$ there is enough gradient on the washboard to cause the particle to fall with the phase increasing at a rate $2eV/\hbar$. As the current reverses and the washboard tilts back, the motion of the ball is again governed by its capacitance. With a large capacitance, the frictional force experienced by the particle will be sufficient to cause it to come to a rest a lower current. This is known as the re-trapping current, and is present in junctions with high capacitances and low damping.

In practice, for tunnel junctions consisting of broad parallel layers, the intrinsic capacitance will be high which produces the condition $\beta_c \gg 1$ where the junction is underdamped (Figure 2.19a). The *I-V* characteristic of the junction will display hysteresis which is generally undesirable for superconducting circuit device development. Different geometries or the inclusion of a large shunt resistance can create an overdamped system $\beta_c \ll 1$ (Figure 2.19b), where the contribution from the capacitance is minimised. For example, one of the advantages of the Dayem bridge junction type is that it allows a minimisation of capacitance.

In the case of an overdamped junction, the simplified RSJ model can instead be employed as such:

$$V = \begin{cases} 0 & \text{for } I < I_c \\ IR_n\sqrt{1-(I_c/I)^2} & \text{for } I \geq I_c \end{cases}. \tag{2.45}$$

2.3.3.3 Temperature dependence of the critical current

Recalling from previously, Equation (2.39) implies that a *DC* supercurrent can flow between weakly coupled superconducting electrodes with zero applied voltage, with the magnitude of the current depending only on the phase difference of the two superconductors $\phi = \phi_1 - \phi_2$. For the case of a tunnelling junction (SIS), the amplitude of the current passing through the junction is temperature dependent, with the behaviour determined as a development of BCS theory by *Ambegaokar* and *Baratoff* [75]:

$$I_c = \frac{\pi}{2}\frac{\Delta(T)}{eR_n}\tanh\left(\frac{\Delta(T)}{2k_bT}\right). \tag{2.46}$$

Here R_n is the normal state resistance and $\Delta(T)$ is the temperature dependent energy gap. For junctions with a normally conducting weak link, the implications of the proximity effect must be considered. It is useful to consider these junctions as the point contact cases outlined by *Kulik* and *Omelyanchuk* which hold true for short metallic constrictions and Dayem bridges [59].

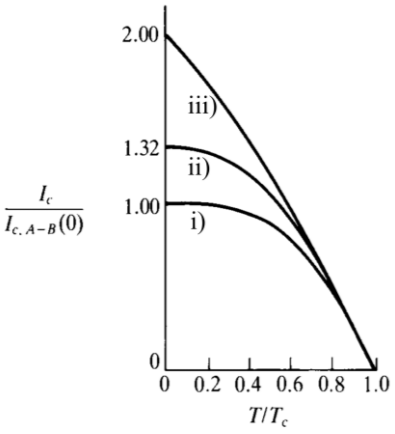

Figure 2.21: Showing the normalised temperature dependence of the critical Josephson current for i) the Ambegaokar-Baratoff relation, ii) KO-1 dirty limit for point contacts and iii) KO-2 clean limit. From *Tinkham* [59].

Firstly, propose a dirty limit where the electron mean free path is significantly shorter than the BCS coherence length $\ell < \xi_0$, known as KO-1 [76]. In this case the length of the junction must also be at most of a similar scale to the coherence length $L \lesssim \xi_0$. In the *Kulik* and *Omelyanchuk* KO-2 clean limit, the junction length can be significantly greater than the coherence length. A comparison of the scaling of these functions with the tunnelling limit established by *Ambegaokar* and *Baratoff* is shown in Figure 2.21. These limits and how they pertain to the proximity effect are discussed further in Section 6.1.

2.3.3.4 Field dependence of the critical current

In the presence of a field, the phases of the order parameters of the superconducting electrodes of a tunnel junction are subject to quantum interference. This causes fluctuations in the critical current as would be expected from Equation (2.39). Considering the enclosed area of the junction between the electrodes, when the flux through the junction is some integer multiple of the flux quantum $\Phi = n\Phi_0$ ($n = 1, 2, 3$ ...), the current through the junction is entirely suppressed.

By considering the spatial variations of the phase difference between the two superconductors perpendicular to magnetic field, we obtain

$$\frac{\delta\phi}{\delta x} = \frac{2\pi}{\Phi_0} B_y d_{eff} \tag{2.47}$$

where d_{eff} is the effective length of the junction due to field penetrating a distance λ_L. Integrating and combining with Equation (2.39) provides

$$I_c(B) = I_c(0)\left|\frac{\sin(\pi\Phi/\Phi_0)}{\pi\Phi/\Phi_0}\right|. \tag{2.48}$$

Here, the penetrating flux $\Phi = B_y d_{eff} W$, with the width of the junction W. This relationship is the familiar Fraunhofer diffraction pattern from optics, as shown in Figure 2.22. The geometric considerations of Equation (2.48) will be expanded upon in Chapter 7.

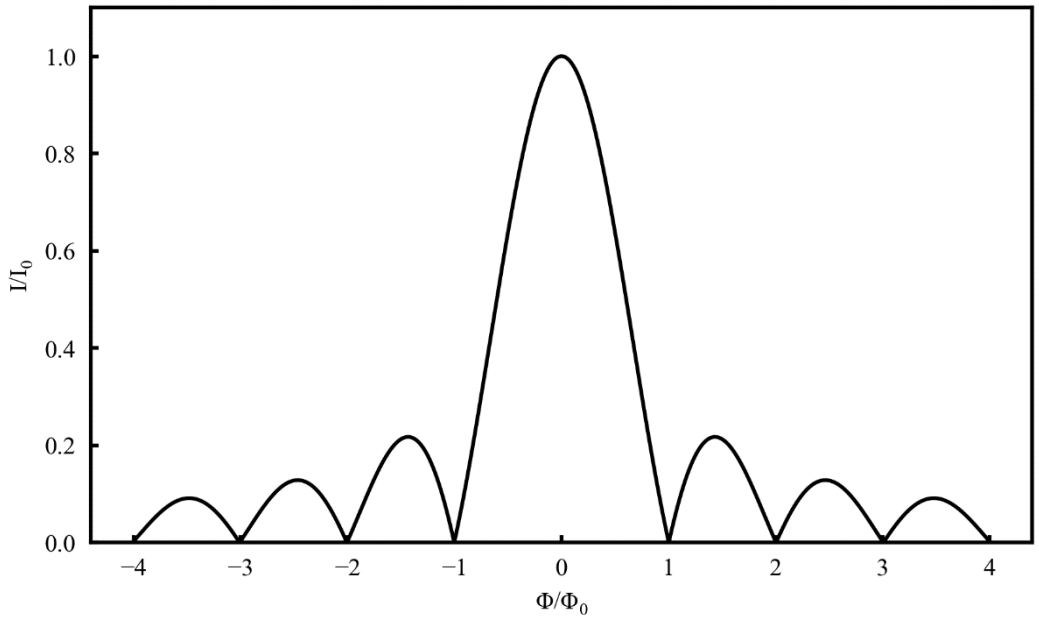

Figure 2.22: Example of the Fraunhofer diffraction pattern that emerges in the critical current in response to a varying field.

2.3.4 Superconducting Quantum Interference Devices

A superconducting quantum interference device (SQUID) allows for extremely sensitive detection of magnetic fields and consists of one or more Josephson junctions connected in a superconducting loop. In brief, the operation of a DC SQUID, utilising two junctions connected in parallel around the loop, is as follows. If a supercurrent I_b enters one side of the loop and exits on the opposite side, it is split in two and crosses the two junctions evenly. The presence of a magnetic field through the loop creates a screening current I_s, creating a field that cancels out the external flux. The resulting supercurrent along each side of the loop becomes $I_b/2 \pm I_s$ and if this total current exceeds the critical current I_c of the junctions a voltage is created. The flux enclosed by the loop must be of integer flux quanta Φ_0, so when the external flux increases beyond $\Phi_0/2$, I_s

changes direction and acts to increase the enclosed flux to Φ_0. When the flux through the loop is exactly Φ_0, I_s is zero. Thus, the total current through the loop oscillates with a period of Φ_0 with a maximum at $n\Phi_0/2$ and a minimum at $n\Phi_0$ (where n is an integer). If the SQUID is operated with $I_b \gtrsim I_c$ a voltage proportional to Φ can be read out from the system. A SQUID schematic and an example read-out scheme are illustrated in Figure 2.23 parts a) to c). As shown in Figure 2.23c, the classic signature of a SQUID in a varying magnetic field perpendicular to the device is an oscillating read-out voltage with amplitude ΔV.

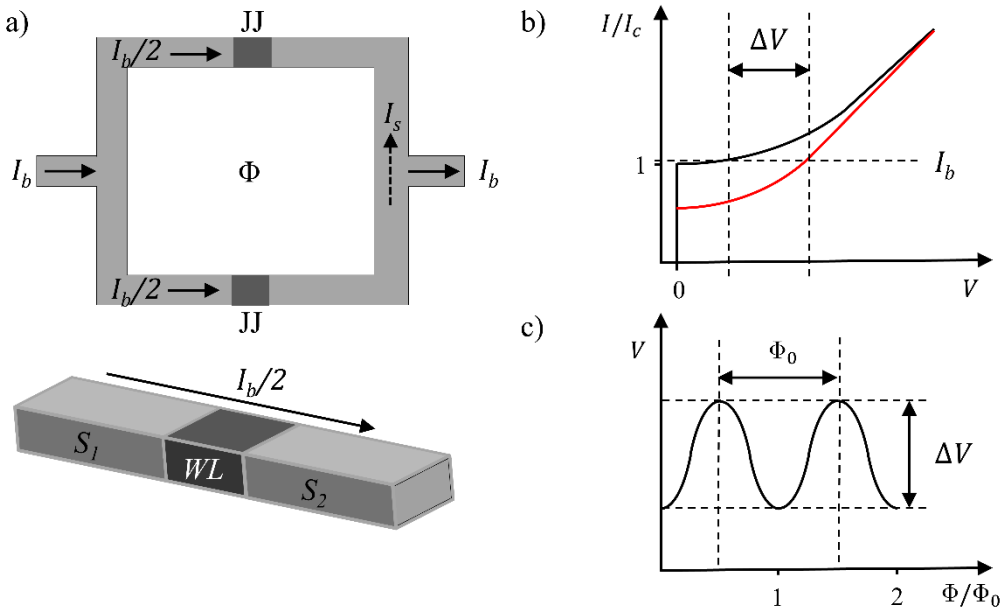

Figure 2.23: The DC SQUID a) Schematic of a DC SQUID, showing the supercurrent I, screening current I_s acting to oppose flux Φ through the enclosed area. Josephson junctions (JJ) consist of superconducting electrodes S_1 and S_2, and a weak link (WL) in the circuit which will either be insulating or normally conducting. b) Example SQUID operating I-V characteristic with bias current I_b. Read-out voltage ΔV emerges comparing $n\Phi_0$ (black line) and $n\Phi_0/2$ (red line) flux through the enclosed SQUID area.

2.4 SUPERCONDUCTIVITY IN B-NCD

Intrinsic diamond has a bandgap of 5.49 eV with the Fermi level located at the middle of the bandgap. *P-type* doping of diamond is achieved with boron due to the fact that it is readily substituted for carbon in the lattice, creating a shallow acceptor level at 0.36 eV [36,37].

The superconducting state was first reported in bulk diamond fabricated with high pressure and high temperature (HPHT) by *Ekimov et al.* in 2004 [77]. This was accomplished by reacting B_4C and graphitic carbon and resulted in a metallically conductive state at room temperature. The temperature dependence of the resistivity is shown in Figure 2.24, with the material achieving a state of negligible resistance with $T_c = 2.3$ K, an upper critical field of $H_{c2} = 3.4$ T and as estimation of the Ginzburg Landau coherence length of $\xi_{GL} = 10$ nm.

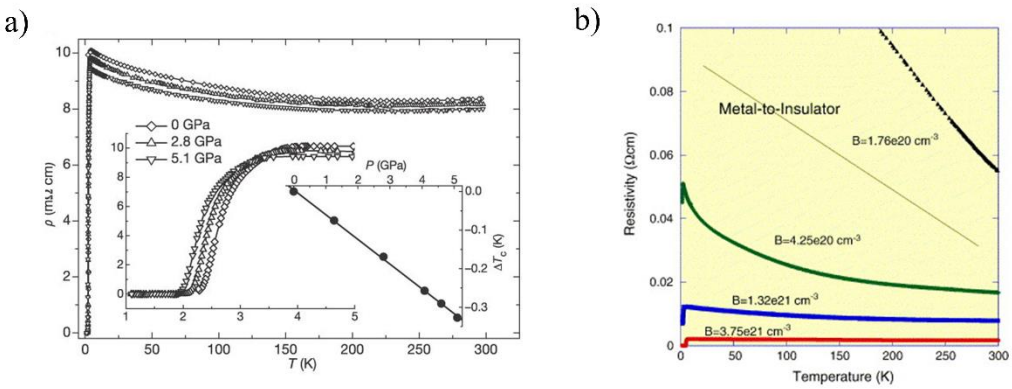

Figure 2.24: Early examples of superconducting diamond. a) The temperature dependence of the resistivity in the first superconducting boron doped diamond grown by *Ekimov et al.* [77] b) superconductivity was also found in in CVD grown polycrystalline film by *Takano et al.* [78]

Chemical vapour deposition (CVD) is a well-studied method for growing both single crystal and granular diamond films [5], which is essential for the development of electronic devices. Superconductivity was first reported in boron doped homoepitaxial single crystal films in 2004 with a gas phase B/C ratio of 2800 ppm producing a film with T_c = 2.1K [79]. In 2005 this was replicated in polycrystalline diamond films by *Takano et al*. with $T_c = 5$ K and $H_{c2} = 7$ T [78]. These films were grown with B/C = 5000 ppm, indicating the dependency of the transition temperature on doping concentration. Further work has established that the metal-insulator transition for diamond occurs at N_A = 4.5×10^{20} cm^{-3} [4,79–81].

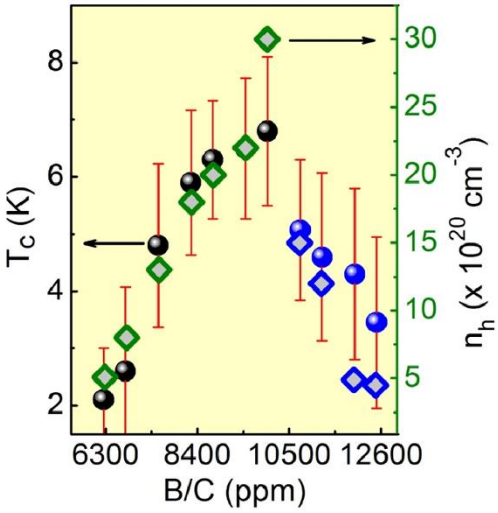

Figure 2.25: Investigations into the effect of doping concentrations on Tc reveal dome shaped behaviour [82]. Spheres correspond to T_c and diamonds to the Hall concentration n_h.

Kumar et al. report a dome shaped response for T_c vs doping concentration for granular films, as shown in Figure 2.25, which has been attributed to disruption of the sp^3 carbon lattice and the formation of defects at higher doping concentrations [82]. While these films were grown with hot filament chemical

vapour deposition, the growth conditions were comparable to the recipe used later in this work, with a H_2/CH_4 gas ratio of 2.7%. This pattern is generally corroborated by results from other groups, with the highest reported critical temperatures in the region of ~4-6 K [78,83,84]. The maximum doping concentrations associated with these higher critical temperatures is also reasonably consistent, with $\left(10^{21} < N_A < 5 \times 10^{21}\right)$ cm^{-3}. However, for a complete understanding of the landscape of growth parameter optimisation we must also consider seeding methods, film growth rates, thicknesses and resulting grain sizes [85–87]. Single crystal diamond (SCD) films have been produced with $T_c =$ 10 K [88], giving some indication of the importance of the film granularity in poly, micro and nano-crystalline diamond films (NCD). The normal state $\sqrt{T}$ dependency of the film resistivity seen in Figure 2.24 has been widely reported in both SCD [89] and NCD [6] films.

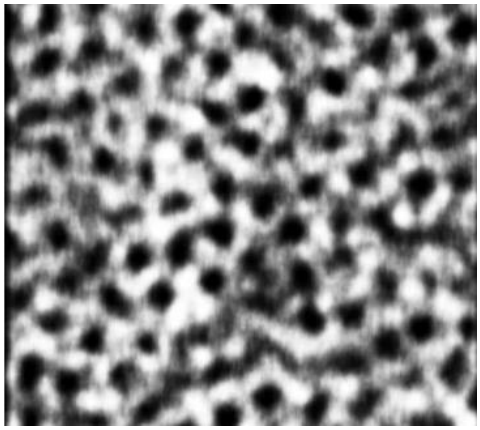

Figure 2.26: Abrisokov vortices in SCD over an area of 1.5×1.5 μm^2 [90].

Conformity to BCS theory has been confirmed in SCD films, with simultaneous imaging of the vortices of the mixed Meissner state via scanning tunnelling microscopy as shown in Figure 2.26 [90]. The film investigated showed no sub-

gap states and a peak in the density of states consistent with $\Delta(0)/k_bT_c$ = 1.74. The nature of superconductivity in granular films is less simple.

While BCS behaviour has been widely confirmed, granular films are subject to effects that cause spatial variation in the superconductivity. In HPHT grown polycrystalline diamond an anomalous resistance peak below T_{onset} has been attributed to quantum confinement and coherence effects of inhomogeneous superconductivity in the presence of the disordered system of grains and grain boundaries [91]. When considering such a system, where only the grains are superconducting, it is intuitive to assume that continuous superconductivity at lengths greater than the size of the grains noted across the film is the result of percolation between the superconducting islands formed by the grains. This resulting superconductivity is referred to as mesoscopic superconductivity. Different levels of boron doping can produce either a semiconducting or metallic material, and the grain boundaries with graphitic and disordered carbon show metallic conductivity [92]. As such, the proximity effect and tunnelling must be considered, and the specific superconducting properties of the grains and the granular matrix (composed of grains and grain boundaries) become a central factor in the overall superconductivity. This model has received general validation in recent years. In boron doped NCD films (B-NCD) with more moderate doping concentrations above the MIT a breakdown of BCS behaviour has been noted. *Willems et al.* noted a modulation of the superconducting gap across a length scale smaller than the size of a typical grain, which is shown in Figure 2.27 [93]. They also found a non-BCS temperature dependence of the gap, attributed to the presence of the proximity effect across the granular matrix.

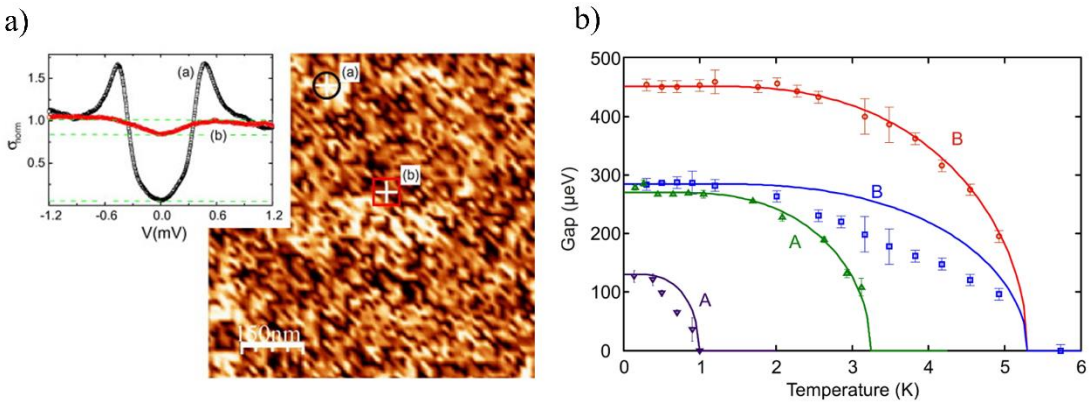

Figure 2.27: Examples of superconducting gap variation a) Modulation of the superconducting gap at sub-grain lengths [93], b) spatial variation of the temperature dependence of the gap [94].

Similar behaviour has been identified elsewhere and has been attributed to local inhomogeneities in boron doping, most likely due to the different rates of crystalline facet uptake [4,86,94,95]. It should be noted, however, that the use of higher doping concentrations is likely to push the system towards general saturation across the grains which would be expected to produce spatially homogenous gap values and maintain BCS temperature dependence. Additionally, lowering the C/H ratio results in a broader spread in the distribution of grain sizes, resulting in a higher frequency of larger grains in the film [86]. It has been found that smaller grains produce a higher T_c, noted to correlate with higher boron concentrations and carrier densities when compared to larger grains, but these results are potentially conflated by the altering of C/H ratio during growth. The trend of thicker films producing higher T_c has been noted by various studies, with thicker films being directly correlated with larger grains and the highest values of H_{c2} [6,93]. The presence of a finite superconducting transition in the granular films is likely principally due to this variation in gap energy and T_c between grains of different sizes, with a percolating path forming between sufficiently well coupled grains within the

disordered matrix [94]. From calculations based on the upper critical field using $\xi_{GL} = \left[\frac{\Phi_0}{2\pi} H_{c2}(0\,K)\right]^{1/2}$, additional values for ξ_{GL} can be compared to the original value from *Ekimov et al.*, with a ξ_{GL} = 15 nm and ξ_0 = 15 nm for boron doped SCD [79,90] and $\xi_{GL} \approx$ 6.9 to 13 nm for B-NCD [78,86]. From $\xi_{GL} = (l\xi_0)^{1/2}$, the electron mean free path can be estimated $l \approx$ 3.9 nm [4], with another boron doped single crystal film providing $l \approx$ 0.5 nm [96]. The mean free path for a boron doped polycrystalline was estimated as $l \approx$ 0.45 nm [97]. It can therefore be said that heavily doped nanocrystalline films are charactersed as dirty limit superconductors.

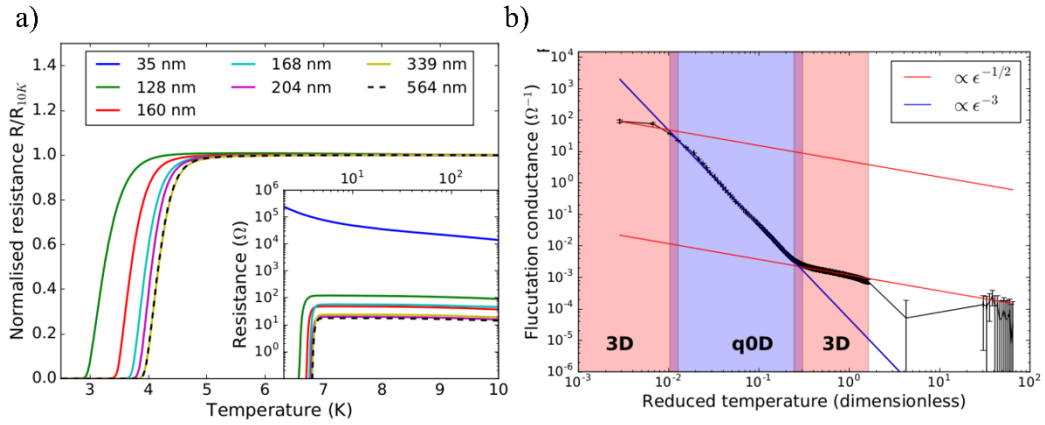

Figure 2.28: The fluctuation spectroscopy study results performed by *Klemencic et al.* [6], with a) the range of film thicknesses measured and their corresponding $R(T)$ curves, and b) the three distinct regions in fluctuation conductance.

A detailed study on the effect of grain size and the superconducting properties of a B-NCD film was carried out by *Klemencic et al.* [6]. Here, mean grain size was controlled by varying the film thickness with consistent growth conditions, with the different thicknesses showing a positive correlation with T_c as shown in Figure 2.28a.

The observation of three distinct regions in the extracted fluctuation conductance with the scaling factors established by Lerner, Varlamov and Vinokur (LVV) are evidence of crossover between states where the Ginzburg Landau coherence length ξ_{GL} intersects with the size of the grains [87]. As discussed previously, ξ_{GL} varies with temperature and therefore in the vicinity of the superconducting transition temperature three regions are noted. At the highest temperatures ξ_{GL} is small compared to the grains and transit as if it were in the *3D* bulk material. With decreasing temperatures ξ_{GL} will at some point be of the order of the gain size, where the material behaves as coupled array of quasi-*0D* superconducting islands. As temperatures decrease further ξ_{GL} increases to the extent that the granularity is not seen by the Cooper pair, with the material again behaving as if in a *3D* bulk. In this case this electronic dimensionality in terms of ξ_{GL} is specifically referring to occurrence of physical dimensions of the system relative to the coherence length. These measurements and LVV theory are revisited in Section 6.2.

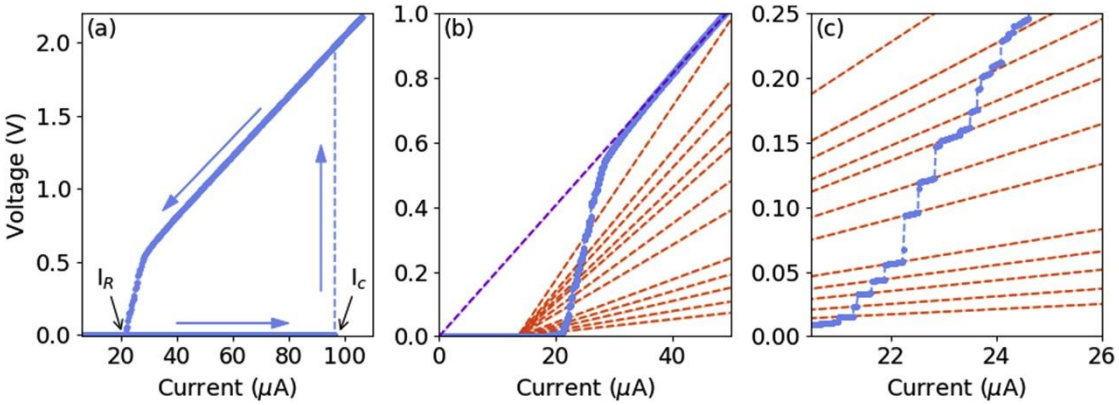

Figure 2.29: The presence of a common intercept for the voltage steps in the *I-V* characteristics presented by *Klemencic et al.* is indicative of phase slip behaviour as described by SBT theory [98].

A useful tool derived from fluctuation spectroscopy is accurate determination of the critical temperature via fitting with $\sigma_{fl} \sim (T - T_c)^{-3}$ and determining the point of divergence [92]. This method is used throughout the current work presented in this thesis.

In separate work *Klemencic et al.* comment further on how the specific microstructure of B-NCD impacts the superconducting properties [98]. They note that the epitaxial growth originating from the seeding process results in competitive columnar growth following the Van der Drift model [99], with these grain columns eventually coalescing into a solid film as a granular matrix.

The presence of residual resistance in the $R(T)$ data and injected-noise induced steps in the *I-V* characteristics of the patterned devices is indicative of phase slips, confirmed by fitting to the *Langer-Ambegaokar-McCumber-Halperin* theory for 1D superconductors [100,101] and predictions from theory presented by *Skocpol*, *Beasley* and *Tinkham* (SBT) [102,103], respectively. The behaviours noted by these theories support the modelling of the superconducting system as an array of Josephson junctions between the grains and, crucially, the physical dimensions of the fabricated structures do not account for any impingement of ξ_{GL} and so any reduced dimensionality can only be explained by the smaller structures of the granular matrix (i.e., grains and grain boundaries). This model is discussed in more detail in Section 7.3.

Later work from *Klemencic et al.* [92] adds further credence to the importance of the grains in the superconducting system, where a glassy state of superconductivity is observed. This refers to the individual grains possessing spatially random superconducting order parameter, with the glassy dynamics attributed to frustration in a system of weakly coupled superconducting clusters. Also presented are two distinct coherence lengths specific to granular films. The coherence length for a Cooper pair within a grain $\xi_g \approx 30$ nm and for a Cooper

pair straddling a grain boundary through tunnelling $\xi_t \approx 7$ nm, with ξ_t being the effective coherence length for the film.

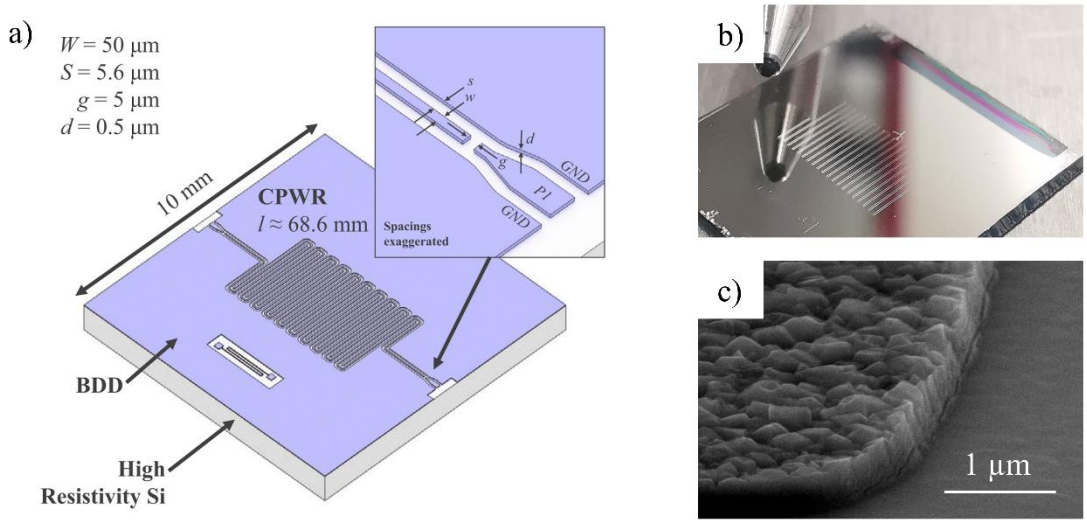

Figure 2.30: The coplanar resonator device measured by *Cuenca et al.* showing a) a schematic [104], b) a photograph prior to etching and c) an SEM image of the ~500 nm thick structure.

Recently *Cuenca et al.* used a microwave coplanar resonator fabricated from B-NCD (shown in Figure 2.30) to measure the penetration of depth of the material, found to be $\lambda_L \approx 3.8$ µm [104]. This value, while in agreement with previous work on B-NCD [105], is considerably higher than what has been measured in single crystal films where $\lambda_L \approx 0.2$ to 1 µm [106,107]. Again, this has been attributed to the granularity of the film and is a consideration relevant in the design of various superconducting devices.

To summarise, we can consider various established properties and quantities for B-NCD. At $T > T_c$ the temperature dependence of the film resistance is expected to have a $T^{1/2}$ dependency as shown in the previous work from the Cardiff Diamond Foundry presented above. The relevance of the grains in the

superconducting system is also clearly established, with spatial inhomogeneity of the superconducting gap across a grain only noted in films with more moderate doping concentrations. Regarding the whole film, variation in the superconducting order parameter is understood as part of a model with random variations between individual grains embedded in a matrix of metallically conducting grain boundaries. The critical temperature of the films has been noted to depend on the boron doping concentration and the size of the grains, which in turn depends on the growth conditions and film thickness. As discussed later in Chapter 5, SQUID devices have been successfully measured in various works with single crystal and B-NCD material, a fact which establishes the weak links in the superconducting circuit as true Josephson junctions rather than strong links that are driven normal.

3 EXPERIMENTAL METHODS

This chapter discusses the experimental methods and techniques used throughout the work undertaken in this thesis. Some of the methods are based on well-established processes but warrant explanation in the context of the specific experiments performed in this work. Various considerations and modifications are necessary to facilitate use of these methods with diamond film due to its extreme properties. Principally among these factors are those pertaining to diamond film growth and device fabrication, the former of which drastically impacts the performance of the material across all domains and the latter covers techniques that require modification to enable diamond processing. Additionally, a novel adjustment to the operation of a dilution refrigerator was necessary to perform stable measurements above its standard operating temperature is introduced. As such, certain topics in this section are intended as a resource for future work using the material or with the specialised techniques developed.

3.1 BORON DOPED NANOCRYSTALLINE DIAMOND GROWTH

The growth of nanocrystalline diamond (NCD) via microwave enhanced chemical vapour deposition (CVD) is a well-established technique [5,108,109].

Altering the electronic properties of the material can be achieved with the addition of boron (discussed previously in Section 2.4) to the growth gases. In this thesis, the films used throughout are grown using the same equipment and with identical recipes.

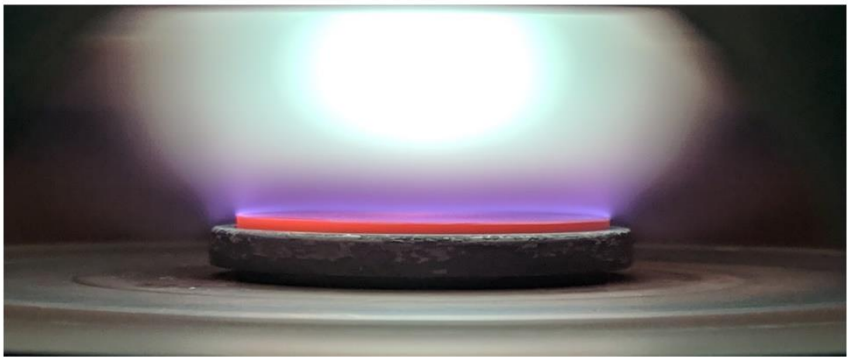

Figure 3.1: Photograph of the inside of a CVD reactor, showing the hot substrate and the plasma ball slightly above its surface.

Growth was performed in a Seki AX6500 series reactor, which features a clam-shell design with the sample mounted on a molybdenum holder which is in turn placed at the centre of a copper electrode. For intrinsic diamond growth, it is common to use growth gasses consisting of a dilute mixture of methane (CH_4) in hydrogen (H_2). Microwaves produced from a magnetron with a frequency of 2.45 GHz are fed into the system via a waveguide and facilitate electron collision mediated disassociation of H_2 molecules in the feed gas mixture [110]. These atomic hydrogen are then able to extract hydrogen from CH_4 to produce the methyl radical CH_3, which is the principal species involved in diamond growth [111].

The growth substrate of high resistivity silicon wafer buffered with 500 nm of SiO_2 is seeded with a monodisperse aqueous colloid of ~5 nm diamond nanoparticles which has been shown to enhance nucleation rates [85,109,112,113].

Growth was performed with a microwave power of 3.5 kW and a pressure of 40 Torr, with a substrate temperature of 755 °C as determined via a pyrometer. The gas mixture consists of a low CH_4/H_2 chemistry (<3% CH_4) [5] and the addition of trimethylboron to provide a gas phase B/C ratio of 12800 ppm, with a total flow rate of 500 sccm [114]. By calculating directly from this B/C ratio and comparing with earlier works it can be assumed that the boron concentration in the samples is greater than $2x10^{21}$ cm^{-3} [115–117]. As discussed previously in Section 2.4, these growth conditions provide samples with consistent superconducting performance.

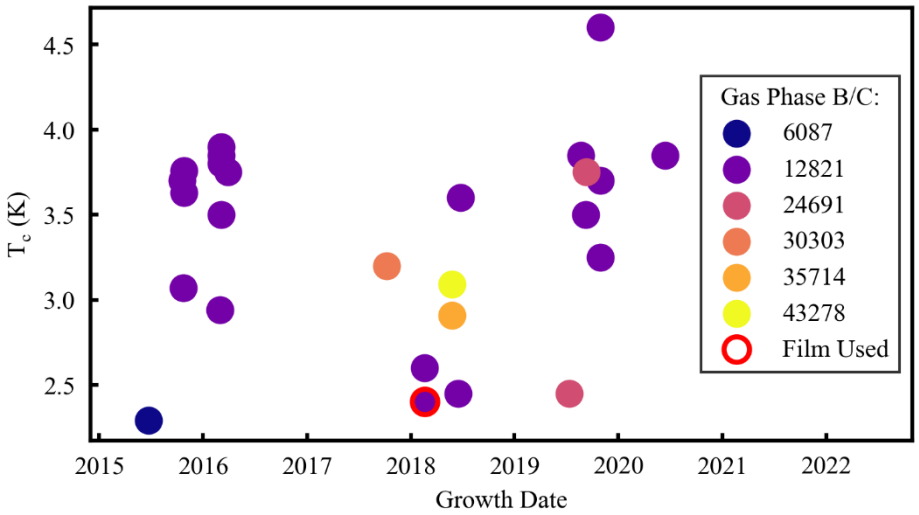

Figure 3.2: The critical temperature of BDD films grown on different dates with various gas phase B/C ratios. The film growths are tuned for different purposes and have various thicknesses but consistently show superconductivity due to sufficient boron doping.

The performance of various films grown using this recipe in the Cardiff Diamond Foundry, quantified in terms of T_c, is presented in Figure 3.2.

3.2 PHOTOLITHOGRAPHY

Photolithography is the process of using light to create highly resolved and detailed patterned thin films. Commonly used in the semiconductor industry for the fabrication of integrated circuits, adjustments to the process can be made to suit other materials. The technique relies on the use of a light reactive polymer, known as photoresist, to transfer the pattern from a mask onto the film. When exposed to light the polymer of the resist denatures and becomes more or less soluble, depending on the resist type.

When engineering a device with small dimensions it is essential to be aware of the smallest dimension that the process is able to produce. This critical dimension (CD) is described by the Rayleigh equation:

$$CD = k_1 \frac{\lambda}{NA}. \tag{3.1}$$

Here λ is the wavelength of the light used in the imaging system, NA is the numerical aperture of the lens and k_1 is a dimensionless, process dependent constant (typically $k_1 = 0.25$ for photolithography). It is also important to consider the thickness of the photoresist as a factor limiting the ultimate resolution of the pattern. With the thickness of the photoresist, h, the resolution is given approximately by [118]:

$$\text{Resolution limit} \approx k\sqrt{\lambda h} \tag{3.2}$$

where k is a constant related to the diffraction limit (equal to $\sqrt{2}$ in most cases). For most standard ultraviolet light sources (365 nm) and photoresists, minimum

feature sizes of approximately 1 μm are easily achievable. When metal lift-off is required, a maximum thickness ratio of 1:3 metal:photoresist is preferred.

A brief description of the photolithographic process flow used throughout this work is described as follows. To ensure reliable pattern transfer and photoresist adhesion it is essential that both the substrate film and the mask are free from dust and contaminants. To ensure consistency and reproducibility, a standard protocol of three solvents was used. Firstly, acetone is a polar solvent that is well suited for the removal of organic contaminants but can cause issues with redeposition due to its high evaporation rate. This high evaporation rate tends to leave stains on the surface so methanol, a solvent with a lower evaporation rate, is used to remove the acetone. Finally, isopropyl alcohol is used as a rinse agent to remove any remaining acetone or methanol, plus any non-organic or particulate contaminates. These solvents are heated in glass beakers on hot plates to 80 °C, with the samples left in each for 3-5 minutes. The final step in the cleaning process is drying with compressed air, which is performed in such a manner as to push any residual fluid off the film.

Prior to the next step, the samples were treated with pre-bake on a hotplate to remove any residual moisture. Following this the photoresist was applied to the film surface. Spin coating is used to ensure uniformity and allows for tuning of the thickness of the photoresist. A second bake is occasionally used after spin-on to control for resist moisture content, which influences exposure and development sensitivity. Three main categories of photoresist are available; positive, negative and image reversal resists. For a positive resist, the portion of the resist exposed to the light becomes soluble to developer solution, with the opposite true of the negative resists. Image reversal resists initially behave like positive resists, but the addition of a "reversal bake" step makes the soluble portion inert.

The proximity of the pattern mask to the sample is a key variable, with many recipes calibrated for direct contact or very slight separation. A consequence of the spin-on process is the formation of an edge bead on the outside of the sample several times thicker than the rest of the resist. Several techniques are commonly used to remove this edge bead, including the use of a dedicated mask pattern and an additional flood exposure and development step, or simply carefully wiping the edge of the sample with a cotton bud soaked in developer solution.

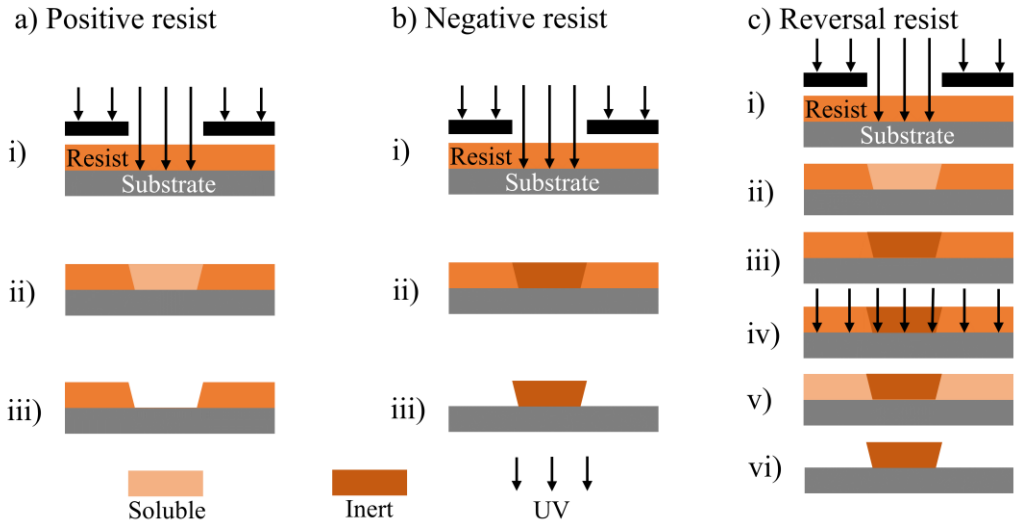

Figure 3.3: Typical photolithographic steps. a) Positive resists, with i) UV exposure through a mask producing ii) a soluble portion of the resist, allowing iii) removal via developer solution. b) Negative resists where the i) UV exposure creates ii) an inert portion of the resist allowing iii) the rest of the resist to be removed by developer solution. c) Image reversal resists where steps i) & ii) are identical to a positive resist, but iii) is a bake step turning the exposed portion inert. iv) A subsequent flood exposure turns the v) remaining resist inert, allowing vi) its removal by developer solution. Arrows indicate UV light.

Figure 3.3 shows process steps for each resist type mentioned above. For the positive and negative resists, the steps are broadly the same. Firstly, the mask is aligned over the sample and the resist is exposed to durations and intensities of light calibrated during process development (part i) across all three processes in Figure 3.3). These parameters will vary with the specific resist and its thickness. The exposure step causes the photoresist to become either soluble or inert to the developer solution for positive or negative resists respectively (part ii) across all three processes in Figure 3.3).

Finally, the sample is placed in a developer solution for a specific amount of time, gently stirred throughout to ensure constant conditions at the resist. To stop the development process the sample is typically dipped into two beakers of distilled water, the first used as an immediate "process stop" and the second as a continuous rinse with gentle stirring. As can be seen in part iii) for all processes in Figure 3.3, the end results for each often result in different edge wall profiles with the overhang in the negative resist making it more suitable for metal lift-off. This undercutting is intrinsic to the negative resists and must be carefully tuned as a function of the exposure and development parameters.

Image reversal resists also have the advantage of creating a tuneable overhang, with the process shown in Figure 3.3c. The initial processing steps are identical to using a positive resist with i) the initial exposure step resulting in ii) a soluble exposed portion of the resist. Next, the sample is placed on a hot plate for iii) the image reversal bake. This is critical for establishing the wall profile, with the temperature and duration carefully controlled. The sample is then allowed to cool and rehydrate in a controlled environment for 5 minutes, after which iv) the whole sample is given a flood exposure sufficiently long enough to denature the remaining photoresist. This results in v) only the initially exposed portion of resist being insoluble, allowing for vi) a clean undercut profile as the final result.

When testing and developing a metal lift-off photolithographic process there are certain factors that need to be controlled and various tuneable attributes to optimise. Considering first the fidelity of the pattern transfer, the cleanliness of the samples, environment and equipment is essential. Proper cleaning must be employed, as mentioned previously, and care must be taken to maintain the reliability of the clean room environment. Dust and particulate matter are often of the size order of the features to be patterned so must be minimised. A key part of this is careful maintenance and dispensing of resist fluids, which are prone to clumping if allowed to dry in storage bottles. All beakers and photomasks must also be thoroughly cleaned. Secondly, the variables of the photolithographic process itself must be systematically investigated. Principal among these are the resist thickness and baking temperature (particularly for image reversal processes), exposure times and pattern development concentrations and times. It is common to require many iterations in exposure and incremental development times until the correct balance of parameters is achieved. For a metal-lift off, the presence of the undercut mentioned previously can be evaluated by oscillating the focus of an optical microscope between the resist and substrate surfaces. The undercut must be tested in a lift off trial to ensure that it is functioning as intended, enhancing the quality of the lift-off and reducing the occurrence of tears and other damage. The specific details of the photolithographic recipes used for this work is covered in Section 4.2.3.

3.3 ELECTRON BEAM LITHOGRAPHY

Electron beam (E-beam) lithography is a maskless method of pattern transfer able to produce spot sizes less than 10 nm [119]. Patterns can be directly written to resists on the sample surface, allowing more rapid design iteration. The nano-scale devices produced in this thesis were fabricated using a recipe developed in

the Cardiff Diamond Foundry by Soumen Mandal and Evan Thomas. The NCD films are first spin coated in PolyMethyl MethAcrylate (PMMA) 950 A4 with an acceleration of 4000 rpm s^{-1} and speed of 4000 rpm for 30 s. The resist is then baked at 180 °C for 5 mins. For the actual writing process a Raith eLine system at Swansea University was used. It is possible to utilise different apertures during the writing process to balance the speed and accuracy requirements for various areas of the desired pattern. Dose testing the smallest aperture is required to optimise the power per area delivered to the resist and thus avoid underexposure or overexposure, which not only influences the edge profile but also final resolution and fidelity of the pattern. For the portions of the device where accuracy is particularly important the 10 μm aperture was used, and with a ~40 pA current a dose of 240 μA s cm^{-2} was found to be optimal. The default beam step size of 0.02 μm produced repeated arc patterns along the straight edges of the design and so was reduced to 0.006 μm.

3.4 DIAMOND ETCHING

Wet etching methods typically used in semiconductor processing are unsuitable for diamond due to its chemical inertness, instead requiring dry etching techniques with inductively coupled plasma reactive ion etching (ICP-RIE) seen as the generally preferred option [120]. ICP-RIE combines the effect of chemical etching with ionised reactive oxygen species in the plasma with physical bombardment of the substrate. Due to the tuneable nature of these effects, highly anisotropic etching can be achieved resulting in vertical edge wall profiles. An example of this is shown in Figure 3.4.

Ni is a well-established etch mask for diamond, with a thin layer of <200 nm being sufficient [31,121]. The physical bombardment component of the etching

process can result in sputtering and redeposition of the etch mask, creating isolated islands of diamond protected by this re-masking (partially visible in the test sample shown in Figure 3.4).

For this reason, SF_6 is included in the plasma chemistry which has been shown to minimise this effect [31,104]. Throughout this thesis etching was performed using an Oxford Instruments Plasmalab 100 ICP-RIE system. The recipe developed by the Cardiff Diamond Foundry has optimised etching parameters requiring an oxygen flow rate of 40 SCCM, a pressure of 10 mTorr, a 25 °C table temperature, an ICP power of 1500 W and an RIE power of 100 W.

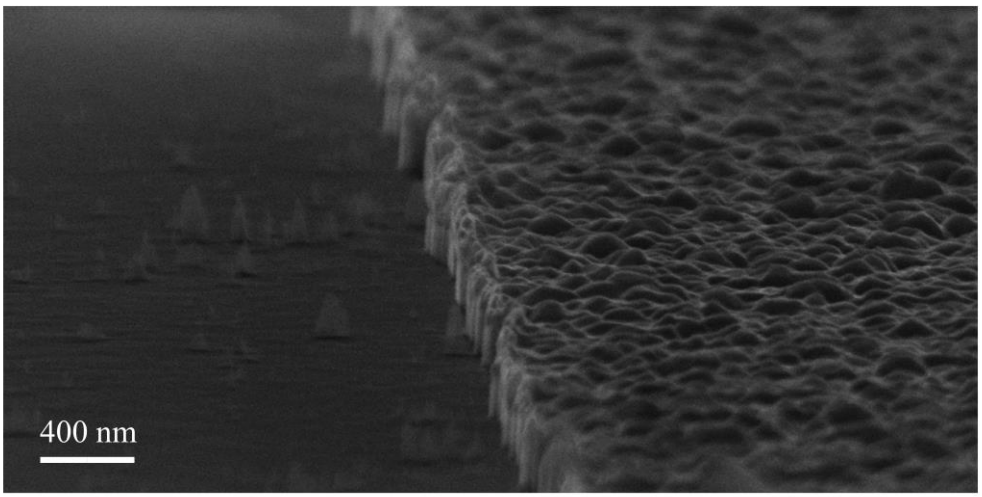

Figure 3.4: Tilted SEM image of an edge wall on a B-NCD film, showcasing the anisotropic etching possible with ICP-RIE.

3.5 RAMAN SPECTROSCOPY

Raman spectroscopy is a non-destructive technique that allows the probing of chemical bonds, relying on the inelastic scattering of photons resulting from the excitation of vibrations in molecular and crystalline materials [122]. An incident

monochromatic light source will result in energy transfer to the electron cloud constituting the chemical bonds of the material. The relaxation of these electrons results in the emission of light of various frequencies as shown in Figure 3.5. Firstly, Rayleigh scattering accounts for the largest proportion of the emitted light and has the same frequency as the original source. A small portion of the energy transferred to the electrons causes excitation of vibrational modes of the system, causing the emitted light to be a longer wavelength.

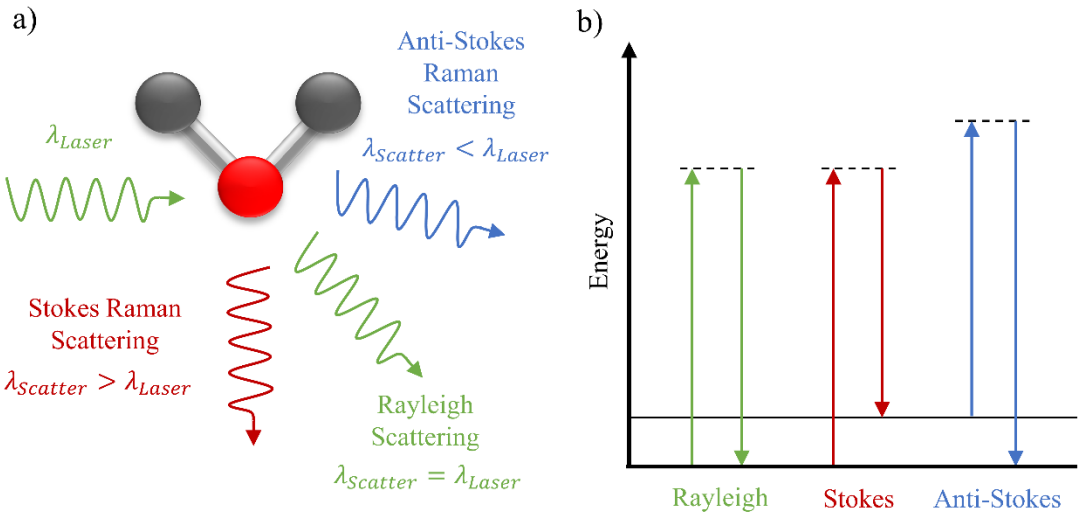

Figure 3.5: Schematic representations of scattering processes in Raman spectroscopy with a) showing the relative wavelengths of the scattered light and b) a simplified energy level diagram.

Comparison of these Stokes scattered photons with the Rayleigh frequency allows direct extraction of the vibrational frequencies of the sample. The reverse of this process also occurs, where the existing excitation of vibrational modes is added to the energy absorbed from the incident light, with the resulting emitted light having a shorter wavelength.

As the vibrational frequency of the bonds is dependent on the atomic masses and the force constant, the emitted light can be used to identify the chemical bonding environment of the sample. The classic Raman signature of diamond is the presence of a strong peak at 1332 cm^{-1} due to the central zone phonon [5]. Further explanation of the specific Raman response of B-NCD will be detailed in Section 4.2.2.

3.6 WIRE BONDING

Wire bonding between a device's electrical contacts and its packaging is often an essential component of device fabrication, testing and implementation. Two techniques were used in this thesis. When forming connections for the measurement of film resistances the use of silver epoxy was preferred for its simplicity.

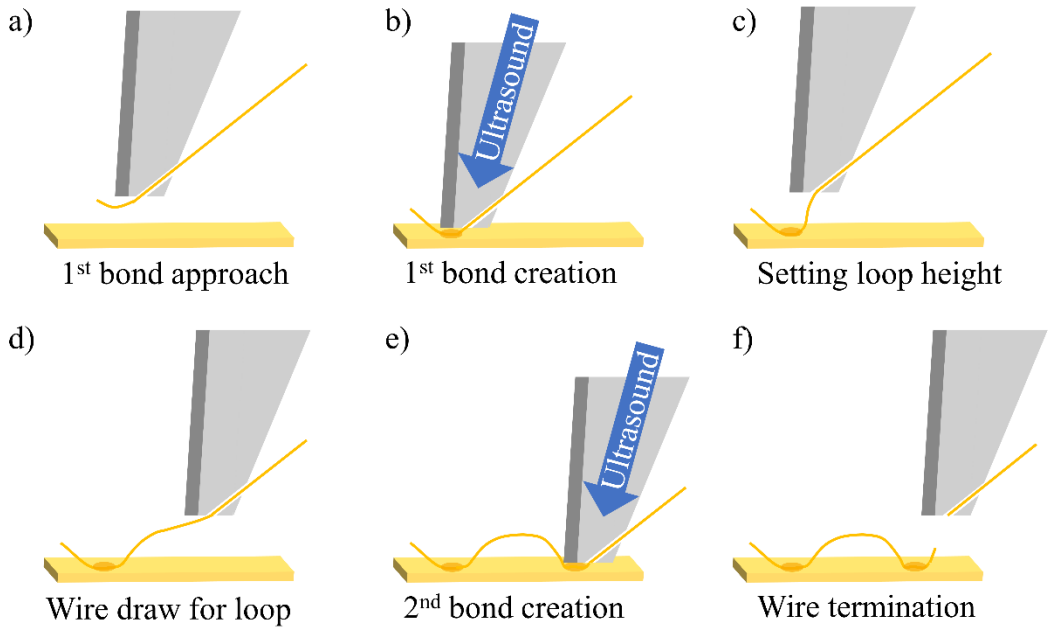

Figure 3.6: Process flow for wedge wire bond formation.

However, high precision is extremely challenging and contact pads are often necessarily densely packed onto device chips. Such situations are better addressed by the advantages of a manual wedge bonder, which allow the formation of extremely fine bonds. These systems use a wedge, effectively a blunted needle, through which the bonded wire is threaded. Bond formation is achieved by the application of ultrasonic vibration passed through the wedge when it is pressed into the sample surface. The process flow of this operation is depicted in Figure 3.6.

First, the approach height for the first bond must be established, with a closer approach often required for more delicate bonds to reduce impact. Next, the wedge tip is pressed into the sample with a pre-set force and duration. As the bonding wire is sandwiched between the two, the application of the ultrasound (again, a variable of careful calibration) causes the wire to partially melt and adhere to the sample surface. After the set duration has elapsed, the wedge head draws back to the desired loop height, which will depend on the specific geometry of the chip package and any routing requirements. The next step is to carefully draw the wire to the location of the second bond. It is possible, but not advised, to gently coerce a curve into the wire if the packaging setup requires it. The second bond is then created similarly to the first, with its own parameters for force, power and duration to allow for different surface materials. In comparison to a ball bonder, a wedge bonder allows for a narrower contact pitch which is often desirable in chips with densely packed contact pads. Images of various wire bonding examples from the various devices measured in this work are presented in Figure 3.7.

The wire bonder used throughout this thesis in a Kulicke & Soffa model 4523 Wedge bonder, using a 1% Si/Al 12 μm wire. The specific bonding variables depended strongly on the materials forming the contact pads. Diamond is a

particularly difficult material to establish effective recipes for due to its extreme hardness resulting in unusual responses, with polished films possessing a very low surface roughness presenting further challenges. The bonding parameters were re-established for each device, but in general it was noted that an exposed diamond surface required relatively high values for the force and power compared to bonding to more conventional metallic surfaces.

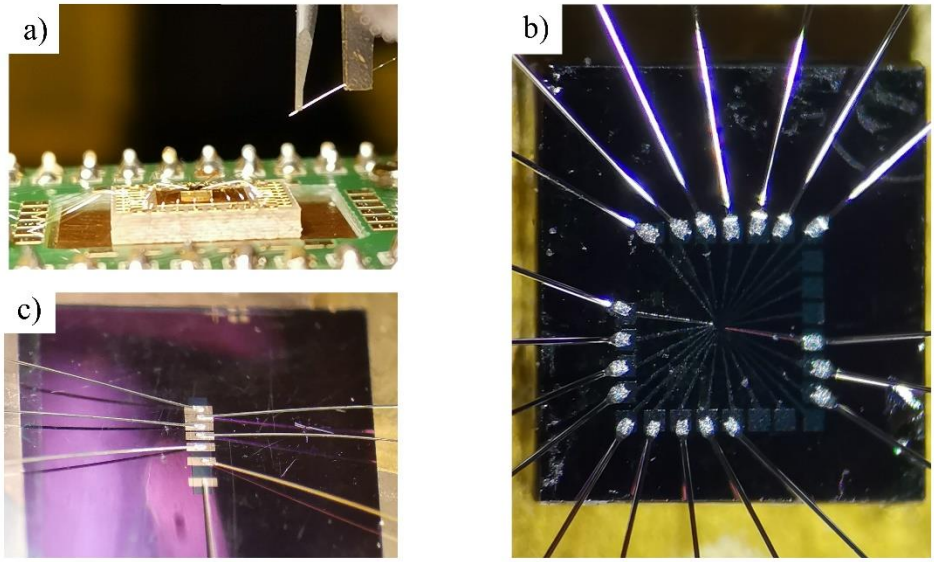

Figure 3.7: Images of the wire bonding process : a) side-view showing the wedge bonding needles and multiple levels of bonding between the device chip and carrier package, b) direct diamond bonds to a junction device chip and c) bonds to metal contact pads on a diamond mesa.

Conversely, with a metal coated contact pad the force and power required would be significantly lower than for standard bonds to a copper surface. This variation in the bonding parameters is due to the hardness of diamond causing the metal coating to tear under the application of the ultrasound when sandwiched between the diamond surface and the bonding wedge. Therefore, bonds to the

diamond surface often required one of two manual interventions. It is possible to slightly damp the impact and modulate the pressure of each bond (either part b) or e) in Figure 3.6) by pressure a finger onto the bonding arm at the appropriate time, which also allows for an increase of the bond surface area to a size and with a force outside of the capacity of the system. Additionally, to drag the bond during contact (at part b) or e) in Figure 3.6) and increase the bond dimensions in the direction of the wire track one can use pressure applied from a finger in conjunction with horizontal movement in the direction of the wire. This alternative method to increase bond surface area can also increase bond stability.

3.7 DILUTION REFRIGERATION

Experiments at the lowest temperatures require specialised refrigeration techniques. There are a few methods that allow for sub-Kelvin temperatures, but dilution refrigeration is the most popular due to its advantages of continuous cooling, base temperatures less than 10 mK and relatively high cooling powers [123]. Dilution refrigeration works by taking advantage of phase changes in a dilute mixture of ^{3}He and ^{4}He isotopes. Two systems were used throughout the work presented. The first is the Quantum Design Physical Property Measurement System (PPMS) which allows continuous temperature control between 1.9 K to 300 K, the second is the Bluefors LD400 which natively is only configured for temperature variation below ~0.8 K. To understand this limit and effectively design a solution which allows for higher temperatures it is necessary to examine the details of operation for the system.

The principal of helium dilution is as follows. A volume of liquid helium is said to be at its saturated vapour pressure (SVP) when the rate of its evaporation is equal to its condensation. The ^{4}He atoms obey Bose-Einstein statistics, whereas

^{3}He atoms are fermions and obey Fermi-Dirac statistics. Below its boiling point of 4.22 K and above the line T_λ in Figure 3.8a, ^{4}He exists in a conventional liquid state known as Helium I where it boils when heated and contracts when its temperature is lowered. Below this lambda line, ^{4}He forms a "two-fluid" state where a fraction of its atoms fall into the ground state becoming Helium II and exhibiting the unusual properties of its superfluid state.

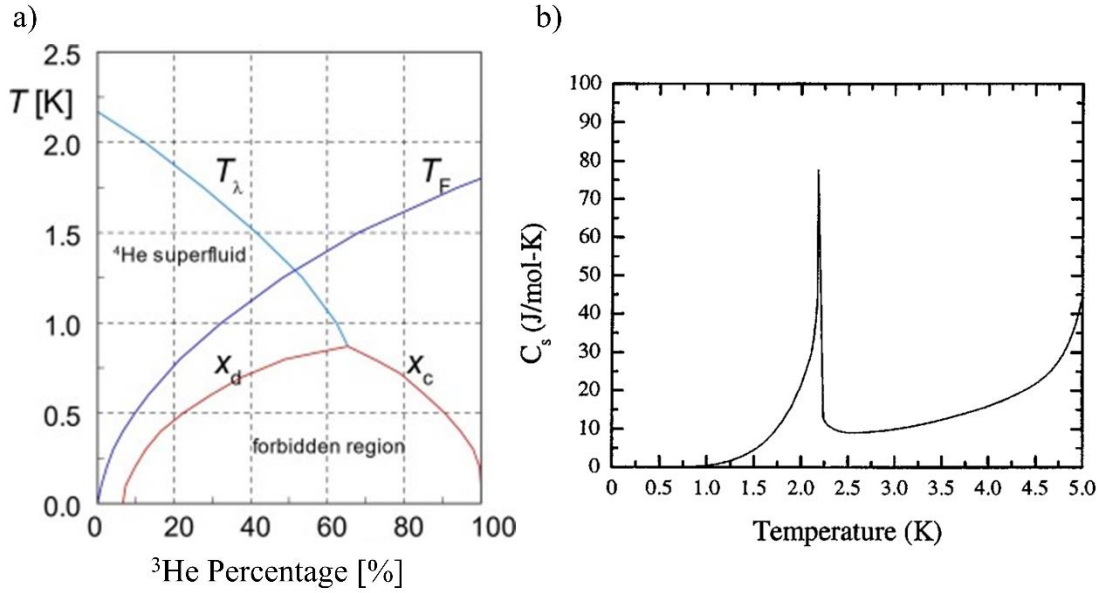

Figure 3.8: Dilution refrigeration phase and heat capacity diagrams
a) Phase diagram for liquid ^{3}He/^{4}He mixtures at the saturated vapour pressure, where the x-axis is the percentage of 3He present. Reproduced from *Zu et al.* [123]. b) ^{4}He has a discontinuity in its heat capacity at the lambda point. Reproduced from *Donnelly et al.* [124].

There is a significant increase in heat capacity (Figure 3.8b) as the temperature decreases through the lambda point, and Helium II also has zero viscosity and zero entropy [124]. Due to its high thermal conductivity, superfluid helium evaporates from its surface rather than boiling. As fermions, the ^{3}He atoms obey the Pauli exclusion principal and do not form a Bose-Einstein condensate.

When mixtures of ^{3}He and ^{4}He are cooled below 870 mK, phase separation occurs around the forbidden region shown in Figure 3.8a to form a concentrated ^{3}He phase and a dilute ^{3}He phase. Below this temperature, the dilute phase contains approximately 6.6% ^{3}He while the concentrated phase is essentially pure ^{3}He. The enthalpy of ^{3}He in the dilute phase is larger than the concentrated phase, requiring heat as it crosses the forbidden region. In a dilution refrigerator, this energy is taken from the isolated environment of the mixing chamber and removed by the pumping line.

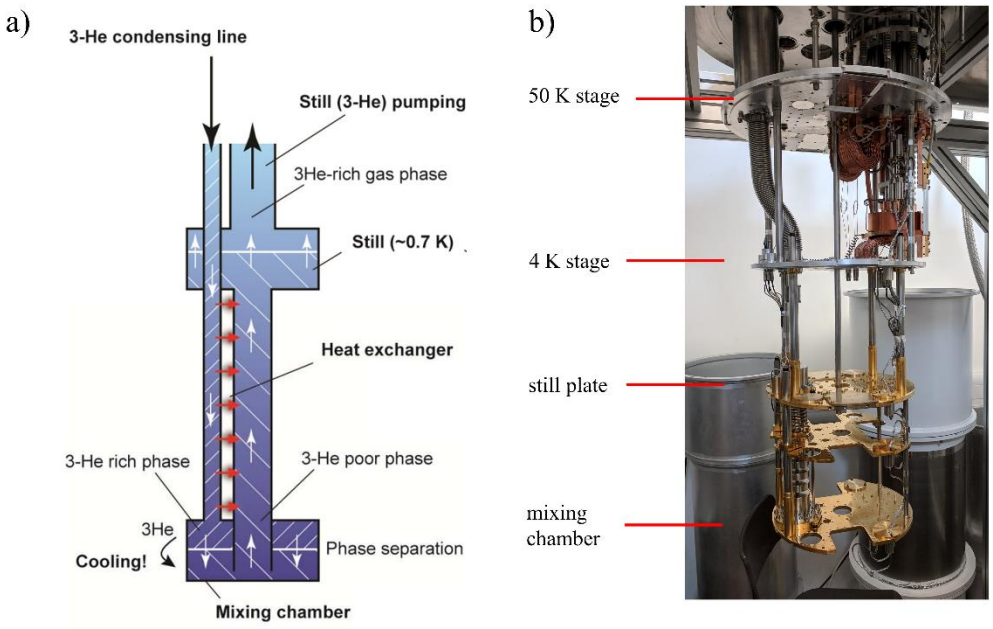

Figure 3.9: Dilution refrigeration layout a) Schematic of the dilution refrigeration unit, encompassing the still and mixing chamber, Reproduced from *Zu et al*. [123] b) the various stages of the Bluefors LD400 dilution refrigerator.

The working gas in a dilution refrigerator is ^{3}He. In traditional "wet" systems the gas is pre-cooled to 4.2 K in a liquid helium bath, whereas the LD400 used in these experiments utilises a Cryomech Inc. pulse tube cooler to reach

temperatures low enough for the dilution cycle. The pulse tube is connected to the 50 K and 4 K stages with flexible copper braid to isolate vibration from the operation of the cooler. Heat switches between the 4 K plate, the still and mixing chamber allow for thermalisation during the initial cooling phase and isolation of the colder plates from the pulse tube during the dilution cycle. In its gaseous state the ^{3}He is first cooled by a heat trap at the 50K stage where impurities are condensed out. As it flows into the main system it is pre-cooled at 4.2 K by the plate connected to the lowest level of the pulse tube (Figure 3.9b). At the start of the dilution cycle the gas passes through a compressor and then the main impedance, which is a capillary with a low flow rate. Gradual condensation of the ^{3}He is achieved as it exits the impedance due to the Joule-Thompson effect. The fully condensed ^{3}He is of sufficient volume to fill the mixing chamber, the heat exchangers and part of the still. The still is cooled to <800 mK by the process of evaporative cooling induced by pumping the still. Below this temperature the incoming liquid ^{3}He undergoes phase separation which continues as it passes through one heat exchanger connected to the still and another that allows thermalisation with cold ^{3}He leaving the mixing chamber. In the mixing chamber the ^{3}He concentrated phase sits on top of the dilute phase with a boundary separating them. ^{3}He crosses this phase boundary, drawing heat from the surroundings, and exits the mixing chamber in the dilute phase and entering the still. Because the saturated vapour pressure of ^{3}He is much higher than ^{4}He, most of the evaporation that occurs when the still is heated is ^{3}He. Thus, the cooling power at the mixing chamber is dependent on the heating of the still and the resulting flow rate of ^{3}He.

Prior to cooling, the system inside the outer vacuum cans is pumped down to $<10^{-4}$ mbar with a turbopump. Initial cooling is performed with the pulse tube cooler. At this point the stages labelled in Figure 3.9b are at their indicated temperatures and the dilution refrigerator unit is at approximately 10 K. A

"Pulse Pre-Cooling" sequence, where mixture is pumped through the low impedance side of the dilution, is then employed to circulated gas through the dilution unit to remove hot spots. Finally, the $^{3}He/^{4}He$ mixture is compressed from the storage tanks into the dilution unit.

Under normal operation it is possible to run experiments on the mixing chamber stage at temperatures up to approximately 1 K due to the temperature required at the still and mixing chamber. There are a few options available in situations where higher temperatures are required, such as external heaters and including partial thermal isolation between the mixing chamber stage and the sample. However, to balance the heating from the samples and to be able to reach 4 K in these experiments, a non-standard setup was used. First, the circulating turbo pump is switched off which reduces the flow rate and therefore cooling power. Next, ~90% of the circulating gas is reclaimed into the storage tanks, which further reduces cooling power and ensures pressures stay low enough to not compromise the delicate components at higher temperatures. Together with careful PID control with a sample mounted heater, stable temperatures up to 4 K were achieved.

4 CONTACT RESISTANCE OF METAL CONTACTS TO SUPERCONDUCTING DIAMOND

4.1 INTRODUCTION

Nanoscale electronic devices require precise fabrication. Diamond presents some unique engineering challenges due to some of the extreme properties mentioned previously. Additionally, to ensure high quality factor NEMS require low surface roughness, which means that NCD films need to be polished [125–127]. Such systems need to operate below the critical temperature of the B-NCD, which has been shown to be approximately 4.2 K [128].

The fabrication of appropriate electrical contacts is an essential element in the realisation of the design goals of a device. However, the formation of low resistance ohmic contacts to wide band gap semiconductors like diamond is typically non-trivial due to the large work function at the interface to metal contacts, with metal on smooth diamond being subject to a potential barrier of

approximately 4 eV [129]. Very low contact resistances are required when dealing with superconducting devices, as any thermal perturbation can significantly affect the device's properties. Any local heating produced at the contact can raise the temperature enough to reduce the critical current density (J_c) of the superconductor, and possibly even exceed the critical temperature (T_c) [130].

In order to correctly model and understand the physical system of an electrical contact to superconducting material, it is necessary to consider charge carrier transport through the contact into the material in the normal and superconducting regimes separately. As discussed in Section 2.3.2, in a junction between a superconductor and a normally conducting material, phase coherent transport can be induced in the normal conductor by the proximity effect [38,131]. In the superconductor, unpaired electrons penetrate causing a reduction in the energy gap and weakening of the superconductivity in the vicinity of the interface. In terms of carrier transport, the system of a metal contact to a highly doped semiconductor that has become superconducting is comprised of three layers. Firstly, the metal itself which is subject to temperature dependent resistivity $\rho(T)$ due to electron scattering where either $\rho \propto T$ or $\rho \propto T^3$ (for transition metals) below the Debye temperature as discussed in Section 2.1. *Wieck* (1988) showed that this metal resistance dominates as the contact resistance vanishes below T_c for contacts to another superconductor [132]. Next there is an interface layer consisting of the region subject to the proximity effect and defects that interfere with the superconductivity of the doped semiconductor, sometimes including an insulating layer depending on the materials involved. Provided that the insulating portion is 1-10 nm thick it is considered to be "tunnel-thin", but this intermediary layer remains a potentially important consideration due to its influence on the potential barrier of the contact [133]. The final layer is the superconductor itself. Assuming low temperatures and thin potential barriers,

transport across semiconductor-superconductor junctions are typically analysed in a framework of a tunnelling mechanism [133]. Electrons from the normal conductor with an energy E (relative to the Fermi energy E_F) below the superconducting gap cannot enter the superconductor and instead undergo Andreev reflection [134].

As discussed in more detail in Section 2.1.1, current transport at normally conducting metal-semiconductor interfaces occurs via either thermionic emission or tunnelling [135,136]. Defects near the contact interface can either narrow the depletion region and increase the probability of tunnelling or lower the effective barrier height. With greater defect or doping concentrations, the tunnelling regime dominates. The reduction in contact resistance associated with annealing and carbide formation is thought to be due to the formation of defects near the metal/diamond interface, which lead to an increase in the tunnelling probability of the carriers [137]. This model of ohmic contacts is further validated by decreases in contact resistance with increasing doping concentrations. Boron doping concentrations in diamond of ~10^{20} cm^{-3} have been shown to maximise this effect [138]. Contacts to diamond with high doping concentrations have been shown to have weak temperature dependence between 30–300 °C [139]. Due to the high boron doping concentrations of superconducting diamond, it could be expected that tunnelling is the dominant carrier transport mechanism and that contact resistance will not increase significantly at very low temperatures.

Table 4.1: Carbide formation energies for transition metals commonly used for contacts with diamond at 600 °C [140].

	Titanium Carbide	Chromium Carbide	Molybdenum Carbide	Tantalum Carbide
ΔG (kJ/mol)	-245	-65	-56	-144

Historically, there are several methods that have been used to fabricate suitable contacts to diamond including the use of high levels of boron doping and the formation of defect rich layers between diamond and the metal [141]. These defect rich layers have typically involved damage from ion bombardment [137] or the formation of metal carbides by annealing [142,143]. Titanium is commonly used as a carbide forming contact to diamond, partially due to its carbide formation being energetically favourable (see Table 4.1). The effect of annealing on the band structure of the junction is shown in Figure 4.1, with both a reduction of the barrier height and creating a narrowing barrier to the tunnelling process.

The annealing of contacts also offers the benefit of increasing contact adhesion [144]. However, care is required when choosing annealing temperatures and times. Degradation and an increase in contact resistance of Ti/Au contacts has been observed upon annealing at 450 °C due to migration of Ti to the surface of the Au [145]. The addition of Pt has been utilised as a diffusion barrier between the Ti and Au layers. It was noted that the Pt and Au layers interdiffused, but as the Pt barrier was not fully consumed it effectively prevented the Ti contamination at the surface [146,147]. In the case of carbon soluble metals, such as Pd, annealing is thought to increase diffusion and has been shown to significantly reduce contact resistance [139].

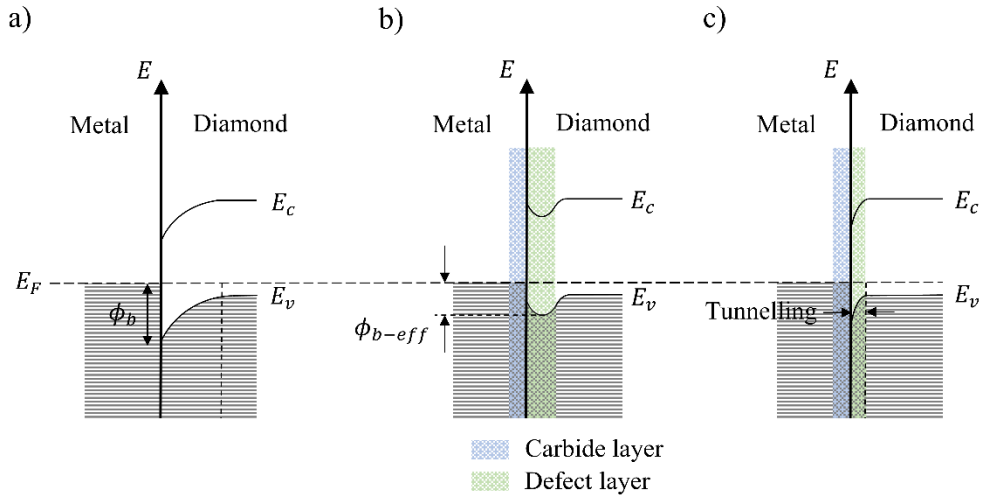

Figure 4.1: Band diagram of metal-diamond interface showing the impact of annealing. a) as deposited with work function ϕ_b, showing rectifying characteristics. After annealing, the contact now has a high concentration of electrically active defects at the diamond surface which both b) decreases the effective barrier height ϕ_{b-eff} and c) allows for an increase in tunnelling.

As-grown CVD diamond exhibits hydrogen termination, which is conductive. When the hydrogen conductive layer is removed from the surface the resistance of the film increases [148]. Oxygen termination is sometimes achieved via wet chemical treatments, for example with CrO_3 or KNO_3. This may not influence hydrogen terminated grain boundaries which contribute to surface p-type conduction [149]. Oxygen termination via wet chemical treatment has been shown to only have a minor impact on surface conductivity of boron doped films [150], but it does allow for better adhesion.

Stable ohmic contacts with low contact resistance have been shown on diamond devices at room temperature and for high power applications with various schemes achieving contact resistances of 10^{-5} Ωcm^2 or less (see Table 4.2 below). Work has also been done to pursue contacts to lightly doped or intrinsic

diamond with high surface conductivity due to hydrogen termination [141,151,152]. *Wang et al.* (2016) showed that palladium offers the possibility of low resistance contacts without carbide formation to single crystal undoped diamond. Also of note is the recent work by *Xing et al.* (2020) which shows the stability of palladium contacts to hydrogen terminated Type IIa single crystal diamond between 300 K and 4 K, with contact resistance increasing from (8.4±1) x 10^{-4} Ωcm^2 to (1.3±0.2) x 10^{-3} Ωcm^2 in this temperature range.

Table 4.2: Comparing contact resistance (Ωcm^2) of different metallisation schemes.

	Ti/Au	Cr/Au	Mo/Au	Ta/Au	Pd
Hoff 1996	8.1×10^{-2}				
Hewett 1993	3.2×10^{-6}		1.2×10^{-3}		
Nakanishi 1994	~10^{-6}		~10^{-6}		
Venkatesan 1993	~10^{-5}				
Chen 2004	~10^{-4}				
Yokoba 1997	~10^{-5}	~10^{-5}	~10^{-5}		~10^{-5}
Fang 1989				1×10^{-3}	
Zhen 2002				7.19×10^{-5}	
Wang 2015					4.93×10^{-7}
Xing 2020					8.4×10^{-4}

Note: Interlayers of Pt as a diffusion barrier are present in some of the above. Where multiple values are provided, the lowest are quoted.

Another important consideration is the effect of post growth surface treatments on electrical contacts. Hydrogen treatment removes sp^2 and has been found to destroy the ohmic nature of titanium contacts to undoped NCD [153].

Conversely, oxygen treatment has been observed to reduce contact resistance by improving the film surface's electron affinity [154].

The work in this chapter seeks to test the efficacy of both carbide-based contacts and palladium contacts on B-NCD down to the cryogenic temperatures necessary for superconducting devices to function.

4.2 EXPERIMENTAL METHODS

4.2.1 Modified TLM measurements

Measurements of the contact resistance were conducted via a linear transmission line model (TLM) pattern, as is typical for contacts to semiconductors and indeed for diamond at room temperature and above [155]. Contact resistances with superconducting materials are often measured with simpler two or four-probe methods, because the effect of sheet resistance is removed [132,156].

In standard TLM measurements it is critical that the contact pads are formed on a mesa, as this avoids lateral current crowding at the contact and an overestimation of the contact resistance [157]. For a four-wire measurement to two contact pads on a semiconducting mesa, the total measured resistance (R_T) will be a combination of the metal resistance (R_M), the sheet resistance (R_S) and the contact resistance (R_C) as follows (see also Figure 4.2c):

$$R_T = 2R_C + 2R_M + R_S \tag{4.1}$$

Acquiring R_T from the measurement of several sets of contact pads with different separations, the contact resistance can be derived from a linear fit of these points. At $x = 0$, $y = 2R_C$ and at $y = 0$, $x = -2L_T$. With standard TLM, L_T is the effective length of the contact due to current crowding. However, because this calculation requires a linear extrapolation to the x-axis intercept assuming constant sheet resistance, the potential for carbide formation at the diamond surface requires the exclusion of this parameter from the TLM calculations. Additionally, in the superconducting regime the concept of such a linear extrapolation, with a gradient R_S/W, becomes nonsensical.

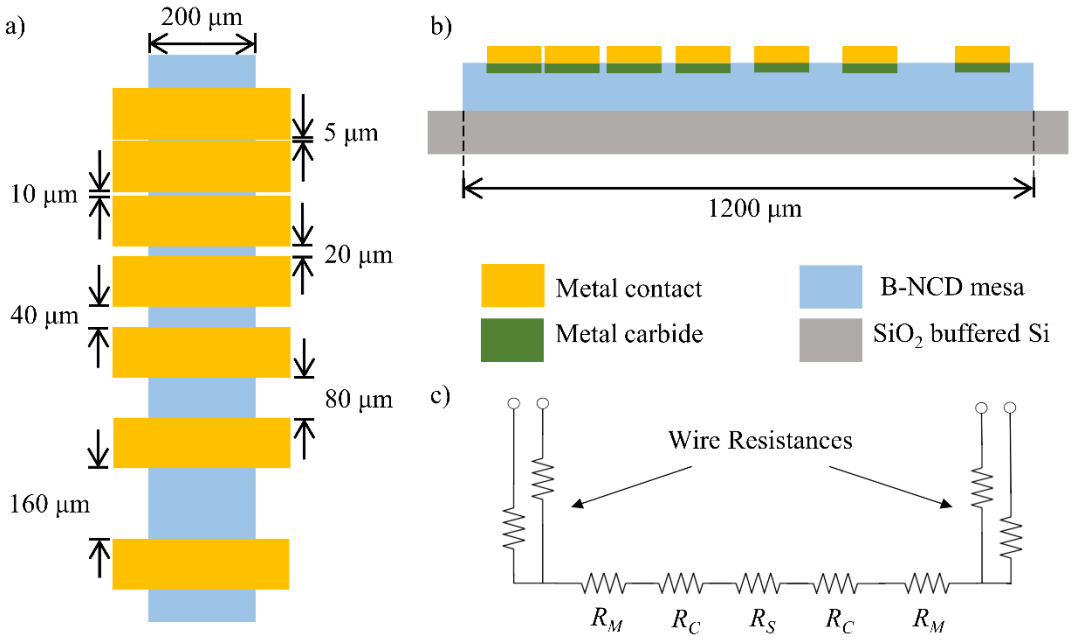

Figure 4.2: TLM schematics. a) plan and a) cross-section diagrams of the TLM patterns used, along with c) a sketch of the circuit components of the measurement, where R_M is the resistance of the metal, R_C is the contact resistance and R_S is the sheet resistance.

The contact resistivity (ρ_C) can be extracted from the y-intercept and the contact width (W) via the following relations:

$$\rho_C = R_C W L_T \tag{4.2}$$

$$\rho_C = R_C W \tag{4.3}$$

4.2.2 Sample Film Characterisation

The films used for these experiments were grown using the recipe described in Section 3.1. The critical temperature for the film was measured in a Quantum Design Physical Properties Measurement System (PPMS) using a standard four-point Van der Pauw pattern. The results of this measurement are shown in Figure 4.3.

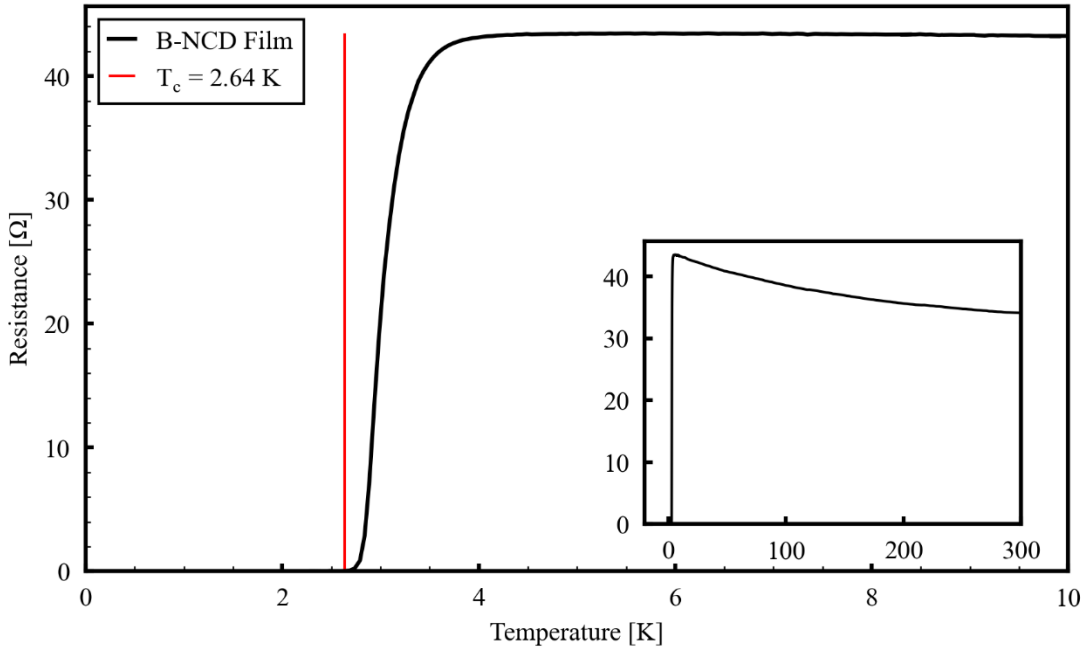

Figure 4.3: Resistance vs. temperature for the film used in the fabrication of the TLM devices, showing T_c = 2.64 K. Inset axis shows entire temperature range 1.9-300 K.

The Raman shift of the film was measured with a Horiba LabRAM HR Evolution equipped with SynapsePlus Back-Illuminated Deep Depletion (BIDD) CCD (see Figure 4.4). Laser wavelengths of 473 nm, 532 nm and 660 nm were used. Analysis of these spectra shows the absence of the typical diamond peak (*D*) at 1332 cm^{-1}, with it red shifted into the Fano-like shoulder (D_F) at 1285 cm^{-1}. Previous work shows that the absence of the *D* peak is an indication of a SIMS measured boron concentrations of at least 10^{21} cm^{-3} [158–160]. A strong peak (*B*) at ~1220 cm^{-1} is also observed, attributed by *Sidorov* and *Ekimov* to carbon-carbon bonding states where the presence of boron leads to local distortions to the lattice structure [2]. The intensity of this peak correlates with the doping concentration [159,160].

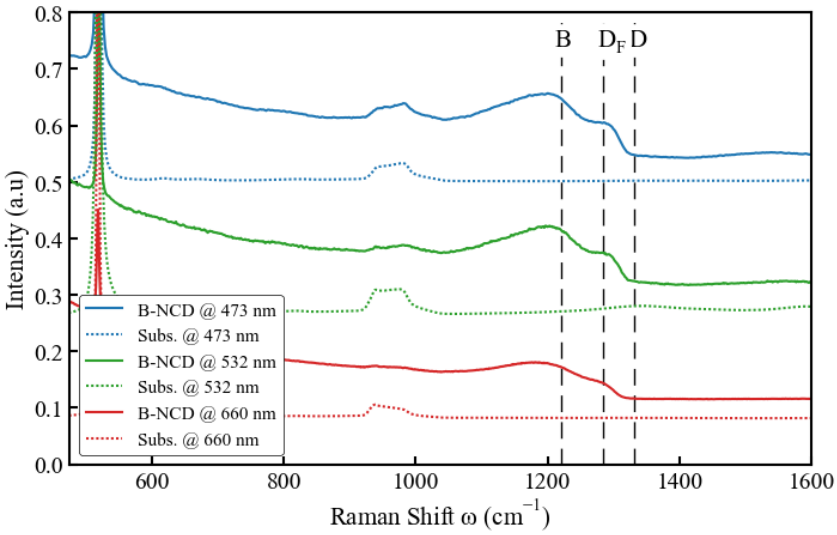

Figure 4.4: Three wavelength Raman shifts of the B-NCD film and substrate (donated "BDD" and "Subs."), where the lack of diamond peak (D) at 1332 cm^{-1} and strong peak (B) at ~1220 cm^{-1} is indicative of high levels of boron doping.

The film thickness was 200 nm and T_c was determined to be approximately 2.4 K via a silver epoxy bonded Van Der Pauw pattern. Superconducting and normal

state properties of the film are consistent with others produced under the same conditions [6], and also comparable to those produced in the same system over several years of operation (see Figure 3.2). Additionally, it assumed that the high doping concentration of the film ensures that the dopant dependent depletion region at the contacts is minimised.

4.2.3 Photolithography

Two photolithographic steps were needed to fabricate the TLM structures. Firstly, to prepare the samples into mesa patterns, the wafer was diced into 5 mm^2 squares. An image reversal recipe was then employed as summarised in Figure 4.5. Standard sample cleaning and a pre-bake at 97 °C was performed for 1 minute. Microchemicals AZ5214E image reversal resist was spun on for 45 s at a speed of 5000 rpm, yielding a resist thickness of ~1.3 μm. A second bake at 97 °C for 1 minute was used to standardise for moisture content. Edge bead removal was achieved with a 30 s flood exposure on a Karl Suss MJB3 mask aligner with a dedicated mask pattern and 40 s development in Microchemicals AZ351B developer solution at a ratio of 1:4 with distilled water. The final pattern was transferred with an exposure time of 2.3 s, after which the image reversal bake was performed at 118 °C. The final development step was performed in a fresh batch of 1:4 AZ351B for 35 s.

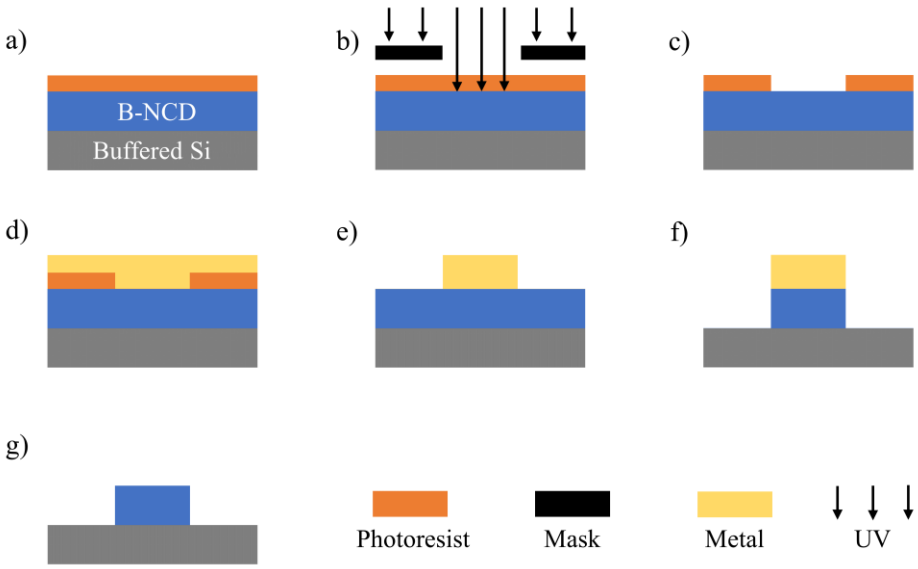

Figure 4.5: Mesa fabrication process flow showing a) photoresist spin-on, b) mask alignment and UV light exposure, c) photoresist development, d) metal etch mask deposition, e) metal lift-off, f) ICP-RIE, g) etch mask removal.

After the establishment of the photolithographic pattern, 200 nm of nickel was deposited via thermal evaporation. Ni is a well-established etch mask for diamond [31,121]. Next, the inductively coupled plasma reactive ion etching step was performed in an Oxford Instruments Plasmalab 100 ICP-RIE system with an oxygen flow rate of 40 SCCM, pressure of 10 mTorr, 25 °C table temperature, an ICP power of 1500 W, an RIE power of 100 W until interferometry indicated that the etch was complete. Finally, the completed mesas were then ashed in an oxygen plasma (1 min at a power of 30 W with 30 SCCM O_2 at a pressure of 0.1 mT) to achieve oxygen termination.

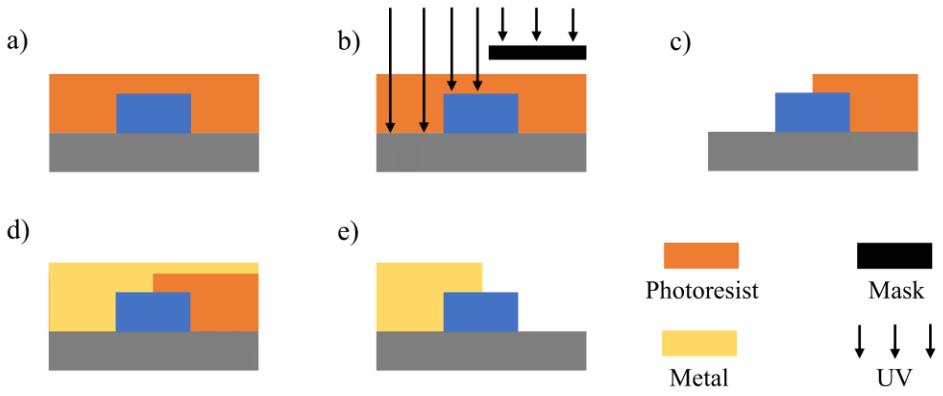

Figure 4.6: Process flow for TLM metal contact pad fabrication, with a) photoresist spin-on over the B-NCD mesa, b) pattern transfer via UV exposure on the mask aligner, c) pattern development, d) metal deposition and e) metal lift-off.

Next, the metal contacts were created via photolithography and metal deposition as shown in Figure 4.6. This process also utilised the image reversal process detailed above, but instead of evaporative deposition the metal contact pads were created with a Kurt J Lesker PVD75 magnetron physical vapour deposition system, which is a sputtering technique. It should be noted that some sputtering techniques tend to be more isotropic and therefore an increase in resist sidewall coating can be observed, limiting the maximum deposition thickness or requiring a rework of the photolithography recipe. This was not an issue for the samples in this work.

The contacts were 200×100 μm, with separations of 160, 80, 40, 20, 10 and 5 μm, giving a range of measurable separations between 5 and 815 μm. This is shown schematically in Figure 4.2. Of the five contact schemes prepared, four involved a carbide forming layer (Ti, Mo, Cr, Ta) and one did not (Pd). The carbide forming schemes were all deposited as a trilayer with Pt and Au, with thicknesses of 50 nm for both the interface metal and Pt layers, and capped with 50 nm of Au in a

magnetron PVD system without breaking vacuum. To increase the yield of the contacts, before lift-off the samples were topped up with 150 nm of Au in a thermal evaporation system for a total contact thickness of 300 nm. The Pd contacts were 200 nm, limited by the cost of the material.

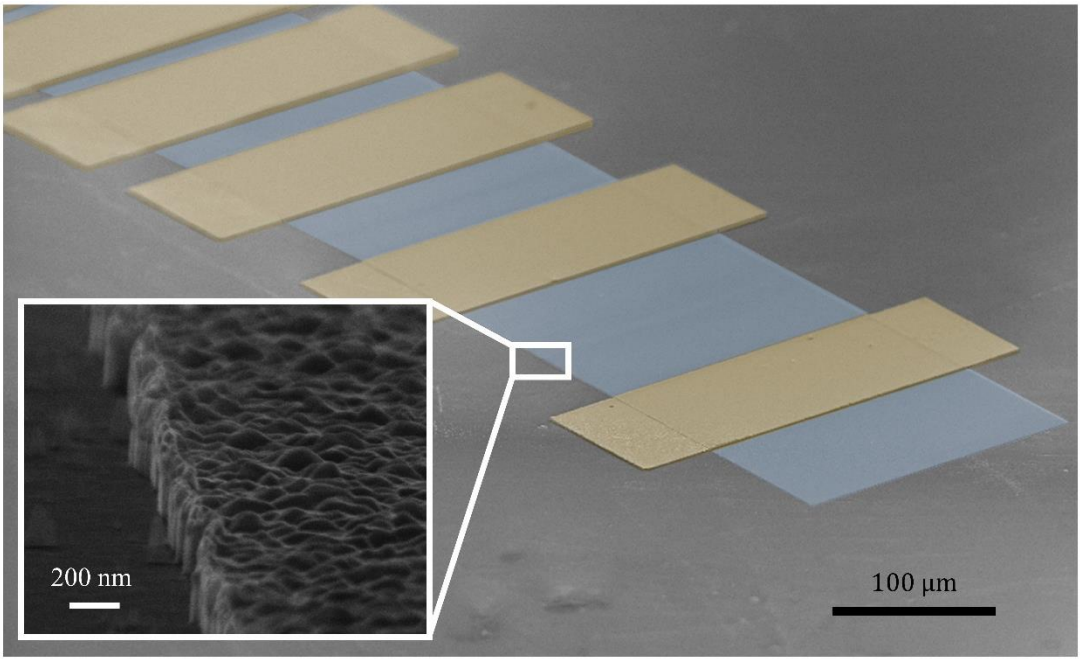

Figure 4.7: False colour tilted SEM of metal contacts on a B-NCD diamond mesa on SiO_2 buffered silicon, with zoomed inset showing the edge profile resulting from the ICP-RIE process.

To increase adhesion and to create a low resistance ohmic contacts, various annealing protocols were investigated for titanium [137,142,161–165], chromium [139], molybdenum [138,139,144], tantalum [166,167] and palladium [139,168]. Annealing parameters of 600˚C for 10 mins for the carbide forming schemes and 400˚C for 3 mins for palladium were chosen as optimal from the reviewed literature. For this work, annealing was carried out in a rapid thermal annealer after a pump/purge cycle with nitrogen.

Samples were taken through a temperature range of 1.9-300 K in the PPMS, and measurements were taken with custom external electronics including a Picowatt AVS-47B Resistance Bridge. Contact pads were wire bonded with 1% Si/Al 12 μm wire to a carrier chip, and then four-point wired to the PPMS sample puck. Some adhesion variability was encountered when wire bonding the contact pads, so resistance measurements of ten contact separations were measured to increase accuracy. An actuator-based switching system was built to operate at room temperature to automate the switching between contact pads, with the measurements run with the National Instruments Labview software suite.

4.3 RESULTS AND DISCUSSION

As discussed in Section 3.6, wire bonding to diamond coated with a thin layer of metal is non-trivial and required significant trial and error. As such, an initial batch of samples had a high failure rate in the contact pads reducing their validity in TLM analysis. However, *I-V* characteristics of these samples were taken at 1.9 K and 300 K. As shown in Figure 4.8 all contacts retained a linear *I-V* relationship, confirming the ohmic nature of the junctions. It should be noted that the measurements were taken with contact pads with various separations so the resistance values extracted are not indicative of the final contact resistance.

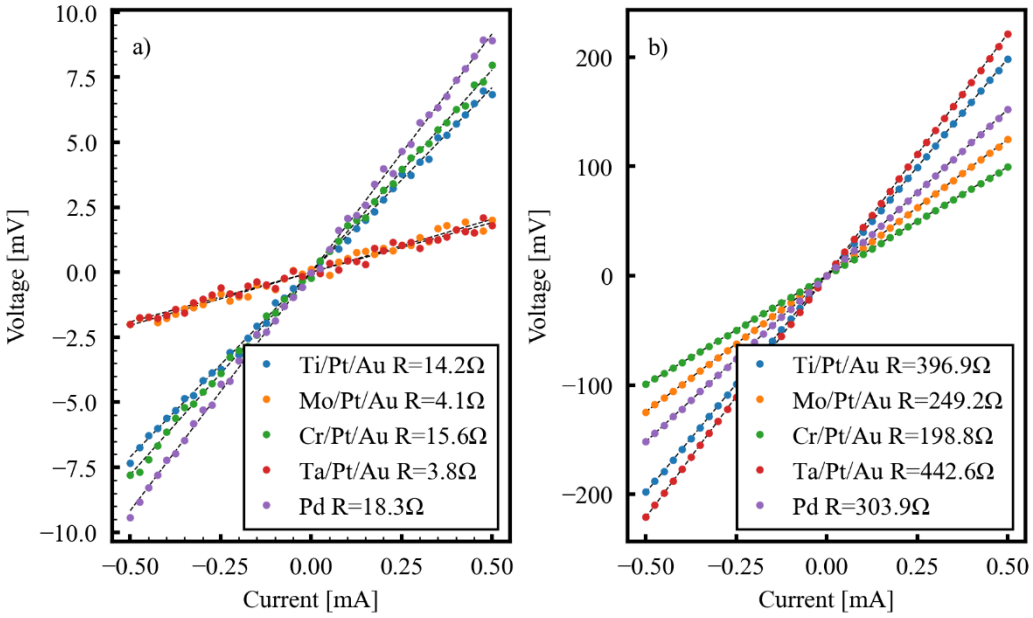

Figure 4.8: *I-V* characteristics of the contacts a) at 1.9 K and b) at 300 K.

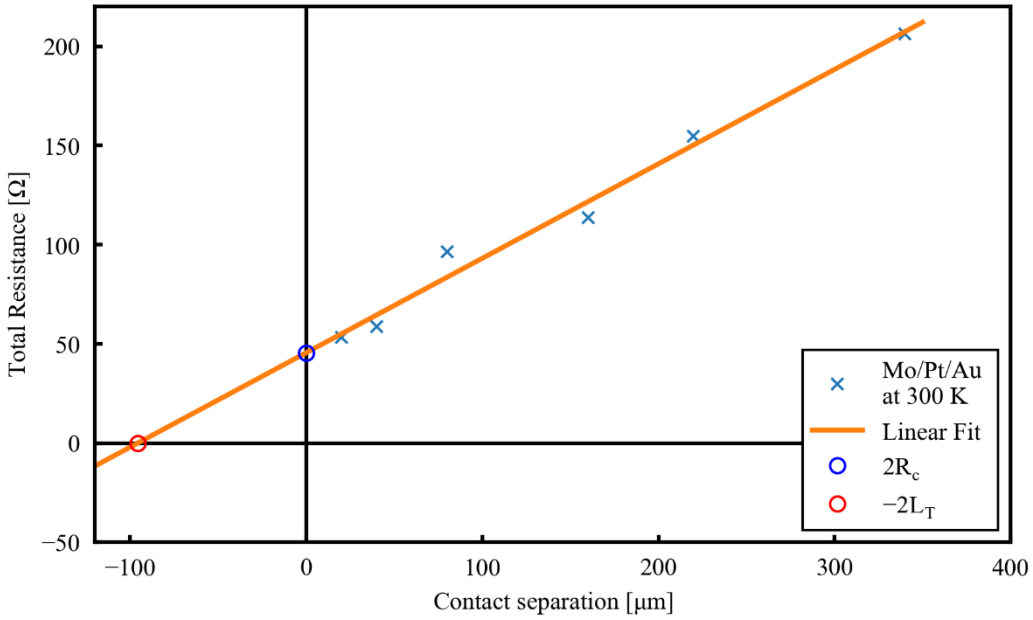

Figure 4.9: Example TLM analysis at a temperature slice. Example linear fit of an isothermal slice through the data (error bars derived from precision of these single resistance measurements are of negligible size).

Resistance measurements between pads of different separations were carried out for each metal contact scheme. Above the superconducting transition, the total resistance of each scheme scales with temperature, with the curve following the expected $T^{1/2}$ dependence [6]. These were then combined to show the dependence of the resistance on separation distance (see Figure 4.9). Isothermal slices of these data were then taken, allowing modified TLM calculations to be carried out at each temperature value using a linear least squares fit (see Figure 4.10). The fitting procedure also provides error values. Figure 4.10b shows that the critical temperature shows only a small variation over the scale of the B-NCD mesa.

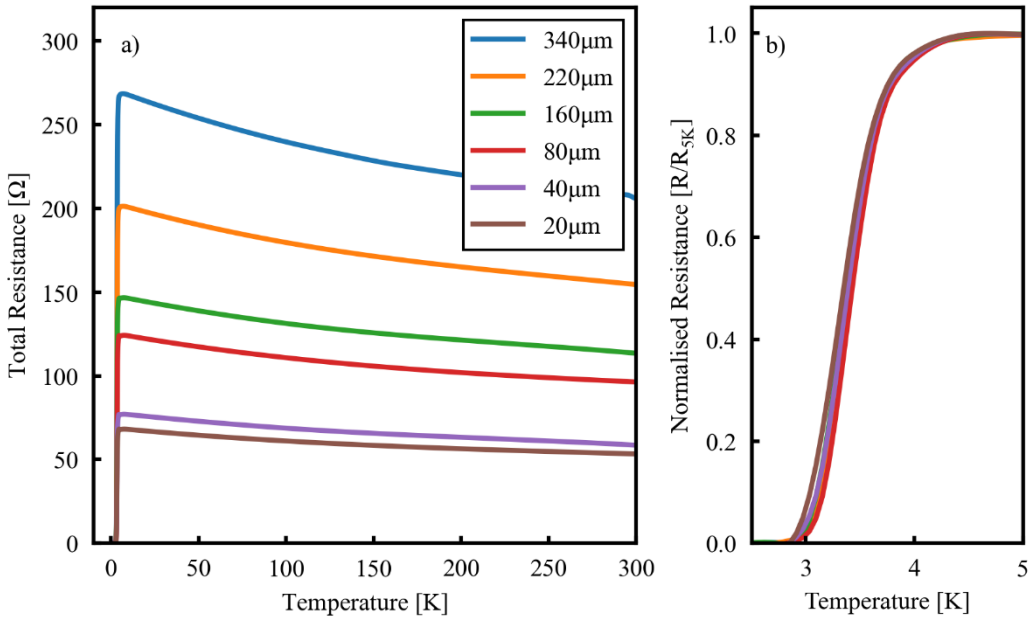

Figure 4.10: Example dataset of total resistances of different contact separations across the temperature range. a) Shows the full temperature range. b) Highlights the consistency of the critical temperature across the contact pads.

As discussed previously the L_T term was excluded from the main calculations. The results are shown in Figure 4.11 and summarised in Table 4.3. During process and adhesion optimisation, measurements were performed on samples taken from a separate wafer grown under the same conditions as the primary film. Despite being limited to a few data points due to bond failure, the Ti based scheme provided contact resistance values of 1.7 x10^{-3} Ω.cm showing reasonable agreement to the final data. To allow comparison to literature values, conventional TLM calculations (with L_T included) were performed at 300 K. The values at 300 K show contact resistivity values in the region of ~10^{-7} Ωcm², which compares favourably to those found in literature.

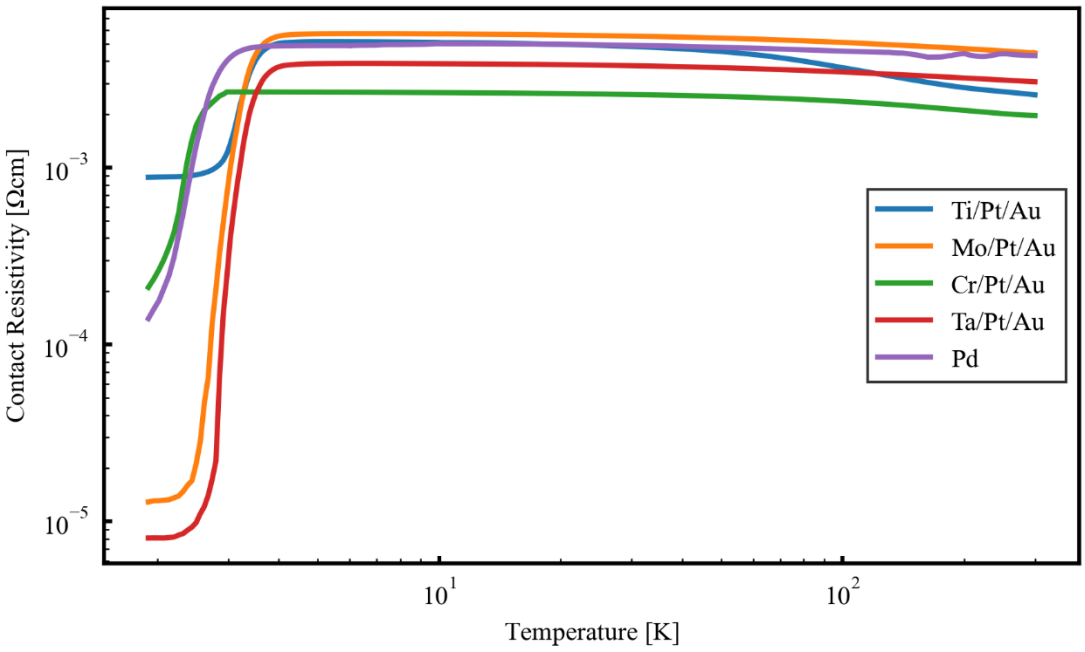

Figure 4.11: Contact resistivity of the various contact schemes scaling with temperature. From 300 K to the superconducting transition all the schemes show a slight increase in resistivity, where a significant reduction of the contact resistivity is then observed.

As typical TLM methods rely on fitting total measured resistance with contact separations, the extrapolation to the contact resistance value includes the sheet resistance of the diamond, which gives rise to the gradient of the fitted line. As such, when the sheet resistance is zero in the superconducting regime, this line becomes flat at $y = 2R_M + 2R_C$ and the measurements effectively approximate typical superconducting two and four probe contact resistance measurement methods. However, it was found that R_T in the superconducting regime was relatively high for all contact schemes, invalidating the possibility of extracting the contact resistance from the four probe measurements. For this reason, TLM calculations were also used in the superconducting regime.

The contact resistance of all metallisation schemes show good stability and minimal signs of a temperature dependence between 300 K and the superconducting transition. A considerable decrease in contact resistance in all samples was noted at approximately 2-4 K, with the variation in the temperature of this decrease attributed to variations in the critical temperature across the film from which the samples were fabricated. All contacts appear to follow approximately the same dependency until this point. This is in contrast to the results obtained by *Xing et al.* (2020), where carbide forming Ti based contacts to undoped single crystal diamond became non-ohmic at low temperatures while Pd contacts remained stable. This is presumably due to high doping levels of superconducting B-NCD allowing greater tunnelling efficiency which eclipses thermionic emission.

Table 4.3: Contact resistance of the tested metallization schemes at 300 K and 1.9 K, with and without the effective contact length factor L_T respectively.

Contact Resistance	Ti/Pt/Au	Cr/Pt/Au	Mo/Pt/Au	Ta/Pt/Au	Pd
At 300 K (incl. L_T) ($x10^{-7}\,\Omega.cm^2$)	2.55±0.1	0.82±0.1	8.03±0.3	3.81±0.4	4.99±0.3
At 300 K (excl. L_T) ($x10^{-3}\,\Omega.cm$)	2.58±0.15	1.97±0.12	4.46±0.29	3.06±0.28	4.48±0.35
At 1.9 K (excl. L_T) ($x10^{-4}\,\Omega.cm$)	8.83±0.10	2.11±0.04	0.13±0.01	0.08±0.01	1.40±0.17

Between 300 K and the superconducting transition, the Ti based contacts compare favourably with the other schemes. In the superconducting regime the Ti contacts did not show the same magnitude of decrease in contact resistance as the other metals, resulting in the highest contact resistance at 1.9 K. The ranking of the contact resistance of the metals is also different between the normal and superconducting regimes. This ordering does not show direct correlation with the carbide formation energies in Table 4.1. However, given the values in Table 4.1 and that all carbide forming metal contacts were annealed with the same parameters, different thicknesses of each carbide might be present in the interface.

In contrast to *Wieck* (1988), a vanishing contact resistance below T_c was not broadly observed, although this behaviour may be masked by the lower T_c in the Cr and Pd contacts. This is perhaps due to the formation of the carbide layers or other defects in the interface layer increasing the height of the potential barrier,

width of the insulating layer or size of the region subject to the proximity effect. Of note is the significantly higher resistivity of titanium carbide compared to the other carbides (Table 4.4), which adds some credence to this theory and perhaps explains the higher contact resistance of the Ti contact in the superconducting regime. Furthermore, this variability in the resistive contribution of the carbide layer justifies the exclusion of the L_T term from the TLM calculations.

Table 4.4: Electrical resistivity of metal carbides at 20 °C.

	Titanium Carbide	Chromium Carbide	Molybdenum Carbide	Tantalum Carbide
ρ (Ωm)	3-8 x 10^{-3} [17]	1.47 x 10^{-8} [169]	9.7 x 10^{-7} [17]	3.6 x 10^{-7} [170]

In the course of testing each pad separation, all samples were taken through numerous temperature cycles between 300 K and 1.9 K without any degradation. While it was occasionally noted that wire bonds would separate from contact pads, this was probably due to mechanical tension necessarily introduced during wire bonding to meet the demands of the layout. Failure of the wire bonds was also noted at the contact pads of the carrier chip and PPMS measurement puck.

It is important to note that the films used in this investigation were not polished, which will eventually be an important consideration when creating devices integrating a resonator (see Section 1.2). There has been some investigation into contact to polished diamond films, with *Wang et al.* [151] noting adhesion with Pd contacts which is notable due to this adhesion only relying on diffusion. Unpolished diamond has a surface roughness correlated with the grain size, with ultra-nanocrystalline diamond (UNCD) films having a roughness as low as ~10 nm. Mechanically stable contacts to higher (>10 nm) are widely reported in the literature as listed above, and these UNCD films also showing adhesion with carbide forming metalisation schemes [154,171]. For films with ~1 nm RMS

adhesion is therefore presumed but should be tested before final device integration.

4.4 CONCLUSION

In terms of the implication to device applications, all the metallisation schemes tested have approximately equivalent contact resistivity (and therefore local heating) at room temperature and down to the superconducting transition, but differences emerge when the substrate is superconducting. In this regime, the titanium scheme performs the least favourably out of the five tested with the molybdenum and tantalum schemes providing the lowest contact resistance. It can therefore be stated that carbide forming and carbon soluble metallisation schemes allow fabrication of suitable contacts to superconducting diamond devices, but some consideration should be given to the use of tantalum over titanium interfaces. The superconducting and NEMS devices which are being developed as part of the ongoing project (see Section 1.2) require both low surface roughness and minimal thermal perturbation. Therefore, the use of tantalum or molybdenum-based contacts is advised. These schemes may be preferable over palladium due to material costs, although palladium offers the simplicity of a single deposition and verified adhesion to low surface roughness NCD.

It has also been shown that the high boron doping concentration ($>10^{20}$ cm^{-3}) of superconducting B-NCD preserves the ohmic nature of carbide forming contacts at low temperatures, whereas contacts to intrinsic diamond with low temperature requirements are perhaps limited to other options.

The mechanical stability of the tested carbide and carbon soluble contacts has also been verified across the temperature range.

5 FABRICATION AND CHARACTERISATION OF B-NCD JOSEPHSON JUNCTIONS

5.1 INTRODUCTION

The use of superconducting diamond in quantum electrical circuits is an attractive field of investigation due to the superlative qualities intrinsic to the material which have been discussed previously in this work. One such avenue of research has been in producing a superconducting quantum interference device (SQUID). A SQUID allows for extremely sensitive detection of magnetic fields and consists of one or more Josephson junctions connected in a superconducting loop.

In the case of B-NCD, with its high upper critical field value of up to 7 T which allows operation of a SQUID in these high fields [3,6,172]. Further, this paves the way for precise detection of the displacement of diamond-based micro and nano-electromechanical systems (MEMS and NEMS) [173], as discussed in Section 1.2.

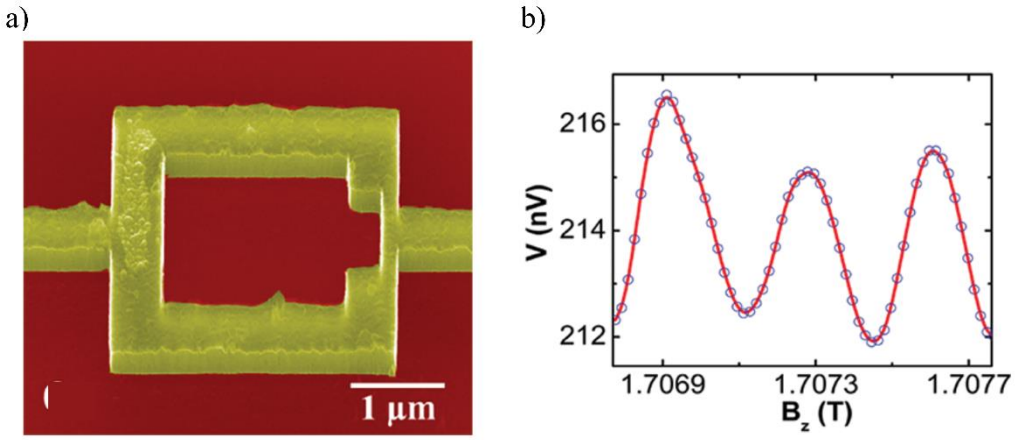

Figure 5.1: B-NCD DC SQUID a) SEM image of the device. b) SQUID voltage oscillations in varying field, from *Mandal et al.* [3].

SQUID devices have been successfully produced with diamond, both with single crystal and with B-NCD films. The first of these (fabricated from B-NCD) was accomplished by *Mandal et al.* (2011), producing a device able to operate up to 4 T [3]. This device consisted of weak link junctions 170 nm wide and 250 nm long and with a loop size of 2.5 μm². It had a critical temperature of 3 K and a critical current close to 1 μA. More recently *Bose et al.* (2021) fabricated a B-NCD SQUID with a washer design with a loop size of 50 nm and junctions with a length of 27 nm and widths between 200 and 500 nm [174]. This device operated up to 2 T, with critical currents between 4.3 and 7.5 μA.

A single crystal diamond Josephson junction was first reported in 2012 by *Watanabe et al.* with a stack planar structure with a normal conducting layer 30 nm thick [175]. This SNS device was reported with $I_c = 3$ mA and $T_c = 4.5$ K. This research group developed this technique into single crystal SQUID with regrowth induced step-edge SS`S junctions, with a weak superconducting region 80 nm long resulting in $I_c = 0.34$ mA [176]. While single crystal diamond has different properties to B-NCD, these results still have some relevance.

Despite these achievements, much is still unknown about the superconducting properties of B-NCD films and the parameters that govern the behaviour of Josephson junctions fabricated from the material. Proper tuning and reliable integration of these devices into more complex quantum circuits requires that the transport properties are more fully understood. The work presented herein seeks to clarify this situation with thorough measurement and analysis of candidate junction devices to confirm Josephson behaviour and to quantify certain variables important for future device development. Due to the complex nature of device fabrication with diamond films, understanding the implications and limitations of device geometry on the critical current and capacitance is particularly important. Operation of a SQUID will occur as the device exits the $V = 0$ regime at I_c. Hysteresis in the *I-V* characteristic of a SQUID should ideally be minimised and can be quantified with the Stewart-McCumber parameter β_c (see Section 2.3.3), which takes the device normal resistance (R_n), capacitance and I_c as parameters.

Recent work has shown conclusively that superconductivity in B-NCD is dominated by effects arising from the specific granularity of the films. The work in the following chapters seeks to prove that the same is true of junction devices.

5.2 FABRICATION

Superconducting B-NCD films were grown using the standard recipe as outlined in Section 3.1. Surface roughness was also controlled by a chemo-mechanical polishing step, which typically yields a roughness of 1.7 nm RMS over 25 μm² and as low as 0.42 nm RMS over ~0.25 μm² [177]. The nano-scale junctions were fabricated using the electron beam lithography recipe as detailed in Section 3.3.

All 5 mm^2 chips were fabricated from the same film (denoted "180321"), with 8 devices per chip. Slight variation in e-beam patterning, metal lift-off and ICP-RIE are relied upon to create the different device geometries and types. Voltage taps are 5 μm apart with the superconducting track 500 nm wide, and devices share a common negative voltage line. Samples were wire bonded between their contact pads and a carrier chip with 1% Si/Al 12 μm wire. Two chips were selected for these experiments.

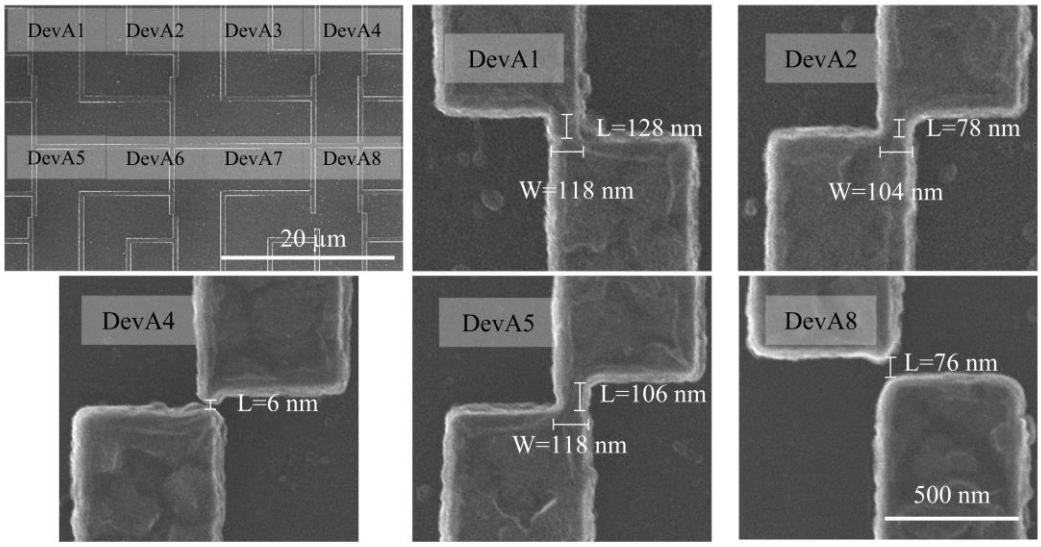

Figure 5.2: SEM image showing the chip A device layout (top left) and devices 1, 2, 4, 5 and 8 and their dimensions as estimated by the software of the SEM with measurement error of ±3 nm (right). Measurement lines are not to scale but provided as a guide to the eye.

Chip A, as shown in the SEM in Figure 5.2, had 5 devices that produces a measurable *I-V* characteristic. Devices 1, 3 and 5 have the appearance of constriction or Dayem bridge SNS junctions. Devices 4 and 8 have gaps where the diamond film has been etched through completely, possibly forming vacuum gap SIS junctions but certainly providing a non-superconducting barrier. For simplicity, devices with a clear etched gap between the superconducting

electrodes are nominally referred to as SIS junctions. Interestingly, while the superconducting coherence length is ~10 nm in diamond, device 8 with a gap length of 76 nm still produces consistent and reproducible results. Typically, junctions of any type are dimensionally constrained to be comparable to the coherence length. It should be noted that the device dimensions quoted are measured using the built-in software of the SEM, with an accuracy of approximately ±3 nm.

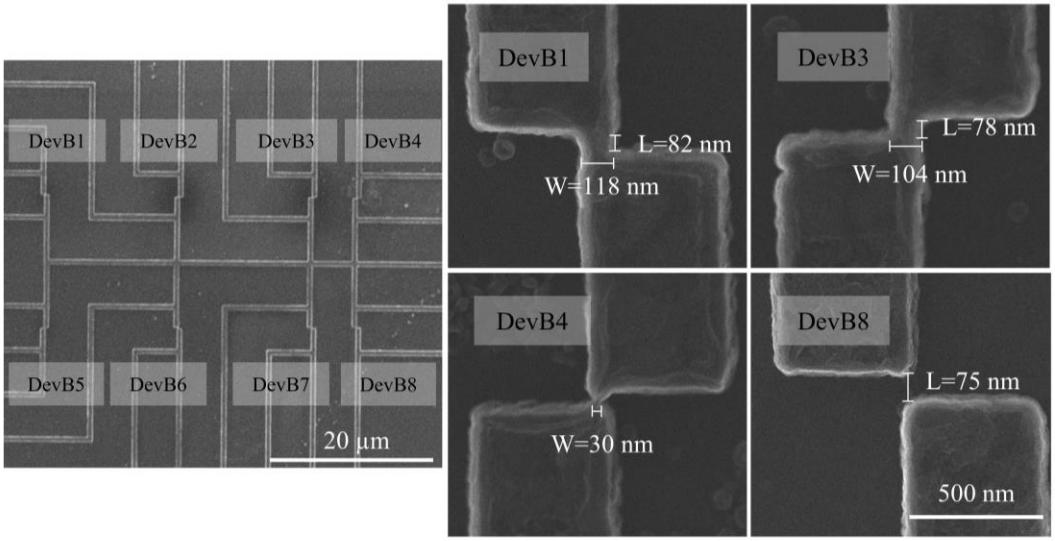

Figure 5.3: SEM image showing the chip B device layout (left) and devices 1, 3, 4 and 8 and their dimensions and their dimensions as estimated by the software of the SEM with measurement error of ±3 nm (right). Measurement lines are not to scale but provided as a guide to the eye.

Chip B contained four working junctions, as shown in Figure 5.3. Of these devices, two are of the constriction type (devices B1 and B3), one appears to be a point contact (device B4) and another is a gap (device B8) similar to device A8. By inspection alone, whether device B4 is an insulating tunnel junction or if the gap contains material remnants from the etching process is unknown.

These chips were chosen as an opportunity to test various geometries and junction types. These are summarised in Table 5.1. Various lengths of SNS and SIS junctions should allow for the parsing out of any dependencies present. Considering the differing dielectric constants of the gap and constriction junctions (ε_r = 1 for a vacuum and ε_r = 5.6 for diamond) the capacitance (C) of each junction was calculated using $C = \varepsilon_0 A/d$ and the device geometries (with area A, separation d and dielectric constant ε_0). The capacitance values are all extremely small (<10^{-26} F) indicating that the RSJ approximation of the RSCJ model can be used.

Table 5.1: Summary of device parameters across both chips.

Device	Type	Length [nm]	Width [nm]
A1	Constriction (SNS)	128	105
A2	Constriction (SNS)	78	108
A4	Gap (SIS)	6	-
A5	Constriction (SNS)	109	118
A8	Gap (SIS)	76	-
B1	Constriction (SNS)	82	118
B3	Constriction (SNS)	78	104
B4	Point Contact	-	30
B8	Gap (SIS)	75	-

5.3 Sample Details and Characteristics

As mentioned previously, all films grown with the recipe detailed above have properties that fall within a narrow range as shown in Figure 3.2. As such, the critical temperature, T_c, thickness, boron content and grain size distribution are expected to be comparable to previous samples.

Figure 5.4 shows that the film reaches a superconducting state at a critical temperature of 2.55 K. T_c is defined as the point at which the resistance diverges from its superconducting state by three standard deviations. This falls withing the expected range for the similarly grown films shown in Figure 3.2. A relatively wide superconducting transition is observed, which is common in similar systems. Intergrain phase fluctuations delay the global onset of Cooper pair condensation, reducing T_c.

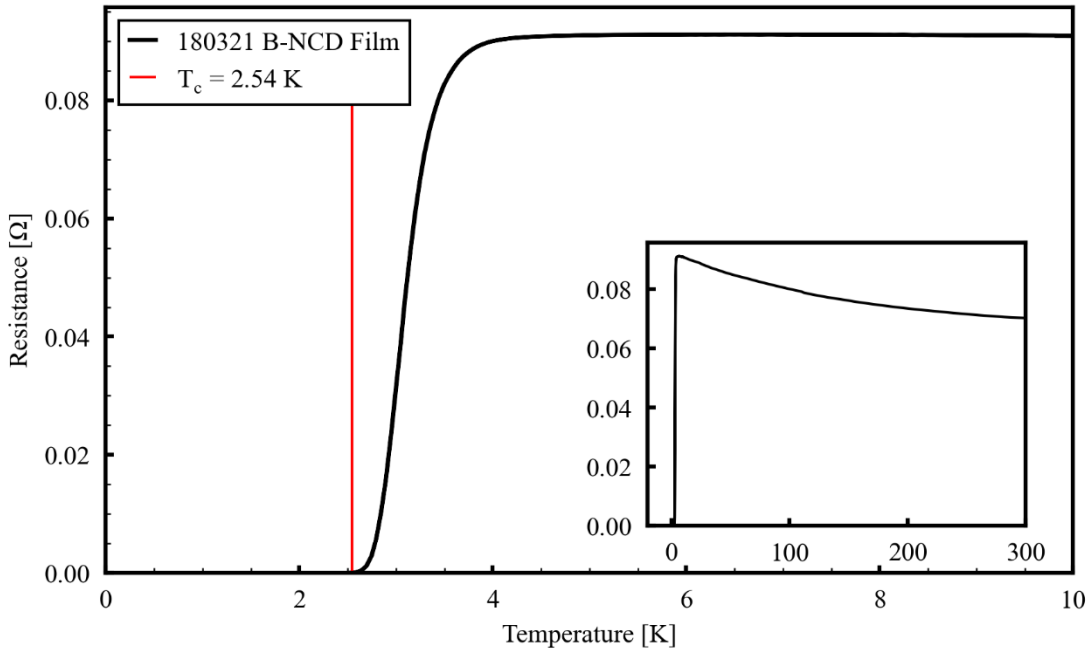

Figure 5.4: T_c for the film from which the junctions were made was determined from resistance versus temperature measurements to be 2.54 K.

The onset of the superconducting state is a much higher temperature than T_c, which indicates that there is a strong phase fluctuation prior to mesoscopic superconductivity. This is typically a sign of disorder in the system, and in the case of B-NCD is likely due to the broad range of grain sizes present in the film. *Zhang et al.* [86] note an increase in transition width due to variation in boron

concentration within and between grains, but this effect is likely minimised in the B-NCD used in this work due to the higher B/C ratio of ~12,800 ppm compared to 5000 ppm. Wider superconducting transitions have also been attributed to greater non-diamond sp^2 carbon, another measure of disorder and the increase in the ratio of B-NCD grains to grain boundary material [114].

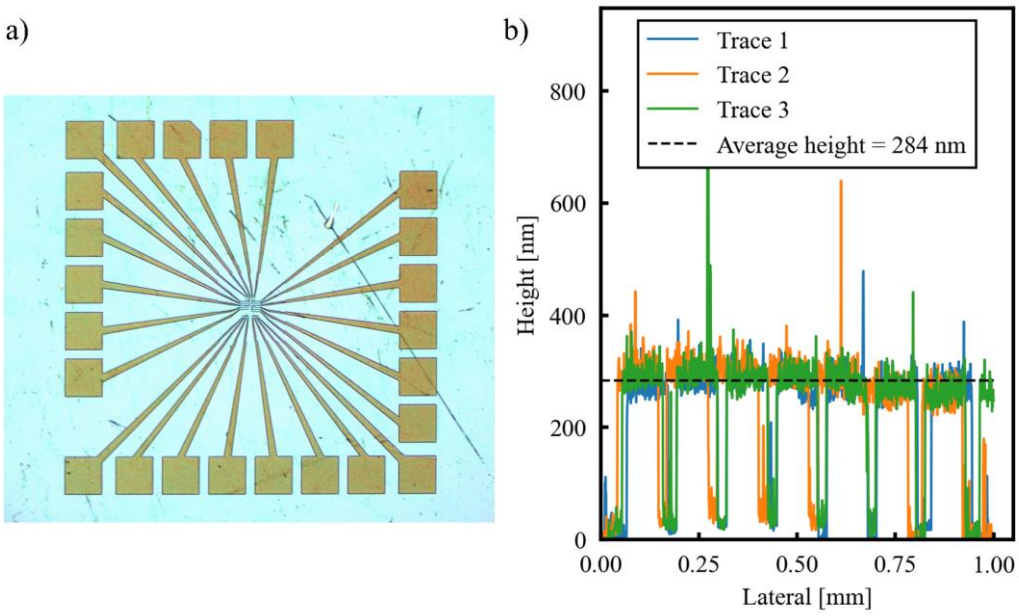

Figure 5.5: Determining the film thickness a) optical microscope image of a typical chip layout from this series of experiments, b) a Dektak height map showing three traces taken at various points across the contact pads shown in a), with an average thickness of the film of 284 nm.

Film thickness was measured with a Bruker Dektak profilometer. Three traces along the contact pads of a chip were measured, and an average of the plateau heights was taken. These results are shown in Figure 5.5, where the average thickness of the film was found to be 284 nm.

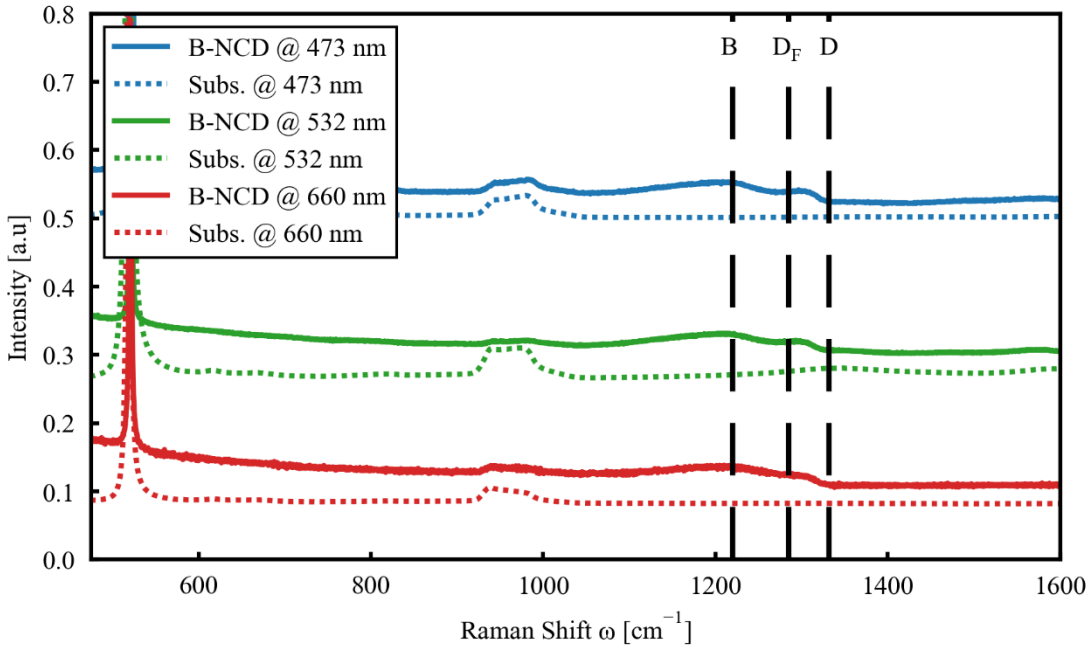

Figure 5.6: Raman spectra at 473, 532 and 660 nm show features typical of superconducting films.

A Raman spectra was obtained using a Horiba LabRAM HR Evolution and is consistent with the results from the film measured in Section 4.2.2. As shown in Figure 5.6, the lack of diamond peak (D) at 1332 cm^{-1} and strong peak (B) at ~1220 cm^{-1} is indicative of the high levels of boron doping required for superconductivity [178].

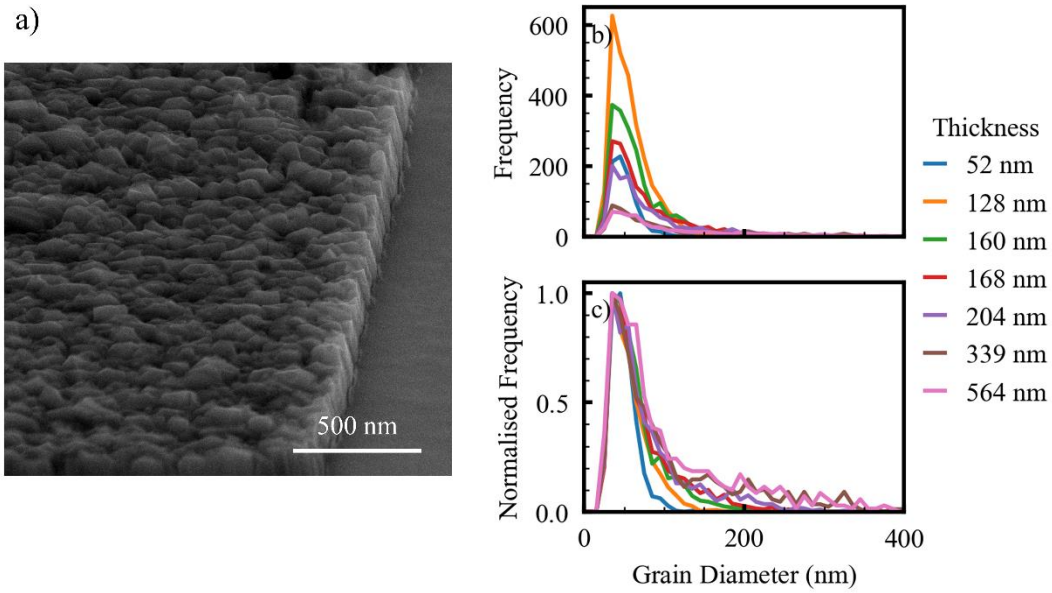

Figure 5.7: Grains in the film a) SEM image of an etched film. Grain size distribution for films grown to various thicknesses, showing b) the frequency, and c) the normalised frequency.

Previous work by *Klemencic et al.* [6] shows the frequency of grain sizes with different film thicknesses, displayed in Figure 5.7. A similar distribution of grain sizes was found by *Zhang et al.*, although the systematic variation in grain size was achieved by varying the methane-carbon ratio during growth [86]. The mean grain diameter is ~35 nm with thicker films tending to have a higher proportion of larger grains. Averaging across the film thickness most similar to the 284 nm in the devices in this experiment (160, 168, 204, and 339 nm films), it was possible to create a probability density function describing these frequencies with a fit to a high degree Legendre polynomial.

This PDF is shown in Figure 5.8. The peak in the distribution occurs at 37.2 nm, with no grains counted below 22 nm. From Figure 5.7 an inter-film variance in the frequency of grains with a diameter between 100-300 nm can be noted.

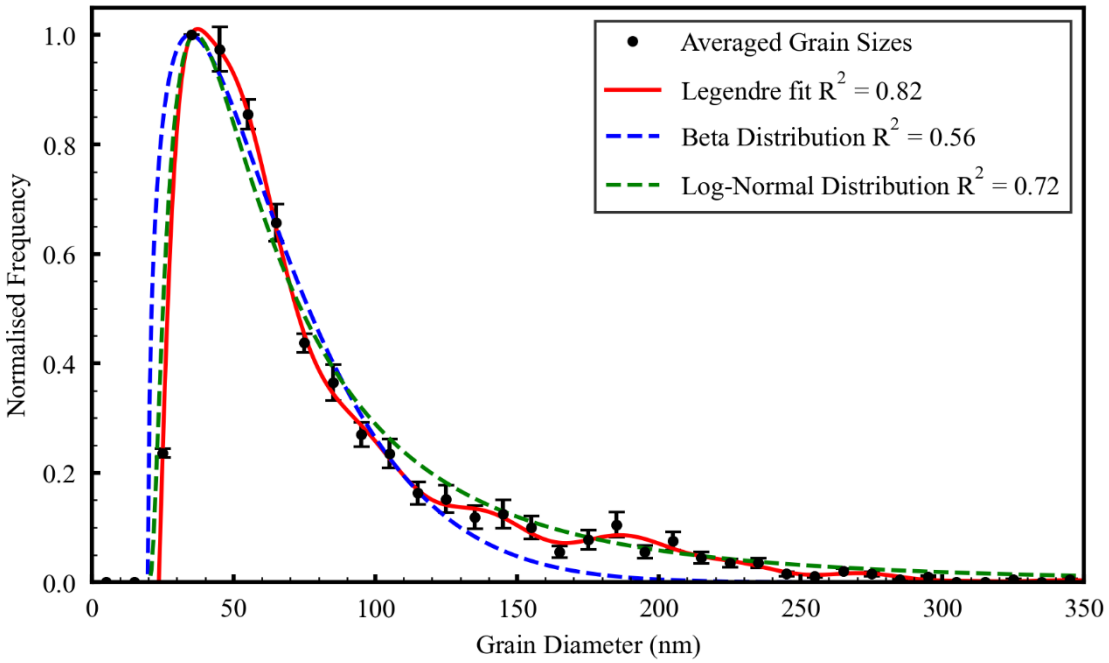

Figure 5.8: Fits of a Legendre polynomial, the Beta distribution and the Log-normal distribution to an average of the 128, 160, 168 and 204 nm films to represent the current sample most accurately. R^2 correlation scores provided to quantify the goodness of fit.

Initial testing (shown later) showed that various aspects of analysis, particularly in magnetic field dependence, are very sensitive to the shape of the distribution and so over or under representation will reduce accuracy. While various distributions (for example the beta and log-normal distributions shown in Figure 5.8) approximate the shape and trend of the grain sizes for the averaged film thicknesses and have been used to model grains and weak links at grain boundaries [179], fitting with a polynomial provides an opportunity to analyse the effects of the variance in grain size present in these films. Given the frequency variance between the films in the 100-300 nm region, an exact match is not expected to the specific grain sizes in the devices.

5.4 EXPERIMENTAL SETUP

Two experimental setups were used in these experiments to accommodate for the use of the magnet added beneath the mixing chamber of the LD400. Wiring outside of the dilution refrigerator was consistent between setups. The measurement lines and those responsible for temperature control were fed through separate looms of wiring in the LD400, in twisted pairs where possible, to reduce cross talk and noise. Driving the current sweeps was a Keithley 220 programmable current source, with an Agilent Technologies 33220A signal generator providing the oscillations on this current necessary for the operation of the lock-in amplifier. These signals were combined in a shielded box in line with a 1 MΩ load resistance. The input signal was then passed through a filter box which has been shown to reduce noise significantly [180]. The lines measuring the response from the sample pass back through the filter box and exit the fridge through the same loom, where they are split between a Stanford Research SR830 Lock-in amplifier (locked to the signal generator) and an Agilent Technologies 34460A Multimeter.

Temperature control across both experiments was performed using a heater driven by a National Instruments USB-6001 DAC with thermometry monitored by a Picowatt AVS-47B resistance bridge. PID control was performed with a native NI Labview script, and tuned for each setup.

The experimental setup used to measure chip A is shown in Figure 5.9. The light-tight sample box was mounted directly onto the mixing chamber stage along with the filter box to ensure that the entire system and effectively cooled.

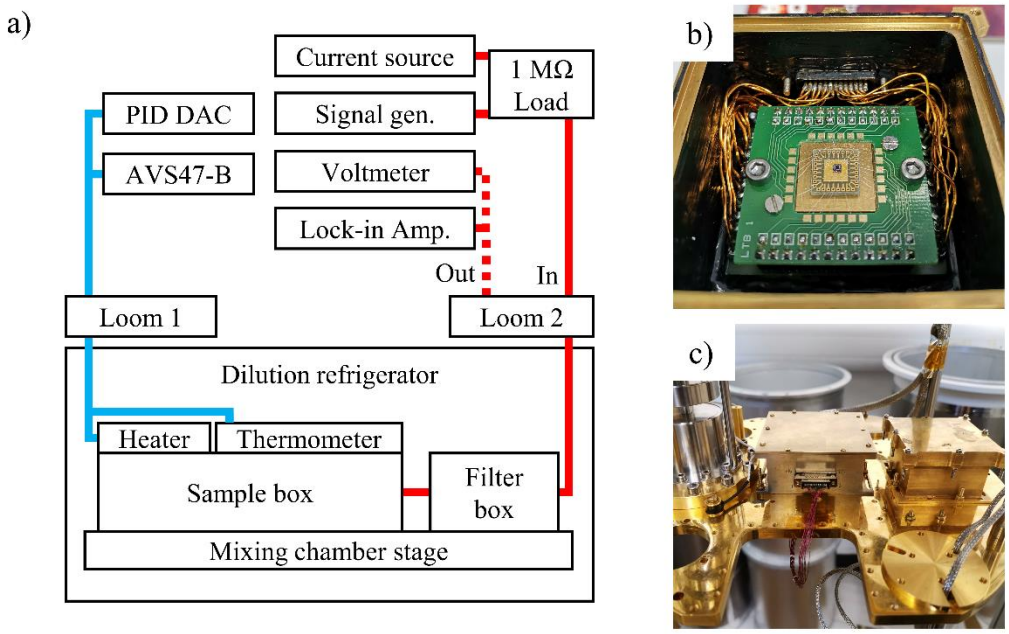

Figure 5.9: Chip A measurement setup a) Diagram showing the equipment setup used for varying the temperature directly on the mixing chamber stage of the dilution refrigerator, b) chip A mounted inside the light-tight sample box, c) sample box mounted on the mixing chamber stage next to the filter box.

Figure 5.10 shows the setup used for chip B. The goal was to enable probing of the device responses with the high field of a superconducting magnet, while also allowing temperature variation. The external equipment is identical to the first setup, however the sample is now mounted on the puck end the end of a magnet probe. The heater and thermometer are also located here.

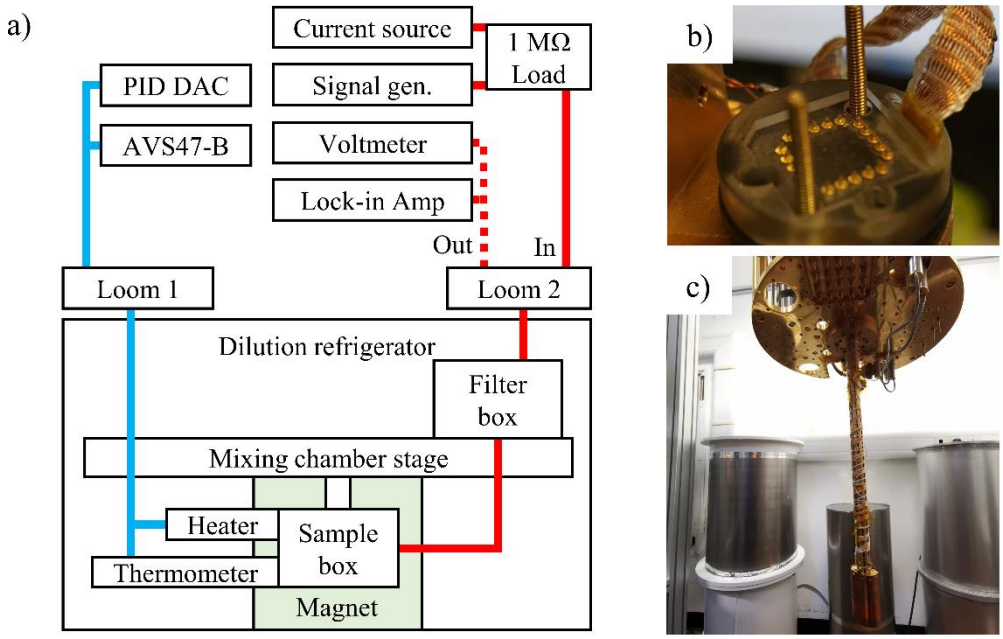

Figure 5.10: Chip B measurement setup a) Diagram showing the equipment setup used for varying the temperature and field with the sample mounted at the end of the magnet probe stick, b) the mounting puck used for chip B, c) the sample in its protective copper housing mounted under the mixing stage.

5.5 Experimental Tuning

Initial current sweeps were taken at a temperature of 500 mK for all devices, between 0 and 200 μA. This is far higher than the base temperature possible for the LD400 (~10 mK) because, as shown in Figure 5.11, local ohmic heating due to the current sweeps covering resistive regions means that the devices were heated to varying degrees throughout the measurement depending on the current. In addition to the problem of local heating, the PID temperature control system necessarily has some lag due to the distance between the heater, the thermometer, the chip and the cooling power of the mixing chamber. The ability

to control this system is also susceptible to the sampling speed of the USB-DAC used as the current source for the heater. The PID tuning achieved a stable temperature with a standard deviation at 0.5 K of $\sigma_{0.5\,K} = 2.5 \times 10^{-4}$ K and a slightly higher value at 4 K of $\sigma_{4\,K} = 6.9 \times 10^{-3}$ K. This increased temperature variation is due to the effect of running the dilution refrigerator at higher temperatures (i.e., more volatile conditions in the mixing chamber).

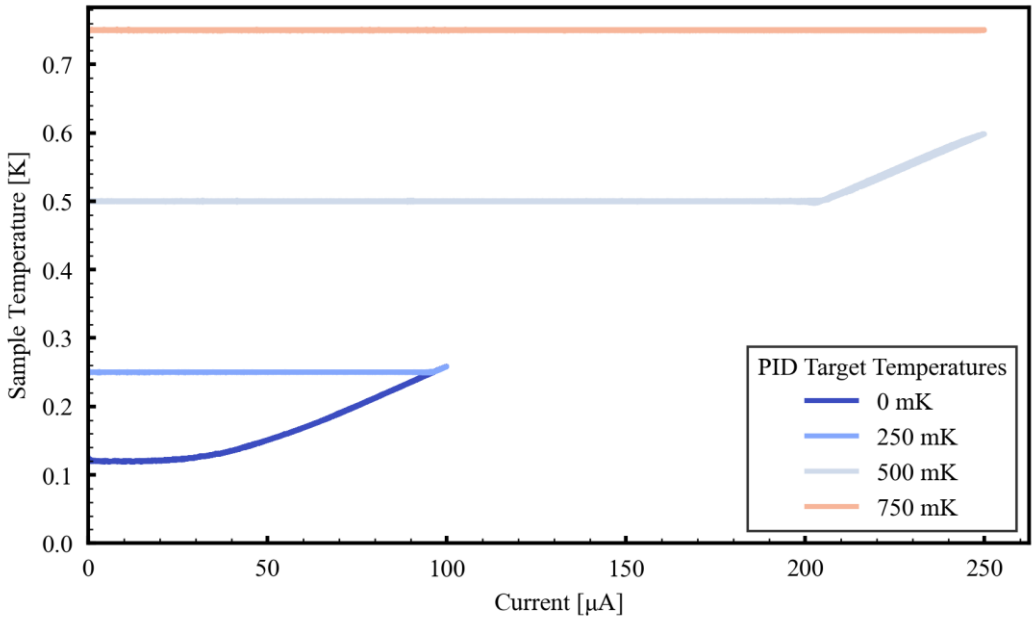

Figure 5.11: The ohmic heating produced by the current sweeps causes a rise in sample temperature.

Testing revealed that slow sweeps in the order of 1 μA/min allow for effective minimising of thermal hysteresis in the data, showing that this sweep rate allows for balance between the local heating, high thermal conductivity of the diamond and the global temperature of the system on the mixing chamber of the LD400. However, due to this requirement of slow data acquisition and a broad area of interest in the current range, the time to conduct a full positive and negative current sweep became prohibitively long. It was therefore decided that one full sweep would be taken for each data device to ensure symmetry, but subsequent

sweeps would only include the positive current polarity. 200 μA was chosen as the current sweep upper limit to preserve the integrity of the devices.

5.6 Low Temperature and zero field results

In general, across the two chips and experimental setups the devices produce some similar results but also have some differences. In these initial results the critical currents are calculated at the point of divergence from the zero-voltage regime. A linear fit of the data is performed as the voltage response stabilises in the resistive regime to establish R_n.

With one exception that will be discussed at the end of this section, no hysteresis was observed in these measurements. The lack of hysteresis and the low device capacitance justify a fit to the simple RSJ model as shown in Equation (2.45).

$$V = IR_n\sqrt{1-(I_c/I)^2} \tag{5.1}$$

All devices showed symmetry in the opposing polarities of their *I-V* characteristics. Chip A, as measured in the light-tight box, showed very clear data across all devices that generally fit well to the RSJ model and produce one transition (again, with one exception). For these devices, the differential resistance data is calculated from the first derivative of the *I-V* characteristic after applying a smoothing filter. For the task of smoothing the data the *Savitzky–Golay* filter was used due to its ability to preserve features in the data while reducing noise. The filter works by taking data centred around a given point with a certain window size and fitting this selection of data with a polynomial. The centre point

of this window is then evaluated with the polynomial. A window size of 15 datapoints and a 3rd order polynomial were chosen a reasonable balance between retaining detail and reducing noise. The devices of chip B, measured at the end of the magnet probe, present very washed out *I-V* curves where the features and transitions are not clear. This lack of clarity introduced a need to use the lock-in amplifier which allows direct measurement of the differential resistance and shows an abundance of peaks and features. It is suspected that this difference is due to the experimental setup rather than any differences in the chips or devices themselves, with the light-tight box seeming to have a beneficial effect. The noise environment in the room where the experiments were performed was a significant and varying issue. Significant efforts were made to test for and remove ground loops and a ground spike was installed to ensure that mains electricity supply was as clean as possible. These changes were largely successful in minimising the general effects of noise such as the shifting of critical currents and lack of a truly flat zero-voltage region, but some sporadic issues persisted for chip A. Unfortunately, the internal dimensions of the superconducting magnet prevented the light-tight box from being used when chip B was measured. The wiring from the sample puck to the base of the magnet probe was also unshielded (see Figure 5.10 parts b and c), although twisted pairs in the wiring were possible.

Device A1 is a constriction with a width of 105 nm and length of 128 nm with an I_c of 2.03 μA. These dimensions are significantly greater than ξ, and yet a good fit to Equation (2.45) was produced. As can be seen in Figure 5.12, there are some step features in the *I-V* characteristic and additional peaks in the differential resistance data.

As can be seen in Figure 5.13, device A2 (another constriction) has notable perturbations in its response after it exits the zero-voltage regime. Compared to

device A1, is has a shorter length of 78 nm and an almost proportionally smaller I_c of 1.41 μA.

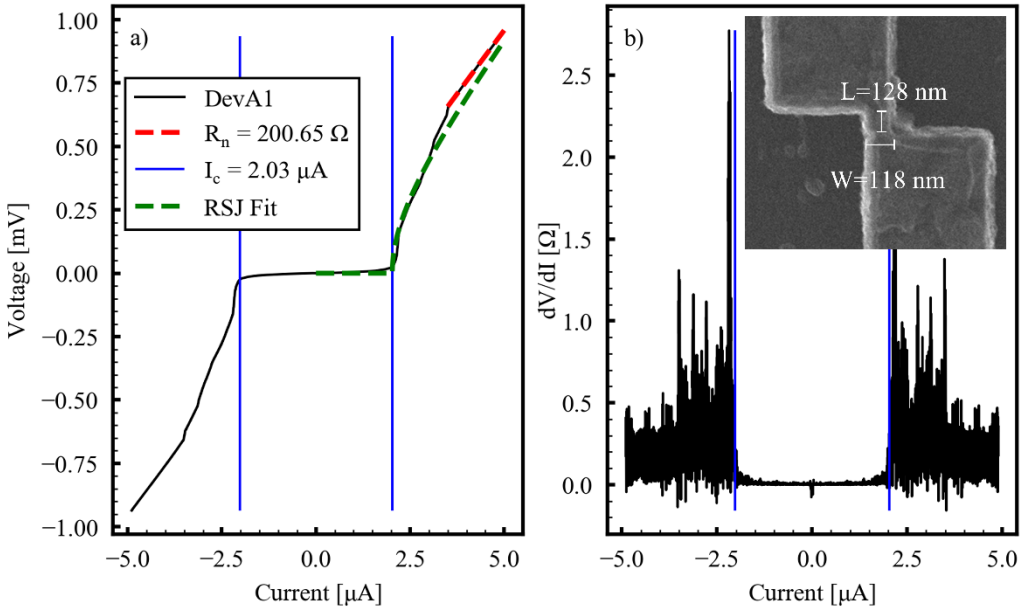

Figure 5.12: Low temperature and zero-field data for Device A1 at 500 mK. a) *I-V* characteristic with fitted parameters, b) *dV/dI* plot taken from the first derivative, with inset SEM of the device.

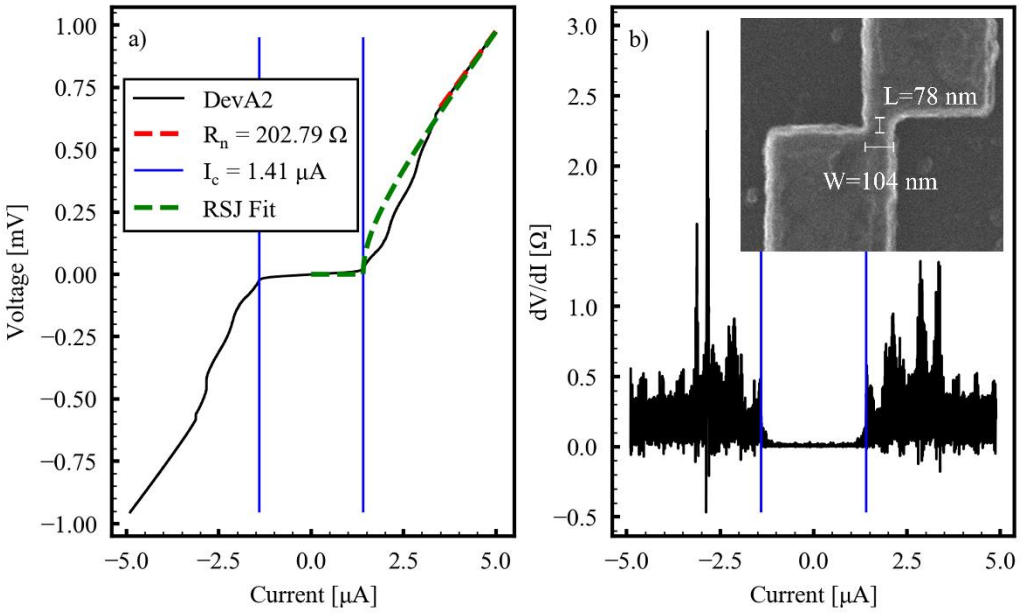

Figure 5.13: Low temperature and zero-field data for Device A2 at 500 mK a) *I-V* characteristic with fitted parameters, b) *dV/dI* plot taken from the first derivative, with inset SEM of the device.

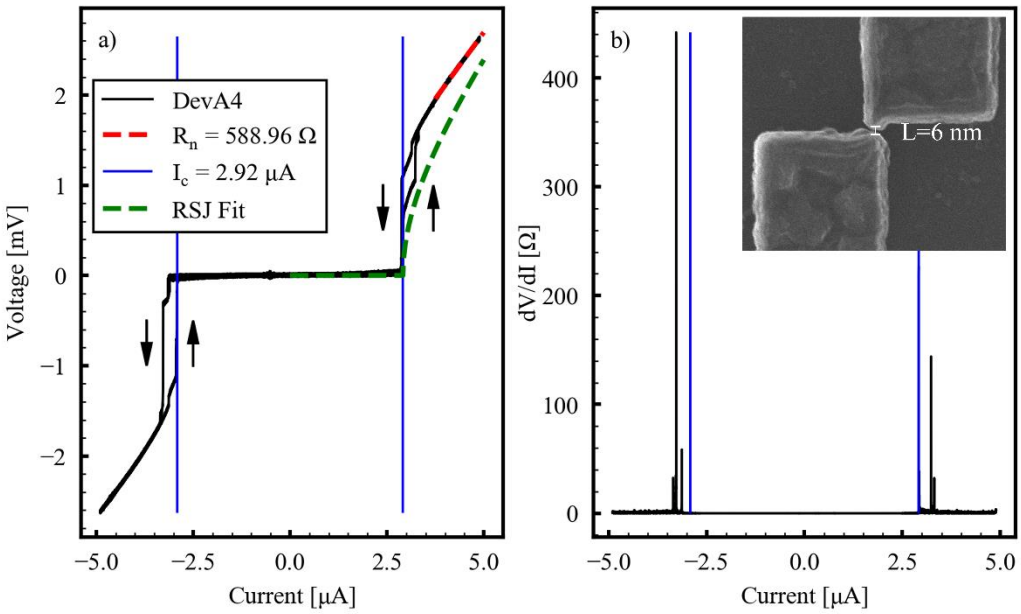

Figure 5.14: Low temperature and zero-field data for Device A4 at 500 mK a) *I-V* characteristic with fitted parameters, b) *dV/dI* plot taken from the first derivative, with inset SEM of the device.

Device A4 produced the sharpest transition from the zero-voltage region across all of the samples, with I_c = 2.92 μA. The sharpness of the transition is often an indication of environmental noise, as discussed later. Device A4 is a vacuum gap junction with a length of 6 nm, which is less than ξ. However, the value of R_n indicates that this device isn't a true vacuum gap. Some hysteresis can be seen in Figure 5.14b, although there is not a symmetrically different re-trapping current value as would be expected from the hysteresis created from an underdamped junction. It should also be noted that current sweep rate optimisations had not yet been performed at the time that this data was acquired.

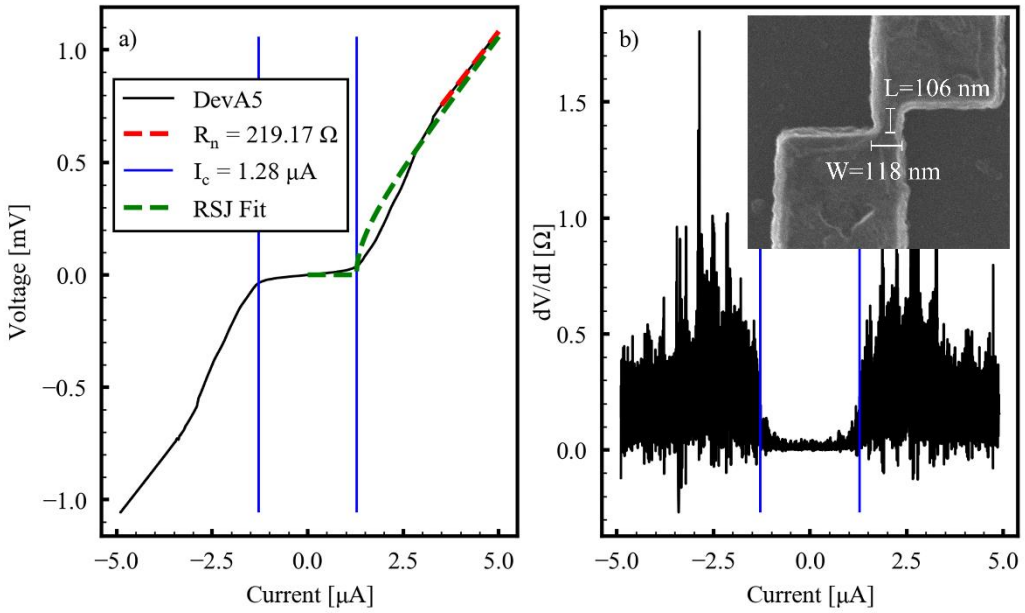

Figure 5.15: Low temperature and zero-field data for Device A5 at 500 mK a) *I-V* characteristic with fitted parameters, b) *dV/dI* plot taken from the first derivative, with inset SEM of the device.

Device A5 does not have a flat zero-voltage region as can be seen in Figure 5.15. As another constriction, comparison to the other devices of the same type is warranted. With a length of 109 nm it would be expected to have a critical current somewhere between the other two devices, which is not the case.

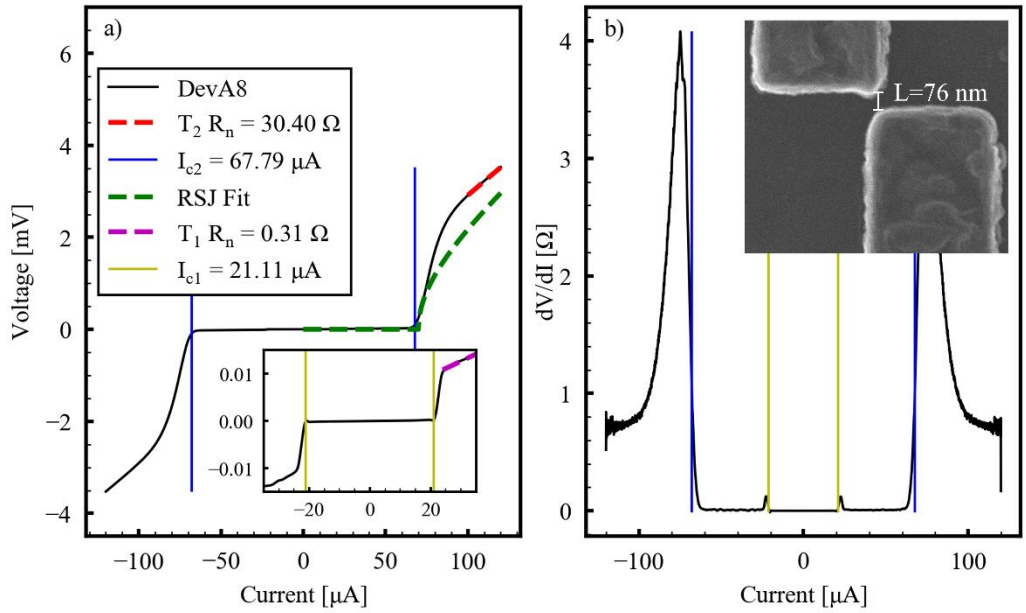

Figure 5.16: Low temperature and zero-field data for Device A8 at 500 mK a) Device A8 *I-V* characteristic with fitted parameters, inset shows a magnified region around the first transition b) *dV/dI* plot taken from the first derivative, with inset SEM of the device.

As shown in Figure 5.16, device A8 has some interesting features in its voltage response to the current sweep. Additionally, this device has a vacuum gap significantly longer (L = 76 nm) than the coherence length of Cooper pairs in diamond, however the value of R_n is low and inconsistent with the other "gap" device A4. There are two transitions, with the first at 21.11 μA and the second at 67.79 μA. This device also has a significantly lower normal state resistance value when compared to the other devices on chip A.

Device B1 is another constriction device with a length of 82 nm. The first transition is at 1.52 μA, which is similar to the other constriction devices on chip A. As can be seen in Figure 5.17, the *I-V* characteristic does not produce a good fit to the RSJ function. As is the case for all devices on chip B, the normal resistance is significantly higher (kΩ compared to ~200 Ω), with a long non-linear resistive

region. Contained in this region are the features mentioned previously. A second and fairly clear transition at 15.32 μA, a region of very densely packed steps/peaks, and a final transition at 110.64 μA.

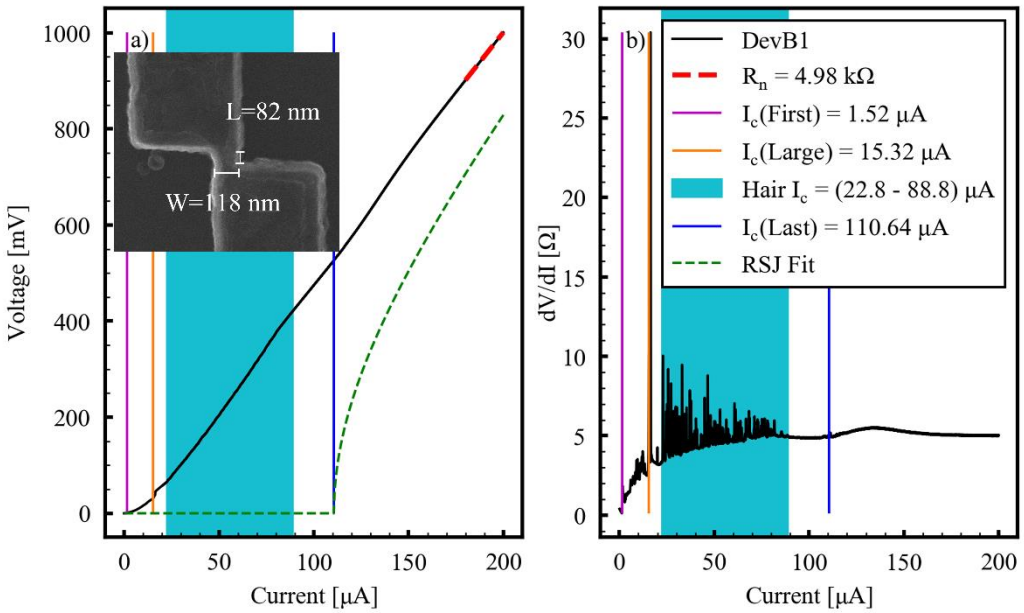

Figure 5.17: Low temperature and zero-field data for Device B1 at 500 mK a) Device B1 *I-V* characteristic with inset SEM of the device, b) *dV/dI* data directly measured, with fitted parameters. Area highlighted in cyan encompasses the dense region of peaks and various notable transitions highlighted.

The results for device B3, as shown in Figure 5.18, are very similar to device B1. However, despite them both being constrictions with similar dimensions the first transition is a significantly higher current of 5.12 μA. As with device B1, and consistent across all chip B devices, there is a final transition before a linear resistive region is observed. This final transition is perhaps similar to the one seen in device A8.

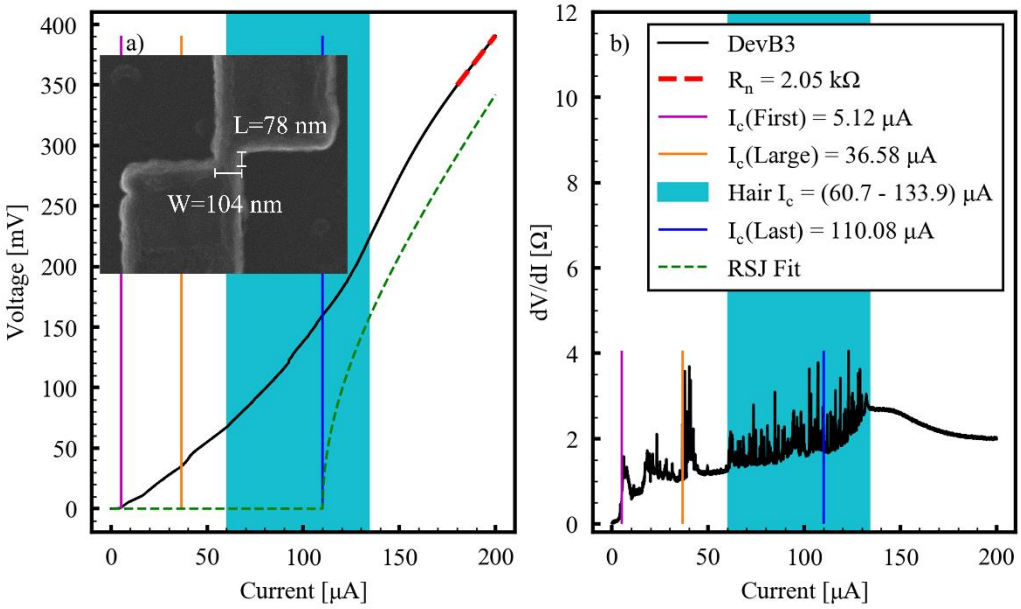

Figure 5.18: Low temperature and zero-field data for Device B3 at 500 mK a) *I-V* characteristic with inset SEM of the device, b) *dV/dI* data directly measured, with fitted parameters. Area highlighted in cyan encompasses the dense region of peaks and various notable transitions highlighted.

Device B4 is the point contact, but the values for the extracted variables are very similar to both the constriction and gap type devices so an inference about the material in the junction cannot be made. These variables are shown in Figure 5.19, along with the rest of the features common to all chip B devices. The normal state resistance of this device is very similar to device B3 (2050 Ω and 2200 Ω), which is unexpected considering the vastly differing geometries.

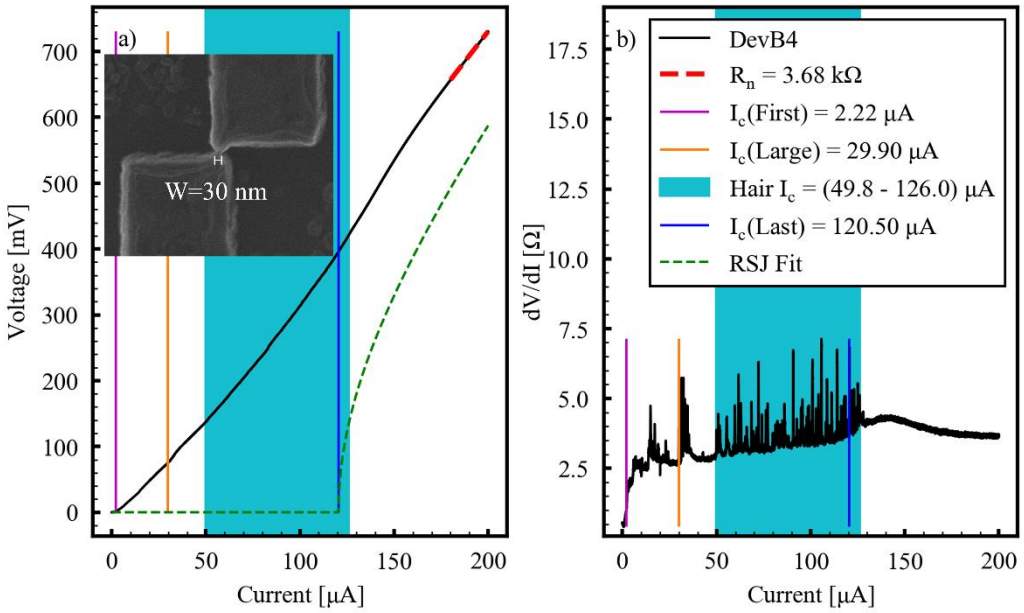

Figure 5.19: Low temperature and zero-field data for Device B4 at 500 mK a) Device B4 *I-V* characteristic with inset SEM of the device, b) *dV/dI* data directly measured, with fitted parameters. Area highlighted in cyan encompasses the dense region of peaks and various notable transitions highlighted.

It was suspected that device B8, being very similar in geometry to device A8, would show similar properties. Even when comparing the initial transition, this occurs at a significantly lower current of 2.18 μA. Compared to the other chip B devices, this one has no significantly greater peak in the differential resistance data, which is similar to the point contact device B4.

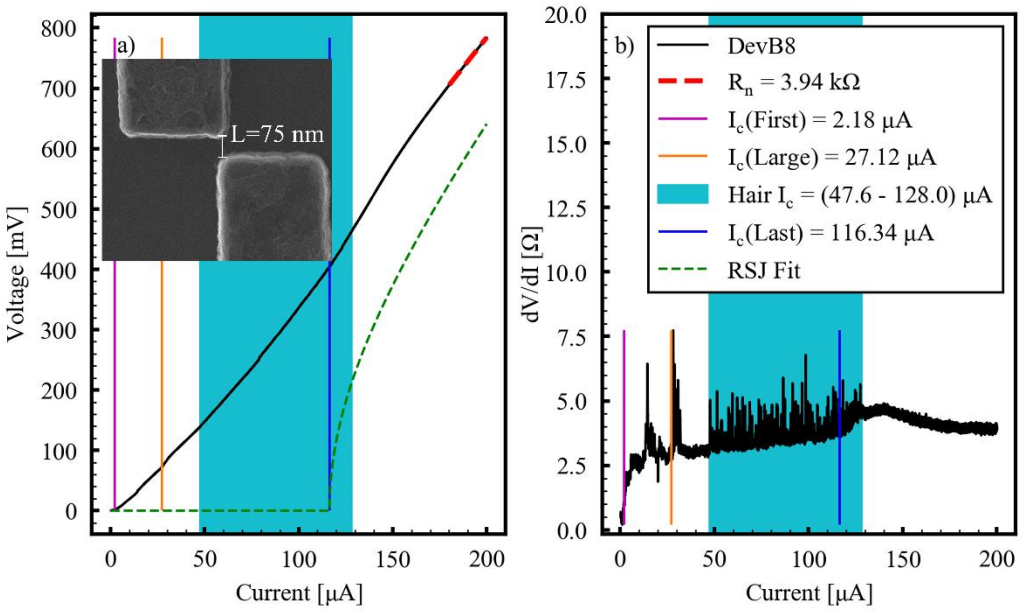

Figure 5.20: Low temperature and zero-field data for Device B8 at 500 mK a) *I-V* characteristic with inset SEM of the device, b) *dV/dI* data directly measured, with fitted parameters. Area highlighted in cyan encompasses the dense region of peaks and various notable transitions highlighted.

As shown in Table 5.2, the lowest current where a transition occurs is typically under 5 μA (except for device A8 with a significantly higher I_c of 22 μA). There does not appear to be any correlation between length of the junction and its first transition critical current, nor its type. Similarly, the observation of a second transition at a higher current seems to occur at an apparently independent value. This lack of trend is also not evident in the I_cR_n values, as shown in Figure 5.21. Significantly different values for the normal state resistance of the different devices were also calculated. The values in chip B were corroborated by measurement in two separate systems as shown in Figure 5.22. A discrepancy was observed between both a direct measurement of the resistance in the Bluefors fridge, a resistance measurement in the PPMS and R_n calculated from

the *I-V* characteristics measured in the Bluefors fridge. All $R(T)$ data were AC measurements with an excitation amplitude of 0.1 μA.

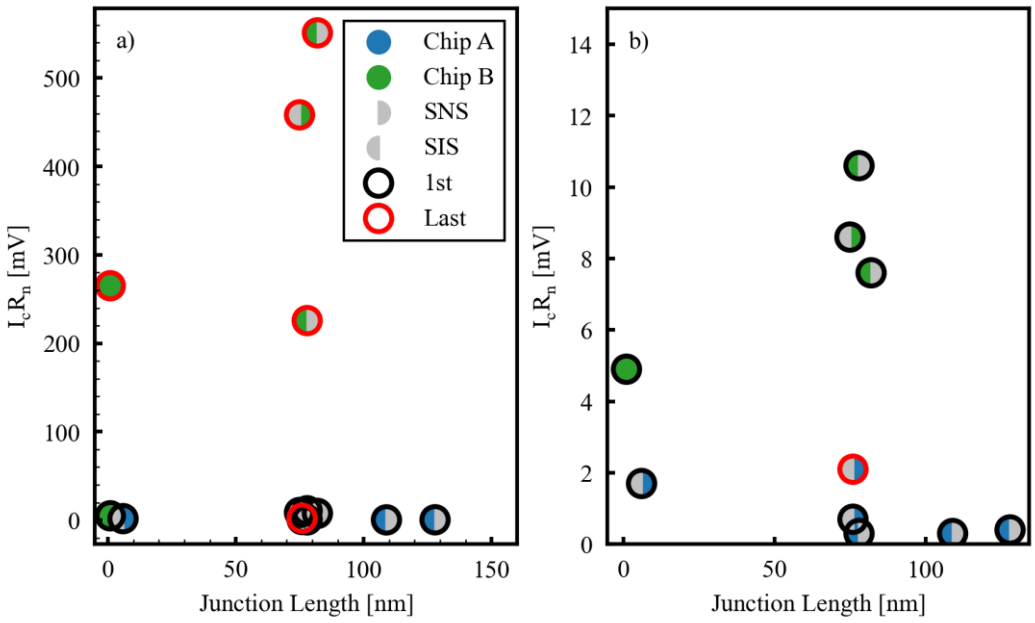

Figure 5.21: I_cR_n for all devices across both chips. Correlations between junction type (SNS/SIS) and geometry are not observed. a) Showing the full range of values and b) zooming on the lower I_cR_n range.

However, the devices on chip B still had a higher resistance than the devices on chip A. This does not affect the analysis significantly, although it should be considered whenever the absolute rather than relative voltage values are used.

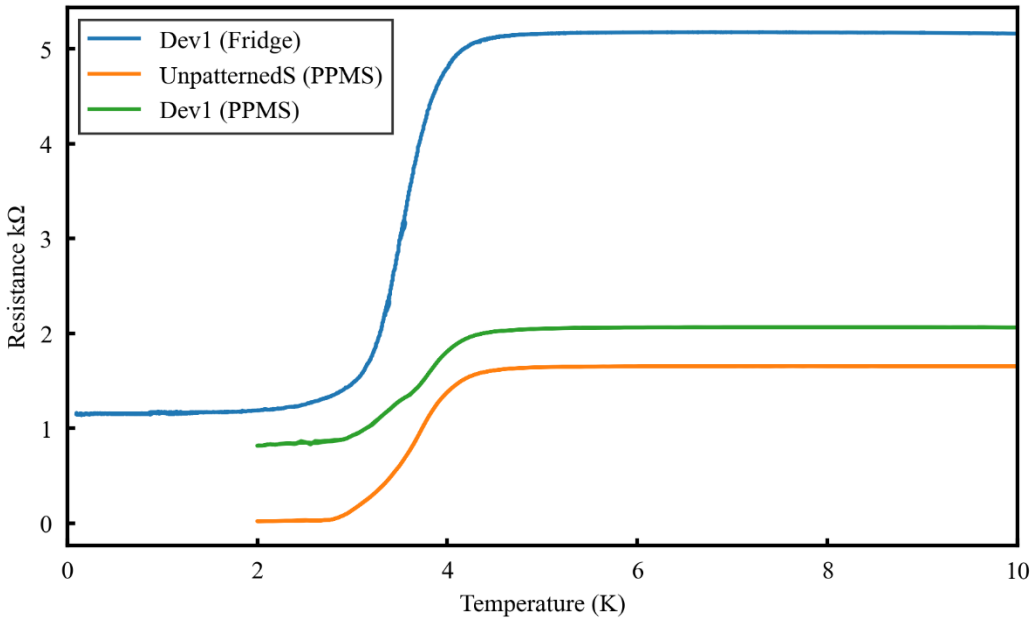

Figure 5.22: Verification of the resistance measurement of the chip B devices indicated an inflated value when measured with the setup used in the Bluefors fridge experiment.

The geometric capacitances calculated for all devices were extremely small (<10^{-25} F), which also leads to small values of β_c (<10^{-1}). This satisfies $\beta_c \ll 1$, indicating overdamped junctions that should not show hysteresis in their *I-V* characteristics. This is generally evident in Figure 5.12 - Figure 5.20. Although some hysteretic behaviour can be observed in devA4 in Figure 5.14, unfortunately more detailed measurement with slower current sweep rate was not performed to rule out thermal effects. With correctly tuned current sweeps hysteresis is not observed in the other devices, indicating that the long lead lines in the fabricated geometry are effective at minimising capacitance. Although hysteresis is frequently found in Josephson junctions, it has been demonstrated that the presence of hysteresis in junctions fabricated with low capacitances is due to heating of the electrons in the resistive regime and is therefore less of a concern in terms of SQUID operation [181].

Table 5.2: Summary of all device parameters across both chips. First and last transitions provided where available.

Dev	Type	$L \times W$ [nm]	R_n [Ω]	I_c [μA]		$I_c R_n$ [mv]	
A1	Constr. (SNS)	128×105	200.65	2.03		0.4	
A2	Constr. (SNS)	78×108	202.79	1.41		0.3	
A4	Gap (SIS)	6×-	588.96	2.92		1.7	
A5	Constr. (SNS)	109×118	219.17	1.28		0.3	
A8	Gap (SIS)	76×-	30.4	22	67.8	0.7	2.1
B1	Constr. (SNS)	82×118	4980	1.52	110.7	7.6	551.1
B3	Constr. (SNS)	78×104	2050	5.12	110.1	10.6	225.7
B4	Point Contact	-×30	2200	2.22	120.5	4.9	265.1
B8	Gap (SIS)	75×-	3940	2.18	116.3	8.6	458.4

An important consideration is the timeline and narrative of the measurements across the two chips. As chip A was measured first, lessons and experimental modifications in the intervening time were only incorporated into the measurement of chip B. It was suspected that the small structures would be sensitive to damage from high currents (>50 μA). This was corroborated by

observation from previous experiments and initial measurements of chip A. For example, the clean results from device A4 could not be reproduced after a brief pause in the experiment due to scheduled sitewide electrical maintenance. This loss of the device was attributed to a spurious current spike. It is now accepted that the primary issue is a sensitivity to the noise environment, although it was not possible to address this sufficiently to restore the response in device A8. However, the tolerance of the devices to higher currents was not learned of until after the measurement of chip B began, so it is possible that all devices on chip A had a second higher current transition.

The magnet probe and accompanying wiring that was used in measuring chip B clearly has less shielding and noise isolation than the light-tight box, leading to the broadened transitions in the *I-V* characteristics and possibly the higher resistance values measured. Careful elimination of noise has been shown to sharpen the rounded character at I_c in a *I-V* curves [182,183]. While making precise determination of I_c is more challenging, the fact that many of the measured values and trends (see later) are similar creates an opportunity for comparison while the downsides can be minimised with careful analysis.

As discussed previously, junctions fall into different classes based on their lengths relative to the coherence length and the type of material between the superconducting electrodes (i.e. SNS or SIS). All types of junction are expected to produce an *I-V* characteristic similar to an idealised junction, and all are expected to have an approximately linear proportionality between their length and the zero voltage critical current I_c [184–187]. Allowing for variability across junction type and across chips, and the situation of multiple transitions, this relationship is not observed for these devices as shown by the values normalised by their normal state resistance in Figure 5.23. This indicates that the fabricated geometry is perhaps not what is governing the Josephson characteristics.

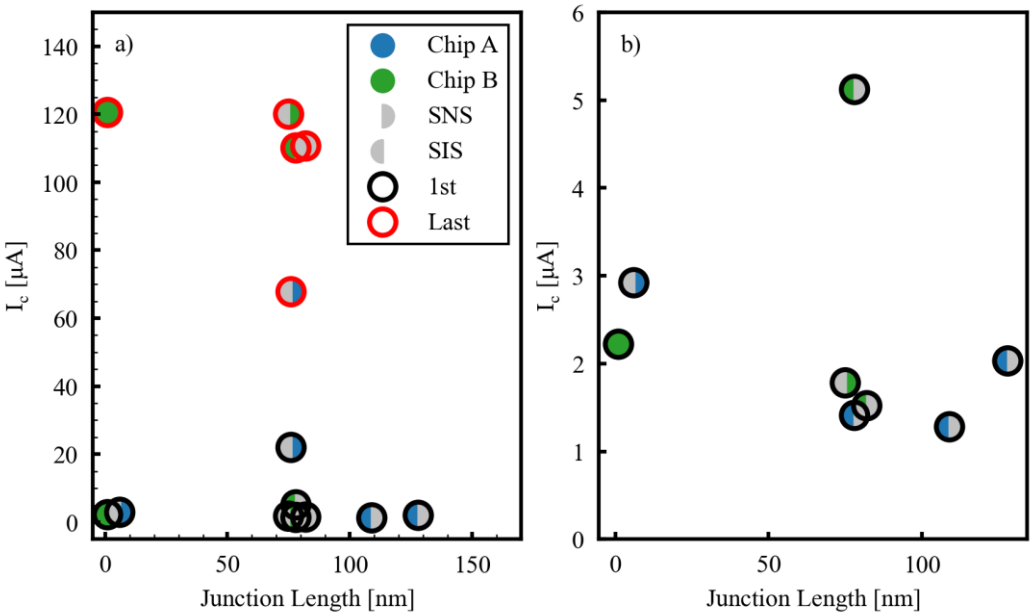

Figure 5.23: I_c for all devices across both chips. Correlations between junction type (SNS/SIS) and geometry are not observed. a) Showing the full range of values and b) zooming on the lower I_c range.

Bose et al. assert that the granularity of the films is not responsible for the measured behaviour of the junctions [174]. These devices were fabricated on films grown by the Cardiff diamond group (therefore having comparable film morphologies and superconducting properties) and consist of small loop size of 50 nm (defined as the square length L and shown in Figure 5.24 as the centre milled hole), Dayem bridge junction lengths of 27 nm and various junction widths. They report SQUID critical currents between 4.3 and 7.5 μA. While these devices do indeed produce SQUID behaviour, they noted two significant anomalies. Firstly, their results state that junctions less than 200 nm wide produced "ohmic" *I-V* characteristics, while noting that Dayem bridges are expected to function at widths of the order of the superconducting coherence length (ξ ~ 10 nm).

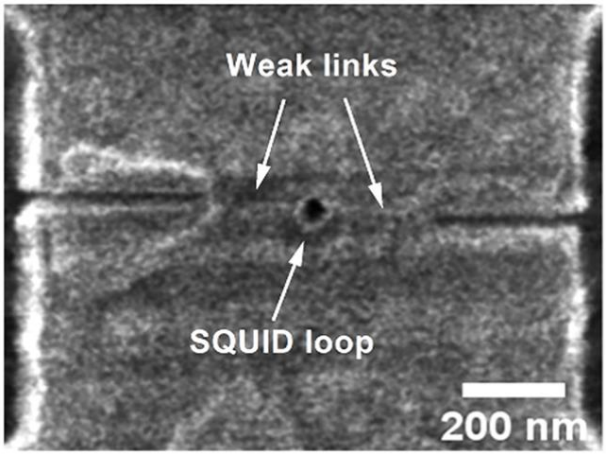

Figure 5.24: SEM of a SQUID device consisting of Dayem bridge weak link junctions in B-NCD. Reproduced from *Bose et al.* [174]

Secondly, a disparity between the physical and effective sizes of the SQUIDS was found when analysing the modulation of I_c as a function of a magnetic field through the device. The two devices detailed (A and B) have a physical loop size of 50 nm, whereas the results indicated expected values of $L_A \approx 22.3$ nm and $L_B \approx 20$ nm. These disparities are not observed in the other diamond SQUIDS mentioned previously.

Given that two devices (devA8 and devB8) presented the current work show tunnelling at lengths greater than the 27 nm milled gaps in the film defining the junctions, it is likely that the results presented by *Bose et al.* are confounded by similar effects. The device geometry may also lend itself to higher capacitances than those presented in this work and the previous work of Mandal *et al.* [3]. Additionally, it is perhaps noteworthy that the measured effective loop sizes are similar to the grain sizes presented in Figure 5.7, and that the superconducting coherence length in bulk superconducting diamond is also in this size range. Previous work with bulk granular superconductors has shown the grains and their boundaries can function as a network of nano-SQUIDs [188,189]. With the grain boundaries or other non-superconducting material present in B-NCD films

and in-plane with the device, it is possible that the measurements are in fact measuring grain or inter-grain junctions and nano-SQUIDs.

5.7 PEAK ANALYSIS

The presence of various transitions in multiple devices clearly warrants consideration and analysis. DevA8 has two very clear transitions and all devices on chip B show numerous transitions between an initial low current value of I_c = 1.52 and 5.12 μA and a final transition between I_c = 110 and 120 μA. It is assumed that this behaviour is due to metastability, phase slips and the underlying granular structure of the film as reported in B-NCD by *Klemencic et al.* [98] and discussed in Section 2.4.

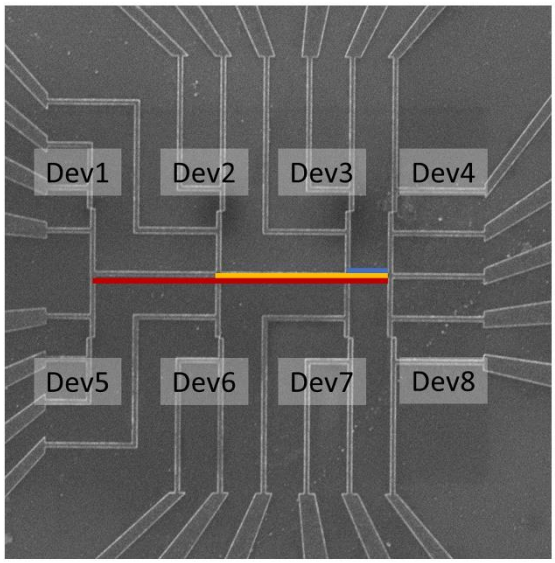

Figure 5.25: SEM image showing the layout of the unpatterned strips on chip B. All strips have a width of 500 nm and lengths are as follows: Small (blue) = 5 μm, Medium (orange) = 22.5 μm and Large (red) = 36.76 μm.

Due to the geometry of the lead lines fabricated into the chips, there was an opportunity to test whether the length of the material between the voltage taps influenced the number of transitions measured. Three lengths are compared on unpatterned strips, where Unpatterned (S) = 5 μm, Unpatterned (M) = 22.5 μm and Unpatterned (L) = 36.76 μm. The layout of this is depicted in Figure 5.25. If there was a correlation between the length of the strip and the number of peaks measured, it would indicate that a narrow normally conducting region corresponding to one or more grains propagates across the width of the strip.

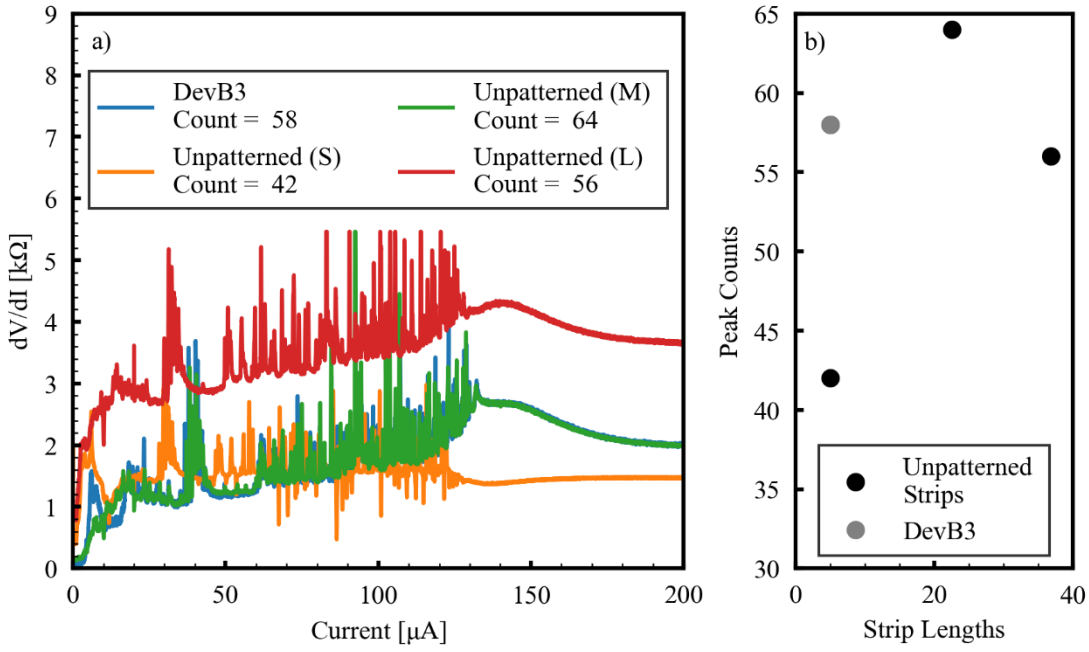

Figure 5.26: Peak count analysis a) A count of the peaks in the different lengths of unpatterned material of width = 500 nm, b) peak counts plotted against the length of each strip.

Figure 5.26 shows the results of this study, where no correlation is observed. An alternative theory is that because the peaks appear at repeatable current values,

they correspond to grains of different sizes switching to the normal state due to surpassing individual values of their critical current density j_c. This is perhaps evidenced by the longer unpatterned strips having higher resistances (shown in Figure 5.26a but similar transition I_c values, where more grains of a similar size and j_c result in a larger total resistance.

Also visible in the comparative plot in Figure 5.26 is that the different peak regions seem be distinct and consistent across all samples and unpatterned strips. The final transition is not obviously visible on the unpatterned strip however it's possible that this feature is either less prominent at the currents measured, or present at higher current values than were measured.

It was not possible to perform analysis on the gradient of the steps in the *I-V* characteristic to confirm the phase slip behaviour. Attempting this with both linear fits to the steps in the *I-V* characteristic and utilising the differential resistance data to quantify the gradient of the line passing through the centre point of the step did not produce coherent results. However, an investigation into the relationship between the spacing of the peaks was undertaken as follows. The goal was to find any correlations between the peak separations or their values in current and voltage.

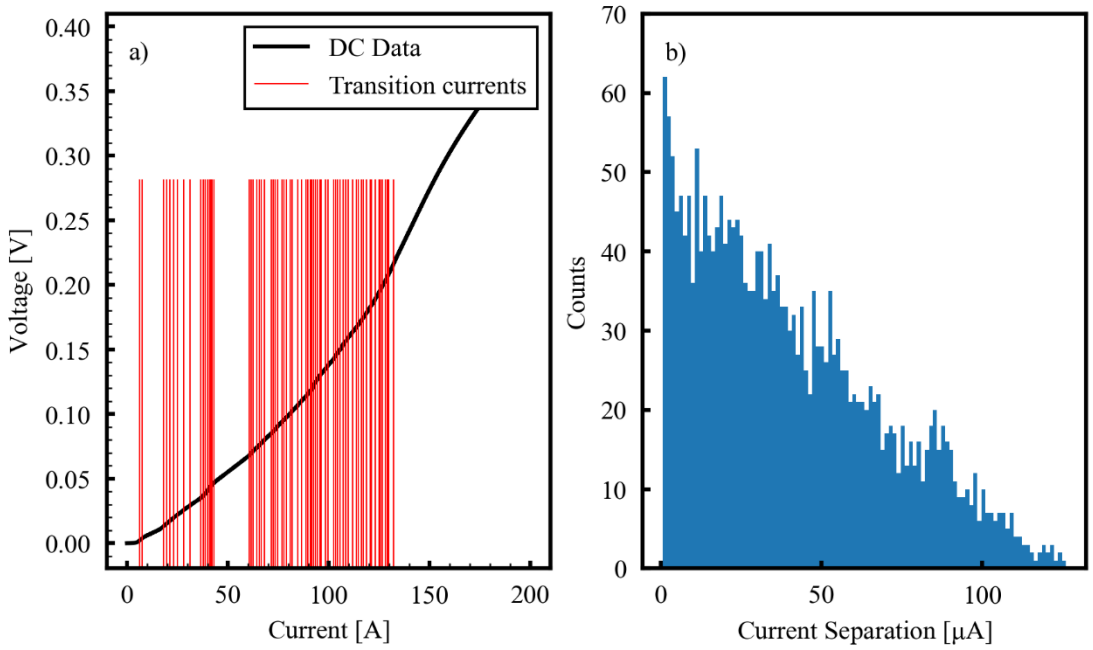

Figure 5.27: Peak separations a) Highlighting the transition points in the *I-V* characteristic derived from the differential resistance measurements, b) counts of the separations between the peaks.

Firstly, the peak positions were established from a simple peak fitting script that smoothed differential resistance data and filtered out the smallest peaks. The separation between all of the resulting peaks was then found (shown in Figure 5.27). The earlier filtering was performed to avoid systematic noise from overcounting the smallest separations. Once these separations were established, these data were run through a counting algorithm that found the frequency of each integer multiple between the separation values, with a 5% tolerance to allow for measurement error. For example, if there are separations of 2, 5, 6 and 8, the separation value of "2" occurs 3 times with up to 4 integer multiples.

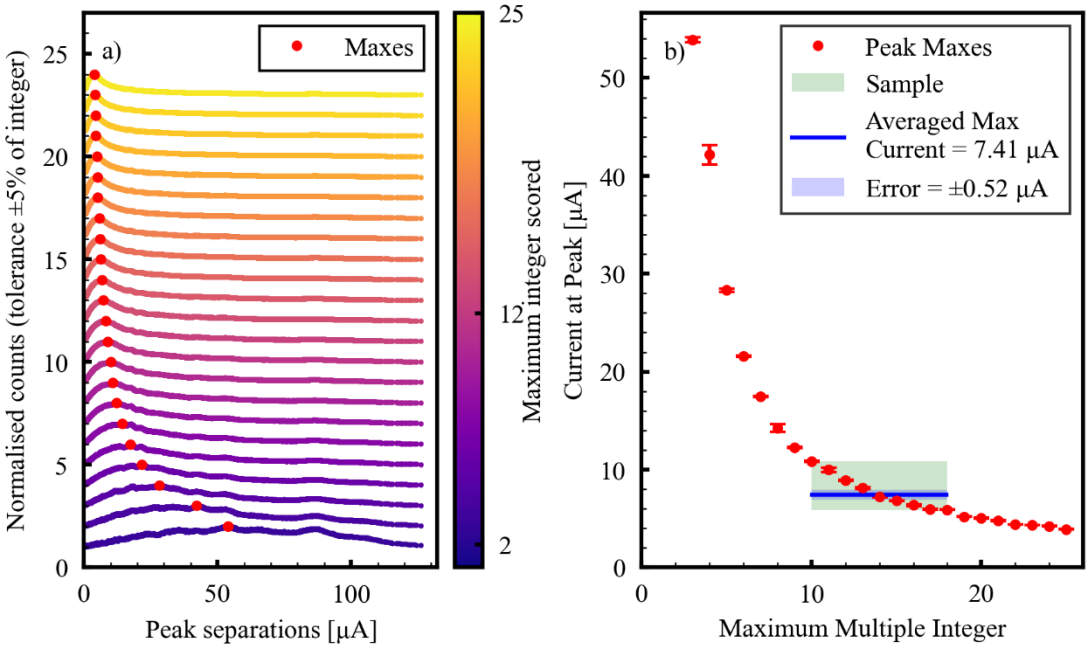

Figure 5.28: Peak count convergence a) Unconstrained, the convergence of the algorithm is significantly influenced by counting the smallest separations. b) A sample of the data, derived from the grain size distribution to give a sensible multiple range, allows for calculation of an average and inference of the correct integer to use.

Running this algorithm for a range of integer multiples gives no direct indication of convergence, although a familiar log-normal type distribution emerged (see Figure 5.28a). This distribution was sensitive to the range of integer multiples that were counted, where if counted without limit and with a large enough tolerance the smallest separations completely dominate. To establish which integer multiples are relevant for this analysis, we must look to the grain size distribution. The grain frequencies were counted with a bin size of 10 nm with the lowest occupied bin covering 20-30 nm. The maximum grain size in films with a similar thickness to the film 180321 was 290-350 nm, as measured by Dektak. Thus, taking $range_{max}/range_{min}$ the range of integers that should be counted is 10-18. This integer range allows selection of a sample as shown in Figure 5.28b,

which in turn allows for the determination of a single integer multiple and its maximum in current separation.

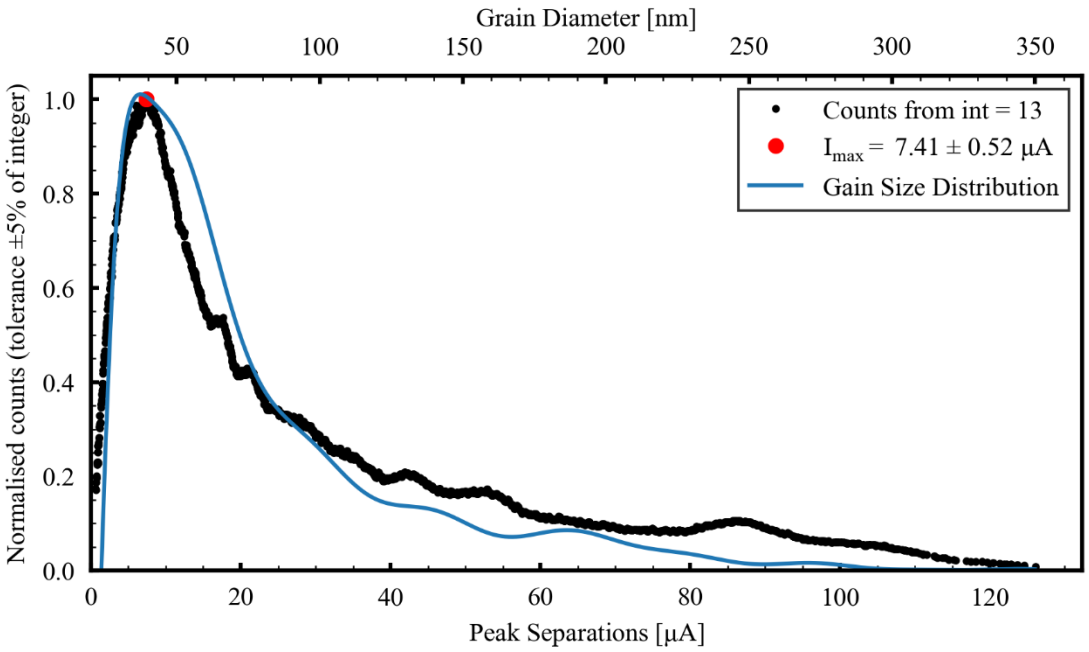

Figure 5.29: Analysis of the frequency of occurrence of the separations between the peaks in a device's differential resistance data produce a relationship that fits well to the grain size distribution mentioned earlier.

The results are shown in Figure 5.29. The most common separation was 7.21 μA corresponding to a grain diameter of 37.2 nm, which is of a similar scale to the first transitions noted previously in this section both in the current measurements and in the literature. Initial testing of this model was performed with a grain size PDF based on the assumption of a thinner film. This resulted in a significant discrepancy between the model at higher peak separations and grain diameters. With the correct film thickness factored in, this effect is minimised.

5.8 PEAK TRACKING

The temperature and field dependence of a Josephson junction can be analysed with relations that model the critical current (I_c) or the voltage gap (V_g) of transitions between different states in the device. For a typical Josephson junction, this is a simple matter of tracking the position of a single feature or peak with increasing field and temperature. However, the data derived from these measurements were more complex with various peaks of different magnitude and character.

Algorithm 5.1: Peak tracking

Find peaks, create array all_peaks((n_{sweeps}, n_{peaks}))
for i = 1, 2…n_{sweeps}
Create array peak_track((n_{sweeps}, n_{peaks}))
    for j = 1, 2…n_{peaks}
        Generate P = all_peaks(i)/peak_track(i-1, j)
        Generate masks m_1, m_2, m_3…m_k
        if max(m_k) = 0
            Check m_{k+1}
        else peak_track(i, j) = m_k

The quantity, density and movement of the differential resistance peaks in both temperature and magnetic field space pose a problem for accurately quantifying their positions and respective dependencies. Often the peaks are located only a few tens of data points apart and so identifying a peak's new position in successive temperature and field increments is a process subject to conflation by the neighbouring features. At the highest temperatures and fields, peaks and

features in the differential resistance sweeps merge into each other, so the number of peaks is not constant. Manual tracking of the peak values is possible, but tracking all of the peaks would take considerable time.

A manual algorithm for tracking the peaks is also vulnerable to unqualified bias and lower levels of accuracy and consistency. Implementing a computerised algorithm allows for greater levels of accuracy, scalability and efficiency. It is also possible to codify and discuss assumptions and bias. Therefore, an algorithm was created that accounts for the behaviour of the peaks and tracks with enough precision to allow comparison to physical models, which is outlined below in Algorithm 7.1. A basic framework was chosen where each peak is compared to the peaks in the previous current sweep. Previous peak locations are grouped based on their percentage proximity to the new peak, and with all of the new peak locations filtered through a series of masked arrays. The first group has the lowest percentage cut-off and therefore the closest proximity. The algorithm steps through the results of these masked arrays, working from the bottom of the group upwards, to find the most likely candidate for the translation of the new peak based on the percentage difference to the previous current sweep.

The size, quantity and cut-offs for the groups are subject to tuning to the whole dataset. For example, in general, field dependence of the peaks results in a more rapid drop-off in I_c when compared to increasing temperatures. Additionally, it is possible to split the filtering into lower and higher field/temperature regimes where there may be a need for larger or more frequent groups.

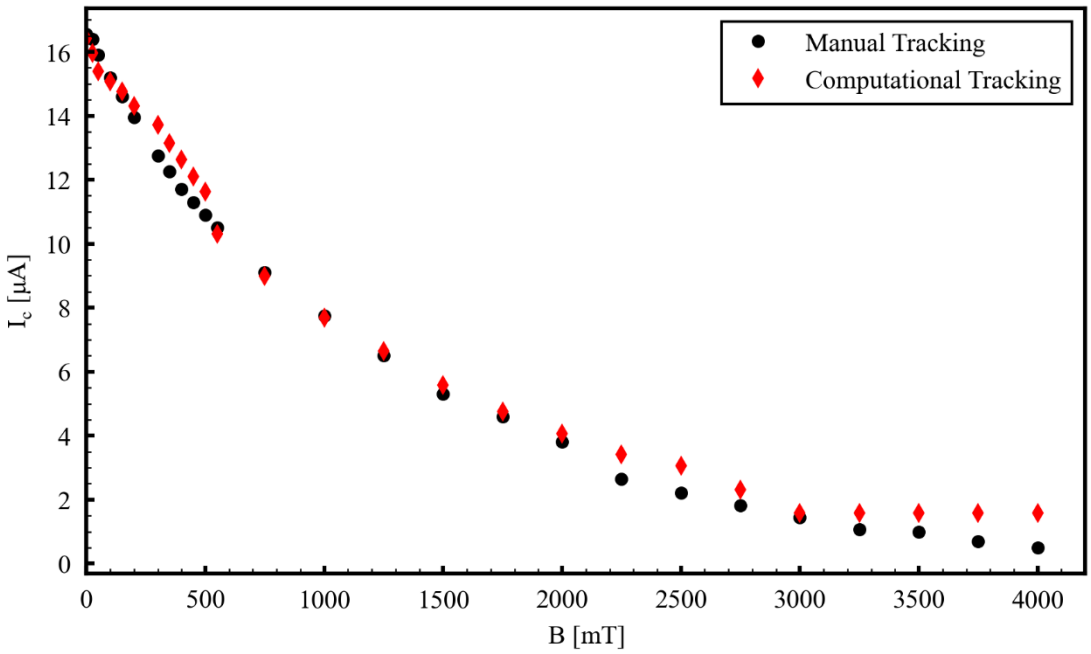

Figure 5.30: Comparing the results of the peak tracking algorithm with a "best guess" manual approach.

As shown in Figure 5.30, the computational peak tracking method is reasonably accurate and removes the subjectivity of performing the tracking by eye. There are two main limitations to the method: 1) Clusters of peaks merge into one peak with increasing field or temperature, which makes accurate tracking of the individual "hair" peaks difficult. 2) When dealing with the highest field and temperature current sweeps where the features start to blend into each other, and the magnitude of the peaks compared to the background values is reduced.

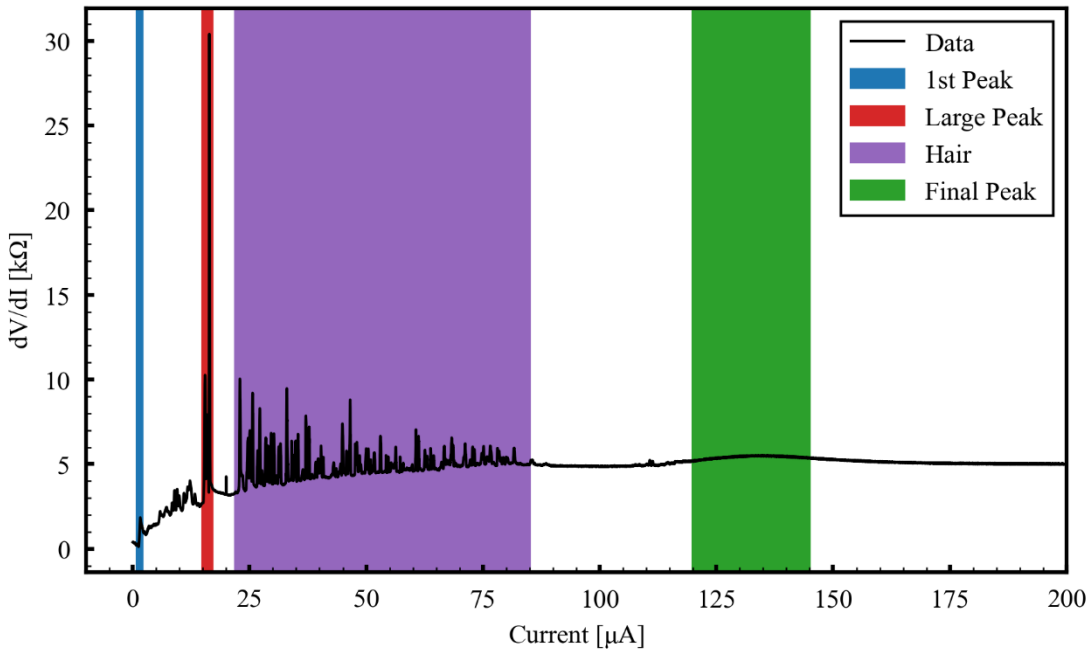

Figure 5.31: Highlighting and naming the peaks observed in the differential resistance data.

However, by simplifying the peaks into five groups and manually checking the results of the peak tracking these limitations are mitigated to the extent that the impact isn't severe. As such, the five main peaks that are tracked are: the first peak, the high magnitude peak, the start of the hair features, the end of the hair and the final broader peak. These are indicated in Figure 5.31. Throughout the course of the experiments detailed in the subsequent chapters, assertions about the nature of the different peaks will be made in reference to their relative temperature and field dependences.

5.9 CONCLUSIONS

The preliminary analysis of the low temperature and zero field states of the devices yield some interesting results. Given the superconducting coherence

length in diamond of ~10 nm, the devices exhibited some unusual behaviour. Not only were several devices operational with dimensions significantly larger than the coherence length, vacuum gaps of length $L \approx 75$ nm produced clear results on both chips. This remains unexplained. Unfortunately, it was not possible to re-measure the chip A in the magnet setup or the B chip in the light tight box. This is partially due to each setup requiring different mounting chips and thus different wire bonding. Breaking and re-bonding to diamond contact pads is extremely unreliable, so this was generally avoided.

There are also signs from the data so far that something other than the fabricated geometry of the devices is governing their response. No proportionality is observed between the length of the junctions and their critical currents, and the junction type does not seem to affect any of the variables listed in Table 5.2. A closer look at the separations between the peaks show that their frequency closely matches the grain boundary distribution, and the lowest current transitions noted in B-NCD junctions are similar in value to the most frequent of the separations. This perhaps indicates the switching of the most frequent grain size into a resistive state dictates the critical current of the device. While the evidence so far does not conclusively prove a completely grain dominated theory, it can certainly be said that these initial results cast significant doubt on the relevance on the parameterisation of devices that do not take grains into account. The analysis in the subsequent sections expands upon this picture.

It can be noted that the chip geometry chosen when designing the devices was successful in minimising the capacitance and suppressing $\beta_c << 1$. This is due to the offset nature of the superconducting terminals and the large distance to the voltage taps.

6 TEMPERATURE DEPENDENCE OF B-NCD JUNCTIONS

6.1 INTRODUCTION

In the case of granular systems, as temperature is reduced towards the critical temperature T_c, superconductivity in the material is initially isolated to superconducting islands within the grains. Low enough temperatures result in intragrain phase coherence of the order parameter, which eventually percolates across the whole granular structure resulting in mesoscopic superconductivity. As discussed previously, the width of this transition in temperature is determined by the disorder of the material which, in the case of B-NCD, is primarily dictated by the grain size distribution and growth conditions.

In simple terms, it is intuitive that the energetic influence of temperature lowers the critical current density for all elements of the superconducting circuit. For a Josephson junction with a simple thin insulating barrier, known as an SIS junction, the temperature dependence of the critical current is well described by a relation formulated by *Ambegaokar* and *Baratoff* [75] and discussed previously in Section 2.3.3.3.

For junctions with a normally conducting weak link, referred to as SNS junctions, there is a special case where conditions related to the proximity effect in the normal region result in qualitative deviations from the *Ambegaokar-Baratoff* limit. As is mentioned previously in Section 2.3.3.3, the work of *Likharev* [190] describes how the proximity effect dominates over effects due to the bulk material energy gap when the length of the junction is significantly greater than the coherence length in the normal material $L \gg \xi_n$. There is an exponential increase in the normalised critical current with a decrease in temperature between approximately $0.3T_c > T > T_c$, which is the characteristic signature of this effect.

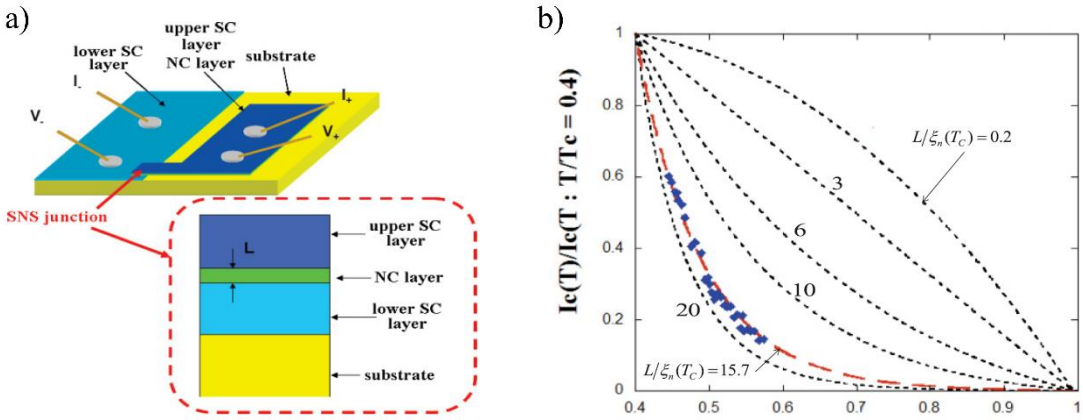

Figure 6.1: Diamond SNS junctions a) SNS single crystal boron doped diamond junctions with a vertical stack structure, producing b) $I_c(T)$ temperature dependence the exponential drop-off expected from the proximity effect present in SNS junctions. Also depicted is the crossover towards the *Ambegoakar-Baratoff* limit with small L/ξ_n ratios. From *Watanbe et al.* [191].

Watanbe et al. [191] observed this exponential-like behaviour in SNS weak links fabricated from a vertical stack of single crystal superconducting-normal-superconducting diamond. The length of the normally conducting region, as

shown in Figure 6.1a, is 50 nm. The results of fitting measured critical current temperature dependence produced an effective length ratio L/ξ_n of 15.7, which allows evaluation of the expected relationship as displayed in Figure 6.1b. They also estimate $\xi_n \approx 3$ nm for highly doped diamond (2×10^{20} cm^{-3}), which allows an approximation for the films in this work in the normally conducting regime. Given this value of ξ_n, the range of junction sizes in this work should predominantly fall into this long limit type with the exception of the point contact device B4. The electron mean free path is the same in the normal and superconducting regimes for a given material, so normally conducting B-NCD behaves as a dirty metallic conductor.

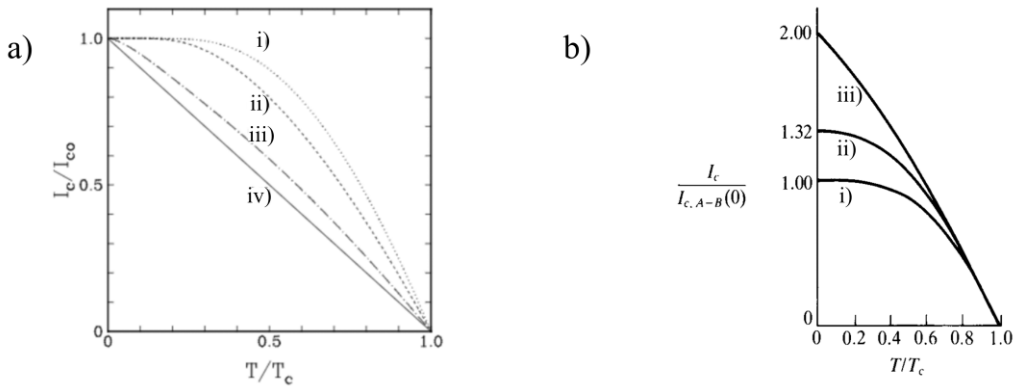

Figure 6.2: Critical current temperature dependence relationships a) Comparing the normalised temperature dependence response for i) the *Ambegaokar-Baratoff* relation, ii) KO-1 dirty limit for point contacts, iii) KO-2 clean limit and iv) the linear relationship sometimes noted to govern high T_c granular superconductors. From *Delin and Kleinsasser* [192]. b) Showing the different scaling of various temperature dependencies at T = 0. Labels the same as a). From *Tinkham* [59].

If the constriction type B-NCD junctions measured in this current work are simply governed by their fabricated geometry, one would expect that a similar

relationship to the above would emerge. However, observation of a breakdown of this relationship has been observed in junctions fabricated with other granular superconductors [192–194]. In these studies, even with high effective length ratios the exponential drop-off is not observed with the temperature dependence instead returning to the *Ambegaokar-Baratoff* limit or the KO-1 dirty limit description of point contacts as discussed previously. This dirty limit, where $L \approx \xi_n$, is also shown in Figure 6.2.

To summarise these temperature dependencies, they are displayed in Figure 6.2 in a simplified plot. In the most standard case, for an SIS junction where the superconducting electrodes are separated by an insulating gap, *Ambegaokar* and *Baratoff* predict that the critical current of the junction will depend on the temperature as follows:

$$I_c = \frac{\pi}{2}\frac{\Delta(T)}{eR_n}\tanh\left(\frac{\Delta(T)}{2k_bT}\right) \tag{6.1}$$

where R_n is the normal state resistance and the temperature dependence of the energy gap $\Delta(T)$ is given by:

$$\frac{\Delta(T)}{\Delta(0)} \approx 1.74\left(1-\frac{T}{T_c}\right)^{1/2}. \tag{6.2}$$

Equation (6.2) provides the temperature dependence of the energy gap as described in BCS theory [59]. As shown in Figure 6.2, the KO-1 dirty limit and KO-2 clean limit for a point contact scale Equation (6.1) by a factor of 1.32 and 2 respectively. Figure 6.2a shows that the dirty limit function (B) closely resembles the standard form of Equation (6.1), while the clean is a quasi-linear response for

the entirety of the reduced current range. These point contact modifications to the $I_c(T)$ response also describe the relationship described previously by *Likharev* with L/ξ_n ratios close to 1, with the traces labelled $L/\xi_n = 0.2$ and $L/\xi_n = 3$ describing the dirty and clean limits respectively. *Delin and Kleinsasser* [192] note that junctions fabricated from other high T_c granular superconductors have been mislabelled as SNS junctions when in fact their underlying mechanisms are not governed by the proximity effect, speculating that instead they behave as arrays of grain boundary pin hole junctions. Often, these junctions exhibit a temperature dependence described in Equation (6.3) and displayed at (d) in Figure 6.2.

$$I_c = I_c(0)\left(1 - \frac{T}{T_c}\right) \tag{6.3}$$

It is likely that the type of barrier that defines the junctions significantly impacts the temperature response. In the case of SNS junctions, this is governed by effects on the superconducting order parameter across the SN interface and by losses in coherence in the normal region. The former has a large effect on the value of I_c, while the latter dictates the length and temperature dependences. SIS junctions are typically well defined by Equation (6.1), while the less clear picture for the SNS case is probably due to the lack of a literal barrier and thus tunnelling effects [192]. *Delin* and *Kleinsasser* argue that this departure from the expected temperature dependence in high T_c superconductors is due to resistive components at the interface between the superconducting and normally conducting regions, effectively becoming SINIS junctions.

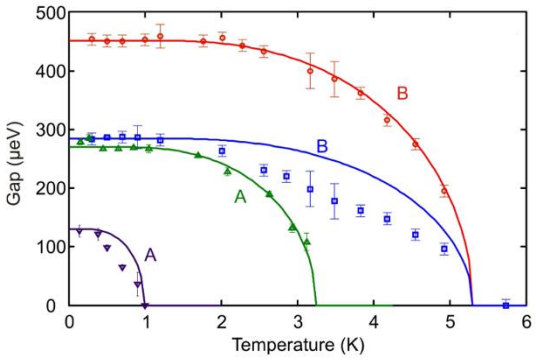

Figure 6.3: A typical BCS response in varying temperature for the energy gap (red) breaks down to a more linear dependence (blue) due to lower boron doping concentrations in certain grains. From *Dahlem et al.* [94].

Inter-grain variations in diamond boron doping concentration have been noted by *Dahlem et al.* [94] to cause a breakdown in BCS behaviour of the energy gap and therefore the $I_c(T)$ relationship that is typified by the BCS *Ambegaokar-Baratoff* I_cR_n formula and in Equations (6.1) and (6.2). They speculate an inverse proximity effect due to interfaces with grains with weaker superconducting coupling. This is characterised by a more linear response to increasing temperatures as shown in Figure 6.3, but does not result in an exponential drop-off. Any exponential signature will therefore be evidence of an SNS junction.

For the devices introduced in the previous chapter, investigating the temperature dependence of the critical currents affords the opportunity to accomplish the following. Firstly, the different junction types and lengths should exhibit the different behaviours outlined above. The constriction devices, having an L/ξ_n ratio greater than 7, should all fit to the functions based on the work of *Likharev* in his investigations of SNS junctions. Conversely, the SIS junctions should fit well to Equation (6.1). An important consideration throughout this analysis will be in the determination of T_c. This will be done, where possible, at the point

where the critical current goes to zero. Due to the noisy nature of these measurements, some extrapolation will be required particularly when dealing with the multiple peaks presented in the devices of chip B. As the temperature dependence of I_c approaching T_c is well defined for each junction type, this should not be a problem.

6.2 FLUCTUATION SPECTROSCOPY

The utilisation of fluctuation spectroscopy to probe granular superconductors was introduced in Section 2.4. *Lerner*, *Varlamov* and *Vinokur* (LVV) observed three distinct regions in $R(T)$ investigations in the vicinity of T_c, which they established were dependent on the coherence length of Cooper pairs and the size of the grains [87]. In brief, as temperature varies around T_c the coherence length also changes. When Cooper pairs have a coherence length much longer than typical grain sizes in the film, superconductivity behaves as a bulk *3D* system agnostic to the granularity. When the coherence length is of a similar size to the grains, the behaviour is that of a *0D* pocket of individual superconductivity. Lastly, in a regime where the coherence length is significantly shorter than the grain sizes, *3D* superconductivity re-emerges. Regions with distinct dependencies on the reduced temperature $\epsilon = (T - T_c)/T_c$ are apparent as follows:

$$\frac{d \ln \sigma_{fl}}{d \ln \epsilon} = \begin{cases} -\frac{1}{2} & (3D) \quad \epsilon \lesssim \epsilon_t \\ -3 & (0D) \quad \epsilon_t \lesssim \epsilon \lesssim \epsilon_g. \\ -\frac{1}{2} & (3D) \quad \epsilon_g \lesssim \epsilon \lesssim 1 \end{cases} \tag{6.4}$$

Here, ϵ_t is the *3D-0D* crossover point which also allows determination of the tunnelling energy Γ via $\epsilon_t = \Gamma/k_B T_c$. At the second crossover point $\epsilon_g =$

$E_{Th}/k_B T_c$ where E_{Th} is the Thouless energy. The Thouless energy can also be expressed as $E_{Th} = \hbar\mathcal{D}/a^2$, where $\mathcal{D}$ is the intragrain diffusion constant and a is the typical grain size for the film. *Klemencic et al.* [6] have previously identified this signature in B-NCD films, confirming the influence of the granular nature of the films on their superconducting properties. Similar analysis is performed here on a range of geometries.

Firstly, the results for the superconducting film from which all the devices were fabricated is presented in Figure 6.4. To accomplish this, first a fit to produce the conductance in the normal region G_n is performed with the following function

$$G_n = a + b\sqrt{T}. \tag{6.5}$$

From this, the fluctuation conductance around T_c is given by $G_{fl} = G - G_n$. Fitting to the simple expression

$$G_{fl} = c\epsilon^{\lambda}. \tag{6.6}$$

allows extraction of the quantity λ which is the exponent described in Equation (6.4). The film clearly shows the distinct regions with the exponent values agreeing reasonably with expectation, which is a confirmation of the LVV theory. In the first 3D regime (blue line in Figure 6.4), the conductance below T_c is only described by a few points so the fit is less reliable. However, it is still possible to observe a different character that crosses over into the 0D regime. This is the case for both subsequent investigations.

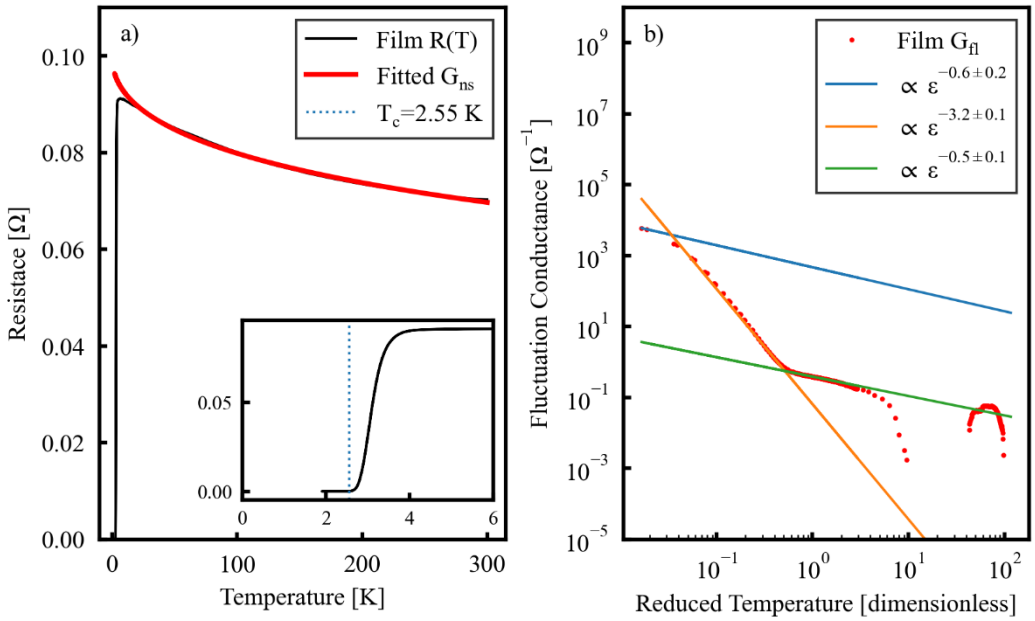

Figure 6.4: Fluctuation spectroscopy analysis of the film a) $R(T)$ fitting and b) three region fluctuation conductance results.

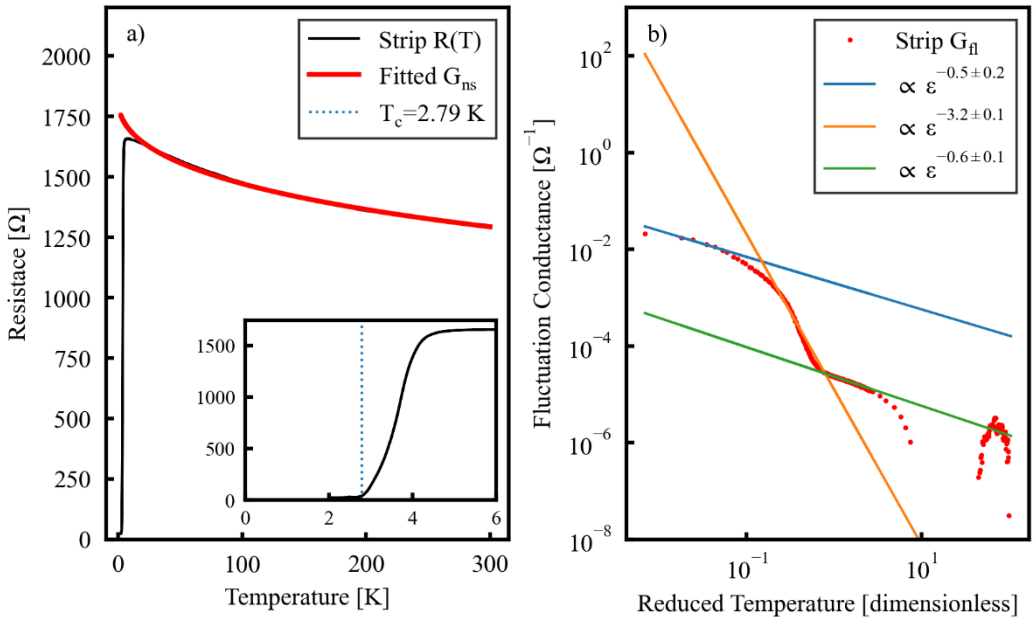

Figure 6.5: Fluctuation spectroscopy analysis of the strip (500 nm by 5 µm) a) $R(T)$ fitting and b) three region fluctuation conductance results.

The next geometry analysed is the short strip of B-NCD as described in Section 5.7. These results are shown in Figure 6.5, again showing the expected response. This strip is 500 nm wide and 5 μm long.

Finally, $R(T)$ data from device B1 was evaluated using the same method. This constriction has a length and width of 128 and 105 nm respectively. Figure 6.6 displays these results, which again show the distinct regions and crossovers. This confirms that granularity of the material dominates the superconducting properties in the geometries investigated.

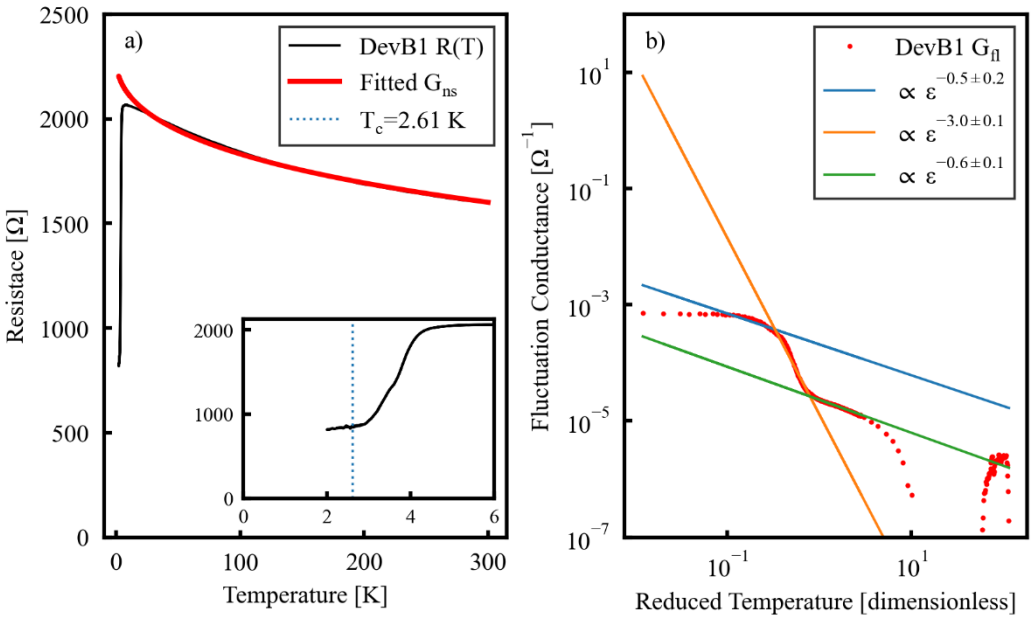

Figure 6.6: Fluctuation spectroscopy analysis of device B1 (constriction 128 by 105 nm) a) $R(T)$ fitting and b) three region fluctuation conductance results.

A summary of the fitted exponents is provided in Table 6.1, which compare reasonably to the values from Equation (6.4). Only the higher temperature 3D regime values are quoted due to the difficulty in fitting at low temperature with fewer points.

Table 6.1: Exponents derived from fluctuation spectroscopy fits.

Device	*0D*	*3D*
Film	3.2 ± 0.1	0.5 ± 0.1
Strip	3.2 ± 0.1	0.6 ± 0.1
Dev B1	3 ± 0.1	0.6 ± 0.1

The parameters extracted from the fits are displayed in Table 6.2, with ϵ_t and ϵ_g derived from the intersection between the lines defining the three regimes. $\mathcal{D}$ is calculated with the mean grain size of the film of 93 nm, which is derived from a linear interpolation of the grain size distributions of the 204 nm and 339 nm films. $\mathcal{D}_{eff}$, the effective diffusion constant, is calculated with the tunnelling energy rather than the Thouless energy. The values from the different geometries are in reasonable agreement with each other. They are also similar to those extracted by *Klemencic et al.*, and other recent work which found the diffusion constant for bulk B-NCD to be 0.6 cm²/s [195].

Table 6.2: Quantities derived from fluctuation spectroscopy fits.

Device	Γ [μeV]	E_{Th} [μeV]	$\mathcal{D}$ [cm²/s]	$\mathcal{D}_{eff}$ [cm²/s]	ξ_g [nm]	ξ_t [nm]
Film	7.8	115	0.15	1×10^{-2}	42	11
Strip	36.1	190	0.21	5×10^{-2}	48	23
Dev B1	74.7	178	2.34	10×10^{-2}	52	33

Also shown in Table 6.2 are coherence lengths corresponding to the Cooper pairs within a grain ξ_g and tunnelling between grains ξ_t, which are calculated using the following relations:

$$\xi_g = \sqrt{\frac{\pi\hbar D}{8k_B T_c}}, \tag{6.7}$$

$$\xi_t = \sqrt{\frac{\pi\hbar D_{eff}}{8k_B T_c}}. \tag{6.8}$$

As shown in Figure 6.7, ξ_g and ξ_t show some signs of scaling inversely with the cross-sectional area of the material measured, and of convergence towards a higher value. This perhaps makes sense when considering that a percolative path for the supercurrent would be more constrained and have less opportunity to tunnel through narrower grain boundaries. More measurements with different geometries would be required to test this observation.

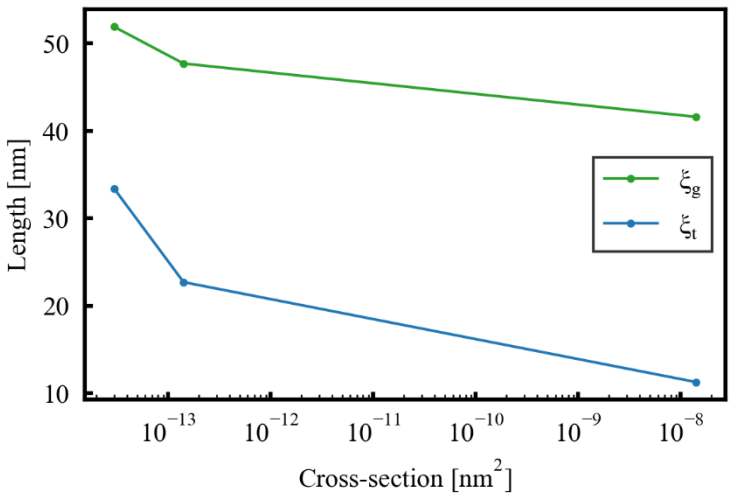

Figure 6.7: Displaying calculated coherence lengths derived from fluctuation spectroscopy.

We can see that the B-NCD structures analysed through this framework are all in the dirty limit, which is well supported by the literature presented in Section 2.4.

6.3 TRACKING I_C IN DC *I-V* AND DIFFERENTIAL RESISTANCE MEASUREMENTS

With the intention of determining the relationships governing the response of the critical currents to a varying temperature, it is first essential to establish a standardised and systematic method for determining I_c. This method will be necessarily different for the DC *I-V* and differential resistance measurements. While this may lead to some systematic inaccuracy in the absolute values obtained, given that the analysis is performed on normalised values this is not to the detriment of the final conclusions or results from which they are derived.

As was the case in Section 5.6, the DC *I-V* I_c values were determined by find the first point where the first derivative of the data exceeded two times its standard deviation. For the differential resistance datasets, peak tracking was performed as discussed in Section 5.8. Critical voltages V_g are extracted using the same methods.

6.3.1 Chip A

Starting with the device A chips, the results here were limited by the apparent failure of most of the devices prior to $I_c(T)$ measurements. Some preliminary studies were performed in the PPMS between 1.95 and 4 K, and low temperature (i.e. not using the "cold finger" configuration) *I-V* characteristics were also taken in the LD400 between 68 and 728 mK. Measurements across the full temperature range of 0.25 to 4 K were taken for device A8.

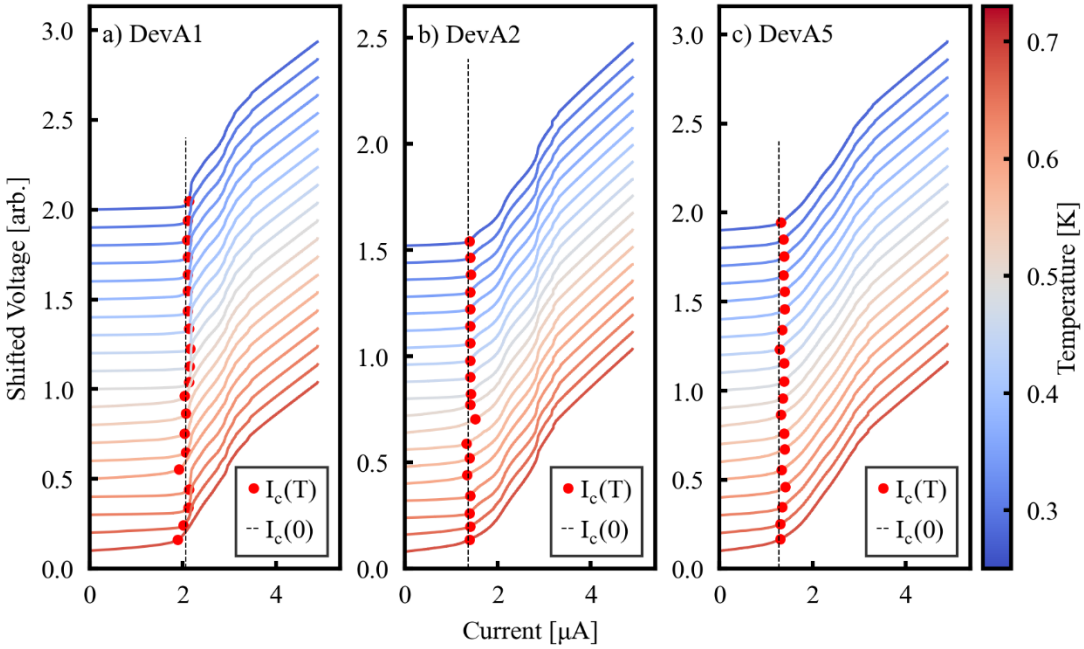

Figure 6.8: Chip A *I-V* characteristics between 68 and 728 mK for a) device A1, b) device A2 and c) device A5. Lines at $I_c(0)$ provided as a guide to the eye.

Figure 6.8a-c show the low temperature results from the LD400 with their voltages shifted in the y-axis direction and truncated at $x = 0$ μA for clarity. As is indicated by the $I_c(0)$ guidelines, I_c does not significantly deviate in this temperature range.

It was possible to extract critical currents closer to T_c for device A5 from preliminary measurements done in the PPMS. While the system does not provide sufficient noise isolation or low enough temperatures for more stringent tests, I_c can be determined by assigning a cut-off for the rate change in the gradients of the curves.

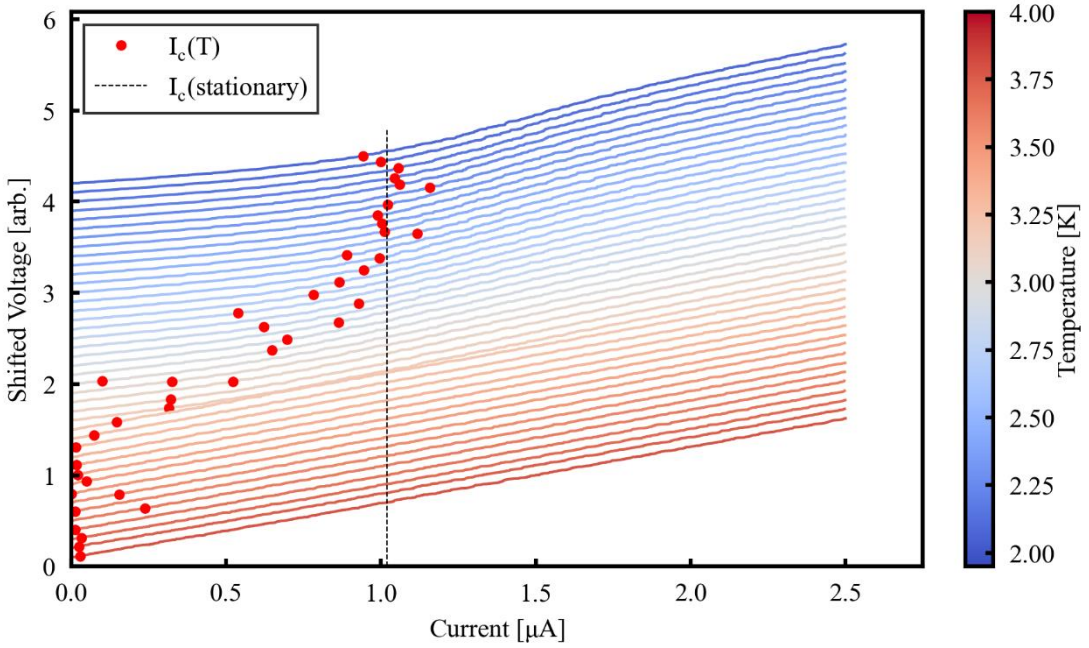

Figure 6.9: PPMS *I-V* characteristics for device A5 between 1.95 and 4 K.

These results are shown in Figure 6.9, with an initially stable region until ~ 2.6 K where I_c decreases until T_c at ~ 3.4 K. Combining these results with the low temperature data in Figure 6.8 we can assert with some confidence that I_c is stationary in between $0 < T \lesssim 0.75T_c$.

$I_c(T)$ data for both transitions present in device A8 is displayed in Figure 6.10, where the critical temperature is clearly much lower in the first transition. The temperature dependence of the energy gap and I_c will allow the distinction between some of the conditions that may cause this.

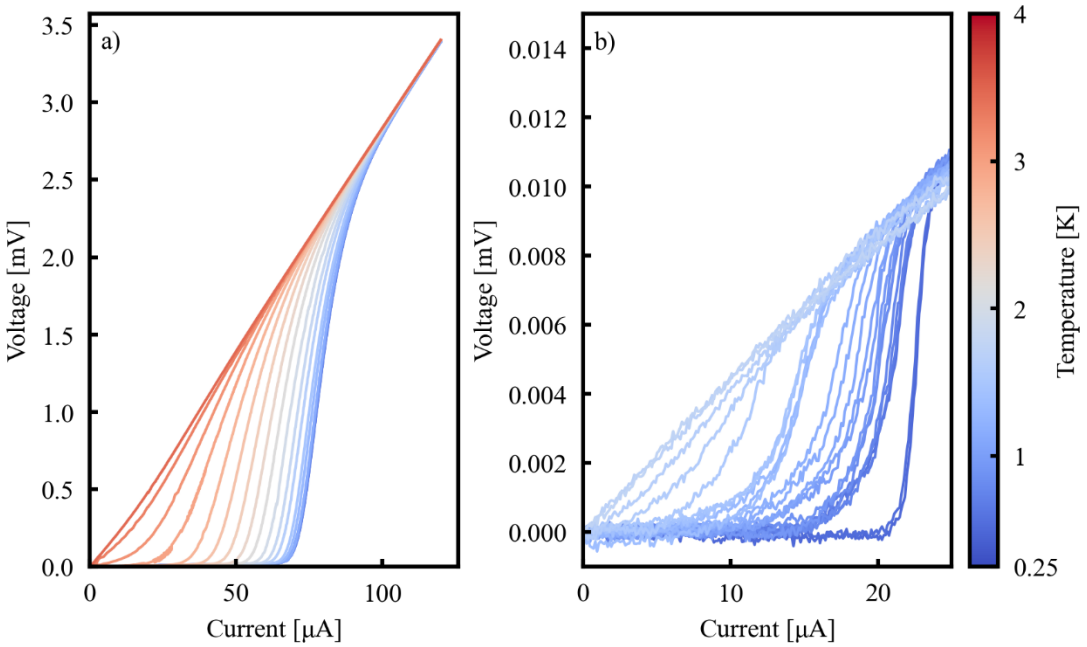

Figure 6.10: $I_c(T)$ data for device A8 , showing a) the full *I-V* sweep and b) a zoomed in region around the lower current transition.

6.3.2 Chip B

The different character of results from the current sweeps performed on the devices of chip B requires different treatment. The procedure for peak tracking, and also a description of the peak types, can be found in Section 5.8. In the plots below, the results are presented with their differential resistance values shifted for each temperature increment for clarity. The tracked peaks are then plotted over the top. It should be noted that the critical current is defined as the top of the peak, which is characteristically different for I_c determined from the chip A *I-V* curves. The normalisation required for the temperature dependence analysis allows for direct and systematic comparison.

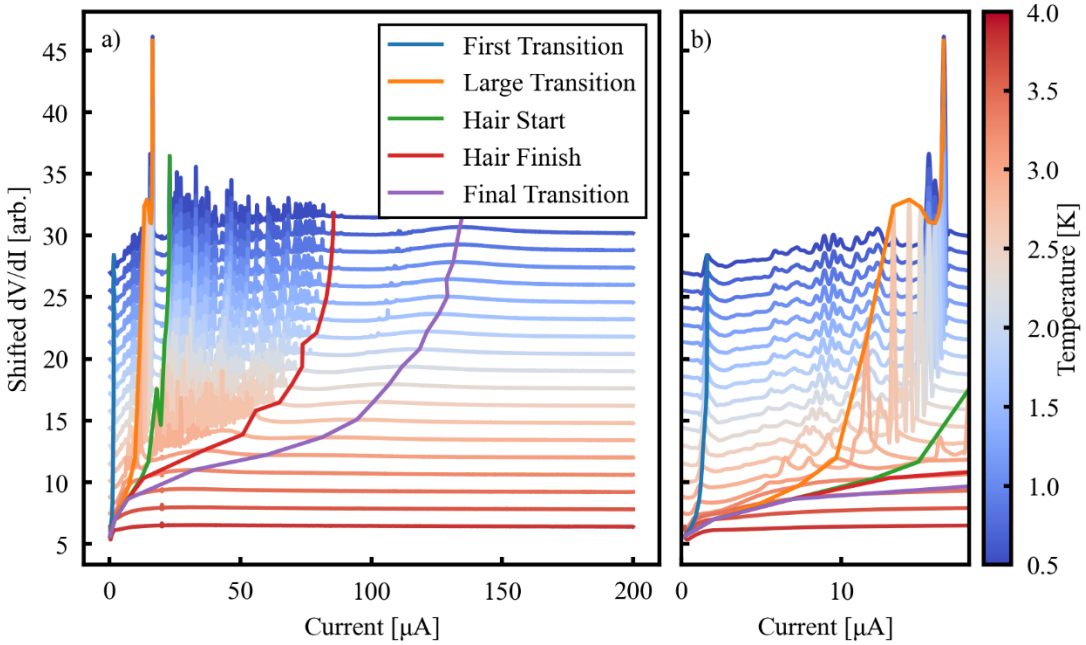

Figure 6.11: $I_c(T)$ differential resistance data for device B1 , with a) the full current sweep with tracked peaks overlayed and b) a zoomed in view of the lowest currents and first transition.

The results for device B1 are shown in Figure 6.11. The fidelity of the peak tracking algorithm was generally good, with the best results being produced for the largest peak. As can be seen in Figure 6.11a, the final peak is both quite broad and has a lower prominence compared to the background, which makes the results slightly more variable. The ability of the algorithm to identify the beginning and end of the hair features also becomes more limited at higher temperatures where peaks have merged into each other and resolution decreases. The tracking appears to follow the character of the various features in the data, as is shown by the zoomed view in Figure 6.11 to Figure 6.14, but limited by the minimum current step length and the loss of resolution at higher temperatures.

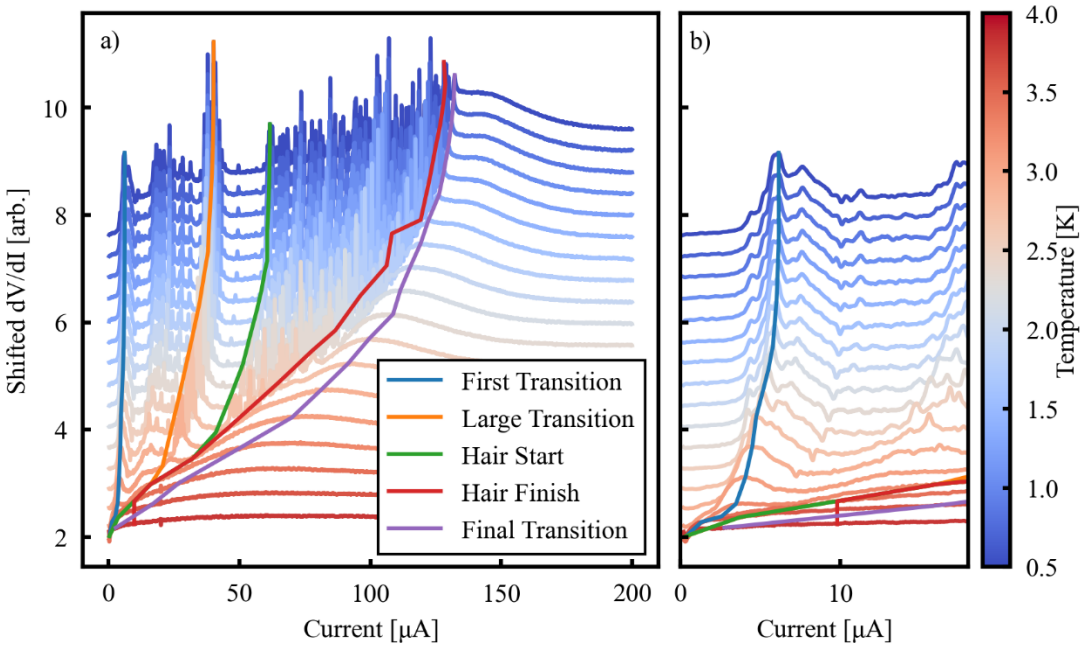

Figure 6.12: $I_c(T)$ differential resistance data for device B3, with a) the full current sweep with tracked peaks overlayed and b) a zoomed in view of the lowest currents and first transition.

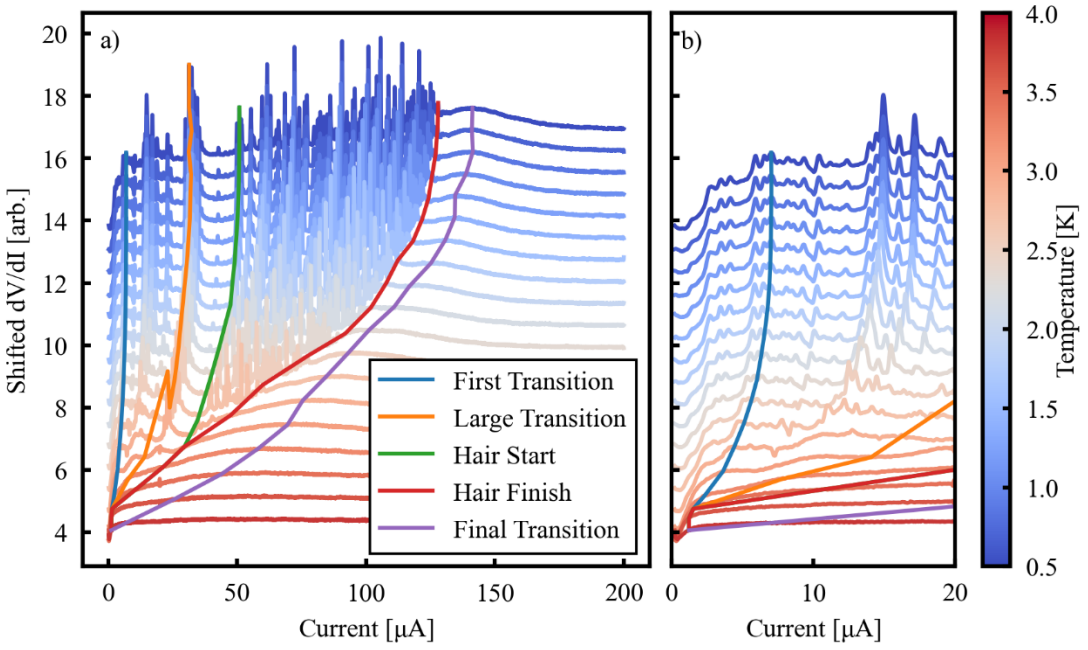

Figure 6.13: $I_c(T)$ differential resistance data for device B4, with a) the full current sweep with tracked peaks overlayed and b) a zoomed in view of the lowest currents and first transition.

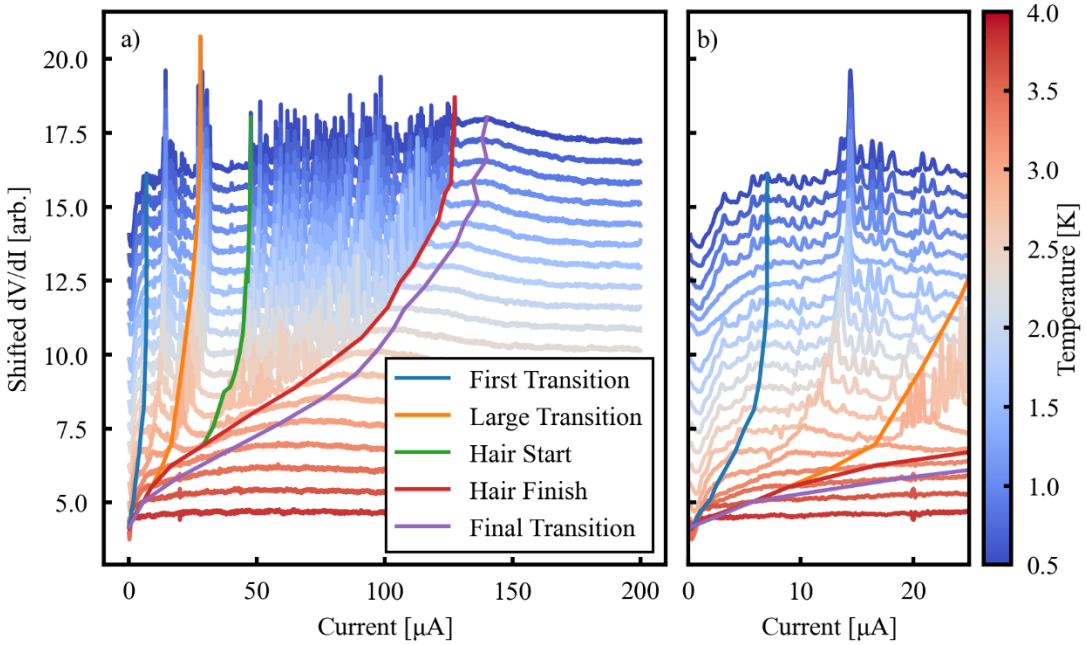

Figure 6.14: $I_c(T)$ differential resistance data for device B8, with a) the full current sweep with tracked peaks overlayed and b) a zoomed in view of the lowest currents and first transition.

Similar peak tracking performance can be noted for devices B3, B4 and B8 shown in Figure 6.12, Figure 6.13 and Figure 6.14. For these devices, the hair features extend on the onset of the final transition.

6.4 TEMPERATURE DEPENDENCE RESULTS AND DISCUSSION

The critical voltages and currents extracted above were then compared to the models presented in Section 6.1. In the case of the chip A devices, as discussed previously, it was not possible to conduct a full suite of measurements on all devices. As such, the low temperature results are presented for devices A1 and A2, and the combined data from the PPMS and LD400 is shown for device A5.

While this situation is not ideal, it does allow certain information to be extracted from normalised plots. It is assumed that T_c and I_c will be approximately the same when measurements are taken with the same device in the PPMS and LD400.

Shown initially without the temperature dependence model for clarity, Figure 6.15 contains the voltage gap results for the combined device A5 data and device A8's two transitions. While the noisier measurements of device A5 have produced a broader spread to the data, the trend is still clear. It is also apparent that both transitions for device A8 show very strong agreement in their voltage gaps.

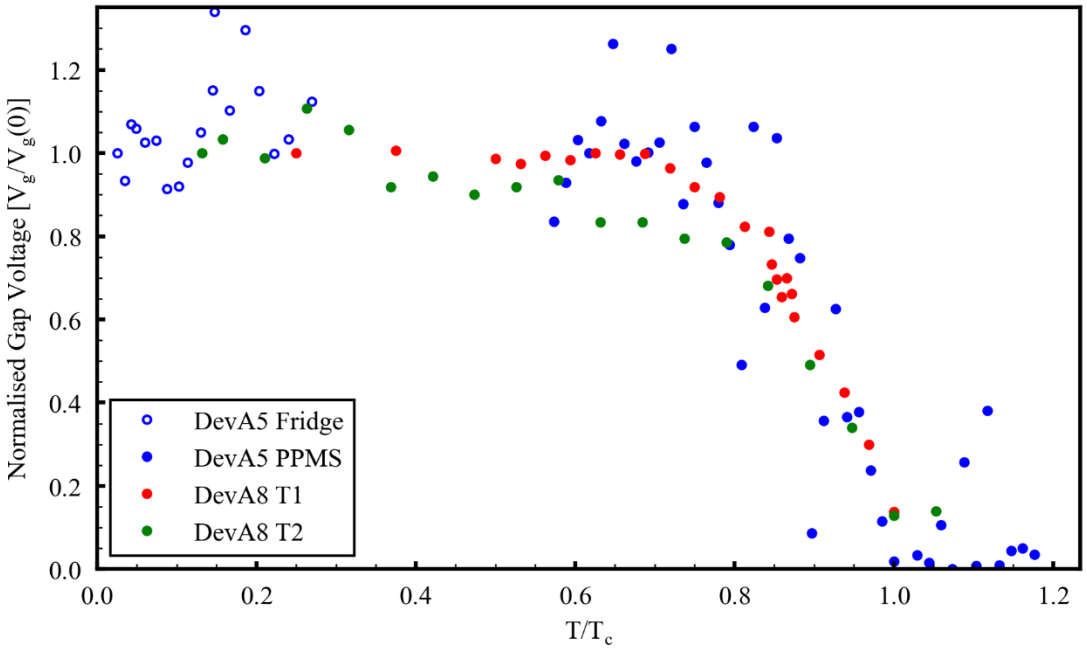

Figure 6.15: Normalised energy gap against temperature normalised to T_c for the chip A devices.

All of the critical currents for the chip A are shown in Figure 6.16. It has been assumed that because devices A1, A2 and A5 are all constriction devices, they will all have similar critical temperatures and have been normalised as such. As

these data only show a stationary I_c up to 728 mK, there is insufficient information to confirm or reject the possibility of the exponential drop off beyond $0.3T_c$. However, even without fitting, devices A5 and A8 clearly do not show this behaviour.

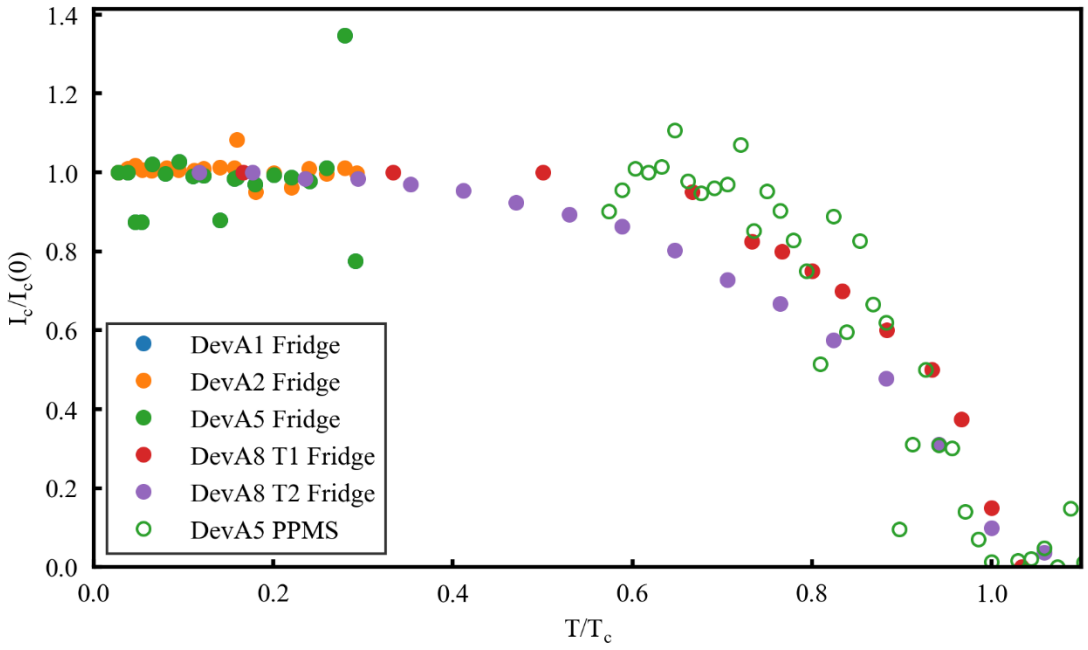

Figure 6.16: Normalised critical currents against temperature normalised to T_c for the chip A devices.

Again, for the sake of clarity and comparison between the different peak types, the results for the chip B devices are initially plotted without the model. Normalised voltage gap values are presented in Figure 6.17. The results for device B1 show remarkable agreement across all peak types, indicating that the different peaks are not likely to be due to departures from a BCS dependency across grains. For the rest of the devices, the first transition provided systematic barriers to reliable extraction of V_g. This is attributed to noise on the voltage measurement, which in the case of the first transition begins to significantly contribute at the required resolution. The hair features for devices B3 and B4 do

seem to show a degree of linearity towards T_c, which might indicate a disruption of BCS behaviour as shown in Figure 6.3 in the work of *Dahlem et al.* [94]. However, it is more likely that this is simply due to the issues inherent in accurately tracking these peaks as they merge and decrease in prominence with increasing temperature.

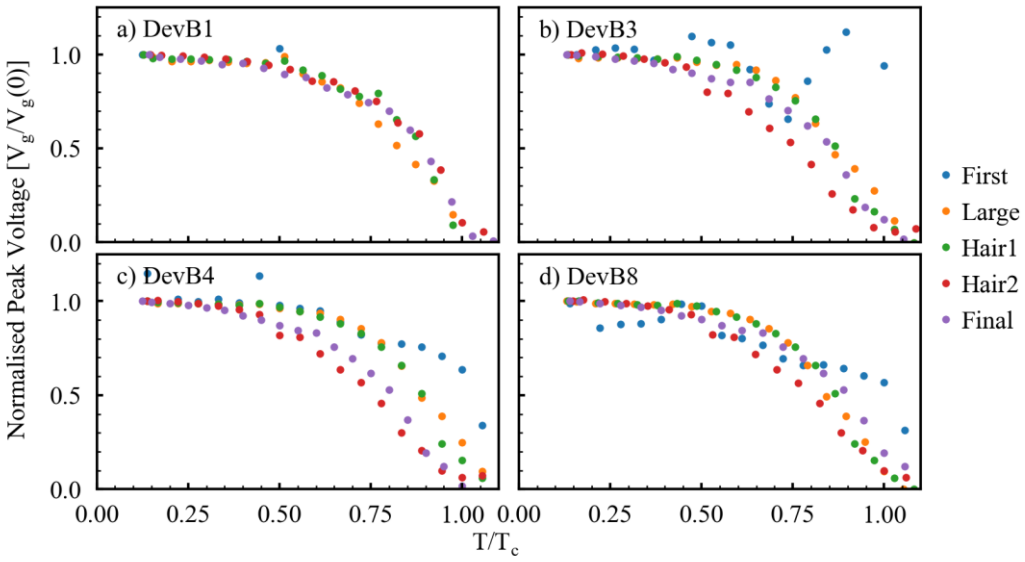

Figure 6.17: Normalised energy gap against temperature normalised to T_c for the chip B devices with a) device B1, b) device B3, c) device B4 and d) device B8.

The $I_c(T)$ data plotted in Figure 6.18 again show a high correlation across peak types for device B1, including the less reliable first, final and transitions at the end of the hair features. There is consistent behaviour with the end of the hair features and final transition producing a more linear response in the other devices, but again the limitations of the peak tracking algorithm for these regions cannot be discounted due to the merging of peaks and reduction of peak prominence. Manual verification of the peak values is also difficult for these reasons. In general, the first, largest and onset of the hair features show strong agreement across all devices.

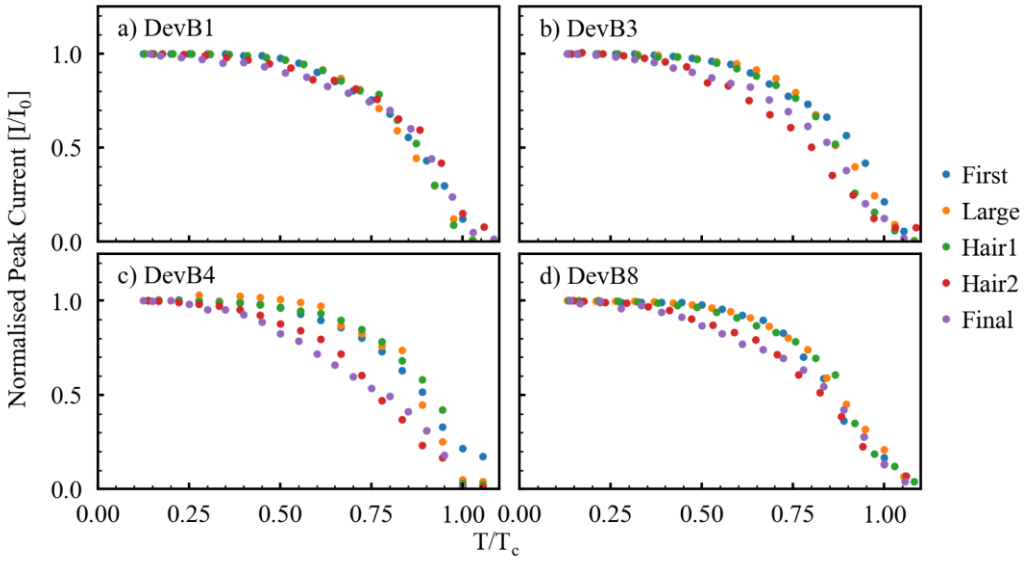

Figure 6.18: Normalised critical currents against temperature normalised to T_c for the chip B devices with a) device B1, b) device B3, c) device B4 and d) device B8.

With the considerations outlined above, it was decided that the largest peak is likely representative of the behaviour of the voltage gap and the critical currents for all peaks across all chip B devices. The results of plotting the normalised voltage gap against the BCS energy gap model (Equation (6.2)) for all devices is shown in Figure 6.19. It is clear that all devices, regardless of type and geometry, agree with the model indicating that their response is consistent with standard BCS theory. It might have been expected that the different geometries could introduce different grain sizes and therefore potentially different boron doping concentrations as the limiting factor in the critical current density, but this effect is absent. The conformity to the BCS energy gap model is probably an indication of a high uniformity in doping across the grain size distribution.

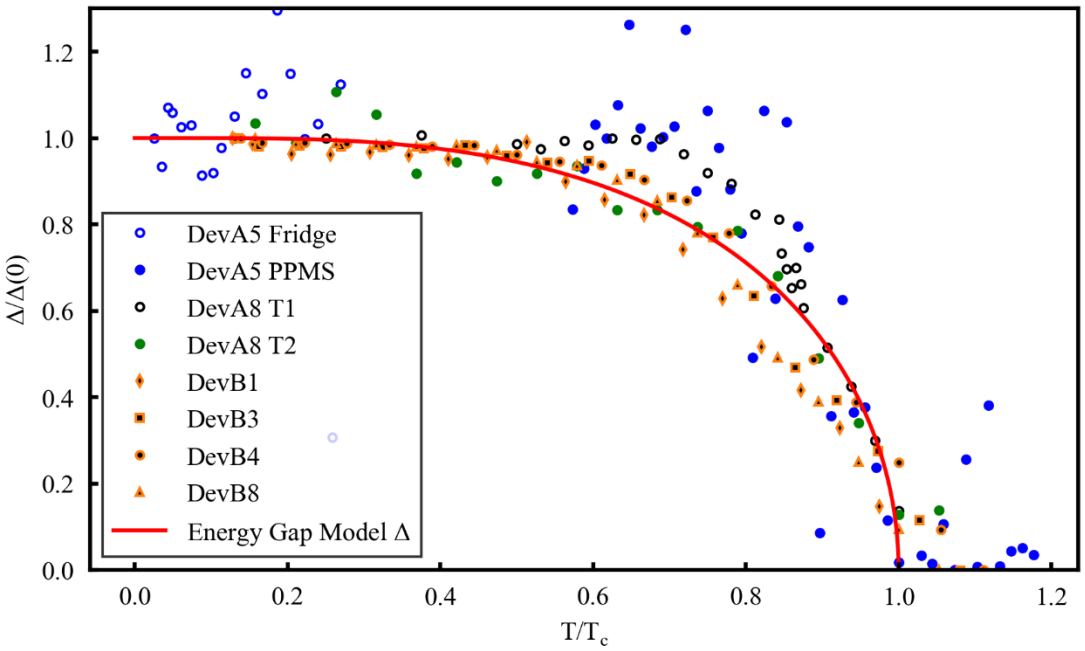

Figure 6.19: Plotting all devices and against the BCS energy gap $\Delta/\Delta(0)$ model , with the largest peaks for the chip B devices used as the most accurate and generally representative.

The $I_c/I_c(0)$ results for all devices plotted with the *Ambegaokar-Baratoff* model (Equation (2.45)) are presented in Figure 6.20. Again, all devices regardless of type and geometry fit this model. Recalling that there are three types of junction present, it is possible to draw some conclusions about the mechanisms governing the behaviour of all B-NCD junctions with a high degree of confidence. Devices A8 and B8 are gap junctions and being of the SIS type would be expected to follow the standard *Ambegaokar-Baratoff* model. The rest of the junctions would conventionally be thought of as either long or short limit SNS junctions, with the point contact in device B4 being the only device to approach this short limit. However, all of these devices show approximately the same temperature dependence, which means that all are governed by the same L/ξ_n ratio. This would have to be in the extreme short limit $L/\xi_n \to 0$, where the SNS behaviour is in the clean limit for a point contact where the length scales are shorter than

the electron mean free path [59]. Given the fabricated geometry of the junctions, this is only possible if the grains or sub-granular structures are governing the transport behaviour.

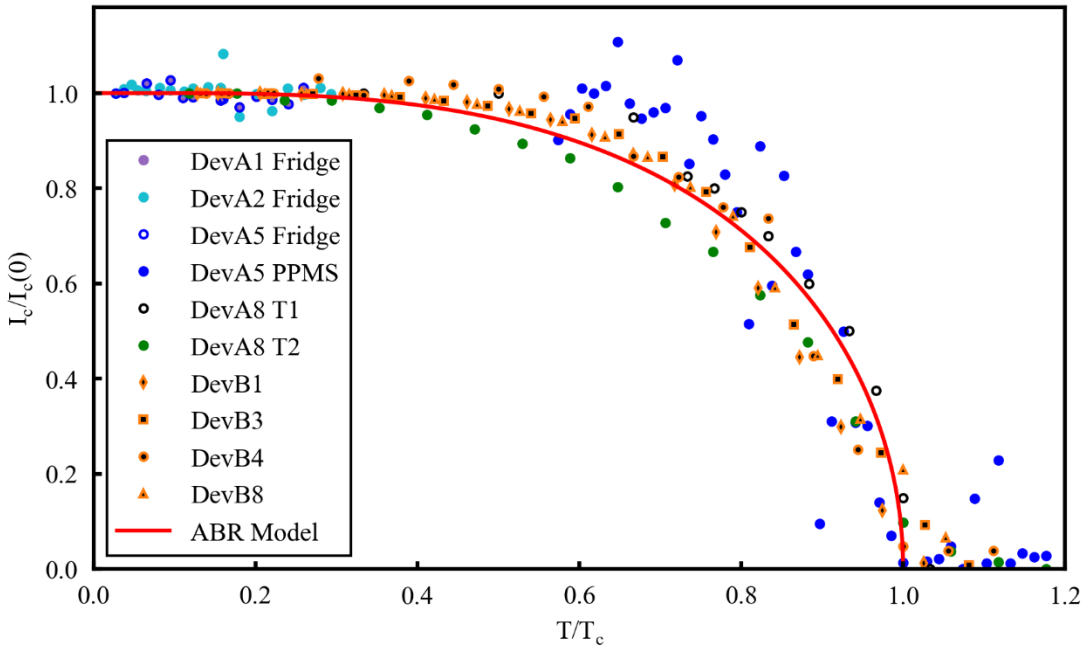

Figure 6.20: Plotting all devices and against the *Ambegaokar-Baratoff* $I_c/I_c(0)$ model, with the largest peaks for the chip B devices used as the most accurate and generally representative.

Given that is also not possible to delineate between the behaviour of the SNS and SIS junctions, it is likely that all are simply dominated by effects due to the grains.

6.5 CONCLUSION

Various aspects of the temperature dependence of B-NCD films and devices have been probed. First, by using fluctuation spectroscopy it has been possible to confirm that the three-regime response from Equation (6.4) in conduction fits to $R(T)$ measurements of a B-NCD film also matches the response to the smaller geometry of the junction devices. The results also agreed with previous work by *Klemencic et al.* and others. The coherence length within the grain ξ_g and tunnelling between grains ξ_t were also extracted from the fluctuation spectroscopy fits. Some signs of convergence are noted between these values at the sample geometry is reduced, but further investigation with additional structure sizes is required to confirm the trend. Given that the tunnelling coherence length must account for Cooper pair interaction with grain boundaries, we might assume that this affords an additional approximation for the coherence length in the normally conducting material in the film $\xi_t \approx \xi_n$.

Next, the temperature dependence of the voltage gap and critical currents for the devices was performed. This was also an opportunity to investigate some of the properties of the different peak types present in both devices A8 and all devices on chip B. As the behaviour of all of these peaks is effectively the same (allowing for the difficulties in peak tracking), it can be stated that the same physics is governing each of them.

Finally, the voltage gap and critical currents were compared to dependencies expected from BCS theory and the *Ambegaokar-Baratoff* relation with approximately the same dependence was noted in all devices and peaks. Recalling the discussion from Section 6.1, this indicates that all junction are behaving as if governed by formulas for SIS or very short SNS junctions. Recalling the definition for the dirty and short limit of an SNS junction $L \approx \xi_n$,

the length scales would imply that the junction lengths are less than $\xi_n \approx 3$ nm. Even considering the approximation $\xi_t \approx \xi_n$, the junction lengths do not fulfil this criterion. Given the various types and geometries measured, it can therefore be stated that B-NCD Josephson junctions have temperature dependences dominated by lengths only explainable by the grain size distribution and sub-grain structures rather than the geometries fabricated here.

7 MAGNETIC FIELD DEPENDENCE OF B-NCD JOSEPHSON JUNCTIONS

7.1 INTRODUCTION

As discussed in Section 2.4, B-NCD is a type-II superconductor subject to an upper critical field of up to 7 T [3,193]. Between the lower and upper critical fields of type-II superconductors, an applied magnetic field penetrates the superconductor in the form of vortices which form a regular lattice. Similar to the effects of temperature on the coherence and percolation of superconductivity in granular systems, starting from a superconducting film, the introduction of an increasing magnetic field will initially disrupt inter-grain phase locking and eventually penetrate through the grains until phase cohesion is completely lost and superconductivity ceases at the higher critical field.

For a Josephson junction, the area of the weak link perpendicular and transparent to the field will govern the majority of the effects on the critical current. A basic schematic of a junction is shown in Figure 7.1. For a rectangular junction, the magnetic field will partially penetrate into the superconducting electrodes with

an additional length λ_L, the London penetration depth. An order of magnitude estimate for the London penetration depth is given by, $\lambda_L = \sqrt{m/\mu_0 n e^2} = 170$ nm where e and m are the electron charge and mass and the doping concentration $n = 10^{21}$ cm^{-3} is used as the minimum value for these films. As mentioned previously, measured penetration depths for single crystal boron doped diamond have been observed at approximately $\lambda_L \approx 0.2 - 1$ μm [196,197]. For B-NCD, much larger values of $\lambda_L \approx 2 - 4$ μm have been reported [105].

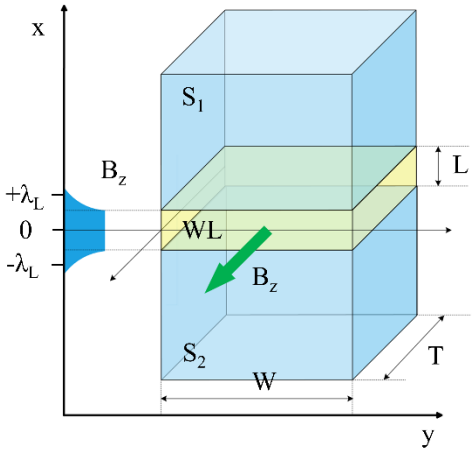

Figure 7.1: Schematic diagram of the components of a Josephson junction with incident field B_z between superconducting electrodes S_1 and S_2 with weak link WL. Here, the film thickness is T, the junction width is W and the length is L, which is modulated by an additional factor of plus or minus the penetration depth λ_L.

The magnetic behaviour of junctions can be split into two classifications that are determined by their geometry relative to λ_L. For "short" junctions where $W \lesssim 4\lambda_L$, the standard oscillatory response in increasing field is expected. Given the parameters outlined above and previously for the junction devices, all fabricated geometries fall into this short limit category.

7.2 INITIAL RESULTS

As discussed in Section 5.4, chip B and its devices were measured in a setup that allows for varying the magnetic field normal to the device geometry. All measurements were conducted at a temperature of 500 mK, which ensures that the devices are isothermal across the whole current range. Current sweeps were taken at field values at 25 mT increments between 0-250 mT, and steps of 250 mT thereafter up to 4 T. It should be noted that this change in increment gives the illusion of additional character in some of the plots below. Section 5.8 explains how the peaks in the differential resistance data are tracked across datasets. The results of this are presented below.

Figure 7.2 shows these results for device B1. The tracking algorithm has generally performed well. It should be noted in this case, and across the other devices, the difficulty in accurately tracking the final peak. This is simply due to the fact that the peak is very broad and lacks prominence compared to the background. Although visual inspection of these tracked values indicates a reasonably good agreement with the data, the results should not be considered perfectly reliable. Similarly, tracking the end of the "hair" features is prone to systematic inaccuracy due to the vanishing of some of these features with increasing field. The first transition tacking in Figure 7.2b shows good agreement to the data, although at the highest fields some inaccuracy is noted. The large transition, having the most prominent peaks, is the most accurate across datasets.

Device B3, as shown in Figure 7.3, shows similar performance to the previous device. The first and largest transitions, as well as the onset of the hair features, are relatively well tracked while the other transitions suffer somewhat from blending into background and neighbouring features. However, the first few datasets at the lowest field values have the most accurate tracking. Devices B1

and B3 are both constrictions of similar dimensions so would be expected to show similar responses in differential resistance and magnetic field dependence, which is what is observed (shown later in Figure 7.19).

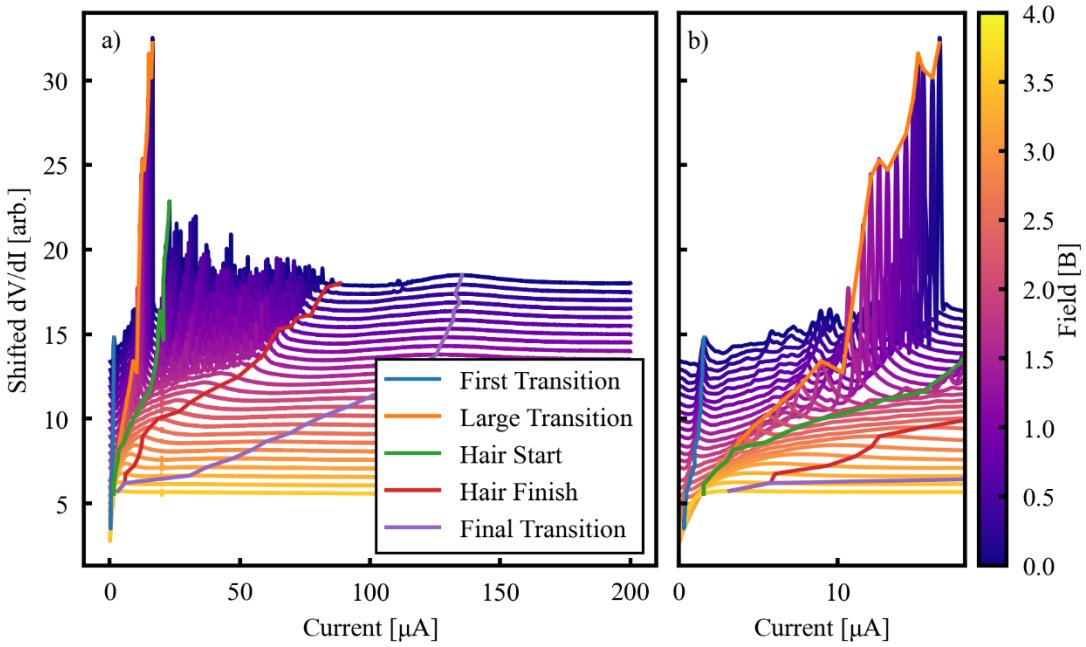

Figure 7.2: Differential resistance data for device B1, with a) the full current sweep with tracked peaks overlayed and b) a zoomed in view of the lowest currents and first transition.

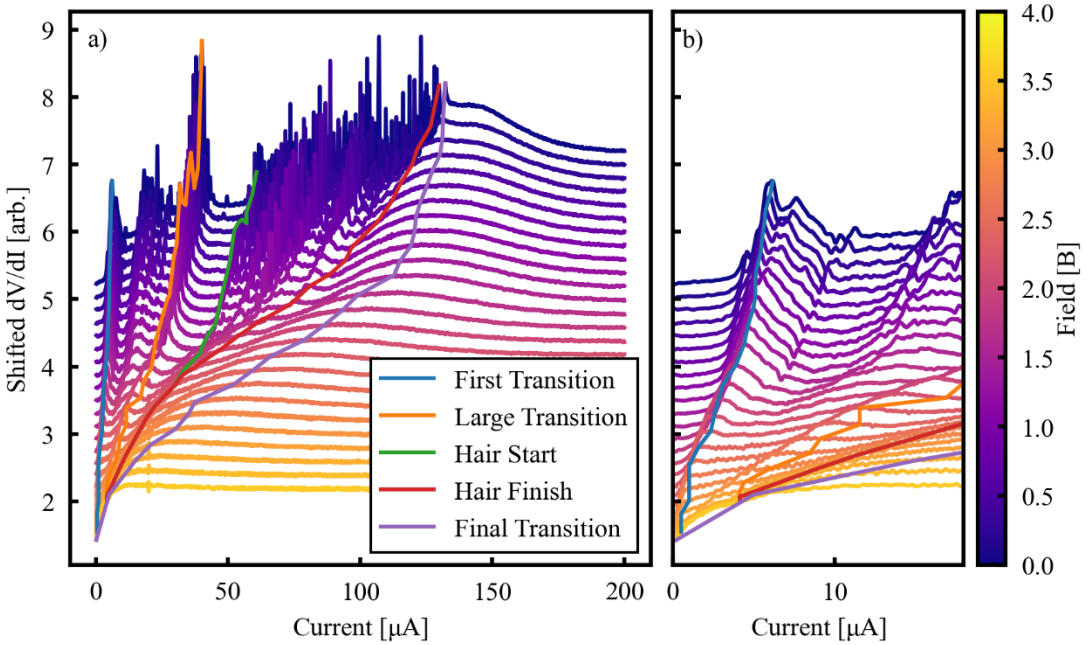

Figure 7.3: Differential resistance data for device B3, with a) the full current sweep with tracked peaks overlayed and b) a zoomed in view of the lowest currents and first transition.

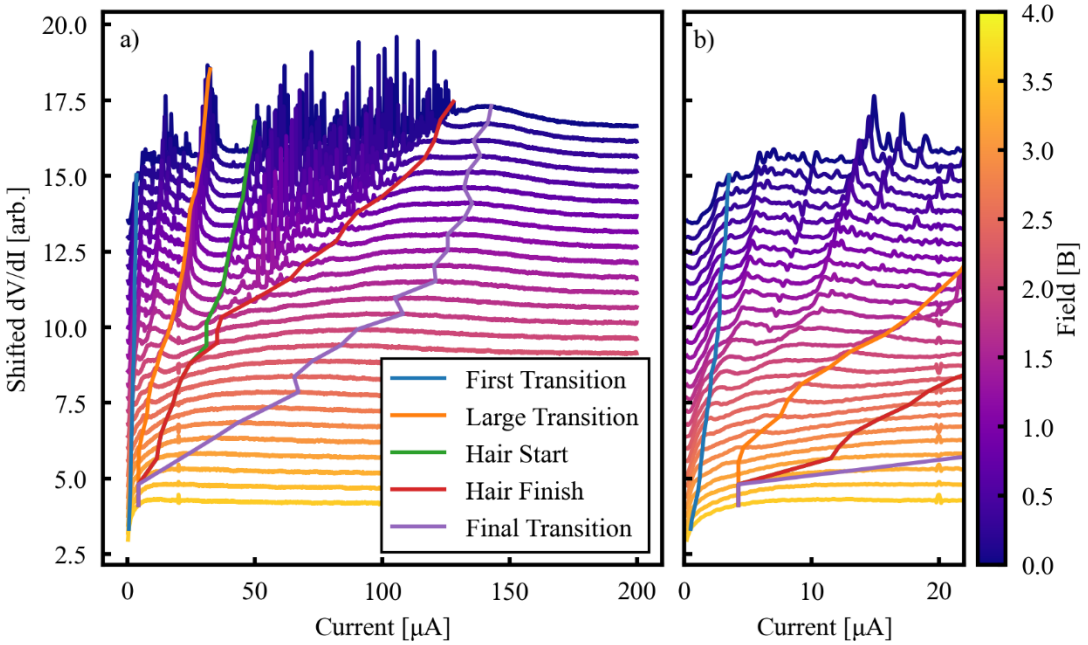

Figure 7.4: Differential resistance data for device B4, with a) the full current sweep with tracked peaks overlayed and b) a zoomed in view of the lowest currents and first transition.

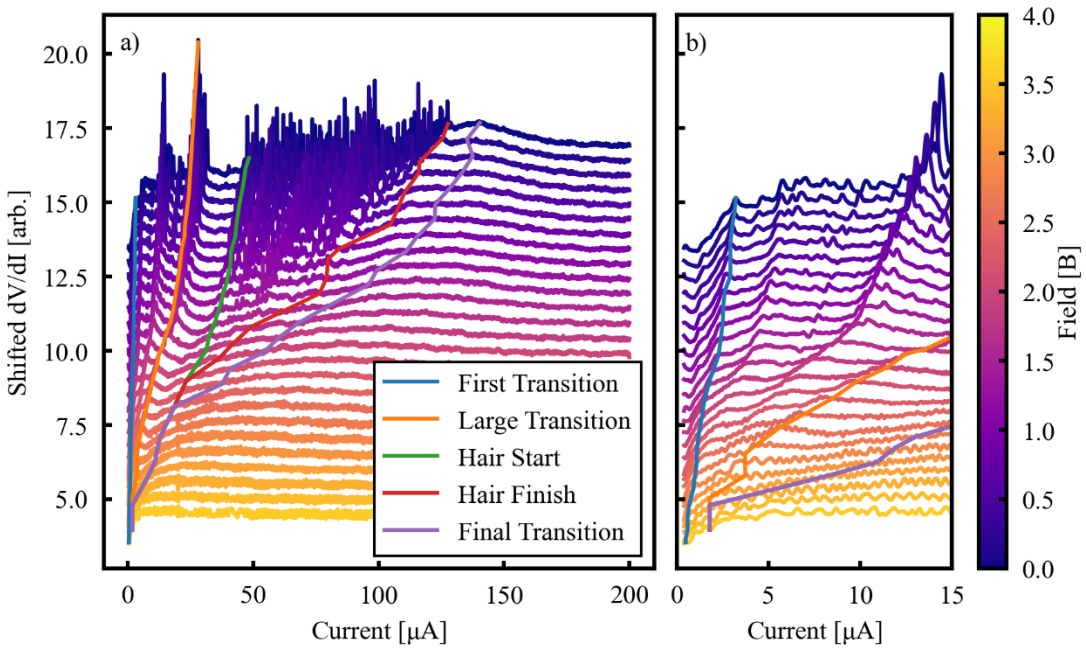

Figure 7.5: Differential resistance data for device B8, with a) the full current sweep with tracked peaks overlayed and b) a zoomed in view of the lowest currents and first transition.

Device B4, the point contact, shows a broadly similar response in differential resistance and the visual character of the tracked peaks with increasing field. Figure 7.4 shows this and highlights the general difficulty in tracking the final peak with a more meandering track through the field datasets.

Across the two chips there were three devices with an insulating gap. Device B8 is an SIS device with a gap of 75 nm, with $I_c(B)$ results shown in Figure 7.5. The peaks are again well tracked by the algorithm.

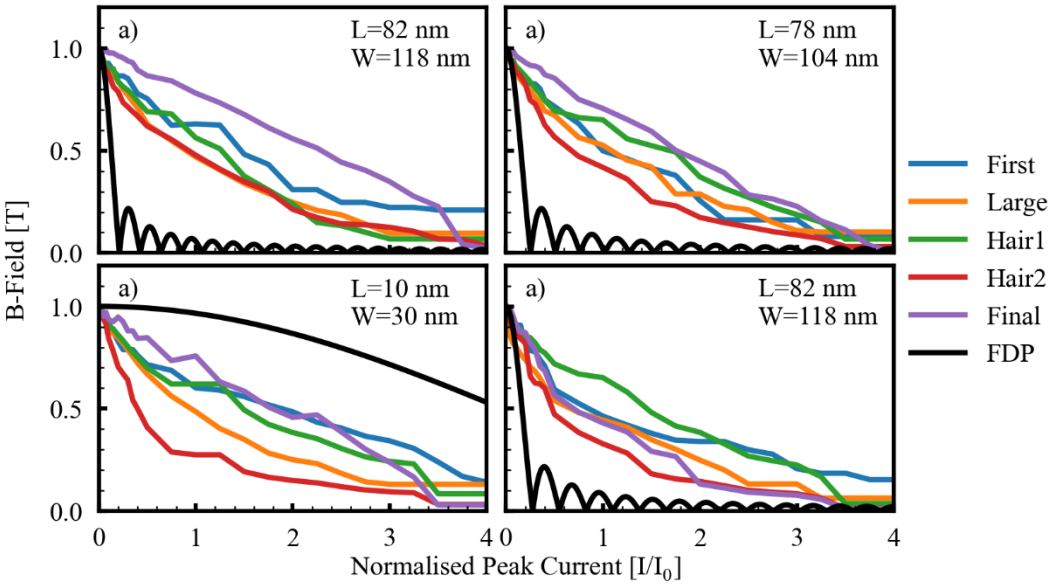

Figure 7.6: The normalised $I_c(B)$ data for all transitions across all devices do not match with the Fraunhofer diffraction pattern (FDP) created from the geometry of the devices, shown in the top right of each subplot. Devices shown are a) Device B1, b) device B3, c) device B4, where a nominal width of 10 nm is used to approximate the point contact, and d) device B8.

Theoretically, fitting the normalised $I_c(B)$ data of the peaks would provide some inference of the active or magnetically transparent junction geometry. For a junction in the short limit, $I_c(B)$ is expected to follow a dependency described by a Fraunhofer diffraction pattern as discussed previously and parameterised in Equation (7.1). Assuming rectangular junctions with geometries equal to those fabricated for the devices, oscillations are expected in the range of fields measured. However, when this analysis is performed (results in Figure 7.6) there is clearly no correlation between the tracked peaks of any device and the Fraunhofer diffraction pattern calculated from their respective geometries. It is clear that these devices do not exhibit behaviour that is well described by a standard Fraunhofer diffraction pattern. Even with the decrease in field step size

at the lowest fields, that might have captured oscillations <250 mT, typical oscillations are not observed. The general character of the normalised $I_c(B)$ at low field is significantly different, showing an immediate drop off similar to a power law.

7.3 A MODEL BASED ON GRAINS AND THEIR BOUNDARIES

B-NCD films are comprised of columnar grains resulting from highly nucleated growth from the seeds. This growth results in a disordered system with different sized grains, grain boundaries and voids. As the thickness of a film increases, grains have a slight lateral spread and so faster growing grains dominate at the surface, producing a positive correlation between film thickness and the number of large grains at the surface [6]. An SEM image of these disordered grains is shown in Figure 7.7a.

The superconducting system can therefore be modelled as a series of approximately columnar polygonal grains with grain boundaries parallel to the growth direction (shown in Figure 7.7b), with the macroscopic supercurrent travelling in plane with the film and across grains and their boundaries [198]. Thus, irrespective of any fabricated junction geometry, the superconducting circuit consists of several structures of note. Firstly, the grains themselves each with individual j_c values due to their size and boron incorporation [86,93–95].

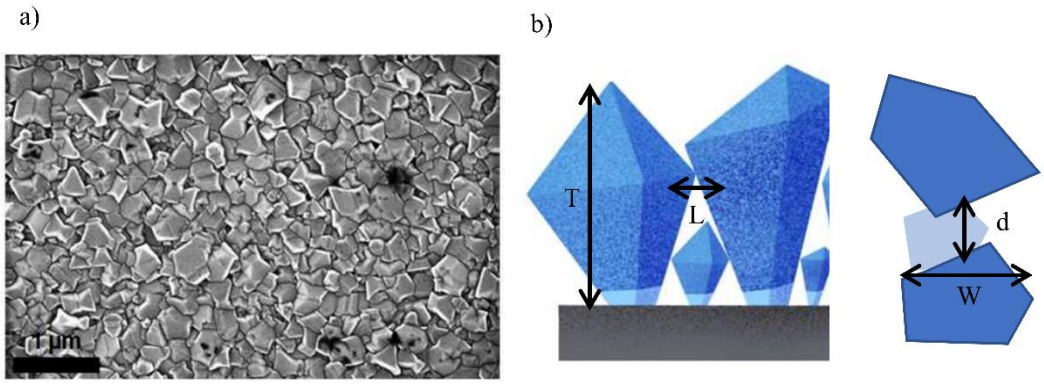

Figure 7.7: Grain geometries a) An SEM of a B-NCD film showing the disordered grains at the surface of the film [98] and b) side (left) and top down (right) schematics of the lengths in the grain system with film thickness *T*, grain separation *L*, width *W* and length *d*.

The grain boundaries, with graphitic and disordered carbon showing metallic-like conductivity [92] and sizes of the order of a nanometre [199]. Additionally, throughout the thickness of the film it's likely that voids are present. The small value of the superconducting coherence length in B-NCD of $\xi \sim 10$ nm suggests that consideration of these smaller barriers is prudent [93]. The thickness and composition of the barriers will influence the local critical current density of the film and determine the temperature and field dependence. The existence of barriers with these dimensions will disrupt phase coherence, which occurs irrespective of the junction type [200]. Although it has been observed that the grain boundaries in B-NCD are approximately parallel to the growth direction [94], it should also be considered that these barriers will not be rectangular, but polygonal and with varying angles with respect to field.

As stated previously, the standard Fraunhofer diffraction pattern that typically describes the behaviour of critical currents in a Josephson junction is given by:

$$I_c(B) = J_m L_T \left| \frac{\sin(\pi B L_T W/\Phi_0)}{\pi B L_T W/\Phi_0} \right|, \tag{7.1}$$

where B is the flux density, Φ_0 is the flux quantum, $L_T = L + 2\lambda_L$ is the total field penetration distance and W is the width of the barrier. The first obstacle of this system of randomly oriented barriers is in accounting for their orientation to the field. *Peterson and Ekin* propose a model which describes this system of disordered polygonal barriers [200]. A summary of the mathematical treatment of their analysis is as follows. The evolution of the phase difference ϕ along the plane of the barrier is given by:

$$\frac{\Phi_0}{2\pi L_T} \nabla\phi = \hat{n} \times \boldsymbol{B}, \tag{7.2}$$

with the flux density in plane with the barrier given by $\boldsymbol{B}$ and $\hat{n}$ is the unit vector normal to the barrier. Integration of Equation (7.2) and substitution into Equation (2.39) gives:

$$J(x) = J_m \sin\left(\frac{2\pi B L_T x}{\Phi_0} + \phi_0\right), \tag{7.3}$$

Taking an ellipse to be a reasonable approximation to the polygonal shape of the barriers in the system, we can recall the area of an ellipse πab, where the a and b are the lengths of the semimajor and semiminor axes, and the equation describing any point on the ellipse is:

$$\frac{x^2}{a^2} + \frac{y^2}{b^2} = 1. \tag{7.4}$$

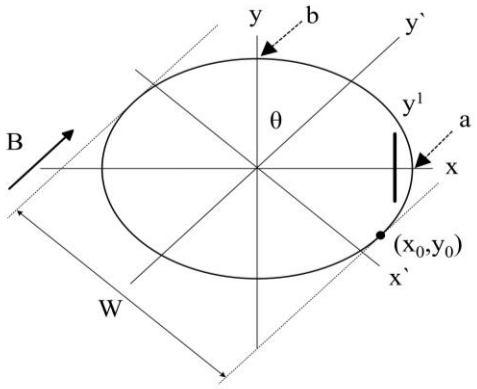

Figure 7.8: Representation of an elliptical barrier in a Josephson junction. Field B is parallel to the plane of the diagram at an angle θ from the principal axis.

A diagram of this geometry is shown in Figure 7.8. With a magnetic field B applied in the direction y' at an angle θ, and incorporating Equation (7.3), the current through the barrier is given by

$$I = J_m \int_{-a}^{a} dx \int_{-y_1}^{y_1} dy \sin\left(kx' + \phi_0\right) \tag{7.5}$$

where $y' = b(1 - x^2/a^2)^{1/2}$, $k = 2\pi B L_T/\Phi_0$ and $x' = x\cos\theta - y\sin\theta$. In order to determine the effective width W of the ellipse normal to the field, the slope at a point (x_0, y_0) is found. This is given by $dy/dx = \cot\theta$. Using

$$S = \left(b^2\cos^2\theta + a^2\sin^2\theta\right)^{1/2} \tag{7.6}$$

we find that $x_0 = (a^2/S)\cos\theta$ and $y_0 = -(b^2/S)\sin\theta$. This provides $W \equiv 2x_0^{'} = 2S$ given that $x_0^{'} = x_0\cos\theta - y_0\sin\theta$. Using the substitution $x = a\cos\alpha$, integration of Equation (7.5) gives

$$I = \frac{aJ_m}{k_s}\int_0^{\pi} d\alpha \sin\alpha\,[\cos(k_c a\cos\alpha - k_s b\sin\alpha + \phi_0) - \cos(k_c a\cos\alpha + k_s b\sin\alpha + \phi_0)] \tag{7.7}$$

where $k_s = k\sin\theta$ and $k_c = k\cos\theta$. Combining $\tan\gamma = (a/b)\cot\theta$ and Equation (7.6) leads to:

$$k_c a\cos\alpha \pm k_s b\sin\alpha = kS(\gamma \pm \alpha). \tag{7.8}$$

This allows the expression of the cosine terms in Equation (7.7) as an infinite series of Bessel functions. Given that only the first order terms (J_1) persist after integrating Bessel functions, Equation (7.7) becomes:

$$I = 2\pi abJ_m\frac{J_1(kS)}{kS}\sin\phi_0. \tag{7.9}$$

Given that:

$$kS = \frac{2\pi BL_T}{\Phi_0}\frac{W}{2}, \tag{7.10}$$

and assigning $A = ab$ (the area of the junction) it is possible to complete the derivation with a function incorporating a first order Bessel function that describes an Airy diffraction pattern.

$$I_c(B) = J_m A \left| \frac{J_1(\pi B d L_T W/\Phi_0)}{\pi B L_T W/\Phi_0} \right| \tag{7.11}$$

This function from *Peterson and Ekin* is insensitive to the orientation of the field and allows for approximation of the polygonal nature of grains, their boundaries and other small features in the film. A comparison of the Airy and Fraunhofer diffraction patterns is shown in Figure 7.9, where a more rapid suppression of the peaks with increasing field can be noted.

Due to the standard diffraction pattern not fitting the data, a new model is proposed. Several examples from previous works exist where similar granular systems have been modelled by an averaging or integration across contributions from feature sizes and relative orientations to the incident field [179,200–204]. Considering the system of grains, grain boundaries and voids described previously, it is assumed that these features may be acting as barriers forming a network of junctions through the devices. When considering the macroscopic field dependence of the devices, the contributions from this network of barriers will be averaged across barrier size and orientation to the field. Equation (7.11) is insensitive to field orientation, so only the size of the barriers must be determined.

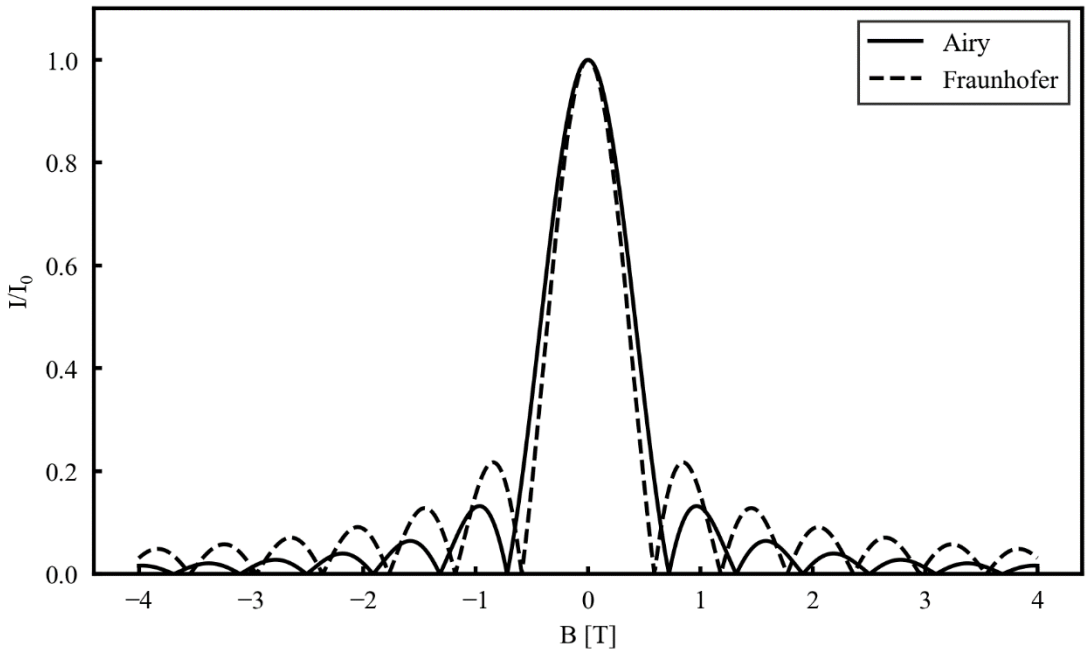

Figure 7.9: Comparing the Airy and Fraunhofer diffraction patterns.

Initial probes of this system reveal that results are highly dependent on the distribution of barrier sizes, with a low number of samples from a normal distribution of grain sizes producing wildly varying results depending on the sizes sampled. The Airy diffraction pattern function takes the length and width of the junction as parameters, so it was decided that one dimension would be set to the grain size distribution and the other a combination of gaussian functions. This allows generation of information about the length of features that contribute to active junction geometries that are not fully described by the grain size distribution, i.e., grain boundaries and voids. Integration across these dimensions to fit to normalised $I_c(B)$ is done computationally. First, feature size samples are generated from the distributions describing each dimension. These are then averaged and fed into Equation (7.11).

7.3.1 Monte-Carlo Metropolis Sampling

With an established probability density function (PDF) describing the frequency of grain sizes across a film it is necessary to create a method to choose discrete points from this distribution, known as sampling. The NumPy package in Python has built in functions that allow this for various standard distributions but producing truly random and accurate samples from a PDF based on a complex function is non-trivial.

One approach for doing this is the inversion method. This involves finding the corresponding cumulative density function (CDF), F_X, for a given PDF of a variable X by integration. F_X takes the input x and outputs the probability that X will take a value less than or equal to x.

$$F_X(x) = P(X \leq x), \text{for all x} \in \text{R} \tag{7.12}$$

As a probability, this output value is between 0 and 1. Therefore, the inverse function $F_X^{-1}(u)$ can take a uniformly distributed value u as an input with $u \sim U(0-1)$ to find x.

$$F_X^{-1}(u) = x \tag{7.13}$$

It is then possible to use built-in uniform random number generators to generate samples x. While this method is conceptually simple and straightforward to implement for certain functions, it faces limitations because not all functions have an inverse and calculating integrals is sometimes intractable, even computationally.

It is also possible to model and sample a more complex PDF with Metropolis-Hastings (MH) Markov Chain Monte-Carlo (MCMC) methods [205–208]. A Markov Chain is a stochastic process for determining a sequence of events or states $X_0, X_1, X_2 \ldots X_t$, where the current state is determined from the previous state. The probability of a new state depends only on the previous state. X_t converges to the target PDF π such that if $X_t \sim \pi(x)$, then $X_{t+1} \sim \pi(x)$. Ideally, the resulting chain is ergodic, i.e., it will eventually visit all parts of the system, with the trajectory of the process representing the average behaviour of the system.

The states on the chain represent samples from the distribution, and the more states recorded on the chain the closer it will resemble π. Navigating in time t between steps in the chain requires a transition kernel, Q. In the case of a MH algorithm, this transition kernel is also known as the proposal distribution i.e. the distribution of possible transitions that may be chosen as an approximation of π. In choosing a new state y given the current state of the chain x, we can write $Q(y|x)$ where Q is a distribution on y given x. The acceptance probability is given by A as follows:

$$A = min\left\{\frac{\pi(y)}{\pi(x)}\frac{Q(y|x)}{Q(x|y)}, 1\right\}. \tag{7.14}$$

Algorithm 9.1: Metropolis Hastings MCMC

Initialise: $X_1 = x_1$

for $t = 1, 2\ldots$

1 **Generate** $Y_t = Q(y|x_t)$

2 **Take** $X_{t+1} = \begin{cases} Y_t, & \text{with probability } \rho(x_t, Y_t) \\ x_t, & \text{with probability } 1 - \rho(x_t, Y_t) \end{cases}$

where $\rho(x, y) = \min\left\{\frac{\pi(y)}{\pi(x)}\frac{Q(y|x)}{Q(x|y)}, 1\right\}$

The random walk MH algorithm is a special simplified case where π is approximated with as little prior knowledge as possible and the proposal distribution is symmetrical where $Q(y|x) = Q(x|y)$. The designation of *random walk* refers to a local exploration of π which infers that the scale of the proposal distribution, and thus the possible step size between X_t and X_{t+1}, is important. The symmetrical condition reduces the acceptance probability to:

$$A = \min\left\{\frac{\pi(y)}{\pi(x)}, 1\right\}. \tag{7.15}$$

Examples of suitable symmetrical proposals are the normal or uniform distributions. Such an algorithm is favourable because it allows for a general case, but additional tuning is required.

A classic toy example of this system is "island hopping", where a person is visiting an island chain and needs to decide which island to visit next. Each day the person picks a neighbouring island and if the island has a larger population than the current island, the person will move to this neighbouring island. If the population of this potential new island is less than the current island, they will choose to move with a probability of $p = p_{\text{neighbour}}/p_{\text{current}}$. Thus, with sufficient total days the person spends time on the islands proportional to their population and allowing an estimation of the distribution of island populations. This potentially very long, but accurate, Markov Chain is referred to as the stationary distribution.

There a several considerations relevant to the application of simulating distributions with this method. Firstly, the samples are not truly independent and therefore convergence happens slowly, subject to a "burn-in" rate where many steps in the chain are required before a reasonable representation of the

target distribution is achieved. The rejection and convergence rates are also sensitive to the step size between states, where the step size is represented by the range or variance of the proposal distribution. Small step sizes can result in a random walk, whereas larger steps may cause higher rejection rates resulting in the chain remaining at a single value for many steps. This step size sensitivity can also cause issues with multimodal distributions. Using similar logic, it is straightforward to intuit that less likely events very rarely occur. These limitations can be mitigated with sufficiently long chains, but greater efficiency can be achieved by tuning the algorithm to suit the system.

While there are various tools and methods available to guide this tuning process [209], a fair amount of trial and error must be used. Firstly, the starting point of the chain must be tested. While the convergence rate should be independent of the initiation point if the algorithm is correctly tuned, starting within the limits of the target distribution is a basic requirement. Trace and autocorrelation plots allow for visualisation of the burn-in rate and the effects of the step size. Trace plots simply show accepted values of the chain. It is desirable for a Markov Chain to traverse all values of the target distribution relatively quickly and not remain at a single value (a sign of high rejection rate) or a region of the distribution for too long.

For a trace plot, the burn-in period is visible as the chain moves fairly linearly from its initiation point to values accepted in the target distribution. A small step size will result in random walk across the distribution with very little rejection occurring, and a large step size will produce a broad proposal distribution with significant portions outside of the distribution, creating a high rejection rate and extended flat regions on a trace plot. Figure 7.10 shows the trace plots for the grain size PDF algorithm for various step size values. Figure 7.10a shows the chain following an entirely random walk pattern associated with a small step

size, with the chain not traversing the full extent of the PDF (20-350 nm) in 4000 iterations. Figure 7.10b shows the results of a step size that is too large, resulting in too many rejections and the chain staying in the same state for numerous iterations. A step size of 40 nm was chosen (Figure 7.10c), which gives the desired result of a full excursion across the distribution with very few or zero sticking points.

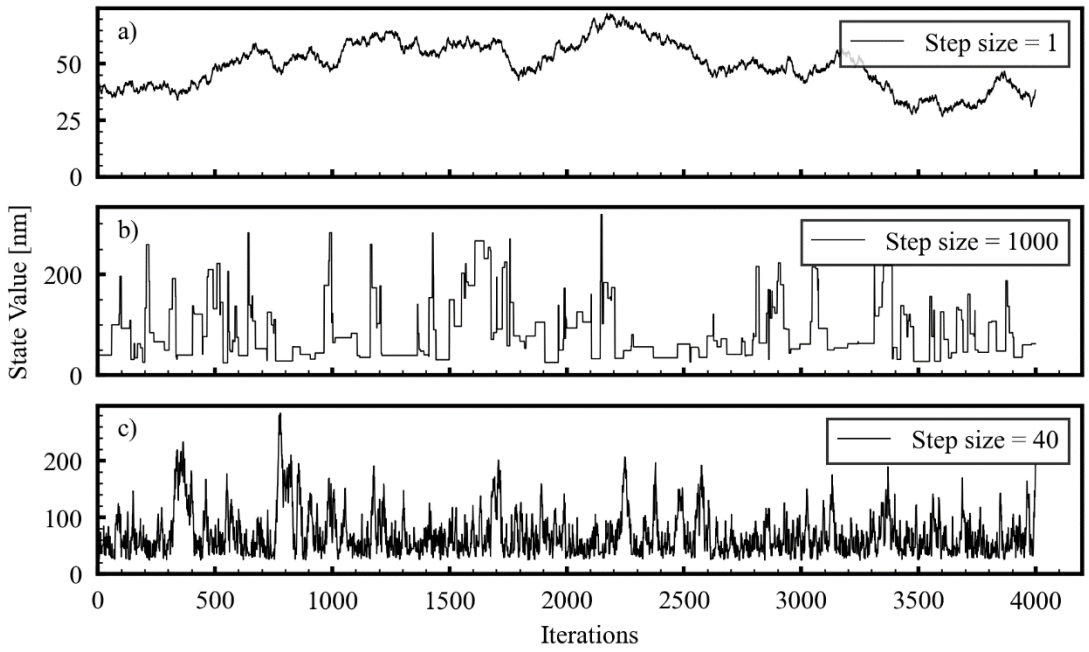

Figure 7.10: Various trace plots for the MH sampling algorithm with different nanometre step sizes across the PDF with a) 1 nm, b) 1000 nm and c) 40 nm, which gives the desired result.

An autocorrelation plot quantifies the correlation between a state in the chain and various lagged values along the chain. Provided that the correlation between samples for increasing lag intervals is decreasing, a good representation of the PDF can be achieved by having a sufficiently long chain. However, such a chain would be very expensive computationally. Consider a square two-dimensional array with a length equal to the number of samples. In python with a *float32* data

type, this array can easily scale into several gigabytes in size which can easily run into hardware limits and result in extremely long computation times. Thus, even though thinning the samples in this dataset fails to result in low values of autocorrelation, it does result in significant efficiency improvements.

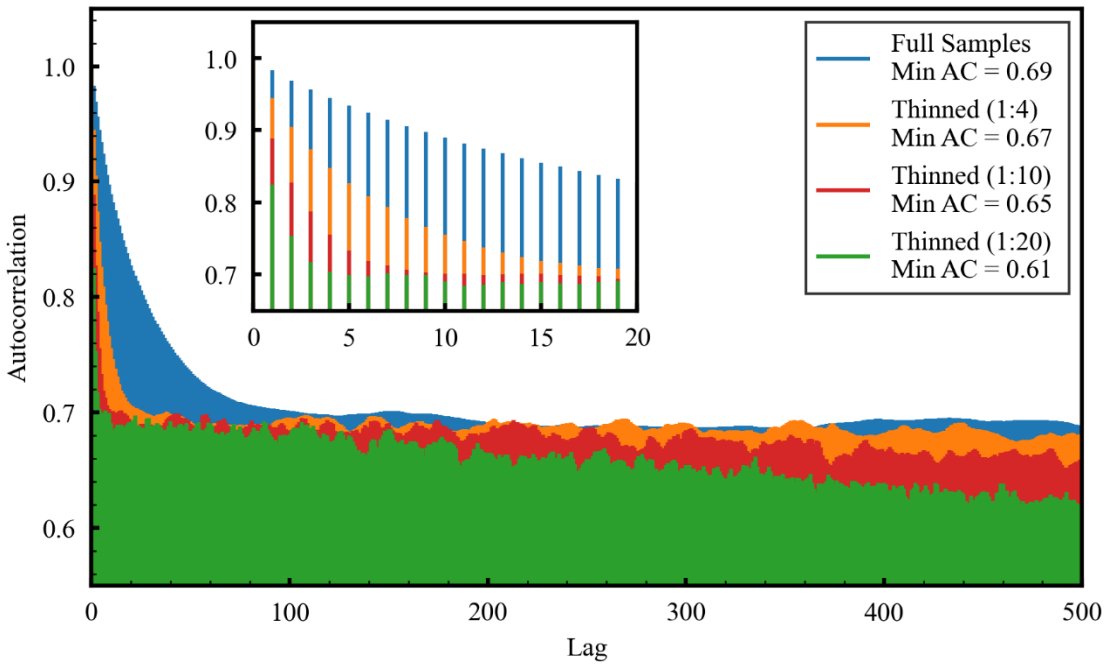

Figure 7.11: Autocorrelation plot of the MH algorithm, where the results of sufficiently thinning the samples is evident from the gradually decreasing correlation.

Algorithm parameters were selected such that the initial value was 35 nm, the step size was 40 nm, 600 samples discarded for burn-in and 1:20 were selected for the final dataset. The results of this, and a comparison between a brute force approach of using 100,000 samples and the optimised approach described above, are shown in Figure 7.12. For the fitting in the subsequent sections, 10,000 samples were used.

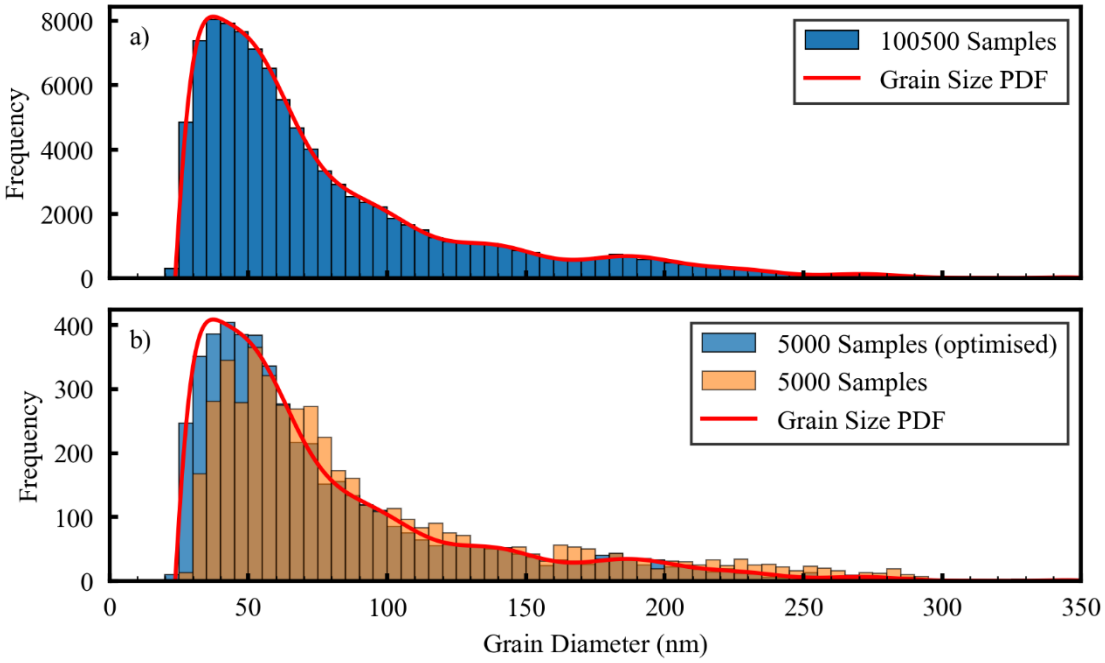

Figure 7.12: Samples of from the MH sampling algorithm with a) sufficient samples to produce reliable results at the cost of computing time and b) a comparison between 5000 optimised and unoptimised samples.

7.3.2 Results of fitting with the grain model

Initially, the normalised $I_c(B)$ for the large transition of device B1 was modelled. This testing revealed that utilising two rather than a single gaussian distribution to provide the feature length distribution perpendicular to the grain size distribution provided a degree of freedom that allowed for a better fit between the model and the data (see Figure 7.13). This is particularly the case for the data in the lowest fields, as shown in in the inset of Figure 7.13a, where the double gaussian better models the power low like drop-off.

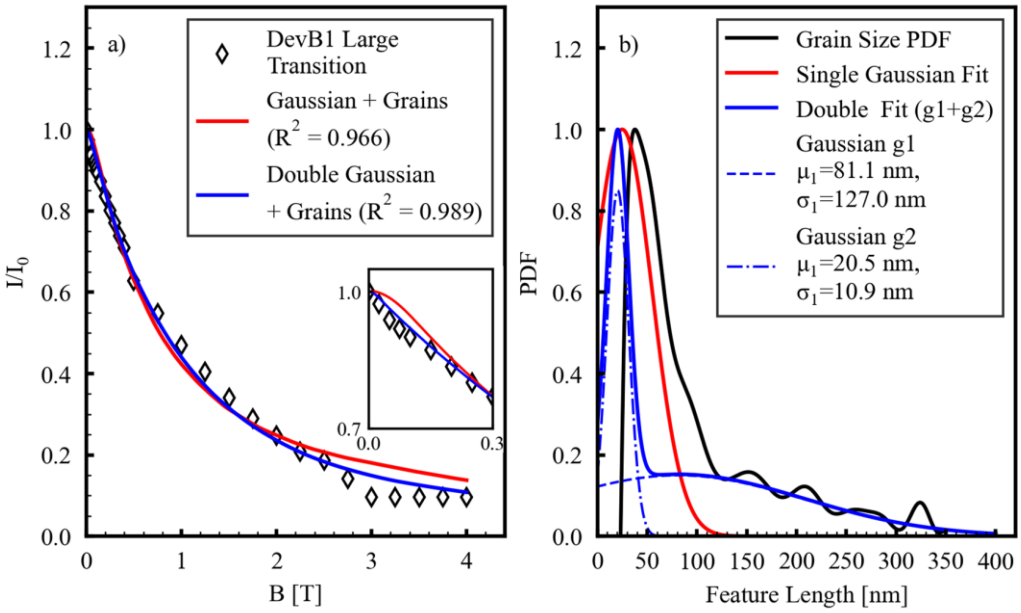

Figure 7.13: a) Fits of the grain model to normalised $I_c(B)$ data for the large transition on device B1. The additional degrees of freedom provided by the second gaussian allows for a better fit, particularly in the low field region. Inset is zoomed around the low field region, showing the double gaussian better models the power law like drop-off. b) Distribution results from a).

One gaussian tended to peak at lengths less than the grain size distribution, and the other would include larger features. The inclusion of larger feature is what provided the quality of fit to the low-field datasets. The proportion of the counts for each gaussian was fixed to a 15-85% split. This produced consistently good results, and while fitting of this parameter was attempted the SciPy curve fitting algorithm failed to converge with the addition of this parameter. This is probably due to the fact that the curve fitting algorithm generally struggles with very small numbers, and the very marginal changes to the fit due to altering the proportions probably pushed the limits of detection.

These initial results from device B1 also show that the fit requires the inclusion of features less than the minimum size of the grains. These are likely to be small subsurface grains, grain boundaries or voids. A deviation from the fit can be noted at the highest currents, but this can be explained by the difficulty in accurately tracking the peaks in the highest field datasets when the features merge and become less prominent compared to the background.

Results from the fits for the remaining peaks in device B1 are shown in Figure 7.14. Inset into each plot are the distributions and their means associated with the fit. The first transition and the onset and cessation of the hair features show good agreement to the model. It is suspected that the addition of further degrees of freedom would increase the quality of the fits in the middle field range. The final transition does not fit well with the model. This situation is the same across most devices and will be discussed later.

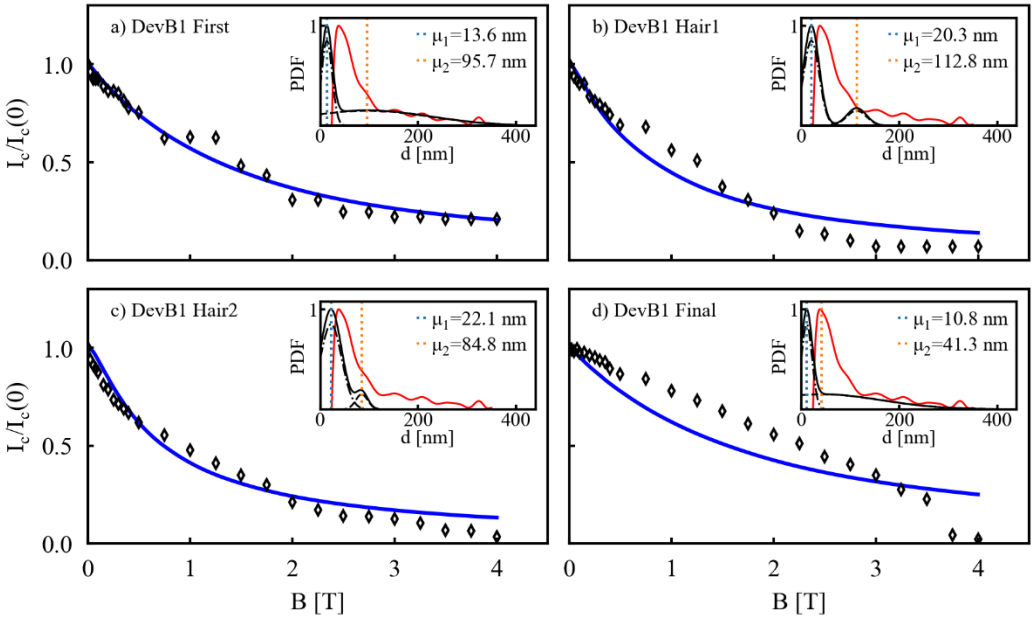

Figure 7.14: a-d) Fits of the grain model to the remaining transitions from device B1.

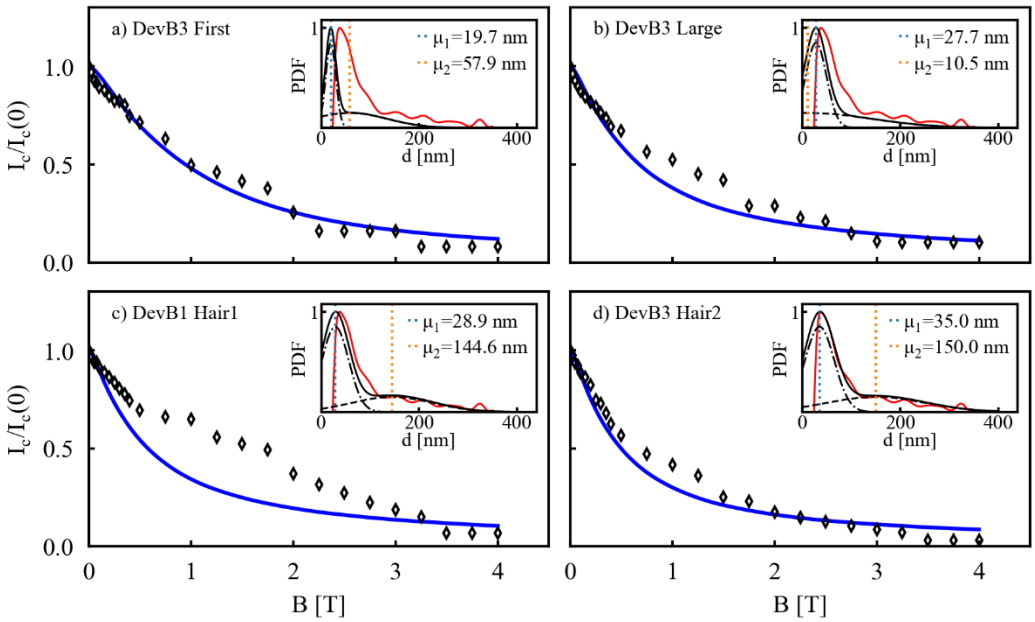

Figure 7.15: a-d) Fits of the grain model to the transitions from device B3.

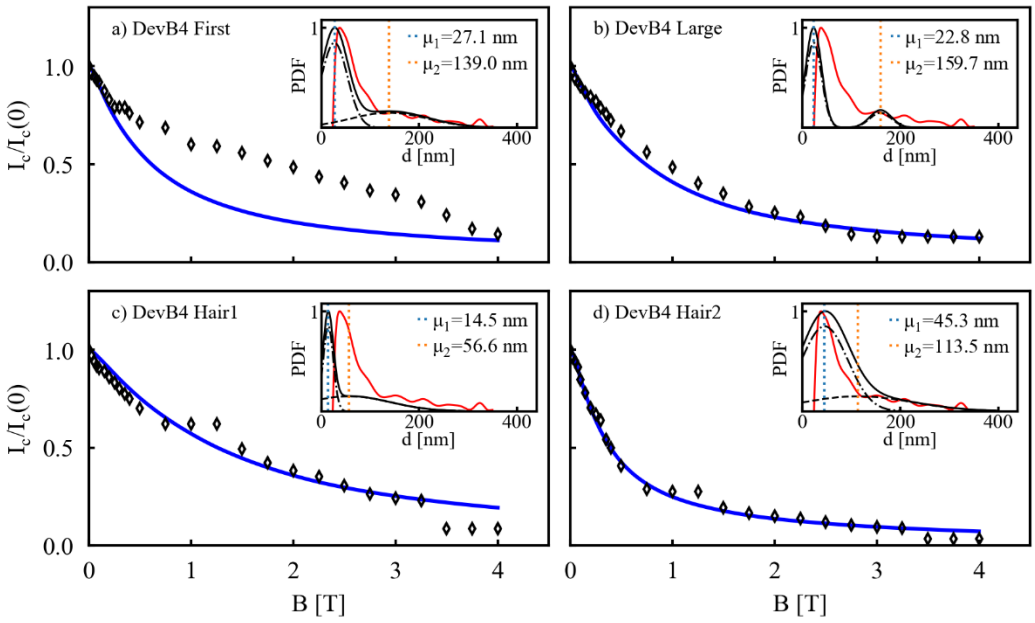

Figure 7.16: a-d) Fits of the grain model to the transitions from device B4.

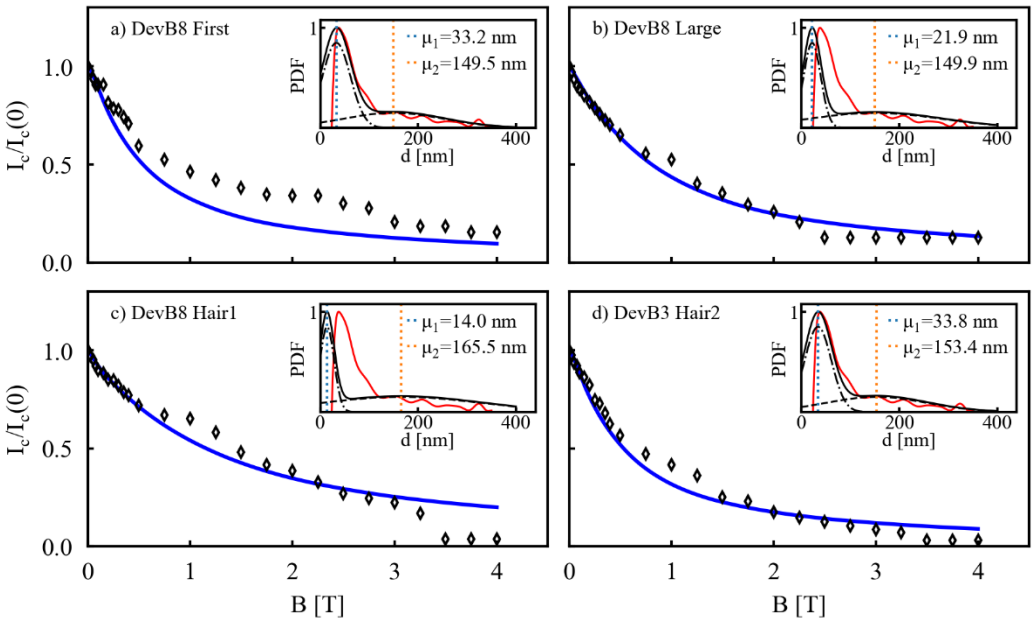

Figure 7.17: a-d) Fits of the grain model to the transitions from device B8.

Figure 7.16 and Figure 7.17 show the results of the fits to the transition of the other devices, with the final transition excluded. All show approximately the same normalised $I_c(B)$ behaviour and fit well with the model. Of particular note is that the low field characteristics are consistently captured. As this is where the peak tracking is most reliable, this is a strong validation of the model.

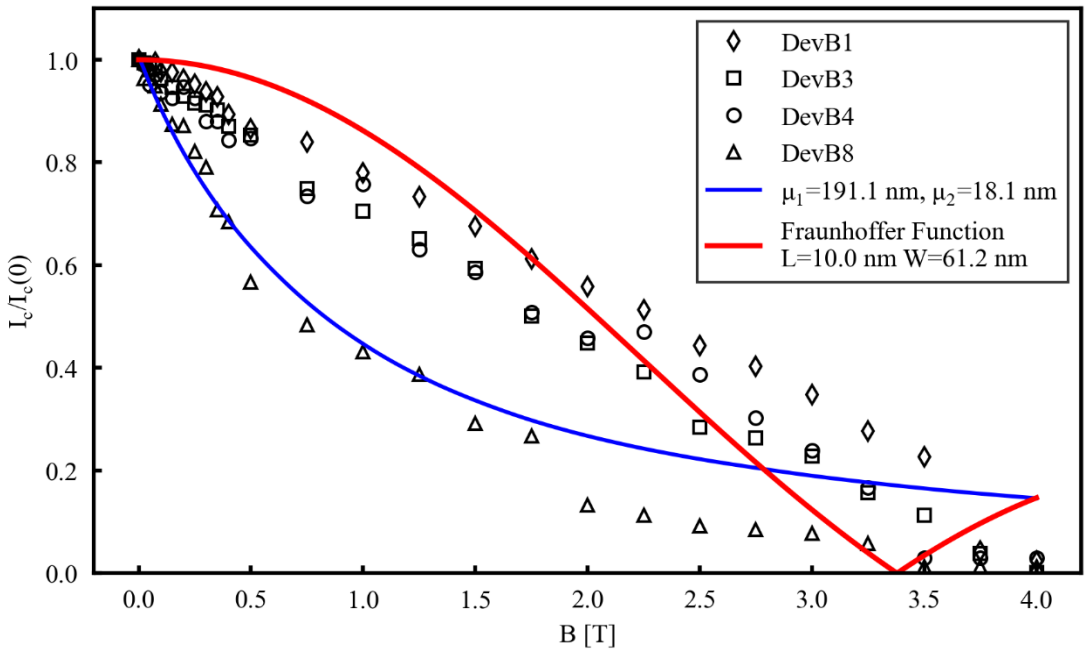

Figure 7.18: Comparing the fits of the standard Fraunhofer function to the grain model for the final transition across all devices. The Fraunhofer function fails to capture the behaviour at low field.

Revisiting the final transition, a plot comparing a fit of the FDP and the grain model are presented in Figure 7.18. Fits were performed to an average of the final transition $I_c(B)$ data for each device. While neither function accurately represents all datasets, the FDP particularly fails in the low current region. Also, the implication of an oscillation in the data is not observed in any of the measurements. The top of the field range was chosen to be 4 T because the $I_c(B)$ response was effectively linear beyond this point. It is likely that the discrepancy observed between the data and the grain model is due to either the inaccuracy of peak tracking for the final peak or some missing degree of freedom in the model that allowed the inclusion of additional variation in the feature sizes included.

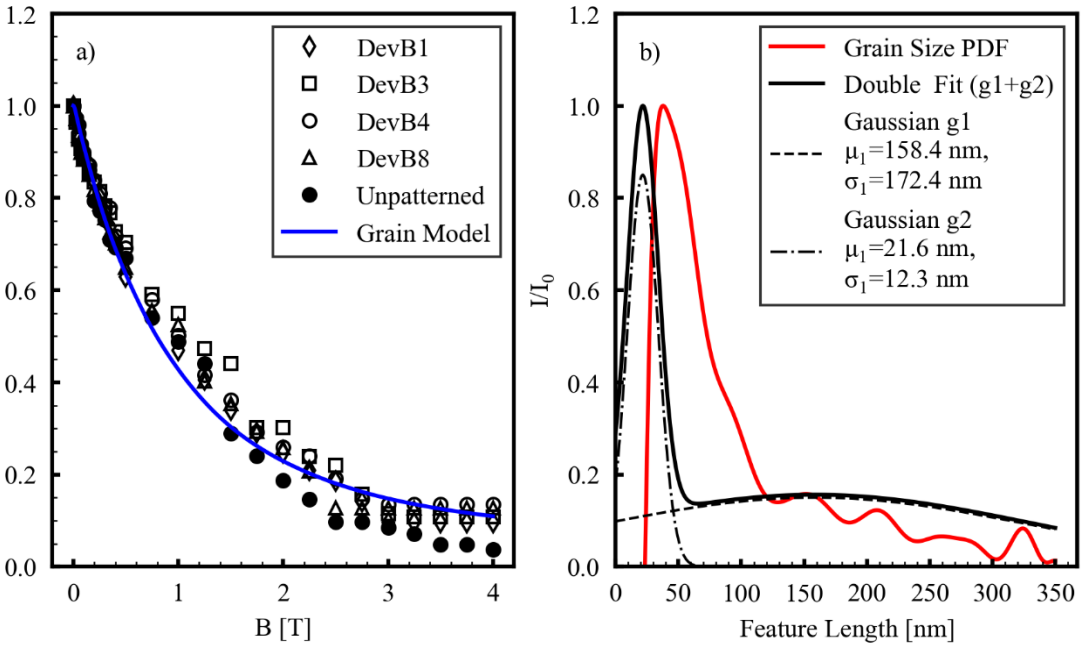

Figure 7.19: Grain model results a) The grain model fits well to an average of large transition $I_c(B)$ data across all devices, including an unpatterned strip with the same dimensions as the devices. b) Distribution results from a) which shows the additional feature lengths used in the fit.

As mentioned previously, the peak tracking algorithm was able to produce its best results for the largest transition of each device throughout the magnetic field range. In Figure 7.19 the normalised $I_c(B)$ data for the large transition for each device is presented in conjunction with the data from an unpatterned strip of material. As discussed in Section 5.7, this strip has the same width as the unpatterned portion of the devices and the same length between the voltage taps. These data all show good agreement with each other, and with a fit of the grain model to their average. This is significant evidence that the fabricated geometry of the junctions does not dominate the junction response.

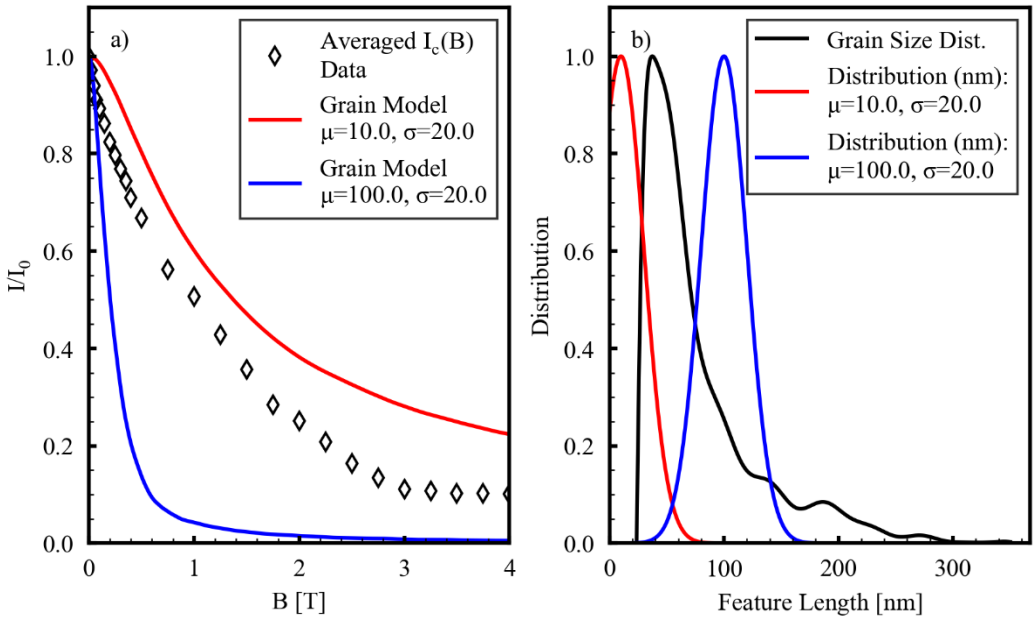

Figure 7.20: Illustrating the dimensional dependence of the grain size model. a) Showing the two unfitted models with test distributions, b) the feature lengths in these distributions.

To illustrate the dimensional dependence of the fit, two unfitted models are presented in Figure 7.20. With the red line showing a model utilising smaller grains, the drop-off in $I_c(B)$ is more gradual and follows the trend of the data reasonably well but the initial behaviour does not take the form of the power-law drop off observed in the data. To capture this effect, the inclusion of larger sized boundaries is required.

As the fits with the grain model produce an output of the additional features required for the fit (in the form of gaussian parameters for the mean and standard deviation of the distributions, μ and σ), it is possible to consider this data. Figure 7.21 shows this information, excluding the data for the final transition. A cut-off at zero feature length is included as a guide to the eye, as none of the features under this line were included in the fits.

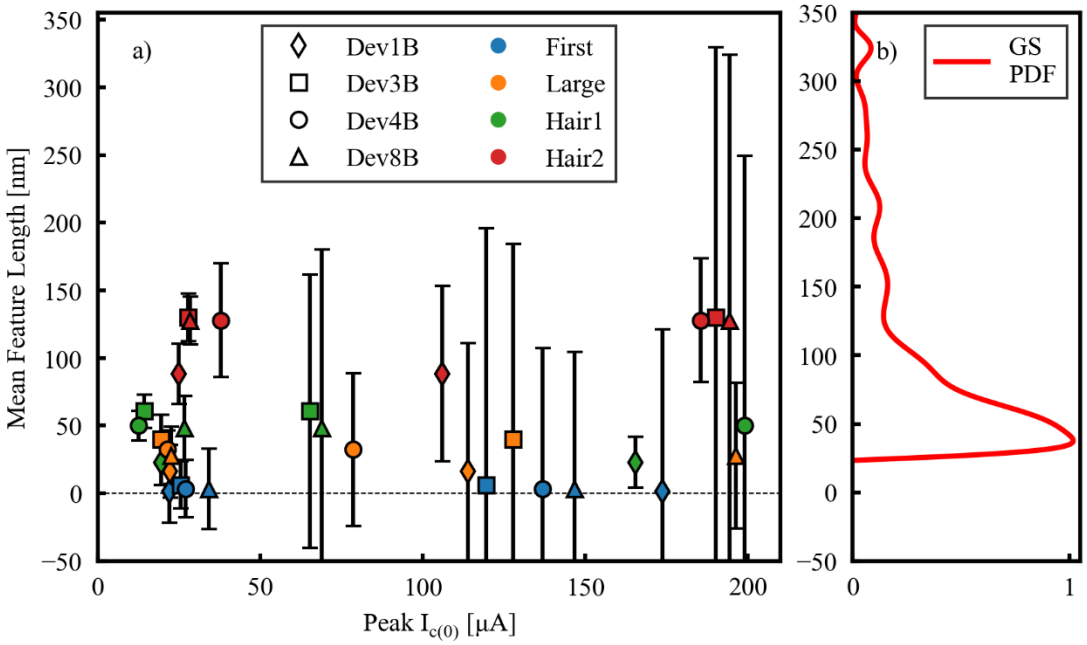

Figure 7.21: Grain model fitting parameters a) Showing the results of the grain size plus double gaussian fits plotted against the zero-field critical currents for each peak across all devices. Points are means μ_1 and μ_2 for each fit and error bars are respective standard deviations. This shows the additional feature lengths that are multiplied with b) the GS distribution to form the ensembles of nano-junctions that fit the data.

Reliably, the fits required features less than the length of the smallest grains with the inclusion of larger structures as well. All fits include a gaussian with a similar shape to the main peak in the grain size distribution, with the second gaussian typically encompassing portions of the distribution representing larger grains. This indicates that while no single grain or feature size is responsible for each transition, perhaps a clustering of similarly sized grains with similar susceptibilities and critical current densities play a role. Regarding the length scales in Figure 7.21, there is some clustering of lower mean feature lengths for

low I_c peaks. Higher I_c peaks generally correspond to larger features and require a broader variation in sizes.

Interestingly, the earliest exploration of the grain model was done with a grain size distribution that assumed a thinner film in the chips. As such, the distribution contained a lower frequency of larger grains in the 100-350 nm range. This resulted in poorer fits the $I_c(B)$ data, and the analysis of the differential resistance peak separations in Section 5.7. This thickness was later confirmed, and the grain model adjusted accordingly.

It should be noted that these results do not include any re-entrant behaviour or oscillation in $I_c(B)$ for any of the peaks across all of the devices. While this re-entrant behaviour is a classic signature of Josephson junctions, the apparent averaging of contributions in granular systems has been noted elsewhere [179,200–204]. As discussed in Section 5.1, various groups have reported Josephson junction and SQUID behaviour with single crystal diamond and B-NCD, so it is therefore theorised that re-entrant $I_c(B)$ character would be noted with better noise isolation and measurements in portions of the *I-V* curves absent of the metastable regions noted here.

7.4 CONCLUSIONS

Measurement of the behaviour of the critical currents for the differential resistance peaks in a varying magnetic field has been analysed. It has been demonstrated that the standard Fraunhofer function does not correctly model this $I_c(B)$ data. A model utilising the grain size distribution of the film was introduced. This model integrates across the grain size PDF introduced previously and uses additional gaussian functions to include additional feature lengths. The model fits well to the $I_c(B)$ data for each transition for all junction

types and geometries, excluding the final transition which was prone to systematic error during peak tracking. Further, identical behaviour is noted between the largest transitions of each device and a strip of B-NCD with the same dimensions as the unpatterned portion of the devices between the voltage taps. This proves that the field response is insensitive to the device type and geometry and lends strong support for the theory that the granularity of the material is what primarily affects junction dynamics. This is in agreement with the recent work probing the effect of the grains on general film superconductivity as discussed earlier in Section 2.4.

In conjunction with the temperature dependence analysis presented in Chapter 6, the production of high fidelity fits to the $I_c(B)$ grain model shows that the granularity of B-NCD and similar materials must be considered as a primary variable in the design of junctions and derivative superconducting circuits.

8 CONCLUSIONS AND FUTURE WORK

With the attractive confluence of desirable material properties and capabilities present in B-NCD, understanding all aspects of the physical processes governing the behaviour of the material relevant to device design should be a principal objective to ensure correct and rapid realisation of said devices.

Since the broad adoption of Ti based diamond electrical contacts at room temperature and above, the general assumption has been that this contact scheme would adequately serve for all temperatures. The work in Chapter 4 sought to test this hypothesis, particularly in regard to whether the doping concentrations in superconducting B-NCD were sufficient to maintain the ohmic nature of the contacts at the lowest temperatures. The contact resistance of both carbide forming and carbon soluble metals was investigated between 1.9 and 300 K using a modified TLM approach. The carbide forming group consisted of Ti, Cr, Mo and Ta. The carbon soluble metal was Pd. All contacts showed mechanical stability and an ohmic response across the temperature range. The Ti contact, while still showing a low contact resistance, performed the worst with the Mo and Ta contacts showing the lowest contact resistance.

The second half of this thesis was dedicated to the investigation of B-NCD Josephson junctions, with the goal of making sense of the interaction between the Ginzburg-Landau coherence length ξ_{GL}, the fabricated junction geometries and their temperature and field dependencies. Various device geometries were measured across two chips which, according to standard junction theory, fall into different junction types categorised by their dimensions relative to ξ_{GL} and the presence or lack of a vacuum gap. Chapter 5 focussed on the low temperature and zero-field states and the method for tracking the various peaks present in the differential resistance data for the chip B devices was also explained. No correlation between the device geometry and the critical current was observed, which is the first sign that some of the assumptions in device design are incorrect. Further, no difference between the junction types was observed. The presence of current transport across the long (L ~ 75 nm) vacuum gap junctions is still unexplained. It is apparent that the dominant transport factors across all devices are similar, perhaps most notably that normal state resistance is not distinct for the physically gapped junctions. This indicates that true SIS behaviour is unlikely. Taking the granular matrix of the material into account we can now say that all devices behave as junctions with geometries defined by their grains and grain boundaries where SNS-type behaviours seem to dominate. While SNS junctions typically show a longer-range phase coherence, the proximity effect is clearly not occurring in a gap of ~ 75 nm.

Chapter 6 investigated the temperature dependence of the critical currents and energy gaps of the devices. While previous work had highlighted the potential for spatial inhomogeneity in the superconducting energy gap in the order of ~30 nm [93,94], standard BCS temperature dependence was observed in all devices which perhaps indicates that the greater boron doping concentrations present in these films pushes the grains towards isotropic saturation regardless of their size and facet effects. The fact that all devices show convergent behaviour in the

temperature dependence of the superconducting energy gap and that all follow the standard *Ambegaokar-Baratoff* relationship for $I_c/I_c(0)$ is unequivocal evidence that the same physics is governing all of the junction geometries and types. The geometry and material nature of the contacts suggests SNS junctions, which therefore forces the short and dirty limit criteria $L \approx \xi_n$. With an upper bound of $\xi_n = 3$ nm based on more lightly doped film [191], it is therefore not possible for the device geometry to be the predominant variable in the functioning of these Josephson junctions. Additionally, comparison of fluctuation spectroscopy analysis on the temperature dependent conductance with previous work by *Klemencic et al.* [6] with the B-NCD film, an unpatterned strip with same dimensions as the material between the device voltage taps and device B1 indicate that the same granular effects dominate the superconducting properties of all three. It is therefore perhaps not surprising that the granular martix strongly influences the Josephson junctions. Further investigation is warranted into the potential for convergence between the coherence length within the grains and tunnelling between the grains with decreasing material dimensions. Existing literature (see Section 2.4) indicates that B-NCD behaves as a dirty superconductor. The coherence lengths extracted from the fluctuation spectroscopy fits confirm this for the films used in this work. Recalling that the coherence length for Cooper pairs tunnelling between grains ξ_t involves an intersection with normally conducting material and grain boundaries, it could be speculated that $\xi_t \approx \xi_n$ which allows for a more direct estimation of ξ_n for the films. Even taking this assumption into account, the modified short limit $L \approx \xi_t$ still precludes device geometries from playing a role in the $I_c(T)$ behaviour.

The field dependences of the devices on chip B were studied in chapter 7. It was immediately apparent that the standard Fraunhofer oscillatory diffraction pattern was not present in any of the devices, prompting the development of a granular model utilising an Airy diffraction pattern and the integration of

geometric contributions across the grain size distribution present in the B-NCD film. A Metropolis Hastings Markov Chain Monte-Carlo algorithm was developed to generate random samples from the grain size distribution. Again, all devices regardless of type and geometry showed strong agreement with each other and with the granular model, providing strong evidence that the grains form an array of Josephson junction in the film and the aggregated sum of these contributions dominate the physics of the devices. A lack of re-entrant oscillations in the field response is noted, however the previous successful SQUID measurements with junctions of similar dimensions indicate that the junctions investigated in this work are in fact true Josephson junctions rather than strong links in the superconducting circuit that have been driven normal.

The nature of the large number of peaks present in the differential resistance data from the devices on chip B is so far unexplained, but there are some clues from their behaviour. In static temperature and field, the number and critical current of the peaks are both repeatable and reasonably consistent across all devices and the unpatterned strips of B-NCD. Additionally, all peaks seem to follow the same temperature and field dependence. It therefore seems likely that each peak corresponds to the state switching of grains with similar sizes, with each adding a resistive component to the percolating path of the supercurrent. The presence of residual resistance has previously been noted for granular superconductors and observed in B-NCD [98,210].

As discussed in Section 2.4, there is now a wealth of evidence indicating that the granularity of the films is what governs the superconducting properties of B-NCD. This should perhaps not be surprising given the lessons learned from the other high temperature granular superconductors. Similarly, it now seems intuitive that the physics in dimensionally sensitive superconducting devices is dictated by the distribution of grains in B-NCD films, with the grains appearing

to form networks of Josephson junctions. Again, this situation has been observed previously in high temperature granular superconductors [203,210–214].

As shown by the fabrication of the two types of B-NCD SQUIDS produced to date, and the varying Josephson junction geometries showing junction characteristics shown previously and in this work, despite the fabrication challenges of B-NCD the material shows a remarkable flexibility when it comes to device design. With the junction mechanics dictated by the granularity, which can be tuned, it is possible to produce various effective junction and SQUID designs to accomplish specific design goals. Additionally, removing the need of for a junction to be fabricated with dimensions of the order of ξ_{GL} significantly simplifies device production.

The next phase in the ongoing project will involve testing these junction geometries in SQUID devices. As the results above indicate, it would be expected that the fabricated geometry of the junctions has little influence on the performance and response in field. Further investigation is perhaps also warranted into the nature of the peaks in the differential resistance data for the chip B devices. Developing a transport theory convergent with the previous work from *Klemencic et al.* seems prudent.

Bibliography

[1] A.T. Collins, Synthetic diamond: Emerging CVD science and technology, 15th ed., John Wiley & Sons, Ltd, 1994. https://doi.org/10.1002/CVDE.19950010109.

[2] V.A. Sidorov, E.A. Ekimov, Superconductivity in diamond, Diam Relat Mater. 19 (2010) 351–357. https://doi.org/10.1016/j.diamond.2009.12.002.

[3] S. Mandal, T. Bautze, O.A. Williams, C. Naud, É. Bustarret, F. Omnès, P. Rodière, T. Meunier, C. Bäuerle, L. Saminadayar, The diamond superconducting quantum interference device, ACS Nano. 5 (2011) 7144–7148. https://doi.org/10.1021/nn2018396.

[4] G. Zhang, S. Turner, E.A. Ekimov, J. Vanacken, M. Timmermans, T. Samuely, V.A. Sidorov, S.M. Stishov, Y. Lu, B. Deloof, B. Goderis, G. Van Tendeloo, J. Van De Vondel, V. V. Moshchalkov, Global and Local Superconductivity in Boron-Doped Granular Diamond, Advanced Materials. 26 (2014) 2034–2040. https://doi.org/10.1002/ADMA.201304667.

[5] O.A. Williams, M. Nesladek, M. Daenen, S. Michaelson, A. Hoffman, E. Osawa, K. Haenen, R.B. Jackman, Growth, electronic properties and applications of nanodiamond, Diam Relat Mater. 17 (2008) 1080–1088. https://doi.org/10.1016/j.diamond.2008.01.103.

[6] G.M. Klemencic, J.M. Fellows, J.M. Werrell, S. Mandal, S.R. Giblin, R.A. Smith, O.A. Williams, Fluctuation spectroscopy as a probe of granular superconducting diamond films, Phys Rev Mater. 1 (2017). https://doi.org/10.1103/PhysRevMaterials.1.044801.

[7] K.L. Ekinci, M.L. Roukes, Nanoelectromechanical systems, Review of Scientific Instruments. 76 (2005) 061101. https://doi.org/10.1063/1.1927327.

[8] M. Imboden, P. Mohanty, Dissipation in nanoelectromechanical systems, Phys Rep. 534 (2014) 89–146. https://doi.org/10.1016/J.PHYSREP.2013.09.003.

[9] G.A. Steele, A.K. Hüttel, B. Witkamp, M. Poot, H.B. Meerwaldt, L.P. Kouwenhoven, H.S.J. Van Der Zant, Strong coupling between single-electron tunneling and nanomechanical motion, Science (1979). 325 (2009) 1103–1107. https://doi.org/10.1126/SCIENCE.1176076/.

[10] V.B. Braginskii, A.B. Manukin, Measurement of weak forces in physics experiments, Ucp. (1977).

[11] Y.T. Yang, C. Callegari, X.L. Feng, K.L. Ekinci, M.L. Roukes, Zeptogram-scale nanomechanical mass sensing, Nano Lett. 6 (2006) 583–586. https://doi.org/10.1021/NL052134M/.

[12] D. Høj, F. Wang, W. Gao, U.B. Hoff, O. Sigmund, U.L. Andersen, Ultra-coherent nanomechanical resonators based on inverse design, Nature Communications 2021 12:1. 12 (2021) 1–8. https://doi.org/10.1038/s41467-021-26102-4.

[13] Y. Tao, J.M. Boss, B.A. Moores, C.L. Degen, Single-crystal diamond nanomechanical resonators with quality factors exceeding one million, Nat Commun. 5 (2014). https://doi.org/10.1038/NCOMMS4638.

[14] M.A. Hopcroft, W.D. Nix, T.W. Kenny, What is the Young's modulus of silicon?, Journal of Microelectromechanical Systems. 19 (2010) 229–238. https://doi.org/10.1109/JMEMS.2009.2039697.

[15] S. Cui, K. Cao, Y. Yu, A.X. Zhang, Ultra-high-Q racetrack microring based on silicon-nitride, (2022). https://arxiv.org/abs/2209.01097v2 (accessed May 8, 2023).

[16] G. Arlt, G.R. Schodder, Some Elastic Constants of Silicon Carbide, J Acoust Soc Am. 37 (1965) 384–386. https://doi.org/10.1121/1.1909336.

[17] D.R. Lide, G. Baysinger, L.I. Berger, R.N. Goldberg, H. V Kehiaian, K. Kuchitsu, D.L. Roth, D. Zwillinger, CRC Handbook of Chemistry and Physics, 79th ed., CRC Press, Boca Raton, FL, 1998.

[18] M. Poot, H.S.J. van der Zant, Mechanical systems in the quantum regime, Phys Rep. 511 (2012) 273–335. https://doi.org/10.1016/J.PHYSREP.2011.12.004.

[19] L. Wei, X. Kuai, Y. Bao, J. Wei, L. Yang, P. Song, M. Zhang, F. Yang, X. Wang, The Recent Progress of MEMS/NEMS Resonators, Micromachines (Basel). 12 (2021). https://doi.org/10.3390/MI12060724.

[20] R. He, X.L. Feng, M.L. Roukes, P. Yang, Self-transducing silicon nanowire electromechanical systems at room temperature, Nano Lett. 8 (2008) 1756–1761. https://doi.org/10.1021/NL801071W.

[21] X.M. Henry Huang, C.A. Zorman, M. Mehregany, M.L. Roukes, Nanoelectromechanical systems: Nanodevice motion at microwave frequencies, Nature. 421 (2003) 496–496. https://doi.org/10.1038/421496A.

[22] Y.T. Yang, K.L. Ekinci, X.M.H. Huang, L.M. Schiavone, M.L. Roukes, C.A. Zorman, M. Mehregany, Monocrystalline silicon carbide nanoelectromechanical systems, Appl Phys Lett. 78 (2001) 162–164. https://doi.org/10.1063/1.1338959.

[23] E. Bustarret, C. Marcenat, P. Achatz, J. Kačmarčik, F. Lévy, A. Huxley, L. Ortéga, E. Bourgeois, X. Blase, D. Débarre, J. Boulmer, Superconductivity in doped cubic silicon, Nature 2006 444:7118. 444 (2006) 465–468. https://doi.org/10.1038/nature05340.

[24] T. Muranaka, Y. Kikuchi, T. Yoshizawa, N. Shirakawa, J. Akimitsu, Superconductivity in carrier-doped silicon carbide, Sci Technol Adv Mater. 9 (2008) 044204. https://doi.org/10.1088/1468-6996/9/4/044204.

[25] A.D. O'Connell, M. Hofheinz, M. Ansmann, R.C. Bialczak, M. Lenander, E. Lucero, M. Neeley, D. Sank, H. Wang, M. Weides, J. Wenner, J.M. Martinis, A.N. Cleland,

Quantum ground state and single-phonon control of a mechanical resonator, Nature 2010 464:7289. 464 (2010) 697–703. https://doi.org/10.1038/nature08967.

[26] S. Etaki, M. Poot, I. Mahboob, K. Onomitsu, H. Yamaguchi, H.S.J. van der Zant, Motion detection of a micromechanical resonator embedded in a d.c. SQUID, Nat Phys. 4 (2008) 785. http://dx.doi.org/10.1038/nphys1057.

[27] Y. Zou, Y. Li, H. Chen, D. Welch, Y. Zhao, B. Li, Thermoelasticity and anomalies in the pressure dependence of phonon velocities in niobium, Appl Phys Lett. 112 (2018) 11901. https://doi.org/10.1063/1.5009617.

[28] S.F. Wang, Y.F. Hsu, J.C. Pu, J.C. Sung, L.G. Hwa, Determination of acoustic wave velocities and elastic properties for diamond and other hard materials, Mater Chem Phys. 85 (2004) 432–437. https://doi.org/10.1016/J.MATCHEMPHYS.2004.02.003.

[29] O.A. Williams, A. Kriele, J. Hees, M. Wolfer, W. Müller-Sebert, C.E. Nebel, High Young's modulus in ultra thin nanocrystalline diamond, Chem Phys Lett. 495 (2010) 84–89. https://doi.org/10.1016/J.CPLETT.2010.06.054.

[30] L. Sekaric, J.M. Parpia, H.G. Craighead, T. Feygelson, B.H. Houston, J.E. Butler, Nanomechanical resonant structures in nanocrystalline diamond, Appl Phys Lett. 81 (2002) 4455. https://doi.org/10.1063/1.1526941.

[31] T. Bautze, S. Mandal, O.A. Williams, P. Rodière, T. Meunier, C. Bäuerle, Superconducting nano-mechanical diamond resonators, Carbon N Y. 72 (2014) 100–105. https://doi.org/10.1016/j.carbon.2014.01.060.

[32] B.G. Streetman, Sanjay. Banerjee, Solid state electronic devices, Prentice Hall, 2000.

[33] C. Kittel, Introduction to Solid State Physics Solution Manual, 8th Edition, John Wiley & Sons, 2004.

[34] S.M. Sze, K.K. Ng, Physics of Semiconductor Devices, Physics of Semiconductor Devices. (2006). https://doi.org/10.1002/0470068329.

[35] G.L. Pearson, J. Bardeen, Electrical Properties of Pure Silicon and Silicon Alloys Containing Boron and Phosphorus, Physical Review. 75 (1949) 865. https://doi.org/10.1103/PhysRev.75.865.

[36] K. Thonke, The boron acceptor in diamond, Semicond Sci Technol. 18 (2003) S20. https://doi.org/10.1088/0268-1242/18/3/303.

[37] H.C. Lu, Y.C. Peng, M.Y. Lin, S.L. Chou, J.I. Lo, B.M. Cheng, Analysis of boron in diamond with UV photoluminescence, Carbon N Y. 111 (2017) 835–838. https://doi.org/10.1016/J.CARBON.2016.10.082.

[38] X. Blase, E. Bustarret, C. Chapelier, T. Klein, C. Marcenat, Superconducting group-IV semiconductors, Nat Mater. 8 (2009) 375–382. https://doi.org/10.1038/nmat2425.

[39] T. Klein, P. Achatz, J. Kacmarcik, C. Marcenat, F. Gustafsson, J. Marcus, E. Bustarret, J. Pernot, F. Omnes, B.E. Sernelius, C. Persson, A. Ferreira Da Silva, C. Cytermann, Metal-insulator transition and superconductivity in boron-doped

diamond, Phys Rev B Condens Matter Mater Phys. 75 (2007) 165313. https://doi.org/10.1103/PhysRevB.75.165313.

[40] G.T. Meaden, G.T. Meaden, The Theory of the Electrical Resistance of Metals, in: Electrical Resistance of Metals, Springer US, 1965: pp. 59–94. https://doi.org/10.1007/978-1-4899-5717-7_3.

[41] D. Cvijović, The Bloch-Gruneisen Function of Arbitrary Order and its Series Representations, 2011.

[42] B. Altshuler, A. Aronov, M. Pollak, A.L. Efros, Electron-Electron Interactions in Disordered Systems, Volume 10 1st Edition, 1st Edition, North Holland (November 11, 2012), 1985.

[43] H. K. Onnes, The superconductivity of mercury, Communications from the Physical Laboratory at the University of Leiden. 122 (1911) 124.

[44] W. Meissner, O. Ochsenfeld, A new effect in penetration of superconductors, Naturwissenschaften. 21 (1933) 787–788.

[45] A. Amirabadizadeh, S. Memarzadeh, N. Tajabor, H. Arabi, Effect of Yb2O3 Nanoparticle Addition on Superconducting Properties of BSCCO (2223)/Ag Tapes by Acetate Precipitation Method, World Journal of Condensed Matter Physics. 02 (2012) 148–152. https://doi.org/10.4236/WJCMP.2012.23024.

[46] F. London, H. London, The electromagnetic equations of the supraconductor, Proceedings of The Royal Society A: Mathematical, Physical and Engineering Sciences. 149 (1935) 71–88. https://doi.org/10.1098/RSPA.1935.0048.

[47] H. Casimir, C.J. Gorter, On supraconductivity I, Physica. 1 (1934) 306–320.

[48] J. Bardeen, L.N. Cooper, J.R. Schrieffer, Theory of superconductivity, Physical Review. 108 (1957) 1175–1204. https://doi.org/10.1103/PHYSREV.108.1175/.

[49] A. Mourachkine, Determination of the Coherence Length and the Cooper-Pair Size in Unconventional Superconductors by Tunnelling Spectroscopy, J Supercond Nov Magn. 17 (2004) 711–724. https://doi.org/10.1007/s10948-004-0831-7.

[50] R.A. Dunlap, BCS theory, Electrons in Solids. (2019). https://doi.org/10.1088/2053-2571/AB2F2CCH9.

[51] N.N. Bogolyubov, A New method in the theory of superconductivity. I, Sov.Phys.JETP. 7 (1958) 41–46. https://doi.org/10.1103/PHYSREV.106.162.

[52] E. Maxwell, Isotope Effect in the Superconductivity of Mercury, Physical Review. 78 (1950) 477. https://doi.org/10.1103/PhysRev.78.477.

[53] P. Townsend, J. Sutton, Investigation by Electron Tunneling of the Superconducting Energy Gaps in Nb, Ta, Sn, and Pb, Physical Review. 128 (1962) 591. https://doi.org/10.1103/PhysRev.128.591.

[54] An experiment on the mechanism of superconductivity, Proc R Soc Lond A Math Phys Sci. 185 (1946) 225–239. https://doi.org/10.1098/RSPA.1946.0015.

[55] W.S. Corak, B.B. Goodman, C.B. Satterthwaite, A. Wexler, Atomic Heats of Normal and Superconducting Vanadium, Physical Review. 102 (1956) 656. https://doi.org/10.1103/PhysRev.102.656.

[56] M.A. Biondi, M.P. Garfunkel, A.O. McCoubrey, Millimeter Wave Absorption in Superconducting Aluminum, Physical Review. 101 (1956) 1427. https://doi.org/10.1103/PhysRev.101.1427.2.

[57] Andrei. Mourachkine, Room-temperature superconductivity, Cambridge International Science Pub, 2004.

[58] L.D. Landau, V.L. Ginzburg, On the theory of superconductivity, Zh. Eksp. Teor. Fiz. 20 (1950) 1064.

[59] Michael. Tinkham, Introduction to superconductivity, Dover Publications, 2004.

[60] A.A. Abrikosov, The magnetic properties of superconducting alloys, Journal of Physics and Chemistry of Solids. 2 (1957) 199–208. https://doi.org/10.1016/0022-3697(57)90083-5.

[61] H.F. Hess, R.B. Robinson, R.C. Dynes, J.M. Valles, J. V. Waszczak, Scanning-Tunneling-Microscope Observation of the Abrikosov Flux Lattice and the Density of States near and inside a Fluxoid, Phys Rev Lett. 62 (1989) 214. https://doi.org/10.1103/PhysRevLett.62.214.

[62] R.D. Parks, Superconductivity, CRC Press, 1969.

[63] A.F. Andreev, Thermal Conductivity of the Intermediate State of Superconductors, Zh. Eksperim. i Teor. Fiz. Vol: 46 (1964).

[64] B. Pannetier, H. Courtois, Andreev Reflection and Proximity effect, J Low Temp Phys. 118 (2000) 599–615. https://doi.org/10.1023/A:1004635226825/METRICS.

[65] G.E. Blonder, M. Tinkham, T.M. Klapwijk, Transition from metallic to tunneling regimes in superconducting microconstrictions: Excess current, charge imbalance, and supercurrent conversion, Phys Rev B. 25 (1982) 4515. https://doi.org/10.1103/PhysRevB.25.4515.

[66] P.G. De Gennes, E. Guyon, SUPERCONDUCTIVITY IN "NORMAL" METALS, Phys. Letters. Vol: 3 (1963) 168–169. https://doi.org/10.1016/0031-9163(63)90401-3.

[67] N.R. Werthamer, Theory of the Superconducting Transition Temperature and Energy Gap Function of Superposed Metal Films, Physical Review. 132 (1963) 2440. https://doi.org/10.1103/PhysRev.132.2440.

[68] B.D. Josephson, Possible new effects in superconductive tunnelling, PhL. 1 (1962) 251–253. https://doi.org/10.1016/0031-9163(62)91369-0.

[69] M. Suzuki, Y. Enomoto, T. Murakami, Study on grain boundary Josephson junctions in BaPb1−xBixO3 thin films, J Appl Phys. 56 (1984) 2083–2092. https://doi.org/10.1063/1.334205.

[70] V. Stepankin, A. Kuznetsov, Weak link behavior of single grain boundary Josephson junction in BaPb1−xBixO3 bicrystals, Applied Superconductivity. 1 (1993) 947–960. https://doi.org/10.1016/0964-1807(93)90401-M.

[71] R. Gross, P. Chaudhari, D. Dimos, A. Gupta, G. Koren, Thermally activated phase slippage in high-Tc grain-boundary Josephson junctions, Phys Rev Lett. 64 (1990) 228–231. https://doi.org/10.1103/PHYSREVLETT.64.228.

[72] Z.G. Ivanov, J.A. Alarco, T. Claeson, P.A. Nilsson, E. Olsson, H.K. Olsson, E.A. Stepantsov, D. Winkler, A. Tzalenchuk, Artificial grain boundary Josephson junctions-properties and applications, Proceedings of the Beijing International Conference: High Temperature Superconductivity (BHTSC '92). (1993) 722.

[73] W.C. Stewart, Current-Voltage Characteristics of Josephson Junctions, ApPhL. 12 (1968) 277–280. https://doi.org/10.1063/1.1651991.

[74] D.E. McCumber, Effect of ac Impedance on dc Voltage-Current Characteristics of Superconductor Weak-Link Junctions, J Appl Phys. 39 (2003) 3113. https://doi.org/10.1063/1.1656743.

[75] V. Ambegaokar, A. Baratoff, Tunneling Between Superconductors, Phys Rev Lett. 10 (1963) 486. https://doi.org/10.1103/PhysRevLett.10.486.

[76] I.O. Kulik, A.N. Omelyanchuk, Contribution to the microscopic theory of the Josephson effect in superconducting bridges, JETP Lett. (USSR) (Engl. Transl.). 21 (1975) 96–97.

[77] E.A. Ekimov, V.A. Sidorov, E.D. Bauer, N.N. Mel'nik, N.J. Curro, J.D. Thompson, S.M. Stishov, Superconductivity in diamond, Nature 2004 428:6982. 428 (2004) 542–545. https://doi.org/10.1038/nature02449.

[78] Y. Takano, M. Nagao, T. Takenouchi, H. Umezawa, I. Sakaguchi, M. Tachiki, H. Kawarada, Superconductivity in Polycrystalline Diamond Thin Films, (n.d.).

[79] E. Bustarret, J. Kacmarcik, C. Marcenat, E. Gheeraert, C. Cytermann, J. Marcus, T. Klein, Dependence of the Superconducting Transition Temperature on the Doping Level in Single-Crystalline Diamond Films, Phys Rev Lett. 93 (2004) 237005. https://doi.org/10.1103/PhysRevLett.93.237005.

[80] T. Klein, P. Achatz, J. Kacmarcik, C. Marcenat, F. Gustafsson, J. Marcus, E. Bustarret, J. Pernot, F. Omnes, B.E. Sernelius, C. Persson, A. Ferreira Da Silva, C. Cytermann, Metal-insulator transition and superconductivity in boron-doped diamond, Phys Rev B Condens Matter Mater Phys. 75 (2007) 165313. https://doi.org/10.1103/PHYSREVB.75.165313/.

[81] M. Abdel-Hafiez, D. Kumar, R. Thiyagarajan, Q. Zhang, R.T. Howie, K. Sethupathi, O. Volkova, A. Vasiliev, W. Yang, H.K. Mao, M.S.R. Rao, High-pressure behavior of superconducting boron-doped diamond, Phys Rev B. 95 (2017) 174519. https://doi.org/10.1103/PHYSREVB.95.174519/.

[82] D. Kumar, M. Chandran, D.K. Shukla, D.M. Phase, K. Sethupathi, M.S. Ramachandra Rao, Tc suppression and impurity band structure in overdoped

superconducting Boron-doped diamond films, Physica C: Superconductivity and Its Applications. 555 (2018) 28–34. https://doi.org/10.1016/J.PHYSC.2018.09.005.

[83] T. Doi, T. Fukaishi, C. Hiramatsu, T. Wakita, M. Hirai, Y. Muraoka, T. Yokoya, Y. Kato, Y. Izumi, T. Muro, Y. Tamenori, Effectiveness of a hot-filament chemical vapor deposition method for preparation of a boron-doped superconducting diamond film with higher superconducting transition temperature, Diam Relat Mater. 25 (2012) 5–7. https://doi.org/10.1016/J.DIAMOND.2012.02.008.

[84] Z.L. Wang, C. Lu, J.J. Li, C.Z. Gu, Influence of growth pressure on the electrical properties of boron-doped polycrystalline diamond films, Appl Surf Sci. 255 (2009) 9522–9525. https://doi.org/10.1016/J.APSUSC.2009.07.086.

[85] J. Hees, A. Kriele, O.A. Williams, Electrostatic self-assembly of diamond nanoparticles, Chem Phys Lett. 509 (2011) 12–15. https://doi.org/10.1016/j.cplett.2011.04.083.

[86] G. Zhang, S.D. Janssens, J. Vanacken, M. Timmermans, J. Vacík, G.W. Ataklti, W. Decelle, W. Gillijns, B. Goderis, K. Haenen, P. Wagner, V. V. Moshchalkov, Role of grain size in superconducting boron-doped nanocrystalline diamond thin films grown by CVD, Phys Rev B Condens Matter Mater Phys. 84 (2011). https://doi.org/10.1103/PHYSREVB.84.214517.

[87] I. V. Lerner, A.A. Varlamov, V.M. Vinokur, Fluctuation spectroscopy of granularity in superconducting structures, Phys Rev Lett. 100 (2008) 117003. https://doi.org/10.1103/PHYSREVLETT.100.117003/.

[88] H. Okazaki, T. Wakita, T. Muro, T. Nakamura, Y. Muraoka, T. Yokoya, S.I. Kurihara, H. Kawarada, T. Oguchi, Y. Takano, Signature of high Tc above 25 K in high quality superconducting diamond, Appl Phys Lett. 106 (2015) 052601. https://doi.org/10.1063/1.4907411.

[89] J. Bousquet, T. Klein, M. Solana, L. Saminadayar, C. Marcenat, E. Bustarret, Phase diagram of boron-doped diamond revisited by thickness-dependent transport studies, Phys Rev B. 95 (2017) 161301. https://doi.org/10.1103/PHYSREVB.95.161301/FIGURES/4/MEDIUM.

[90] B. Sacépé, C. Chapelier, C. Marcenat, J. Kačmarčik, T. Klein, M. Bernard, E. Bustarret, Tunneling Spectroscopy and Vortex Imaging in Boron-Doped Diamond, Phys. Rev. Lett. 96 (2006).

[91] G. Zhang, T. Samuely, J. Kačmarčík, E.A. Ekimov, J. Li, J. Vanacken, P. Szabó, J. Huang, P.J. Pereira, D. Cerbu, V. V. Moshchalkov, Bosonic Anomalies in Boron-Doped Polycrystalline Diamond, Phys Rev Appl. 6 (2016) 064011. https://doi.org/10.1103/PHYSREVAPPLIED.6.064011/FIGURES/6/MEDIUM.

[92] G.M. Klemencic, J.M. Fellows, J.M. Werrell, S. Mandal, S.R. Giblin, R.A. Smith, O.A. Williams, Observation of a superconducting glass state in granular superconducting diamond, Scientific Reports 2019 9:1. 9 (2019) 1–6. https://doi.org/10.1038/s41598-019-40306-1.

[93] B.L. Willems, V.H. Dao-, J. Vanacken, L.F. Chibotaru, V. V Moshchalkov, I. Guillamón, H. Suderow, S. Vieira, S.D. Janssens, O.A. Williams, K. Haenen, P. Wagner, Intrinsic granularity in nanocrystalline boron-doped diamond films measured by scanning tunneling microscopy, (n.d.). https://doi.org/10.1103/PhysRevB.80.224518.

[94] F. Dahlem, P. Achatz, O.A. Williams, D. Araujo, E. Bustarret, H. Courtois, Spatially-correlated microstructure and superconductivity in polycrystalline Boron-doped diamond, 2010.

[95] K. Ushizawa, K. Watanabe, T. Ando, I. Sakaguchi, M. Nishitani-Gamo, Y. Sato, H. Kanda, Boron concentration dependence of Raman spectra on {100} and {111} facets of B-doped CVD diamond, Diam Relat Mater. 7 (1998) 1719–1722. https://doi.org/10.1016/S0925-9635(98)00296-9.

[96] K. Ishizaka, R. Eguchi, T. Yokota, S. Shin, Observation of a superconducting gap in boron-doped diamond by laser-excited photoemission spectroscopy, (2007). https://doi.org/10.1103/PhysRevLett.98.047003.

[97] K. Winzer, D. Bogdanov, C. Wild, Electronic properties of boron-doped diamond on the border between the normal and the superconducting state, Physica C: Superconductivity and Its Applications. 432 (2005) 65–70. https://doi.org/10.1016/J.PHYSC.2005.07.011.

[98] G.M. Klemencic, D.T.S. Perkins, J.M. Fellows, C.M. Muirhead, R.A. Smith, S. Mandal, S. Manifold, M. Salman, S.R. Giblin, O.A. Williams, Phase slips and metastability in granular boron-doped nanocrystalline diamond microbridges, Carbon N Y. 175 (2021) 43–49. https://doi.org/10.1016/J.CARBON.2020.12.042.

[99] P. Smereka, X. Li, G. Russo, D.J. Srolovitz, Simulation of faceted film growth in three dimensions: microstructure, morphology and texture, Acta Mater. 53 (2005) 1191–1204. https://doi.org/10.1016/J.ACTAMAT.2004.11.013.

[100] J.S. Langer, V. Ambegaokar, Intrinsic Resistive Transition in Narrow Superconducting Channels, Physical Review. 164 (1967) 498. https://doi.org/10.1103/PhysRev.164.498.

[101] D.E. McCumber, B.I. Halperin, Time Scale of Intrinsic Resistive Fluctuations in Thin Superconducting Wires, Phys Rev B. 1 (1970) 1054. https://doi.org/10.1103/PhysRevB.1.1054.

[102] M. Tinkham, The interaction of phase-slip centers in superconducting filaments, Journal of Low Temperature Physics 1979 35:1. 35 (1979) 147–151. https://doi.org/10.1007/BF00121726.

[103] W.J. Skocpol, M.R. Beasley, M. Tinkham, Phase-slip centers and nonequilibrium processes in superconducting tin microbridges, Journal of Low Temperature Physics 1974 16:1. 16 (1974) 145–167. https://doi.org/10.1007/BF00655865.

[104] J.A. Cuenca, T. Brien, S. Mandal, S. Manifold, S. Doyle, A. Porch, G.M. Klemencic, O.A. Williams, Superconducting boron doped nanocrystalline diamond microwave coplanar resonator, (2022). https://doi.org/10.1016/J.CARBON.2022.08.084.

[105] B. Oripov, D. Kumar, C. Garcia, P. Hemmer, T. Venkatesan, M.S.R. Rao, S.M. Anlage, Large Microwave Inductance of Granular Boron-Doped Diamond Superconducting Films, (2021). https://doi.org/10.1063/5.0051227.

[106] M. Ortolani, S. Lupi, L. Baldassarre, U. Schade, P. Calvani, Y. Takano, M. Nagao, T. Takenouchi, H. Kawarada, Low-energy electrodynamics of superconducting diamond, Phys Rev Lett. 97 (2006) 097002. https://doi.org/10.1103/PHYSREVLETT.97.097002/.

[107] K. Winzer, D. Bogdanov, C. Wild, Electronic properties of boron-doped diamond on the border between the normal and the superconducting state, Physica C: Superconductivity and Its Applications. 432 (2005) 65–70. https://doi.org/10.1016/J.PHYSC.2005.07.011.

[108] B. Bekdüz, J. Twellmann, J. Mischke, al -, S. Okada Shinya Okada, H. Matsumura Hideki Matsumura -, Diamond growth by chemical vapour deposition, J Phys D Appl Phys. 43 (2010) 374017. https://doi.org/10.1088/0022-3727/43/37/374017.

[109] O.A. Williams, Nanocrystalline diamond, Diam Relat Mater. 20 (2011) 621–640. https://doi.org/10.1016/J.DIAMOND.2011.02.015.

[110] F. Silva, K. Hassouni, X. Bonnin, A. Gicquel, Microwave engineering of plasma-assisted CVD reactors for diamond deposition, Journal of Physics: Condensed Matter. 21 (2009) 364202. https://doi.org/10.1088/0953-8984/21/36/364202.

[111] M.N.R. Ashfold, P.W. May, C.A. Rego, N.M. Everitt, Thin film diamond by chemical vapour deposition methods, Chem Soc Rev. 23 (1994) 21–30. https://doi.org/10.1039/CS9942300021.

[112] S. Mandal, Nucleation of diamond films on heterogeneous substrates: a review, RSC Adv. 11 (2021) 10159–10182. https://doi.org/10.1039/D1RA00397F.

[113] O.A. Williams, O. Douhéret, M. Daenen, K. Haenen, E. Osawa, M. Takahashi, Enhanced diamond nucleation on monodispersed nanocrystalline diamond, Chem Phys Lett. 445 (2007) 255–258. https://doi.org/10.1016/J.CPLETT.2007.07.091.

[114] S. Mandal, H.A. Bland, J.A. Cuenca, M. Snowball, O.A. Williams, Superconducting boron doped nanocrystalline diamond on boron nitride ceramics, Nanoscale. 11 (2019) 10266–10272. https://doi.org/10.1039/c9nr02729g.

[115] W. Gajewski, P. Achatz, O.A. Williams, K. Haenen, E. Bustarret, M. Stutzmann, J.A. Garrido, Electronic and optical properties of boron-doped nanocrystalline diamond films, Phys Rev B Condens Matter Mater Phys. 79 (2009) 045206. https://doi.org/10.1103/PhysRevB.79.045206.

[116] E. Bustarret, J. Kacmarčik, C. Marcenat, E. Gheeraert, C. Cytermann, J. Marcus, T. Klein, Dependence of the superconducting transition temperature on the doping level in single-crystalline diamond films, Phys Rev Lett. 93 (2004) 237005. https://doi.org/10.1103/PhysRevLett.93.237005.

[117] P. Achatz, W. Gajewski, E. Bustarret, C. Marcenat, R. Piquerel, C. Chapelier, T. Dubouchet, O.A. Williams, K. Haenen, J.A. Garrido, M. Stutzmann, Low-temperature transport in highly boron-doped nanocrystalline diamond, Phys Rev B

Condens Matter Mater Phys. 79 (2009) 201203. https://doi.org/10.1103/PhysRevB.79.201203.

[118] M. Gadonna, D. Bosc, A. Maalouf, An improvement in standard photolithography resolution based on Kirchhoff diffraction studies, Article in Journal of Physics D Applied Physics. 42 (2008) 11. https://doi.org/10.1088/0022-3727/42/1/015106.

[119] R.A. Lawson, A.P.G. Robinson, Overview of materials and processes for lithography, Frontiers of Nanoscience. 11 (2016) 1–90. https://doi.org/10.1016/B978-0-08-100354-1.00001-6.

[120] E.L.H. Thomas, Nanocrystalline diamond for nano-electro-mechanical systems, Cardiff University, 2017.

[121] G.F. Ding, H.P. Mao, Y.L. Cai, Y.H. Zhang, X. Yao, X.L. Zhao, Micromachining of CVD diamond by RIE for MEMS applications, Diam Relat Mater. 14 (2005) 1543–1548. https://doi.org/10.1016/J.DIAMOND.2005.04.011.

[122] C.R. Brundle, C.A.Jr. Evans, S. Wilson, Encyclopedia Of Materials Characterization, Butterworth-Heinemann, 1992.

[123] H. Zu, W. Dai, A.T.A.M. de Waele, Development of dilution refrigerators—A review, Cryogenics (Guildf). 121 (2022) 103390. https://doi.org/10.1016/J.CRYOGENICS.2021.103390.

[124] R.J. Donnelly, C.F. Barenghi, The Observed Properties of Liquid Helium at the Saturated Vapor Pressure, J Phys Chem Ref Data. 27 (2009) 1217. https://doi.org/10.1063/1.556028.

[125] G. Palasantzas, Random surface roughness influence on gas damped nanoresonators, Appl Phys Lett. 90 (2007) 041914. https://doi.org/10.1063/1.2435328.

[126] O. Ergincan, G. Palasantzas, B.J. Kooi, Influence of surface modification on the quality factor of microresonators, Phys Rev B Condens Matter Mater Phys. 85 (2012) 205420. https://doi.org/10.1103/PhysRevB.85.205420.

[127] S. Mandal, E.L.H. Thomas, L. Gines, D. Morgan, J. Green, E.B. Brousseau, O.A. Williams, Redox agent enhanced chemical mechanical polishing of thin film diamond, Carbon N Y. 130 (2018) 25–30. https://doi.org/10.1016/j.carbon.2017.12.077.

[128] G.M. Klemencic, S. Mandal, J.M. Werrell, S.R. Giblin, O.A. Williams, Superconductivity in planarised nanocrystalline diamond films, Sci Technol Adv Mater. 18 (2017) 239–244. https://doi.org/10.1080/14686996.2017.1286223.

[129] K.L. Moazed, R. Nguyen, J.R. Zeidler, Ohmic Contacts to Semiconducting Diamond, IEEE Electron Device Letters. 9 (1988) 350–351. https://doi.org/10.1109/55.740.

[130] D.A. Conte, W.D. Brown, S.S. Ang, H.A. Naseem, Normal metal, ohmic contacts to high-temperature superconducting YBa,Cu,O, _ 6 thin films suitable for multichip modules, Thin Solid Films. 270 (1995).

[131] J. Clarke, The proximity effect between buperconducting and normal thin films in zero field, Journal de Physique Colloques. 29 (1968). https://doi.org/10.1051/jphyscol:1968201ï.

[132] A.D. Wieck, Vanishing contact resistance on polycrystalline YBa 2 Cu 3 O 7−x, Appl. Phys. Lett. 52 (1988) 1017. https://doi.org/10.1063/1.99231.

[133] G. V Kuznetsov, G. V Kuznetsov, Transport of charge carriers in a superconductor – semiconductor contact, Low Temperature Physics. 30 (2004) 778–782. https://doi.org/10.1063/1.1808195.

[134] B.J. Van Wees, P. De Vries, P. Magnée, T.M. Klapwijk, Excess conductance of superconductor-semiconductor interfaces due to phase conjugation between electrons and holes, Phys Rev Lett. 69 (1992) 510–513. https://doi.org/10.1103/PhysRevLett.69.510.

[135] C.Y. Chang, S.M. Sze, Carrier transport across metal-semiconductor barriers, Solid State Electron. 13 (1970) 727–740. https://doi.org/10.1016/0038-1101(70)90060-2.

[136] C.Y. Chang, Y.K. Fang, S.M. Sze, Specific contact resistance of metal-semiconductor barriers, Solid State Electron. 14 (1971) 541–550. https://doi.org/10.1016/0038-1101(71)90129-8.

[137] T. Tachibana, B.E. Williams, J.T. Glass, Correlation of the electrical properties of metal contacts on diamond films with the chemical nature of the metal-diamond interface. II. Titanium contacts: A carbide-forming metal, Phys Rev B. 45 (1992) 11975–11981. https://doi.org/10.1103/PhysRevB.45.11975.

[138] J. Nakanishi, A. Otsuki, T. Oku, O. Ishiwata, M. Murakami, Formation of ohmic contacts to p-type diamond using carbide forming metals, J Appl Phys. 76 (1994) 2293–2298. https://doi.org/10.1063/1.357649.

[139] M. Yokoba, Y. Koide, a Otsuki, F. Ako, T. Oku, M. Murakami, Carrier transport mechanism of Ohmic contact to p -type diamond, 81 (1997) 6815–6821. https://doi.org/10.1063/1.365240.

[140] S.R. Shatynski, The Thermochemistry of Transition Metal Carbides, Oxidation of Metals. 13 (1979).

[141] H.J. Looi, L.Y.S. Pang, M.D. Whitfield, J.S. Foord, R.B. Jackman, Engineering low resistance contacts on p-type hydrogenated diamond surfaces, Diam Relat Mater. 9 (2000) 975–981.

[142] C.A. Hewett, M.J. Taylor, J.R. Zeidler, M.W. Geis, Specific contact resistance measurements of ohmic contacts to semiconducting diamond, J Appl Phys. 77 (1995) 755–760. https://doi.org/10.1063/1.358996.

[143] J. Nakanishi, A. Otsuki, T. Oku, O. Ishiwata, M. Murakami, Formation of ohmic contacts to p-type diamond using carbide forming metals, J Appl Phys. 76 (1994) 2293–2298. https://doi.org/10.1063/1.357649.

[144] C.A. Hewett, J.R. Zeidler, Ohmic contacts to epitaxial and natural diamond, Diam Relat Mater. 2 (1993) 1319–1321. https://doi.org/10.1016/0925-9635(93)90176-3.

[145] H.A. Naseem, I. Meyyappan, C.S. Prasad, W.D. Brown, Au-based metallizations on diamond substrates for multichip module applications, International Journal of Microcircuits and Electronic Packaging. 16 (1993) 257–269.

[146] H.A. Hoff, G.L. Waytena, C.L. Vold, J.S. Suehle, I.P. Isaacson, M.L. Rebbert, D.I. Ma, K. Harris, Ohmic contacts to semiconducting diamond using a Ti/Pt/Au trilayer metallization scheme, Diam Relat Mater. 5 (1996) 1450–1456. https://doi.org/10.1016/S0925-9635(96)00566-3.

[147] G.L. Waytena, H.A. Hoff, D.I. Ma, I.P. Isaacson, M.L. Rebbert, C. Marrian, J.S. Suehle, The Use of a Double Mask System to Prevent Ti Diffusion from a Ti/Pt/Au Ohmic Contact on Diamond, J Electrochem Soc. 143 (1996) 2392. https://doi.org/10.1149/1.1837013.

[148] J. Shirafuji, T. Sugino, Electrical properties of diamond surfaces, Diam Relat Mater. 5 (1996) 706–713. https://doi.org/10.1016/0925-9635(95)00415-7.

[149] H. Kawarada, Hydrogen-terminated diamond surfaces and interfaces, Surf Sci Rep. 26 (1996) 205–206. https://doi.org/10.1016/S0167-5729(97)80002-7.

[150] S.A. Grot, G.S. Gildenblat, C.W. Hatfield, C.R. Wronski, A.R. Badzian, T. Badzian, R. Messier, The Effect of Surface Treatment on the Electrical Properties of Metal Contacts to Boron-Doped Homoepitaxial Diamond Film, IEEE Electron Device Letters. 11 (1990) 100–102. https://doi.org/10.1109/55.46942.

[151] W. Wang, C. Hu, F.N. Li, S.Y. Li, Z.C. Liu, F. Wang, J. Fu, H.X. Wang, Palladium Ohmic contact on hydrogen-terminated single crystal diamond film, Diam Relat Mater. 63 (2016) 175–179. https://doi.org/10.1016/j.diamond.2016.01.019.

[152] K. Xing, A. Tsai, S. Rubanov, D.L. Creedon, S.A. Yianni, L. Zhang, W.C. Hao, J. Zhuang, J.C. McCallum, C.I. Pakes, D.C. Qi, Palladium forms Ohmic contact on hydrogen-terminated diamond down to 4 K, Appl Phys Lett. 116 (2020) 111601. https://doi.org/10.1063/1.5141775.

[153] S. Jeedigunta, P. Spagnol, J. Bumgarner, A. Kumar, Electrical contacts to nitrogen incorporated nanocrystalline diamond films, Diam Relat Mater. 17 (2008) 2037–2040. https://doi.org/10.1016/J.DIAMOND.2008.06.012.

[154] X. Chen, M. Mohr, K. Brühne, H.J. Fecht, Highly Conductive Nanocrystalline Diamond Films and Electronic Metallization Scheme, Materials. 14 (2021). https://doi.org/10.3390/MA14164484.

[155] G.K. Reeves, H.B. Harrison, Obtaining the specific contact resistance from transmission line model measurements, IEEE Electron Device Letters. EDL-3 (1982) 111–113. https://doi.org/10.1109/EDL.1982.25502.

[156] Y. Tzeng, A. Holt, R. Ely, High performance silver ohmic contacts to YBa 2 Cu 3 O 6+x superconductors, (1988). https://doi.org/10.1063/1.99036.

[157] V. Venkatesan, D.M. Malta, K. Das, A.M. Belu, Evaluation of ohmic contacts formed by B+ implantation and Ti-Au metallization on diamond, J Appl Phys. 741 (1993) 1179–16104. https://doi.org/10.1063/1.358510.

[158] P.W. May, W.J. Ludlow, M. Hannaway, P.J. Heard, J.A. Smith, K.N. Rosser, Raman and conductivity studies of boron-doped microcrystalline diamond, facetted nanocrystalline diamond and cauliflower diamond films, Diam Relat Mater. 17 (2008) 105–117. https://doi.org/10.1016/j.diamond.2007.11.005.

[159] M. Bernard, A. Deneuville, P. Muret, Non-destructive determination of the boron concentration of heavily doped metallic diamond thin films from Raman spectroscopy, Diam Relat Mater. 13 (2004) 282–286. https://doi.org/10.1016/j.diamond.2003.10.051.

[160] P. Szirmai, T. Pichler, O.A. Williams, S. Mandal, C. Bäuerle, F. Simon, A detailed analysis of the Raman spectra in superconducting boron doped nanocrystalline diamond, Physica Status Solidi (b). 249 (2012) 2656–2659. https://doi.org/10.1002/pssb.201200461.

[161] K. Das, V. Venkatesan, T.P. Humphreys, Ohmic contacts on diamond by B ion implantation and TiC-Au and TaSi 2 -Au metallization, J Appl Phys. 76 (1994) 2208–2212. https://doi.org/10.1063/1.358510.

[162] W.P. Leroy, C. Detavernier, R.L. Van Meirhaeghe, A.J. Kellock, C. Lavoie, Solid-state formation of titanium carbide and molybdenum carbide as contacts for carbon-containing semiconductors, J Appl Phys. 99 (2006). https://doi.org/10.1063/1.2180436.

[163] P.E. Viljoen, Reaction between diamond and titanium for ohmic contact and metallization adhesion layers, Journal of Vacuum Science & Technology B: Microelectronics and Nanometer Structures. 12 (1994) 2997. https://doi.org/10.1116/1.587549.

[164] K.L. Moazed Richard Nguyen, J.R. Zeidler Senior Meiber Ieee, Ohmic Contacts to Semiconducting Diamond, 1988.

[165] Y. Jingu, K. Hirama, H. Kawarada, Ultrashallow TiC source/drain contacts in diamond MOSFETs formed by hydrogenation-last approach, IEEE Trans Electron Devices. 57 (2010) 966–972. https://doi.org/10.1109/TED.2010.2043311.

[166] F. Fang, C.A. Hewett, M.G. Fernandes, S.S. Lau, Ohmic contacts formed by ion mixing in the si-diamond system, IEEE Trans Electron Devices. 36 (1989) 1783–1786. https://doi.org/10.1109/16.34243.

[167] C.M. Zhen, Y.Y. Wang, Q.F. Guo, M. Zhao, Z.W. He, Y.P. Guo, Ohmic contacts on diamond by B ion implantation and Ta–Au metallization, Diam Relat Mater. 11 (2002) 1709–1712. https://doi.org/10.1016/S0925-9635(02)00144-9.

[168] W. Wang, C. Hu, F.N. Li, S.Y. Li, Z.C. Liu, F. Wang, J. Fu, H.X. Wang, Palladium Ohmic contact on hydrogen-terminated single crystal diamond film, Diam Relat Mater. 59 (2015) 90–94. https://doi.org/10.1016/j.diamond.2015.09.012.

[169] C.H. Hsu, C.F. Chen, H.C. Lo, Field emission characteristics of chromium carbide capped carbon nanotips, Thin Solid Films. 515 (2006) 1025–1027. https://doi.org/10.1016/j.tsf.2006.07.072.

[170] A. Nino, T. Hirabara, S. Sugiyama, H. Taimatsu, Preparation and characterization of tantalum carbide (TaC) ceramics, Int J Refract Metals Hard Mater. 52 (2015) 203–208. https://doi.org/10.1016/j.ijrmhm.2015.06.015.

[171] J.E. Gerbi, O. Auciello, J. Birrell, D.M. Gruen, B.W. Alphenaar, J.A. Carlisle, Electrical contacts to ultrananocrystalline diamond, Appl Phys Lett. 83 (2003) 2001–2003. https://doi.org/10.1063/1.1609043.

[172] G. Zhang, S. Turner, E.A. Ekimov, J. Vanacken, M. Timmermans, T. Samuely, V.A. Sidorov, S.M. Stishov, Y. Lu, B. Deloof, B. Goderis, G. Van Tendeloo, J. Van De Vondel, V. V. Moshchalkov, Global and local superconductivity in boron-doped granular diamond, Advanced Materials. 26 (2014) 2034–2040. https://doi.org/10.1002/adma.201304667.

[173] T. Bautze, S. Mandal, O.A. Williams, P. Rodière, T. Meunier, C. Bäuerle, Superconducting nano-mechanical diamond resonators, Carbon N Y. 72 (2014) 100–105. https://doi.org/10.1016/j.carbon.2014.01.060.

[174] M. Bose, D.L. Creedon, A. Barlow, M. Stuiber, G.M. Klemencic, S. Mandal, O. Williams, G. Van Riessen, C.I. Pakes, Low-Noise Diamond-Based D.C. Nano-SQUIDs, ACS Appl Electron Mater. (2022). https://doi.org/10.1021/ACSAELM.2C00048/.

[175] M. Watanabe, A. Kawano, S. Kitagoh, T. Yamaguchi, Y. Takano, H. Kawarada, Stacked SNS Josephson junction of all boron doped diamond, Physica C: Superconductivity and Its Applications. 470 (2010) S613–S615. https://doi.org/10.1016/J.PHYSC.2009.11.061.

[176] T. Kageura, M. Hideko, I. Tsuyuzaki, A. Morishita, A. Kawano, Y. Sasama, T. Yamaguchi, Y. Takano, M. Tachiki, S. Ooi, K. Hirata, S. Arisawa, H. Kawarada, Single-crystalline boron-doped diamond superconducting quantum interference devices with regrowth-induced step edge structure, Scientific Reports 2019 9:1. 9 (2019) 1–9. https://doi.org/10.1038/s41598-019-51596-w.

[177] E.L.H. Thomas, G.W. Nelson, S. Mandal, J.S. Foord, O.A. Williams, Chemical mechanical polishing of thin film diamond, Carbon N Y. 68 (2014) 473–479. https://doi.org/10.1016/J.CARBON.2013.11.023.

[178] S.A. Manifold, G. Klemencic, E.L.H. Thomas, S. Mandal, H. Bland, S.R. Giblin, O.A. Williams, Contact resistance of various metallisation schemes to superconducting boron doped diamond between 1.9 and 300 K, Carbon N Y. 179 (2021) 13–19. https://doi.org/10.1016/J.CARBON.2021.02.079.

[179] C.A.C. Passos, M.T.D. Orlando, G.L.L. Keller, J.L. Passamai, J.A. Ferreira, E.V.L. de Mello, Description of the transport critical current density behavior of polycrystalline superconductors as a function of the applied magnetic field, Physica B Condens Matter. 404 (2009) 3123–3126. https://doi.org/10.1016/J.PHYSB.2009.07.062.

[180] M. Salman, Design Considerations for Weak Links Made of Boron Doped Diamond & Simulations for the Interaction Between a dc SQUID and an Integrated Micromechanical Doubly Clamped Cantilever, Cardiff University, 2021.

[181] H. Courtois, M. Meschke, J.T. Peltonen, J.P. Pekola, Origin of hysteresis in a proximity josephson junction, Phys Rev Lett. 101 (2008) 067002. https://doi.org/10.1103/PHYSREVLETT.101.067002/FIGURES/4/MEDIUM.

[182] G. Tancredi, S. Schmidlin, P.J. Meeson, Note: Cryogenic coaxial microwave filters, Review of Scientific Instruments. 85 (2014) 026104. https://doi.org/10.1063/1.4863881.

[183] A. Lukashenko, A. V. Ustinov, Improved powder filters for qubit measurements., Undefined. 79 (2008). https://doi.org/10.1063/1.2827515.

[184] M.Y. Kupriyanov, K.K. Likharev, V.F. Lukichev, Influence of effective electron interaction on the critical current of Josephson weak links, (n.d.).

[185] W.J. Johnson, A. Barone, Effect of Junction Geometry on Maximum Zero-Voltage Josephson Current, J Appl Phys. 41 (1970) 2958. https://doi.org/10.1063/1.1659343.

[186] D.L. Stuehm, C.W. Wilmsen, Geometrical Dependence of the Maximum dc Josephson Current, J Appl Phys. 42 (1971) 869. https://doi.org/10.1063/1.1660109.

[187] N. Savvides, Niobium step-edge superconducting junctions, Supercond Sci Technol. 21 (2008). https://doi.org/10.1088/0953-2048/21/4/045013.

[188] N. Khare, A.K. Gupta, Z. Hossain, R. Nagarajan, L.C. Gupta, Radio-frequency SQUID effect due to natural grain-boundary junctions in ErNi2B2C and DyNi2B2C magnetic borocarbide superconductors, Appl Phys Lett. 75 (1999) 1775. https://doi.org/10.1063/1.124816.

[189] N. Khare, A.K. Gupta, S. Khare, L.C. Gupta, R. Nagarajan, Z. Hossain, R. Vijayaraghavan, Radio frequency-SQUID effect in YNi2B2C due to natural grain boundary weak links, Appl Phys Lett. 69 (1998) 1483. https://doi.org/10.1063/1.116915.

[190] K.K. Likharev, Superconducting weak links, Rev Mod Phys. 51 (1979) 101–159. https://doi.org/10.1103/RevModPhys.51.101.

[191] M. Watanabe, R. Kanomata, S. Kurihara, A. Kawano, S. Kitagoh, T. Yamaguchi, Y. Takano, H. Kawarada, Vertical SNS weak-link Josephson junction fabricated from only boron-doped diamond, Phys Rev B Condens Matter Mater Phys. 85 (2012) 184516. https://doi.org/10.1103/PHYSREVB.85.184516/FIGURES/7/MEDIUM.

[192] K.A. Delin, A.W. Kleinsasser, Stationary properties of high-critical-temperature proximity effect Josephson junctions, Supercond Sci Technol. 9 (1996) 227. https://doi.org/10.1088/0953-2048/9/4/001.

[193] G. Zhang, S. Turner, E.A. Ekimov, J. Vanacken, M. Timmermans, T. Samuely, V.A. Sidorov, S.M. Stishov, Y. Lu, B. Deloof, B. Goderis, G. Van Tendeloo, J. Van De Vondel, V. V. Moshchalkov, Global and local superconductivity in boron-doped granular diamond, Advanced Materials. 26 (2014) 2034–2040. https://doi.org/10.1002/ADMA.201304667.

[194] F. Tafuri, J.R. Kirtley, Weak links in high critical temperature superconductors, Reports on Progress in Physics. 68 (2005) 2573–2663. https://doi.org/10.1088/0034-4885/68/11/R03.

[195] N. Titova, A.I. Kardakova, N. Tovpeko, S. Ryabchun, S. Mandal, D. Morozov, G.M. Klemencic, S.R. Giblin, O.A. Williams, G.N. Goltsman, T.M. Klapwijk, Slow Electron-Phonon Cooling in Superconducting Diamond Films, IEEE Transactions on Applied Superconductivity. 27 (2017). https://doi.org/10.1109/TASC.2016.2638199.

[196] M. Ortolani, S. Lupi, L. Baldassarre, U. Schade, P. Calvani, Y. Takano, M. Nagao, T. Takenouchi, H. Kawarada, Low-energy electrodynamics of superconducting diamond, Phys Rev Lett. 97 (2006) 097002. https://doi.org/10.1103/PHYSREVLETT.97.097002/.

[197] K. Winzer, D. Bogdanov, C. Wild, Electronic properties of boron-doped diamond on the border between the normal and the superconducting state, Physica C: Superconductivity and Its Applications. 432 (2005) 65–70. https://doi.org/10.1016/J.PHYSC.2005.07.011.

[198] F. Dahlem, P. Achatz, O.A. Williams, D. Araujo, E. Bustarret, H. Courtois, Spatially correlated microstructure and superconductivity in polycrystalline boron-doped diamond, Phys Rev B Condens Matter Mater Phys. 82 (2010) 3–6. https://doi.org/10.1103/PhysRevB.82.033306.

[199] D.M. Gnien, Nanocrystalline Diamond Films, Annual Review of Materials Science. 29 (2003) 211–259. https://doi.org/10.1146/ANNUREV.MATSCI.29.1.211.

[200] R.L. Peterson, J.W. Ekin, Critical-current diffraction patterns of grain-boundary Josephson weak links, 1990.

[201] A.R.R. Papa, E. Altshuler, Jc vs B curves and the Josephson junction assembly model for Y-Ba-Cu-O superconductors, Solid State Commun. 76 (1990) 799–801. https://doi.org/10.1016/0038-1098(90)90630-T.

[202] E. Afsaneh, H. Yavari, Magnetic field dependence of the critical current in a granular s-wave Superconductor, (n.d.).

[203] R.L. Peterson, J.W. Ekin, Josephson-junction model of critical current in granular YIBa2Cu307-q superconductors, 1988.

[204] J.L. Gonzalez, E.V.L. Mello, M.T.D. Orlando, E.S. Yugue, E. Baggio-Saitovitch, Transport critical current in granular samples under high magnetic fields, Physica C: Superconductivity and Its Applications. 364–365 (2001) 347–349. https://doi.org/10.1016/S0921-4534(01)00792-4.

[205] N. Metropolis, A.W. Rosenbluth, M.N. Rosenbluth, A.H. Teller, E. Teller, Equation of State Calculations by Fast Computing Machines, J Chem Phys. 21 (1953) 1087. https://doi.org/10.1063/1.1699114.

[206] W.K. Hastings, Monte Carlo sampling methods using Markov chains and their applications, Biometrika. 57 (1970) 97–109. https://doi.org/10.1093/BIOMET/57.1.97.

[207] R.Y. Rubinstein, D.P. Kroese, Simulation and the Monte Carlo Method., (2016) 435.

[208] J.M. Hammersley, D.C. Handscomb, Monte Carlo Methods, Springer Netherlands, Dordrecht, 1964. https://doi.org/10.1007/978-94-009-5819-7.

[209] G.O. Roberts, J.S. Rosenthal, Optimal scaling for various Metropolis-Hastings algorithms, Https://Doi.Org/10.1214/Ss/1015346320. 16 (2001) 351–367. https://doi.org/10.1214/SS/1015346320.

[210] P.R. Apte, R. Pinto, A.G. Chourey, Surface resistance, residual losses, and granularity in Ag-doped YBa2Cu3O7−δ thin films, J Appl Phys. 75 (1994) 4258. https://doi.org/10.1063/1.355965.

[211] G. Costabile, R. De Luca, S. Pace, A. Saggese, A.M. Testa, Temperature and magnetic field dependence of critical currents in granular superconductors, IEEE Transactions on Applied Superconductivity. 5 (1995) 1395–1398. https://doi.org/10.1109/77.402825.

[212] D.A. Balaev, A.A. Dubrovskiy, · S I Popkov, K.A. Shaykhutdinov, · M I Petrov, Magnetic Field Dependence of Intergrain Pinning Potential in Bulk Granular Composites YBCO + CuO Demonstrating Large Magneto-Resistive Effect, 21 (2008) 243–247. https://doi.org/10.1007/s10948-008-0324-1.

[213] A.C. Wright, K. Zhang, A. Erbil, Dissipation mechanism in a high-Tc granular superconductor: Applicability of a phase-slip model, Phys Rev B. 44 (1991) 863. https://doi.org/10.1103/PhysRevB.44.863.

[214] W.A.C. Passos, P.N. Lisboa-Filho, W.A. Ortiz, Magnetic field dependence of the critical current of tridimensional YBa2Cu3O7−δ Josephson junction arrays, J Magn Magn Mater. 226–230 (2001) 293–295. https://doi.org/10.1016/S0304-8853(00)01346-9.